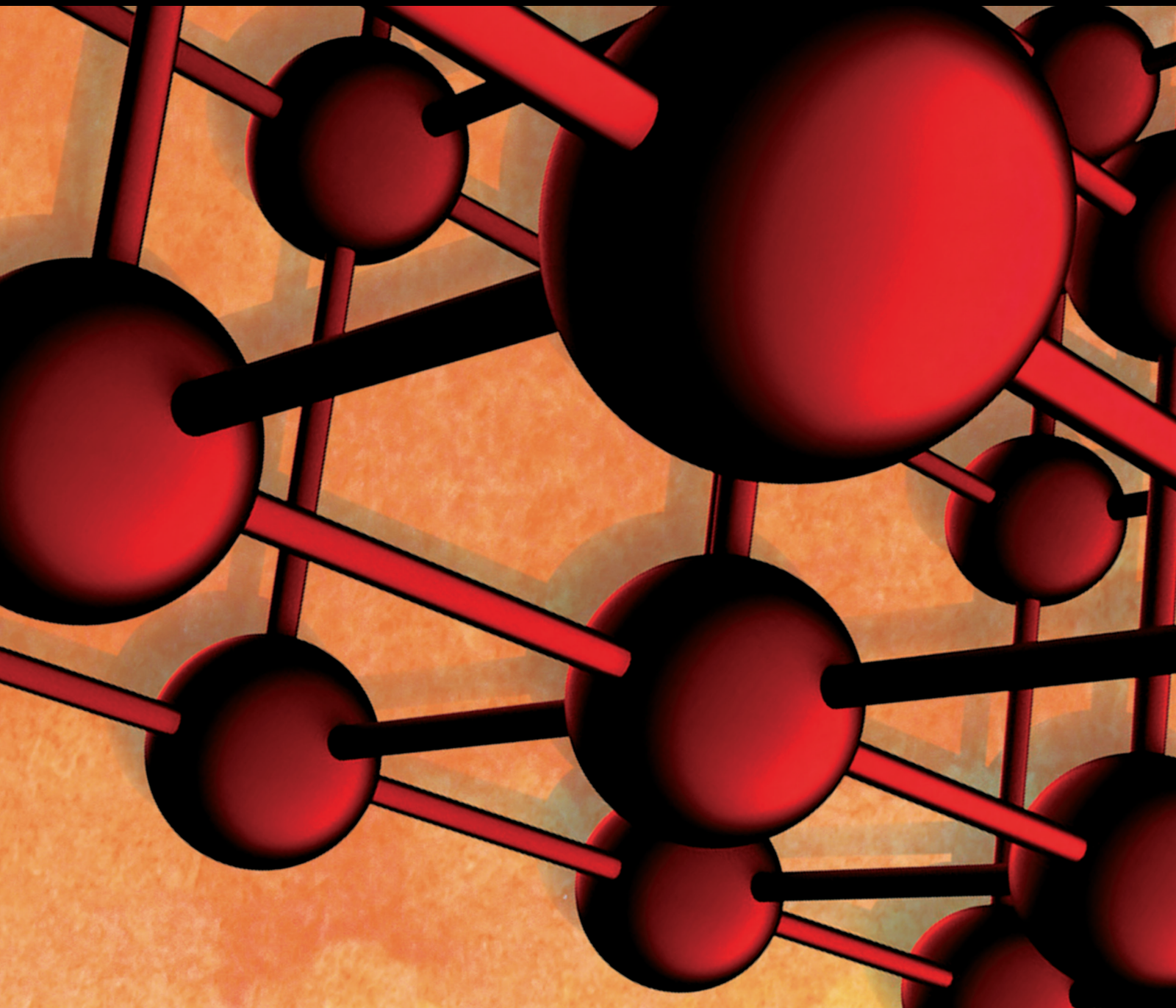


Advances in Materials Science and Engineering

Advances in Multiferroic Materials: Bulk, Nano, and Thin Films

Lead Guest Editor: Ashwini Kumar

Guest Editors: Poorva Sharma, Arvind Yogi, Qi Li, and Guolong Tan





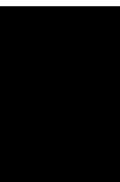
Advances in Multiferroic Materials: Bulk, Nano, and Thin Films

Advances in Materials Science and Engineering

**Advances in Multiferroic Materials:
Bulk, Nano, and Thin Films**

Lead Guest Editor: Ashwini Kumar


Guest Editors: Poorva Sharma, Arvind Yogi, Qi Li,
and Guolong Tan



Copyright © 2021 Hindawi Limited. All rights reserved.

This is a special issue published in "Advances in Materials Science and Engineering." All articles are open access articles distributed under the Creative Commons Attribution License, which permits unrestricted use, distribution, and reproduction in any medium, provided the original work is properly cited.

Chief Editor
















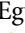
Amit Bandyopadhyay , USA

Associate Editors

Vamsi Balla , India
Mitun Das , USA
Sandip Harimkar, USA
Ravi Kumar , India
Peter Majewski , Australia
Enzo Martinelli , Italy
Luigi Nicolais , Italy
Carlos R. Rambo , Brazil
Michael J. Schütze , Germany
Kohji Tashiro , Japan
Zhonghua Yao , China
Dongdong Yuan , China
Wei Zhou , China

Academic Editors

Antonio Abate , Germany
Hany Abdo , Saudi Arabia
H.P.S. Abdul Khalil , Malaysia
Ismael Alejandro Aguayo Villarreal , Mexico
Sheraz Ahmad , Pakistan
Michael Aizenshtein, Israel
Jarir Aktaa, Germany
Bandar AlMangour, Saudi Arabia
Huaming An, China
Alicia Esther Ares , Argentina
Siva Avudaiappan , Chile
Habib Awais , Pakistan
NEERAJ KUMAR BHOI, India
Enrico Babilio , Italy
Renal Backov, France
M Bahubalendruni , India
Sudharsan Balasubramanian , India
Markus Bambach, Germany
Irene Bavasso , Italy
Stefano Bellucci , Italy
Brahim Benmokrane, Canada
Jean-Michel Bergheau , France
Guillaume Bernard-Granger, France
Giovanni Berselli, Italy
Patrice Berthod , France
Michele Bianchi , Italy
Hugo C. Biscaia , Portugal

Antonio Boccaccio, Italy
Mohamed Bououdina , Saudi Arabia
Gianlorenzo Bussetti , Italy
Antonio Caggiano , Germany
Marco Cannas , Italy
Qi Cao, China
Gianfranco Carotenuto , Italy
Paolo Andrea Carraro , Italy
Jose Cesar de Sa , Portugal
Wen-Shao Chang , United Kingdom
Qian Chen , China
Francisco Chinesta , France
Er-Yuan Chuang , Taiwan
Francesco Colangelo, Italy
María Criado , Spain
Enrique Cuan-Urquizo , Mexico
Lucas Da Silva , Portugal
Angela De Bonis , Italy
Abílio De Jesus , Portugal
José António Fonseca De Oliveira
Correia , Portugal
Ismail Demir , Turkey
Luigi Di Benedetto , Italy
Maria Laura Di Lorenzo, Italy
Marisa Di Sabatino, Norway
Luigi Di Sarno, Italy
Ana María Díez-Pascual , Spain
Guru P. Dinda , USA
Hongbiao Dong, China
Mingdong Dong , Denmark
Frederic Dumur , France
Stanislaw Dymek, Poland
Kaveh Edalati , Japan
Philip Eisenlohr , USA
Luis Evangelista , Norway
Michele Fedel , Italy
Francisco Javier Fernández Fernández , Spain
Spain
Isabel J. Ferrer , Spain
Massimo Fresta, Italy
Samia Gad , Egypt
Pasquale Gallo , Finland
Sharanabasava Ganachari, India
Santiago Garcia-Granda , Spain
Carlos Garcia-Mateo , Spain

Achraf Ghorbal , Tunisia
Georgios I. Giannopoulos , Greece
Ivan Giorgio , Italy
Andrea Grilli , Italy
Vincenzo Guarino , Italy
Daniel Guay, Canada
Jenő Gubicza , Hungary
Xuchun Gui , China
Benoit Guiffard , France
Zhixing Guo, China
Ivan Gutierrez-Urrutia , Japan
Weiwei Han , Republic of Korea
Simo-Pekka Hannula, Finland
A. M. Hassan , Egypt
Akbar Heidarzadeh, Iran
Yi Huang , United Kingdom
Joshua Ighalo, Nigeria
Saliha Ilican , Turkey
Md Mainul Islam , Australia
Ilia Ivanov , USA
Jijo James , India
Hafsa Jamshaid , Pakistan
Hom Kandel , USA
Kenji Kaneko, Japan
Rajesh Kannan A , Democratic People's
Republic of Korea
Mehran Khan , Hong Kong
Akihiko Kimura, Japan
Ling B. Kong , Singapore
Pramod Koshy, Australia
Hongchao Kou , China
Alexander Kromka, Czech Republic
Abhinay Kumar, India
Avvaru Praveen Kumar , Ethiopia
Sachin Kumar, India
Paweł Kłosowski , Poland
Wing-Fu Lai , Hong Kong
Luciano Lamberti, Italy
Fulvio Lavecchia , Italy
Laurent Lebrun , France
Joon-Hyung Lee , Republic of Korea
Cristina Leonelli, Italy
Chenggao Li , China
Rongrong Li , China
Yuanshi Li, Canada



Guang-xing Liang , China
Barbara Liguori , Italy
Jun Liu , China
Yunqi Liu, China
Rong Lu, China
Zhiping Luo , USA
Fernando Lusquiños , Spain
Himadri Majumder , India
Dimitrios E. Manolakos , Greece
Necmettin Maraşlı , Turkey
Alessandro Martucci , Italy
Roshan Mayadunne , Australia
Mamoun Medraj , Canada
Shazim A. Memon , Kazakhstan
Pratima Meshram , India
Mohsen Mhadhbi , Tunisia
Philippe Miele, France
Andrey E. Miroshnichenko, Australia
Ajay Kumar Mishra , South Africa
Hossein Moayedi , Vietnam
Dhanesh G. Mohan , United Kingdom
Sakar Mohan , India
Namdev More, USA
Tahir Muhmood , China
Faisal Mukhtar , Pakistan
Dr. Tauseef Munawar , Pakistan
Roger Narayan , USA
Saleem Nasir , Pakistan
Elango Natarajan, Malaysia
Rufino M. Navarro, Spain
Miguel Navarro-Cia , United Kingdom
Behzad Nematollahi , Australia
Peter Niemz, Switzerland
Hiroschi Noguchi, Japan
Dariusz Oleszak , Poland
Laurent Orgéas , France
Togay Ozbakkaloglu, United Kingdom
Marián Palcut , Slovakia
Davide Palumbo , Italy
Gianfranco Palumbo , Italy
Murlidhar Patel, India
Zbyšek Pavlík , Czech Republic
Alessandro Pegoretti , Italy
Gianluca Percoco , Italy
Andrea Petrella, Italy

Claudio Pettinari , Italy
Giorgio Pia , Italy
Candido Fabrizio Pirri, Italy
Marinos Pitsikalis , Greece
Alain Portavoce , France
Simon C. Potter, Canada
Ulrich Prah, Germany
Veena Ragupathi , India
Kawaljit Singh Randhawa , India
Baskaran Rangasamy , Zambia
Paulo Reis , Portugal
Hilda E. Reynel-Avila , Mexico
Yuri Ribakov , Israel
Aniello Riccio , Italy
Anna Richelli , Italy
Antonio Riveiro , Spain
Marco Rossi , Italy
Fernando Rubio-Marcos , Spain
Francesco Ruffino , Italy
Giuseppe Ruta , Italy
Sachin Salunkhe , India
P Sangeetha , India
Carlo Santulli, Italy
Fabrizio Sarasini , Italy
Senthil Kumaran Selvaraj , India
Raffaele Sepe , Italy
Aabid H Shalla, India
Poorva Sharma , China
Mercedes Solla, Spain
Tushar Sonar , Russia
Donato Sorgente , Italy
Charles C. Sorrell , Australia
Damien Soulat , France
Adolfo Speghini , Italy
Antonino Squillace , Italy
Koichi Sugimoto, Japan
Jirapornchai Suksaeree , Thailand
Baozhong Sun, China
Sam-Shajing Sun , USA
Xiaolong Sun, China
Yongding Tian , China
Hao Tong, China
Achim Trampert, Germany
Tomasz Trzepieciński , Poland
Kavimani V , India



Matjaz Valant , Slovenia
Mostafa Vamegh, Iran
Lijing Wang , Australia
Jörg M. K. Wiezorek , USA
Guosong Wu, China
Junhui Xiao , China
Guoqiang Xie , China
YASHPAL YASHPAL, India
Anil Singh Yadav , India
Yee-wen Yen, Taiwan
Hao Yi , China
Wenbin Yi, China
Tetsu Yonezawa, Japan
Hiroshi Yoshihara , Japan
Bin Yu , China
Rahadian Zainul , Indonesia
Lenka Zaji#c#kova# , Czech Republic
Zhigang Zang , China
Michele Zappalorto , Italy
Gang Zhang, Singapore
Jinghuai Zhang, China
Zengping Zhang, China
You Zhou , Japan
Robert Černý , Czech Republic

Contents

Observation of Spin Reorientation Transitions in Lead and Titanium-Modified BiFeO₃ Multiferroics

Ashwini Kumar , Poorva Sharma , Qi Li, Fujun Qiu, Jianhui Yan, Jingyou Tang, and Guolong Tan
Research Article (9 pages), Article ID 5525158, Volume 2021 (2021)



Investigation of Structural, Electrical, and Vibrational Properties of Bi_{1.98}A_{0.02}Fe₄O₉ (A = Ba, Ce) Multiferroic Ceramics

Ashwini Kumar , Poorva Sharma , Nikhil Bhardwaj, Jingyou Tang, and Guolong Tan
Research Article (8 pages), Article ID 5597415, Volume 2021 (2021)


Design of Hydraulic Bulging Die for Automobile Torsion Beam and Optimization of Forming Process Parameters

Kefan Yang , Youmin Wang, and Kexun Fu
Research Article (18 pages), Article ID 9982515, Volume 2021 (2021)


Study on Injection Molding Process Simulation and Process Parameter Optimization of Automobile Instrument Light Guiding Support

Hu Wu , Youmin Wang , and Mingyue Fang
Research Article (13 pages), Article ID 9938094, Volume 2021 (2021)

Study on Automotive Back Door Panel Injection Molding Process Simulation and Process Parameter Optimization

Guoqing Wang , Youmin Wang, and Deyu Yang
Research Article (15 pages), Article ID 9996423, Volume 2021 (2021)

Numerical Investigation and Mold Optimization of the Automobile Coat Rack Compression Molding

Youmin Wang, Xiangli Li , and He Sui
Research Article (19 pages), Article ID 6665753, Volume 2021 (2021)

Thermal Analysis and Structural Optimization of High-Efficiency Fuel Submersible Hot Water Machine

Zhaozhe Zhu , Youmin Wang , and Yingshuai Zhang 
Research Article (17 pages), Article ID 5566153, Volume 2021 (2021)

Research Article

Observation of Spin Reorientation Transitions in Lead and Titanium-Modified BiFeO₃ Multiferroics

Ashwini Kumar ¹, Poorva Sharma ¹, Qi Li,² Fujun Qiu,¹ Jianhui Yan,¹ Jingyou Tang,¹ and Guolong Tan^{1,3}

¹Key Laboratory of Multifunctional Materials, School of Electrical and Electronics Engineering, Luzhou Vocational and Technical College, Luzhou, Sichuan-646000, China

²School of Physics, Southeast University, Nanjing-211189, China

³Institute of New Materials, Wuhan University of Technology, Wuhan-430070, China

Correspondence should be addressed to Ashwini Kumar; ashu.dhanda2@hotmail.com and Poorva Sharma; poorva@nuaa.edu.cn

Received 6 May 2021; Accepted 23 September 2021; Published 14 October 2021

Academic Editor: Alicia E. Ares

Copyright © 2021 Ashwini Kumar et al. This is an open access article distributed under the Creative Commons Attribution License, which permits unrestricted use, distribution, and reproduction in any medium, provided the original work is properly cited.

We report the synthesis and basic characterization details of bulk Bi_{1-x}Pb_xFe_{1-x}Ti_xO₃ ($x = 0.05$ and 0.1) polycrystalline samples, which have been synthesized using the conventional solid-state route. We studied the effects of partially doping of Pb and Ti ion on structural, vibrational, and magnetic properties of multiferroic BiFeO₃. X-ray diffraction (XRD) was used for crystallographic studies, followed by Rietveld refinement, and phase formation of the compounds was confirmed, which indicates that the sample has rhombohedral ($R3c$, 100%) symmetry for $x = 0.05$ and $R3c$ (98%) + $P4mm$ (2%) symmetry for $x = 0.1$. X-ray absorption spectroscopy has been probed at Fe $L_{2,3}$ and O K edges to determine the valence (charge) state of Fe in BiFeO₃. Interestingly, the magnetic measurement results revealed the existence of spin reorientation transition in Pb and Ti-modified BiFeO₃, which indicates that the BiFeO₃ samples studied may find promising applications in memory and spintronic devices.

1. Introduction

A good understanding of the structure-property relationships can be used to develop new functional materials and devices. In recent years, multiferroics have great interest because in these materials, the electrical polarization emerges caused by the symmetry destruction of magnetic structure at magnetic ordering temperature. Rhombohedral distorted perovskite multiferroic BiFeO₃ (BFO) prepared under conventional synthesis conditions showed rich variety of subtle interaction among spin, charge, orbital, and lattice degrees of freedom. BFO shows G-type antiferromagnetic spin configuration below to Neel temperature (T_N) = 643 K and a ferroelectric order at around Curie temperature (T_C) = 1103 K [1, 2]. The ferroelectric perovskite PbTiO₃ (PTO) is a well-known tetragonal-distorted perovskite, with a space group of $P4mm$, $T_C = 763$ K, and a large anisotropic thermal expansion [3]. The tetragonal symmetry is obtained below

T_C , where PTO belongs to the space group $P4mm$, while above T_C , the cubic ($Pm3m$) symmetry describes the system [4]. These perovskite materials have attracted great interest due to their low-cost synthesis, interesting physical properties, and potential applications [5, 6]. In addition, due to the observation that ultrafast spin rotation times have possible industrial applications, the spin orientation transition (SRT) in antiferromagnetic insulators has attracted the attention of researchers [7–10]. SRTs above and below room temperature have been reported in BiFeO₃ [2, 10]. However, single crystal magnetic and neutron scattering studies have not yet revealed this reorientation transition in BiFeO₃ and are therefore questioned [2, 10, 11].

Bhattacharjee et al. reported a clear indication of SRT in $(1-x)$ BFO- (x) PTO solid solution using magnetization and neutron scattering studies over a small composition range ($0.27 < x < 0.31$) [10]. The spin reorientation present in $(1-x)$ BFO- (x) PTO is different

from the SRT in RFeO_3 , but it appears to be Morin transition in hematite. Gaikwad et al. also observed two magnetic anomalies around 124 and 213 K from low temperature infrared absorption spectra and magnetization data, which are related to the spin reorientation of Fe^{3+} ions and spin glass state [2]. The local structure of the FeO_6 octahedra has distortion and provides a mark for robust spin-phonon coupling in the BFO along with spin reorientation of Fe^{3+} [2]. Zhu et al. [12] reported the presence of a morphotropic phase boundary (MPB) area in a series of $(1-x)$ BFO- x PTO solid solutions. In these solid solutions, the tetragonal phase, rhombohedral phase, and an orthorhombic phase existed at the same time with a large tetragonality in the tetragonal phase segment. The tetragonal symmetry had huge anisotropy [13, 14]. According to the first principle calculations, the hybridization between the electronic states of cations and anions is crucial to ferroelectricity [14, 15]. Sati et al. [16] studied the effect of varying Pr and Ti codoping concentration on the structural, magnetic, vibrational, and impedance characteristics of BiFeO_3 synthesized by the conventional solid-state reaction method. Rietveld-refined XRD patterns indicate that as the doping concentration increases, a compositional driven crystal structure transformation from rhombohedral to an orthorhombic phase existed. Dielectric measurements showed the enhancement in dielectric properties with reduced dielectric loss with increase in doping concentration. Impedance analysis confirmed that with the increase of Pr and Ti concentrations in BiFeO_3 , the decrease in electrical conductivity was attributed to the enhancement of barrier performance, resulting in the suppression of the lattice conduction path due to lattice distortion. Due to codoping, the magnetic properties of the material are improved, attributed to the breakdown of the balance between antiparallel sublattice magnetization of Fe^{3+} ions and the collapse of the spatially modulated spin structure caused by the structural transformation [16].

Here, we report the synthesis and analysis of structural and magnetic properties of polycrystalline $\text{Bi}_{1-x}\text{Pb}_x\text{Fe}_{1-x}\text{Ti}_x\text{O}_3$ ($x=0.05, 0.1$) samples. Rietveld refinement method has been used to analyze the structural parameters. We have been studied the effect of Pb and Ti ions doping on structural, vibrational, and magnetic properties in BiFeO_3 . Polycrystalline ceramics of $\text{Bi}_{1-x}\text{Pb}_x\text{Fe}_{1-x}\text{Ti}_x\text{O}_3$ ($x=0.05$ and 0.1) are abbreviated as BPFTO-05 and BPFTO-10, respectively, for further communication.

2. Experimental Details

The polycrystalline $\text{Bi}_{1-x}\text{Pb}_x\text{Fe}_{1-x}\text{Ti}_x\text{O}_3$ ($x=0.05$ and 0.1) samples were prepared by the conventional solid-state route. High-purity oxides such as Bi_2O_3 (99.99% purity), Fe_2O_3 (99.9% purity), PbO (99.99% purity), and TiO_2 (99.99% purity) were used as starting reagents. Starting reagents were carefully weighed and mixed in stoichiometric ration in an agate mortar for 6 hours using high-purity alcohol as a

medium and then calcined at 650°C for 6 hours. The leaching process was carried out with distilled water and HNO_3 to remove impurities from the samples. The precipitated precursor particles at the bottom were collected, and the excess salts at the top layer were discarded. Pour out the particles repetitively with distilled water and HNO_3 to eliminate impurities. Then, the washed particles were dried at room temperature and further calcined at 700°C for 5 hours [17, 18]. XRD measurements were carried out with $\text{CuK}\alpha_1$ (1.5406 Å) radiation using a Bruker D8 Advance X-ray diffractometer and analyzed with the Rietveld refinement method [17]. The Raman spectrum was carried out by “Jobin-Yovon Horiba LABRAM (System HR800) spectrometer with a 488 nm excitation source equipped with a Peltier cooled CCD detector (1024 × 256 pixels of 26 microns)” [17]. DC magnetization measurements were performed using the physical property measurement system (Quantum Design, PPMS-9). Zero-field cooling (ZFC) and field cooling (FC) processes were used to acquire the temperature dependence of magnetization [19]. XAS was used at normal incidence using the linearly polarized light and in the total electron yield mode at photoelectron station of Beijing Synchrotron Radiation Facility (BSRF), Beijing. The resolution of XAS is 0.3 eV [20].

3. Results and Discussion

3.1. Structural Study. Figure 1 shows the X-ray diffraction pattern for $\text{Bi}_{1-x}\text{Pb}_x\text{Fe}_{1-x}\text{Ti}_x\text{O}_3$ ($x=0.05, 0.1$) samples which are abbreviated as BPFTO-05 and BPFTO-10, respectively. X-ray diffraction data suggest that BPFTO-05 sample possesses rhombohedral structure with the $R3c$ space group. All the obtained diffraction peaks completely match the standard crystal data corresponding to JCPDS file 86-1518 [17], while the sample BPFTO-10 shows the mixed phase ($R3c$, 98% + $P4mm$, 2%) symmetry [21], it matches with the reference data (JCPDS file number 72-1832) completely, except for low-intensity impurity peaks near $2\theta = 27.86^\circ$ and 29.04° related to $\text{Bi}_2\text{Fe}_4\text{O}_9$. The peak splitting is decreasing in BPFTO-10 in comparison to BPFTO-05 [22] results coexistence of two phases. The tetragonal phase had large anisotropy [23]. Thorough important crystallographic parameters acquired through the refinements are given in Table 1.

3.2. Rietveld Refinement of XRD Data. The room temperature XRD patterns of BPFTO-05 and BPFTO-10 ceramics were refined using FullProf software, as shown in Figures 2(a) and 2(b). In the refining process, lattice parameters and profile parameters were refined, while atomic positions and anisotropic displacement parameters were fixed to the values given by earlier reports [24]. The calculated XRD pattern of these two samples are in good agreement with the experimentally observed XRD data with mostly small R values as given in Table 1. The lattice coordinates of the samples are given in Table 2. For BPFTO-05, the refined lattice parameters such as $a = 5.5785 \text{ \AA}$ and

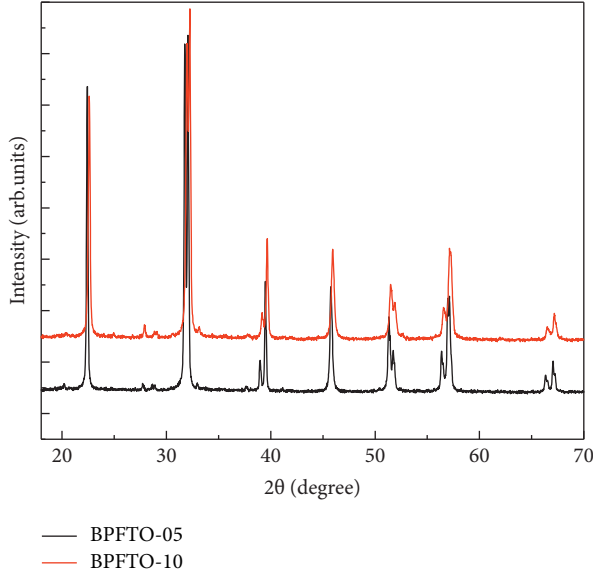


FIGURE 1: X-ray powder diffraction (XRD) pattern of $\text{Bi}_{1-x}\text{Pb}_x\text{Fe}_{1-x}\text{Ti}_x\text{O}_3$ ($x=0.05$ and 0.1) bulk ceramic at room temperature.

TABLE 1: Details of Rietveld-refined XRD parameters for $\text{Bi}_{1-x}\text{Pb}_x\text{Fe}_{1-x}\text{Ti}_x\text{O}_3$ ($x=0.05$ and 0.1) samples.

Parameters	$x=0.05$	$x=0.1$
2θ range (deg.)	20° – 80°	20° – 80°
Step size (deg.)	0.02°	0.02°
Wavelength	1.5406 \AA	1.5406 \AA
Number of refined parameters	25	21
Space group	$R3c$ (100%)	$R3c$ (99%) + $P4mm$ (1%)
a (\AA)	5.5865 (3)	5.5854 (5)/4.5854 (5)
b (\AA)	5.5865 (3)	5.5854 (5)/4.5854 (5)
c (\AA)	13.8757 (3)	13.8595 (3)/5.9453 (4)
Volume (\AA^3)	374.88 (1)	374.451 (1)/125.021 (2)
R_F	3.68	4.05/59.1
R_{Bragg}	4.48	5.12/91.9
R_{wp}	12.4	12.0
R_{exp}	6.94	9.37
R_p	14.3	20.0
χ^2	2.89	1.638
GOF	1.7	1.3

$c = 13.8547 \text{ \AA}$ and crystalline angles, i.e., $\alpha = \beta = 90^\circ$, $\gamma = 120^\circ$, match well with rhombohedral $R3c$ symmetry described in another reports [17, 25].

3.3. SEM Micrograph Analysis. Figure 3 shows the SEM micrograph for BPFTO-05 and BPFTO-10 samples. SEM micrographs clearly exhibits flakes such as morphology of polycrystalline-prepared sample, and the dopant Pb and Ti ions highly influenced the morphology of BFO. Micrograph shows dense structure with nonuniformity in the size of flakes. Also, the fracture type surface in the BPFTO-10

sample was noticeably more transgranular, demonstrating expressively stronger internal stresses, perhaps due to the higher tetragonal distortion for this composition [22, 26]. For both the samples, an inhomogeneous grain growth was found that resulted in notable residual porosity. The average crystallite size for BPFTO-05 is about $0.8\text{--}1 \mu\text{m}$ and for BPFTO-10 is $0.5\text{--}0.8 \mu\text{m}$. The average crystallite size can be reduced by adding Pb and Ti ions BiFeO_3 attributed to the distinct ionic size of Pb^{2+} and Ti^{4+} ions than Bi^{3+} in BiFeO_3 .

3.4. XAS Spectra. XAS measurements were performed on both BPFTO-05 and BPFTO-10 samples. Due to large $2p$ core hole spin-orbit coupling energy, the measured Fe $L_{2,3}$ edge XAS spectra are divided into L_3 ($2p_{3/2}$) and L_2 ($2p_{1/2}$) regions for BPFTO-05 and BPFTO-10, as shown in Figure 4(a) [27]. When Fe ions are located at the L_3 and L_2 edges, strong absorption peaks appeared at the photon energies of 709.6 eV (t_{2g}) – 710.2 eV (e_g) and 722 eV (t_{2g}) – 723.8 eV (e_g), respectively. The line shape of Fe $L_{2,3}$ edge determines the valence state information of Fe ions [27]. We observed the prominent presence of XAS signal in Fe $L_{2,3}$ edge [20]. These results indicate that the samples have the electronic configuration such as $\alpha\text{-Fe}_2\text{O}_3$ and LaFeO_3 , and Fe^{3+} is the leading oxidation states of Fe ions. The electrostatic interaction is between O $2p$ and Fe $3d$ t_{2g} and e_g orbitals, hybridization of O $2p$ with Bi $6s/6p$ orbitals, hybridization of O $2p$ with Fe $4s/4p$ orbitals clearly exists in the prepared systems. Figure 4(b) shows the normalized OK edge XAS spectra for both of these prepared samples, which are evidently showing vacant O $2p$ state in the conduction band [28]. The first two bands denote the hybridization of O $2p$ through unoccupied Fe $3d$ orbitals which splits in t_{2g} and e_g initiated by the electrostatic interaction concerning the O $2p$ and Fe $3d$ orbitals [28]. Although, another band feature starting at about $\sim 540 \text{ eV}$ corresponds to the hybridization of O $2p$ with Fe $4s/4p$ orbitals. Improvement in the hybridization of Bi $6s^2$ lone pair with O $2p$ orbitals is liable for the enhanced ferroelectric behavior as detected in prepared samples [20, 27, 28].

3.5. Magnetic Analysis. Temperature dependence zero-field cooling, ZFC (plotted with blue circle), and the field cooling, FC (plotted with red circle), magnetic curves for both BPFTO-05 and BPFTO-10 samples are shown in Figures 5(a) and 5(b). The samples were cooled down to the temperature of 10 K without an external applied magnetic field in the ZFC mode. Then, we measured the magnetization of the sample with increase in temperature with the applied magnetic field of 0.1 T. Whereas, in the FC mode, the magnetization was measured while cooling down the sample to temperature of 10 K (as shown in Figures 5(a) and 5(b)). In the FC process, the magnetization reduces with temperature increases. Meanwhile, in the ZFC process, the magnetization takes a magnetic transition around temperature of 160 and 232 K. A noticeable anomaly is observed around 233 K in the BPFTO-05 sample in the FC mode, which reveals its AFM behavior, and is matched well with previously reported data [29, 30].

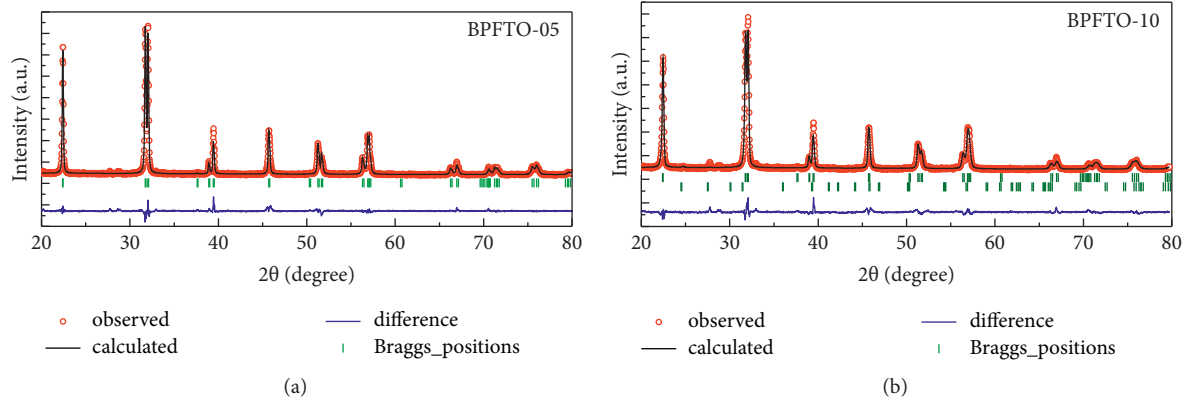


FIGURE 2: Rietveld refined XRD pattern for $\text{Bi}_{1-x}\text{Pb}_x\text{Fe}_{1-x}\text{Ti}_x\text{O}_3$ ($x=0.05$) and $\text{Bi}_{1-x}\text{Pb}_x\text{Fe}_{1-x}\text{Ti}_x\text{O}_3$ ($x=0.1$) bulk ceramic. The open red circles represent the observed patterns; continuous black and blue color lines represent calculated and difference patterns, respectively. The green tick marks correspond to the position of the allowed Bragg reflections. (a) BPFTO-05. (b) BPFTO-10.

TABLE 2: Refined structural parameters for $\text{Bi}_{1-x}\text{Pb}_x\text{Fe}_{1-x}\text{Ti}_x\text{O}_3$ ($x=0.05$ and 0.1) bulk ceramics.

	x	y	z
BiFeO_3 ($R3c$) [25]			
Bi	0.0	0.0	0.2755
Fe	0.0	0.0	0.0
O	0.6679	0.7647	0.5489
$x=0.05$ $R3c$ (100%)			
Bi/Pb	0.0	0.0	0.2755
Fe/Ti	0.0	0.0	0.0
O	0.6684	0.7648	0.5492
$x=0.1$ $R3c$ (99%) + $P4mm$ (1%)			
Bi/Pb	0.0/0.0	0.0/0.0	0.2723/0.0
Fe/Ti	0.0000/0.5	0.0/0.5	0.0/0.5973
O-1	—/0.5	—/0.5	—/0.1784
O-2	−1.5575/0.5	−0.062/0.0	−0.1786/0.685

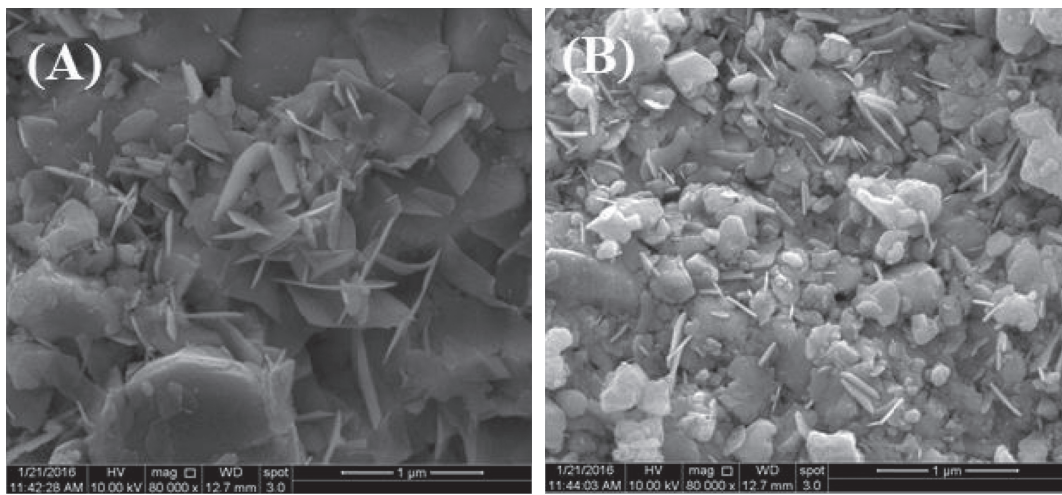


FIGURE 3: SEM micrograph of $\text{Bi}_{1-x}\text{Pb}_x\text{Fe}_{1-x}\text{Ti}_x\text{O}_3$ ($x=0.05$ and 0.1) pellet ceramics. (a) $x=0.05$; (b) $x=0.1$.

Another magnetic transition occurs below the temperature of 160 K in the ZFC mode. The obtained experimental result shows that a change in spin ordering at low temperature attributes to spin reorientation of Fe^{3+} ions in

BiFeO_3 comparable with other rare earth orthoferrites. Though, for bulk BFO single crystal, the spin reorientation has been described close to 50 K [2, 25, 31, 32]. This deviation in BFO can be attributed to the particle size effect or

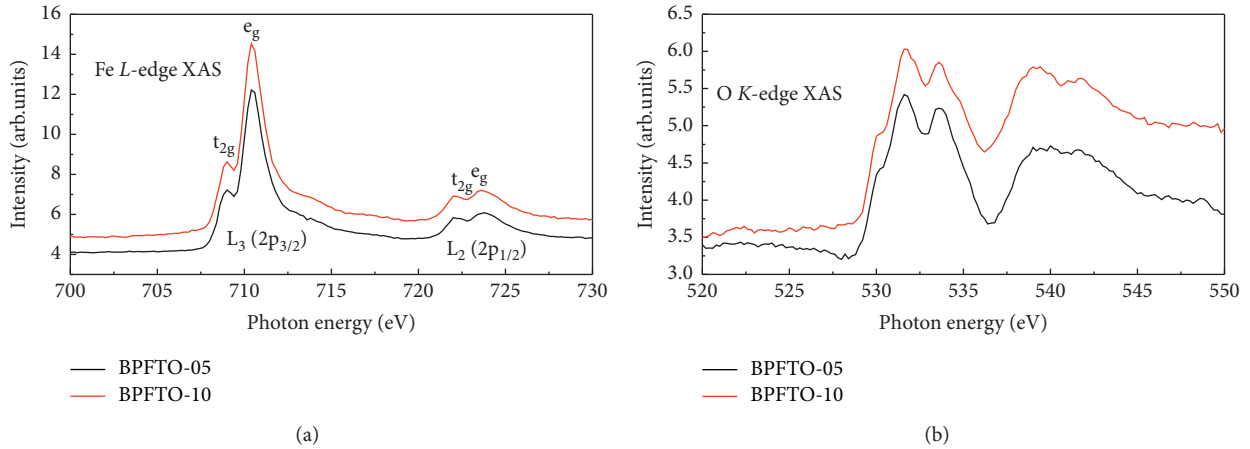


FIGURE 4: XAS spectra are divided into (a) $L_3 (2p_{3/2})$ and $L_2 (2p_{1/2})$ regions due to the large $2p$ core hole spin-orbit coupling energy for BPFTO-05 and BPFTO-10. (b) The OK edge spectrum of BPFTO-05 and BPFTO-10 samples results from excitations to O $2p$ orbitals interacting with Fe orbitals.

presence of flakes in SEM micrographs, which is the cause of induced strain, distortion, and lattice disorder. Below 160 K, the magnetization is observed to decrease in the ZFC curve until 50 K and then increase again until 10 K. However, in the FC curve, no significant change in the magnetization with the decrease in temperature was detected, but it changed around temperature of 232 K. The origin of observed SRT is due to the orientation of Fe^{3+} spins, and the orientation of Fe^{3+} spins is caused by the destruction of the antiferromagnetic spiral order. For the BFO system, the magnetic ordering is very complicated due to the Dzyaloshinskii-Moriya (DM) interaction, which leads to a canted AFM ordering of Fe^{3+} spins in the system [2].

According to Gaikwad et al., “the AFM ordering results in rotation of spins, and the order parameter of this helical ordering is 62 nm. The particles having size less than 62 nm, breaking of the helical ordering of the spins along AFM, are observed. It suppresses the modulated spin structure and improves magnetization” [2]. On increasing the Pb ion substitution in BFO, there is not a prominent transition like BPFTO-05, but there is little sign of presence of magnetic transitions around temperature of 94, 174, and 224 K in BPFTO-10. Somehow, we revealed small shift in transition temperature for BPFTO-10 as compared to the BPFTO-05 sample. As it is well known that $BiFeO_3$ is an antiferromagnet and $PbTiO_3$ is diamagnetic, thus as Pb and Ti ion increases, it affects the magnetic properties obviously and may vanish the magnetic transitions completely as $PbTiO_3$ is completely ferroelectric material till it is having a tetragonal phase. According to the structural analysis, BPFTO-10 exists simultaneously in two phases rhombohedral and tetragonal near the MPB region. Consequently, it is sensible to recommend that each of these phases undergoes an antiferromagnetic ordering at a different temperature, leading to an anomaly on the temperature dependence of magnetic moment [12]. The T_N for both phases decreases with the increase in x across the MPB region [12]. The magnetic curve in the ZFC mode decreases first and then increases at spin reorientation region

temperature, a behavior distinctly different from the FC magnetic data that continuously decrease with lowering in temperature. This behavior is evocative of weak ferromagnetism (FM) associated with magnetic glassiness or cluster glass (CG) behavior [33].

Figures 5(c) and 5(d) represent the magnetization versus magnetic field at two different temperatures of 10 and 300 K. Magnetization loops recorded at 300 K show a remnant value of $\sim 0.004 \mu_B$, as shown in Figures 5(c) and 5(d). This weak ferromagnetic moment or canted antiferromagnetic ordering, seeming small when compared with that of other $BiFeO_3$ -based compositions such as $Bi_{0.7}Ba_{0.3}FeO_3$ [34], may take place within a tetragonal phase allowing lattice transverse softening. We can observe in Figures 5(c) and 5(d) that magnetization loops recorded at 10 K show a very less remnant value of $\sim 0.001 \mu_B$, for both the samples. Magnetic moments at 10 K show true antiferromagnetic ordering in both prepared samples. However, possibly the enhancement in the resultant magnetic moment attributed to the broken cycloid spin structure caused by the variation in crystallographic arrangement with Pb and Ti doping in $BiFeO_3$ [35–38].

3.6. Raman Analysis. For the vibrational study, we probed the Raman spectroscopy at room temperature for BPFTO-05 and BPFTO-10 samples with an excitation wavelength of 514 nm, as shown in Figure 6. Distorted rhombohedral-structured BFO yields 18 optical phonon modes and which can be summarized using following irreducible representation: $\Gamma_{opt} = 4A_1 + 5A_2 + 9E$ [16]. According to the group theory, 13 modes ($\Gamma_{Raman, R3c} = 4A_1 + 9E$) are Raman active, while 5 A_2 modes be Raman inactive [17, 39, 40]. A_1 modes are related with Fe ions and E modes are allied with Bi ions. The mode positions dependency on parent BFO and doped BFO is given in Table 3 [17, 39, 41]. In the present work, as obtained, ten Raman active phonon modes of BPFTO-05 and BPFTO-10 samples including A_1 -1, A_1 -2, A_1 -3, E-3, E-4, E-5, E-6, E-7, E-8, and E-9 modes at 134 (135), 165 (166), 214

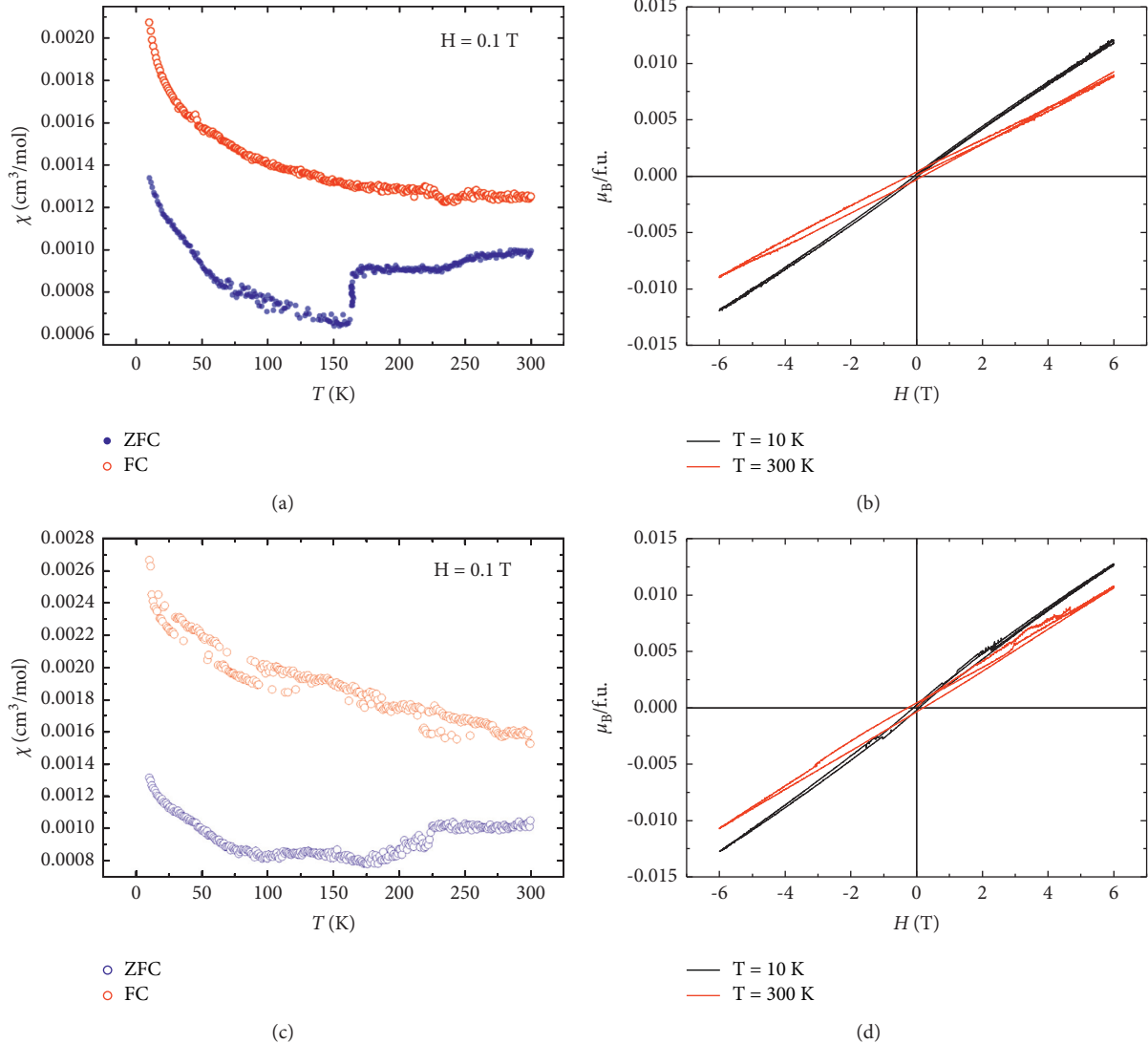


FIGURE 5: Temperature dependence of ZFC and FCC magnetization curve for (a) BPFTO-05, (b) BPFTO-10, (c) M-H loop for BPFTO-05, and (d) BPFTO-10.

(216), 269 (264), 308 (309), 368 (362), 475 (470), 514 (524), 542 (542), and 624 (625) cm^{-1} are in good agreement with earlier reported data [41, 42]. The stereochemical activity of the Bi ion lone pair electron which is principally responsible for the change in both Bi–O covalent bonds originates ferroelectricity in BFO. It is believed that the six characteristic modes, i.e., E-1, A_1 -1, A_1 -2, A_1 -3, A_1 -4, and E-2 are accountable for the ferroelectric nature of the BFO samples [17]. As evident from the X-ray diffraction, the crystal symmetry contains rhombohedral ($R3c$) and (rhombohedral ($R3c$) + tetragonal phase ($P4mm$)) on subsequent doping of Pb ion and Ti ion at A-site and B-site of BFO samples, and there are changes in Raman modes as compared to BFO.

These alterations in crystallographic structure is ascribed the A-site and B-site disorder created by Pb and Ti ion substitution, “which leads to the shifting of Raman modes at higher and lower frequencies” with sudden disappearance of mode (E-8 in BPFTO-05 and A_1 -4, E-1, and E-2 in both of

the prepared samples) [17]. Additional E-1 and E-2 modes at 68 and 75 cm^{-1} appear in doped BFO samples, but is too weak to detect in the prepared sample. These phenomena reveal the change of Bi–O covalent bonds with increasing doping concentration as compared to BFO and induced ferroelectricity. Moreover, a shift in the Raman characteristic modes towards the higher wavenumber is noted with increasing doping concentration in prepared BPFTO ceramics as compared to pure BFO, which are due to Bi–O bond vibrations [43, 44]. This can be attributed to the lower atomic weight of Pb (207.2) compared to Bi^{+3} (208.98) and Ti (47.86) compared to Fe^{+3} (55.84) [17]. Furthermore, for BPFTO-05 and BPFTO-10 samples, the intensity of E-modes increase, whereas A_1 mode intensity decreases significantly. This might be due to some contractions in unit cell volume of the structural phase as rhombohedral ($R3c$) and (rhombohedral ($R3c$) + tetragonal ($P4mm$)) in BPFTO-10, respectively, and account for the fact that doping affects the

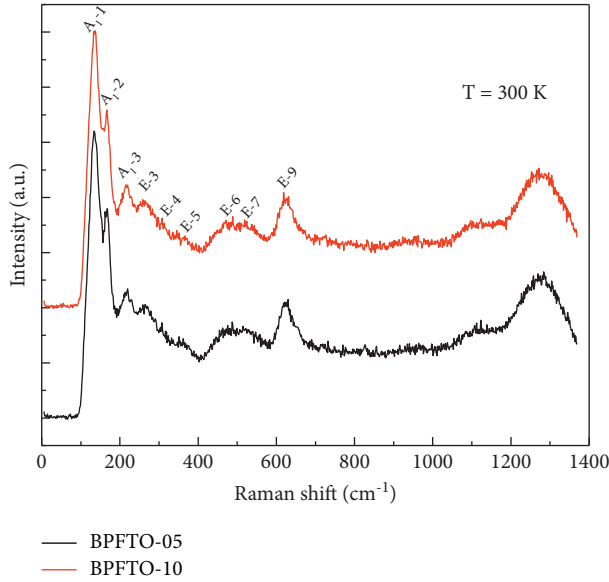


FIGURE 6: Raman spectra for $\text{Bi}_{1-x}\text{Pb}_x\text{Fe}_{1-x}\text{Ti}_x\text{O}_3$ ($x = 0.05$ and 0.1) at room temperature with excitation wavelength of 514 nm.

TABLE 3: Comparison of Raman modes (cm^{-1}) from $\text{Bi}_{1-x}\text{Pb}_x\text{Fe}_{1-x}\text{Ti}_x\text{O}_3$ ($x = 0.05$ and 0.1) bulk ceramics and literature.

Raman modes (cm^{-1})	Present study		Literature BFO [39]
	$x = 0.05$	$x = 0.1$	
A ₁₋₁	165	166	178 (A)
A ₁₋₂	214	216	229 (A)
A ₁₋₃	—	—	502 (A)
A ₁₋₄	—	—	591 (A)
E-1	—	—	81 (E)
E-2	134	135	175 (E)
E-3	269	264	242 (E)
E-4	308	309	276 (E)
E-5	368	362	346 (E)
E-6	475	470	368 (E)
E-7	514	524	430 (E)
E-8	—	542	468 (E)
E-9	624	625	616 (E)

symmetry in BFO [16]. The two-magnon features are almost invisible in the Raman spectrum, but they are advantageous in this study. We detected the broad peak approximately at 964 (955) cm^{-1} in BPFTO-05 and BPFTO-10, respectively, in the frequency region of 800 – 1500 cm^{-1} . The peak position of the scattering frequency of two-magnon may be equal to twice energy of zone boundary magnon estimated from the exchange parameters of prepared ceramics [20]. We have observed peaks at 1107 (1108) cm^{-1} and 1279 cm^{-1} for BPFTO-05 and BPFTO-10 samples. The above explained peaks were assigned as the two-phonon Raman scattering process of the prepared samples [45].

4. Conclusions

In conclusion, $\text{Bi}_{1-x}\text{Pb}_x\text{Fe}_{1-x}\text{Ti}_x\text{O}_3$ ($x = 0.05, 0.1$) polycrystalline bulk ceramics were synthesized by the

conventional solid-state route. X-ray diffraction along with the Rietveld refinement show that BPFTO-05 and BPFTO-10 samples have ($R3c$) and ($R3c + P4mm$) symmetry, respectively, which are confirmed by Raman scattering data. Through the magnetic data, we have observed the spin re-orientation transition above 100 K. It is necessary to use advanced techniques such as neutron scattering to study the properties of observed phenomena in more detail.

Data Availability

The data used to support the findings of this study are included within the article and are available from the corresponding author upon request.

Disclosure

The manuscript is presented in abstract form at the International Conference on Minerals Metallurgy and Materials.

Conflicts of Interest

The authors declare that they have no conflicts of interest.

Acknowledgments

The authors acknowledge the financial support from the National Natural Science Foundation of China (11774276) and Key Project of Science and Technology of Sichuan Province (2021YFS0355). Kumar and Sharma acknowledge the Luzhou Vocational and Technical College for providing them start-up research grants and well support and also acknowledge the Luzhou talent work leading group office for job incentive and resettlement subsidies for high-level talents. The authors are grateful to Dr. S. Satapathy for their long-term collaboration and numerous fruitful discussion.

References

- [1] D. I. Woodward, I. M. Reaney, R. E. Eitel, and C. A. Randall, "Crystal and domain structure of the BiFeO_3 – PbTiO_3 solid solution," *Journal of Applied Physics*, vol. 94, p. 3314, 2009.
- [2] V. M. Gaikwad and S. A. Acharya, "Investigation of spin phonon coupling in BiFeO_3 based system by f," *Journal of Applied Physics*, vol. 114, no. 19, Article ID 193901, 2013.
- [3] J. Hong and D. Vanderbilt, "Mapping the energy surface of PbTiO_3 in multidimensional electric-displacement space," *Physical Review B*, vol. 84, no. 11, Article ID 115107, 2011.
- [4] K. Abd elmadjid, F. Gheorghiu, M. Zerdali, M. Kadri, and S. Hamzaoui, "Preparation, structural and functional properties of PbTiO_3 - δ ceramics," *Ceramics International*, vol. 45, no. 7, pp. 9043–9047, 2019.
- [5] A. K. Kalyani, R. Garg, and R. Ranjan, "Competing A-site and B-site driven ferroelectric instabilities in the $(1-x)\text{PbTiO}_3$ – $(x)\text{BiAlO}_3$ system," *Applied Physics Letters*, vol. 94, no. 20, Article ID 202903, 2009.
- [6] S. Aoyagi, A. Sawada, J. Harada et al., "Evidence for Pb-O covalency in tetragonal PbTiO_3 ," *Physical Review Letters*, vol. 87, Article ID 217601, 2001.
- [7] R. Nathas, S. J. Pickart, H. A. Alperin, and P. J. Brown, "Polarized-neutron study of hematite, phys rev 136: a1641; schroerer D and nininger jr RC (1967) Morin transition in

- α -Fe₂O₃ microcrystals,” *Physical Review Letters*, vol. 19, p. 632, 1964.
- [8] C. Frandsen and S. Morup, “Spin rotation in α -Fe₂O₃ nanoparticles by interparticle interactions,” *Physical Review Letters*, vol. 94, Article ID 027202, 2005.
- [9] K. Zhang, K. Xu, X. Liu et al., “Resolving the spin reorientation and crystal-field transitions in TmFeO₃ with terahertz transient,” *Scientific Reports*, vol. 6, no. 1, Article ID 23648, 2016.
- [10] S. Bhattacharjee, A. Senyshyn, H. Fuess, and D. Pandey, “Morin-type spin-reorientation transition below the Néel transition in the monoclinic compositions of (1 - x) BiFeO₃-xPbTiO₃ (x = 0.25 and 0.27): a combined dc magnetization and x-ray and neutron powder diffraction study,” *Physical Review B: Condensed Matter*, vol. 87, Article ID 054417, 2013.
- [11] M. Ramazanoglu, W. Ratcliff, Y. J. Choi, S. Lee, S.-W. Cheong, and V. Kiryukhin, “Temperature-dependent properties of the magnetic order in single-crystal BiFeO₃,” *Physical Review B*, vol. 83, no. 17, Article ID 174434, 2011.
- [12] W.-M. Zhu, H.-Y. Guo, and Z.-G. Ye, “Structural and magnetic characterization of multiferroic (BiFeO₃)_{1-x}(PbTiO₃)_x solid solutions,” *Physical Review B: Condensed Matter*, vol. 78, Article ID 014401, 2008.
- [13] H. Yabuta, H. Tanaka, T. Furuta et al., “Enhancement of tetragonal anisotropy and stabilisation of the tetragonal phase by Bi/Mn-double-doping in BaTiO₃ ferroelectric ceramics,” *Scientific Reports*, vol. 7, no. 1, Article ID 45842, 2017.
- [14] K. K. Mishra, R. M. Sarguna, S. Khan, and A. K. Arora, “x-T phase diagram of La-substituted BiFeO₃-PbTiO₃,” *AIP Advances*, vol. 1, no. 3, Article ID 032126, 2011.
- [15] R. E. Cohen, “Origin of ferroelectricity in perovskite oxides, nature 358:136–138; benedek NA, fennie CJ (2013) why are there so few perovskite ferroelectrics,” *Journal of Physical Chemistry C*, vol. 117, pp. 13339–13349, 1992.
- [16] P. C. Sati, M. Arora, S. Chauhan, M. Kumar, and S. Chhoker, “Structural, magnetic, vibrational and impedance properties of Pr and Ti codoped BiFeO₃ multiferroic ceramics,” *Ceramics International*, vol. 40, no. 6, pp. 7805–7816, 2014.
- [17] A. Kumar and D. Varshney, “Crystal structure refinement of Bi_{1-x}NdxFeO₃ multiferroic by the Rietveld method,” *Ceramics International*, vol. 38, no. 5, pp. 3935–3942, 2012.
- [18] V. R. Palkar, D. C. Kundaliya, S. K. Malik, and S. Bhattacharya, “Magnetolectricity at room temperature in the Bi_{0.9-x}TbxLa_{0.1}FeO₃ system,” *Physical Review B*, vol. 69, no. 21, Article ID 212102, 2004.
- [19] P. Sharma, Y. Xu, H. Fan et al., “Spin reorientation functionality in antiferromagnetic TmFe_{1-x}InxO₃ polycrystalline samples,” *Journal of Alloys and Compounds*, vol. 789, pp. 80–89, 2019.
- [20] A. Kumar, P. Sharma, W. Yang, J. Shen, D. Varshney, and Q. Li, “Effect of La and Ni substitution on structure, dielectric and ferroelectric properties of BiFeO₃ ceramics,” *Ceramics International*, vol. 42, no. 13, pp. 14805–14812, 2016.
- [21] C. M. Fernández-Posada, A. Castro, J.-M. Kiat et al., “A novel perovskite oxide chemically designed to show multiferroic phase boundary with room-temperature magnetoelectricity,” *Nature Communications*, vol. 7, no. 1, Article ID 12772, 2016.
- [22] J. Cheng, S. Yu, J. Chen, Z. Meng, and L. E. Cross, “Dielectric and magnetic enhancements in BiFeO₃-PbTiO₃ solid solutions with La doping,” *Applied Physics Letters*, vol. 89, no. 12, Article ID 122911, 2006.
- [23] L. F. Cotica, V. F. Freitas, I. B. Catellani, I. A. Santos, D. Garcia, and J. A. Eiras, “High-resolution structural studies and covalent bond interactions in BiFeO₃-PbTiO₃ compounds: the role of ferroism,” *Applied Physics Letters*, vol. 101, no. 17, Article ID 172903, 2012.
- [24] A. Basu, R. Jana, R. Ranjan, and G. D. Mukherjee, “Pressure effects on model ferroelectric BiFeO₃-PbTiO₃: m,” *Physical Review B*, vol. 93, no. 21, Article ID 214114, 2016.
- [25] A. Jaiswal, R. Das, K. Vivekanand, P. Mary Abraham, S. Adyanthaya, and P. Poddar, “Effect of reduced particle size on the magnetic properties of chemically synthesized BiFeO₃ nanocrystals,” *Journal of Physical Chemistry C*, vol. 114, no. 5, pp. 2108–2115, 2010.
- [26] J.-R. Cheng, N. Li, and L. E. Cross, “Structural and dielectric properties of Ga-modified BiFeO₃-PbTiO₃ crystalline solutions,” *Journal of Applied Physics*, vol. 94, no. 8, pp. 5153–5157, 2003.
- [27] K.-T. Ko, M. H. Jung, Q. He et al., “Concurrent transition of ferroelectric and magnetic ordering near room temperature,” *Nature Communications*, vol. 2, no. 1, p. 567, 2011.
- [28] A. Kumar, J. Shen, H. Zhao, Q. Zhengjian, and Q. Li, “Crystallographic and magnetic properties of nanocrystalline perovskite structure SmFeO₃ orthoferrite,” *Journal of Crystal Growth*, vol. 490, pp. 1–5, 2018.
- [29] D. M. Giaquinta, G. C. Papaefthymiou, W. M. Davis, and H.-C. Zur Loye, “Synthesis, structure, and magnetic properties of the layered bismuth transition metal oxide solid solution Bi₂Fe_{4-x}GaxO₉,” *Journal of Solid State Chemistry*, vol. 99, no. 1, pp. 120–133, 1992.
- [30] M. G. Rozova, V. V. Grigoriev, I. A. Bobrikov et al., “Synthesis, structure and magnetic ordering of the mullite-type Bi₂Fe_{4-x}CrxO₉ solid solutions with a frustrated pentagonal Cairo lattice,” *Dalton Transactions*, vol. 45, no. 3, pp. 1192–1200, 2016.
- [31] M. K. Singh, W. Prellier, M. P. Singh, R. S. Katiyar, and J. F. Scott, “Spin-glass transition in single-crystal BiFeO₃,” *Physical Review B*, vol. 77, no. 14, Article ID 144403, 2008.
- [32] A. B. Kuzmenko, D. van der Marel, P. J. M. van Bentum, E. A. Tishchenko, C. Presura, and A. A. Bush, “Infrared spectroscopic study of CuO: signatures of strong spin-phonon interaction and structural distortion,” *Physical Review B: Condensed Matter*, vol. 63, Article ID 094303, 2001.
- [33] Z. Qu, Y. Zou, S. Zhang, L. Ling, L. Zhang, and Y. Zhang, “Spin-phonon coupling probed by infrared transmission spectroscopy in the double perovskite Ba₂YMoO₆,” *Journal of Applied Physics*, vol. 113, no. 17, Article ID 17E137, 2013.
- [34] V. A. Khomchenko, D. A. Kiselev, J. M. Vieira et al., “Effect of diamagnetic Ca, Sr, Pb, and Ba substitution on the crystal structure and multiferroic properties of the BiFeO₃ perovskite,” *Journal of Applied Physics*, vol. 103, no. 2, Article ID 024105, 2008.
- [35] D. I. Woodward, I. M. Reaney, R. E. Eitel, and C. A. Randall, “Crystal and domain structure of the BiFeO₃-PbTiO₃ solid solution,” *Journal of Applied Physics*, vol. 94, no. 5, pp. 3313–3318, 2003.
- [36] X. Jiang, Y. Jiang, J. Chen et al., “Structural and multiferroic characterization of BiFeO₃-PbTiO₃-based solid solution with an extra phase,” *Ceramics International*, vol. 44, no. 18, pp. 23315–23319, 2018.
- [37] N. Kumar, B. Narayan, A. K. Singh, and S. Kumar, “Enhanced magneto-capacitance in Sr²⁺ modified BiFeO₃-PbTiO₃ solid solutions,” *Materials Chemistry and Physics*, vol. 252, Article ID 123313, 2020.
- [38] R. P. Singh and S. Saha, “Additives effect on the multiferroic behaviour of BiFeO₃-PbTiO₃,” *Ceramics International*, vol. 47, no. 21, pp. 29815–29823, 2021.

- [39] M. K. Singh, H. M. Jang, S. Ryu, and M. H. Jo, "Polarized Raman scattering of multiferroic BiFeO₃ epitaxial films with rhombohedral R3c symmetry," *Applied Physics Letters*, vol. 88, Article ID 42907, 2006.
- [40] R. Haumont, J. Kreisel, P. Bouvier, and F. Hippert, "Phonon anomalies and the ferroelectric phase transition in multiferroic BiFeO₃," *Physical Review B*, vol. 73, no. 13, Article ID 132101, 2006.
- [41] J. Hlinka, J. Pokorny, S. Karimi, and I. M. Reaney, "Angular dispersion of oblique phonon modes in BiFeO₃ from micro-Raman scattering," *Physical Review B: Condensed Matter*, vol. 83, Article ID 020101, 2011.
- [42] R. Palai, H. Schmid, J. F. Scott, and R. S. Katiyar, "Raman spectroscopy of single-domain multiferroic BiFeO₃," *Physical Review B: Condensed Matter*, vol. 81, Article ID 064110, 2010.
- [43] L. Luo, W. Wei, X. Yuan, K. Shen, M. Xu, and Q. Xu, "Multiferroic properties of Y-doped BiFeO₃," *Journal of Alloys and Compounds*, vol. 540, pp. 36–38, 2012.
- [44] Z. Hu, D. Chen, S. Wang, N. Zhang, L. Qin, and Y. Huang, "Facile synthesis of Sm-doped BiFeO₃ nanoparticles for enhanced visible light photocatalytic performance," *Materials Science and Engineering: B*, vol. 220, pp. 1–12, 2017.
- [45] N. Koshizuka and S. Ushioda, "Inelastic-light-scattering study of magnon softening in ErFeO₃," *Physical Review B*, vol. 22, no. 11, pp. 5394–5399, 1980.

Research Article

Investigation of Structural, Electrical, and Vibrational Properties of $\text{Bi}_{1.98}\text{A}_{0.02}\text{Fe}_4\text{O}_9$ (A = Ba, Ce) Multiferroic Ceramics

Ashwini Kumar ¹, Poorva Sharma ¹, Nikhil Bhardwaj,² Jingyou Tang,¹
and Guolong Tan^{1,3}

¹Key Laboratory of Multifunctional Materials, Department of Electronic Engineering, Luzhou Vocational and Technical College, Luzhou, Sichuan 646000, China

²School of Physics, Devi Ahilya University, Indore 452001, India

³Institute of New Materials, Wuhan University of Technology, Wuhan, 430070, China

Correspondence should be addressed to Ashwini Kumar; 101101216@seu.edu.cn and Poorva Sharma; poorva@nuaa.edu.cn

Received 31 January 2021; Revised 1 July 2021; Accepted 5 July 2021; Published 15 July 2021

Academic Editor: Francisco Javier Fernández Fernández

Copyright © 2021 Ashwini Kumar et al. This is an open access article distributed under the Creative Commons Attribution License, which permits unrestricted use, distribution, and reproduction in any medium, provided the original work is properly cited.

In this paper, we report the synthesis, phase formation, and basic characterization of polycrystalline $\text{Bi}_2\text{Fe}_4\text{O}_9$, $\text{Bi}_{1.98}\text{Ba}_{0.02}\text{Fe}_4\text{O}_9$, and $\text{Bi}_{1.98}\text{Ce}_{0.02}\text{Fe}_4\text{O}_9$ samples prepared by the sol-gel technique. The crystal structure of the prepared samples has been characterized by means of X-ray diffraction and Raman scattering spectroscopy. All the obtained XRD peaks can be indexed to the orthorhombic *Pbam* structure and reveal the formation of $\text{Bi}_2\text{Fe}_4\text{O}_9$. The Raman spectrum identifies A_g , B_{2g} , and B_{3g} active optical phonon modes. The crystallite size and morphology of the nanoparticles have been analyzed using scanning electron microscope (SEM). Dielectric constant (ϵ') decreases as the frequency increases, and it is constant at the higher frequency region which can be explained based on the ionic conduction phenomenon in the low frequency region. The ϵ' values of $\text{Bi}_2\text{Fe}_4\text{O}_9$ (650–850), $\text{Bi}_2\text{Fe}_4\text{O}_9$ (800–850), $\text{Bi}_{1.98}\text{Ba}_{0.02}\text{Fe}_4\text{O}_9$, and $\text{Bi}_{1.98}\text{Ce}_{0.02}\text{Fe}_4\text{O}_9$ samples at 10 Hz frequency are about 37, 75, 90, and 393, respectively. The observed properties signify that these materials are very useful in advanced technological and practical applications.

1. Introduction

In the past few years, there has been great attention in bismuth ferrite $\text{Bi}_2\text{Fe}_4\text{O}_9$ because of its potential applications in information and technology applications, digital memory, catalytic as well as in gas sensing [1, 2]. $\text{Bi}_2\text{Fe}_4\text{O}_9$ has an orthorhombic (space group *Pbam*) structure and belongs to family of mullite-type crystal structures [3, 4]. A unit cell of $\text{Bi}_2\text{Fe}_4\text{O}_9$ contains two formula units with evenly Fe ions distributed between octahedral (FeO_4) and tetrahedral (FeO_4) sites. In addition, Bi^{3+} ions are surrounded by eight oxygen ions. The perovskite BiFeO_3 (BFO), which is both FE ($T_{CE} = 1103$ K) and antiferromagnetic (AFM) ($T_N = 640$ K), is one of the well-known multiferroics [5]. However, it is difficult to obtain phase-pure BFO avoiding the formation of second phases during the conventional synthesis process. Various impurity phases have been reported to occur, such

as $\text{Bi}_2\text{Fe}_4\text{O}_9$, $\text{Bi}_4\text{Fe}_2\text{O}_{72}$, and $\text{Bi}_{25}\text{FeO}_{40}$ [6, 7]. Among the impurity phases, $\text{Bi}_2\text{Fe}_4\text{O}_9$ is a well-known material, which has been extensively studied over the past several decades for various functional applications such as a semiconductor gas sensor and as a catalyst for ammonia oxidation [8, 9]. An unexpected multiferroic effect, which is observed as a coexistence of antiferromagnetism and ferroelectric polarization, was reported in $\text{Bi}_2\text{Fe}_4\text{O}_9$, attributed to the frustrated spin system coupled with phonons [10]. In the past, bulk $\text{Bi}_2\text{Fe}_4\text{O}_9$ were synthesized by solid-state reaction, and the multiferroic properties have been studied, displaying ferroelectric hysteresis loops at $T = 250$ K and antiferromagnetic (AFM) ordering $T_N = 260$ K [11]. It is also claimed that $\text{Bi}_2\text{Fe}_4\text{O}_9$ is one of the promising multiferroic materials. However, the evidence for ferroelectricity is not very strong. Few authors reported hysteresis data [5, 12, 13] in which the P-E field curves tend to give oval rather than ferroic-shaped hysteresis

loops. $\text{Bi}_2\text{Fe}_4\text{O}_9$ with a band gap of about 1.53 eV presents catalytic activity under visible light irradiation [14, 15].

Sol-gel processing, which gives a polycrystalline material, can control particle size of the crystallized phase and can eliminate any pores. We can also design the shape/form of precursor (bulk, thin-film, and so on) [16]. In addition, metastable phases, which are hardly synthesized via solid-state route, often crystallize in ceramics prepared by sol-gel route or hydrothermal method [17, 18]. Therefore, the processing has been studied intensively in order to produce the sophisticated functional materials. In recent times, Mohapatra et al. studied Ho^{3+} doped $\text{Bi}_2\text{Fe}_4\text{O}_9$ samples and reported that Bi/Fe-site substitution in $\text{Bi}_2\text{Fe}_4\text{O}_9$ strongly affects its magnetic properties with the observation of an increase in the Neel temperature accompanied by the enhanced magnetodielectric coupling as compared with pure $\text{Bi}_2\text{Fe}_4\text{O}_9$ [19]. Verseils et al. investigated the magnetic and crystallographic transitions as well as spin-lattice coupling in the Cairo pentagonal magnet $\text{Bi}_2\text{Fe}_4\text{O}_9$ through infrared synchrotron-based spectroscopy as a function of temperature (20–300 K) and pressure (0–15.5 GPa) [20]. Liang et al. studied the structural, magnetic, and electrical properties of Ba-modified $\text{Bi}_2\text{Fe}_4\text{O}_9$ samples which were prepared by sol-gel method. They observed the significant enhancement in remnant magnetization, saturation magnetization, dielectric constant as well as conductivity due to substitution of Ba content in $\text{Bi}_2\text{Fe}_4\text{O}_9$ [21]. In another recent work, $\text{Bi}_2\text{Fe}_4\text{O}_9$ and Gd-doped $\text{Bi}_2\text{Fe}_4\text{O}_9$ samples were synthesized by solid-state mechanochemical ball milling technique, and it revealed the remarkable changes in magnetic and dielectric properties for Gd-doped $\text{Bi}_2\text{Fe}_4\text{O}_9$ samples due to electron-hole hopping mechanism and spin-orbital coupling through D-M interaction. In addition, they also found that the Gd-doped $\text{Bi}_2\text{Fe}_4\text{O}_9$ samples had much higher photocatalytic degradation of MB dye than the undoped $\text{Bi}_2\text{Fe}_4\text{O}_9$ [22]. From the point of theory, Ameer et al. used the first-principle calculations to study the effect of 3d transition metal (TM) ions (Sc, Ti, V, Cr, Mn, Co, Ni, Cu, and Zn) on the structural, electronic, and magnetic properties of ferromagnetic $\text{Bi}_2\text{Fe}_4\text{O}_9$ and provided a comprehensive understanding of the possible effects of 3d TM dopants on $\text{Bi}_2\text{Fe}_4\text{O}_9$ [23].

Studies of electric and dielectric properties are important from both fundamental and application point of view. Dielectric and magnetic behavior of ferrites is greatly influenced by an order of magnitude of conductivity and is mostly dependent on the preparation method and sintering conditions [5, 24]. Sol-gel technique to prepare samples has been recognized as one of the most important synthetic methods, with the advantages of low cost, simple process, and controllable morphology. Therefore, the method of obtaining fine $\text{Bi}_2\text{Fe}_4\text{O}_9$ powder by the sol-gel method has become the goal of many researchers in this field. Therefore, in this paper, we have synthesized the pristine $\text{Bi}_2\text{Fe}_4\text{O}_9$ and Ba^{2+} and Ce^{3+} doped $\text{Bi}_2\text{Fe}_4\text{O}_9$ by sol-gel technique to study their structural and physical properties. In order to obtain a suitable ceramic phase, we examined the phase formation

and physical properties and the glassy precursor was subjected to different heat-treatments at different temperatures and for different durations. Despite the evident importance of $\text{Bi}_2\text{Fe}_4\text{O}_9$ as a functional material, very few reports have appeared. Here, we report the phase formation, physical properties, and vibrational properties of polycrystalline $\text{Bi}_2\text{Fe}_4\text{O}_9$ ceramic synthesized.

2. Experimental Details

2.1. Synthesis. $\text{Bi}_2\text{Fe}_4\text{O}_9$, $\text{Bi}_{1.98}\text{Ba}_{0.02}\text{Fe}_4\text{O}_9$, and $\text{Bi}_{1.98}\text{Ce}_{0.02}\text{Fe}_4\text{O}_9$ ceramics have been successfully synthesized by sol-gel route. All the chemicals are analytical grade and used without further purification. High purity nitrates such as $\text{Bi}(\text{NO}_3)_3 \cdot 5\text{H}_2\text{O}$ and $\text{Fe}(\text{NO}_3)_3 \cdot 9\text{H}_2\text{O}$ were carefully weighed and stoichiometrically mixed. It utilizes multifunctional organic acids capable of chelating metal ions into stable complexes. Suitable metal salts are introduced into the ethylene glycol, citric acid, which is added in large excess to form metal citrates.

$\text{Bi}_2\text{Fe}_4\text{O}_9$: The precursors of $\text{Bi}(\text{NO}_3)_3 \cdot 5\text{H}_2\text{O}$ and $\text{Fe}(\text{NO}_3)_3 \cdot 9\text{H}_2\text{O}$ are taken in a ratio (molar ratio) of 1:1. For 10 gm of sample, we weighed 12.3553 g $\text{Bi}(\text{NO}_3)_3 \cdot 5\text{H}_2\text{O}$ and 20.5805 g $\text{Fe}(\text{NO}_3)_3 \cdot 9\text{H}_2\text{O}$ precursors. Appropriate amount of deionized water is added to dissolve, and then the solution is stirred on a magnetic stirrer. While stirring, citric acids ($\text{C}_6\text{H}_8\text{O}_7$) are introduced in 1.5:1 M ratio with respect to the metal nitrates as a complexing agent and maintained the pH value (6-7) of mixed solution by adding ammonia [11]. Temperature was supplied to allow the gel to form up to a temperature of 100°C, and the xero-gel was completely burned into ash. It was then calcined at 650°C for 2 hours. For the same powder, we carried out the second calcination at 850°C for 2 hours and observed its changes. In another heating treatment, the calcination was done at 800°C and then calcined at 850°C again after grinding. The powder obtained was then ground in agate mortar and pestle. Finally, powder products were reground and pressed into the pellets and then sintered in a muffle furnace at temperature 850°C for 8 hours.

Ba and Ce-doped $\text{Bi}_2\text{Fe}_4\text{O}_9$: Nitrate precursors of Bi, Fe, Ba, and Ce (i.e., $\text{Bi}(\text{NO}_3)_3 \cdot 5\text{H}_2\text{O}$ and $\text{Fe}(\text{NO}_3)_3 \cdot 9\text{H}_2\text{O}$, $\text{Ba}(\text{NO}_3)_2$, and $\text{Ce}(\text{NO}_3)_3 \cdot 6\text{H}_2\text{O}$) are taken in 1:1 molar ratio. Appropriate deionized water was added to dissolve, and solution was then stirred on magnetic stirrer. During stirring, we have added the citric acid ($\text{C}_6\text{H}_8\text{O}_7$) in 1.5:1 M ratio with respect to the metal nitrates as complexant, and the solution was adjusted to a pH value ~6-7 by addition of ammonia. Temperature was supplied to form gel up to 100°C and after that xero-gel was completely burned to form ash. First calcination was done at 650°C, and second calcination was done at 850°C with intermediate grinding. Finally, the pellets were sintered in a muffle furnace at the temperature of 850°C for 8 hours.

2.2. Experimental Techniques. In order to study the crystal structure and phase formation, we obtained the X-ray diffraction (XRD) pattern for the powder samples using a Bruker D8 Advance X-ray diffractometer with a step size of 0.02° and $\text{CuK}\alpha$ (1.5406 \AA) radiation. The surface morphology of the prepared samples (pellet form) was investigated using a JEOL, JSM-5600 scanning electron microscope. Further, the particle sizes were estimated from SEM micrographs using ImageJ software. Raman measurements on as synthesized sample were carried out on Jobin-Yovn Horiba LABRAM (System HR800) spectrometer with a 632.8 nm excitation source equipped with a Peltier cooled CCD detector. Dielectric measurements were made as a function of frequency in the range of 1 Hz – 10 MHz on the Novocontrol alpha-ANB impedance analyzer at room temperature. The dielectric measurements were performed on the circular pellet (10 mm diameter and 1 mm thickness) samples with silver paint coated on two sides as the electrodes. The real (ϵ') and imaginary (ϵ'') parts of the complex dielectric constant were calculated from raw data and the pertinent sample dimensions as follows:

$$\begin{aligned} c_0 &= \epsilon_0 \frac{A}{d}, \\ \epsilon' &= \frac{C d}{\epsilon_0 A}, \\ \epsilon'' &= \epsilon \tan \delta, \end{aligned} \quad (1)$$

where C is the capacitance, d is the thickness of the pellet, A is the area of sintered pellet, and ϵ_0 is the permittivity of vacuum.

3. Results and Discussion

3.1. Crystal Structure Analysis. Figure 1 shows the X-ray powder diffraction (XRD) pattern of pristine $\text{Bi}_2\text{Fe}_4\text{O}_9$, Ba, and Ce-doped $\text{Bi}_2\text{Fe}_4\text{O}_9$ samples carried out at room temperature. As we mentioned before, the $\text{Bi}_2\text{Fe}_4\text{O}_9$ samples were calcined at different temperatures and are further designated as $\text{Bi}_2\text{Fe}_4\text{O}_9(650-850)$ for $\text{Bi}_2\text{Fe}_4\text{O}_9$ calined at 650°C and 850°C and $\text{Bi}_2\text{Fe}_4\text{O}_9(800-850)$ for $\text{Bi}_2\text{Fe}_4\text{O}_9$ sample calcined at 800°C and 850°C . Finally, these both samples have been sintered at 850°C for 8 hours. For the samples $\text{Bi}_2\text{Fe}_4\text{O}_9(650-850)$ and $\text{Bi}_2\text{Fe}_4\text{O}_9(800-850)$, the diffraction peaks are well indexed with the orthorhombic structure of $\text{Bi}_2\text{Fe}_4\text{O}_9$ (space group: $Pbam$) and match well with JCPDS card No. 74-1098 [25]. These results confirm that phase-pure $\text{Bi}_2\text{Fe}_4\text{O}_9$ can be synthesized by sol-gel route. The XRD peak close to 11° is of bismuth due to the presence of $\text{Bi}(\text{NO}_3)_3 \cdot 5\text{H}_2\text{O}$ [26]. From (a) and (b) in Figure 1, we can observe the broadening of the peaks in $\text{Bi}_2\text{Fe}_4\text{O}_9(650-850)$ sample due to low calcination temperature, whereas due to high calcination temperature, proper crystalline phase has been observed in $\text{Bi}_2\text{Fe}_4\text{O}_9(800-850)$ sample. Due to calcination temperature variation, double peaks transform into a single peak from sample $\text{Bi}_2\text{Fe}_4\text{O}_9(650-850)$ to $\text{Bi}_2\text{Fe}_4\text{O}_9(800-850)$. Furthermore, the refined lattice parameters of sample $\text{Bi}_2\text{Fe}_4\text{O}_9(650-850)$ are

$a = 7.94 \text{ \AA}$, $b = 8.40 \text{ \AA}$, and $c = 5.92 \text{ \AA}$ and $a = 7.95 \text{ \AA}$, $b = 8.45 \text{ \AA}$, and $c = 5.94 \text{ \AA}$ for $\text{Bi}_2\text{Fe}_4\text{O}_9(800-850)$, revealing the slight expansion in both the ab plane and the c axis with doping contents increasing. In addition, with the increase in calcination temperature, there is a limited intensity increasing and narrowing of the diffraction peaks, indicative of better crystallization and the increase in crystalline sizes. Using the Debye Scherrer formula, the average crystalline size can be estimated to be about 52 nm , 80 nm for $\text{Bi}_2\text{Fe}_4\text{O}_9(650-850)$ and $\text{Bi}_2\text{Fe}_4\text{O}_9(800-850)$.

XRD for alkaline earth metal Ba^{+2} ion and rare earth Ce^{+3} ion-doped $\text{Bi}_2\text{Fe}_4\text{O}_9$ ceramics are shown in (c) and (d) of Figure 1. For the doped samples, the diffraction peaks are well indexed with the orthorhombic structure of $\text{Bi}_2\text{Fe}_4\text{O}_9$ (space group: $Pbam$) and match well with (JCPDS: 25-0090). As witnessed from (c) and (d) in Figure 1 in the doped $\text{Bi}_2\text{Fe}_4\text{O}_9$ samples, there is a shift in lower theta value due to ionic radius mismatch of dopant (ionic radius of $\text{Ba} = 1.35$ and $\text{Ce} = 1.01$) with Bi^{+3} (0.96) ion. The ionic radius of Ba and Ce ions is greater than that of Bi ion; that is why we are getting a shifting at lower theta value as compared with parent $\text{Bi}_2\text{Fe}_4\text{O}_9$ ceramic. The lattice parameters were obtained using indexing such as $a = 7.101 \text{ \AA}$, $b = 8.50 \text{ \AA}$, and $c = 5.94 \text{ \AA}$ for $\text{Bi}_{1.98}\text{Ba}_{0.02}\text{Fe}_4\text{O}_9$ and $a = 7.99 \text{ \AA}$, $b = 8.48 \text{ \AA}$, and $c = 5.93 \text{ \AA}$ for $\text{Bi}_{1.98}\text{Ce}_{0.02}\text{Fe}_4\text{O}_9$ sample. The crystalline size for Ce^{+3} and Ba^{+2} ions-doped ceramics is found to be 62 and 65 nm , respectively.

3.2. Microstructure Analysis. As the dielectric, optical, and magnetic properties are highly dependent on composition and microstructure acquired by the samples, we used the scanning electron microscope (SEM) to study the surface morphological and microstructural characteristics of pristine and doped $\text{Bi}_2\text{Fe}_4\text{O}_9$ compounds. Figures 2–2 show typical SEM images of $\text{Bi}_2\text{Fe}_4\text{O}_9(650-850)$, $\text{Bi}_2\text{Fe}_4\text{O}_9(800-850)$, $\text{Bi}_{1.98}\text{Ba}_{0.02}\text{Fe}_4\text{O}_9$, and $\text{Bi}_{1.98}\text{Ce}_{0.02}\text{Fe}_4\text{O}_9$ samples, respectively. Compared with the pristine $\text{Bi}_2\text{Fe}_4\text{O}_9$ sample, the grains of the doped $\text{Bi}_2\text{Fe}_4\text{O}_9$ sample are randomly oriented and have the smaller grain size. We determined average grain size using ImageJ Software and found to be nearly 0.8 – 1.2 micrometer. As we can see in the SEM images, the micrograph revealed that $\text{Bi}_2\text{Fe}_4\text{O}_9$ materials mostly consist of nonuniform grains and each grain is interconnected edge by edge. Distribution of grains is homogeneous and agglomerations of the particles. Samples seem to be porous in nature, which is expected to highly influence the dielectric properties. Therefore, we can say that the particle size increases with increase in the calcination temperature as we can see in SEM image of $\text{Bi}_2\text{Fe}_4\text{O}_9(800-850)$ sample. The typical SEM images reveal that microstructures comprise of nonuniform grains with varying particles size indicating polycrystalline nature of as-prepared samples [27].

3.3. Raman Scattring Analysis. The Raman spectrum of $\text{Bi}_2\text{Fe}_4\text{O}_9$ at room temperature is depicted in Figure 3. The Raman active modes of the structure can be summarized using the irreducible representation $12A_g + 12B_1g + 9B_2g + 9B_3g$, which is employed to describe Raman modes of orthorhombic

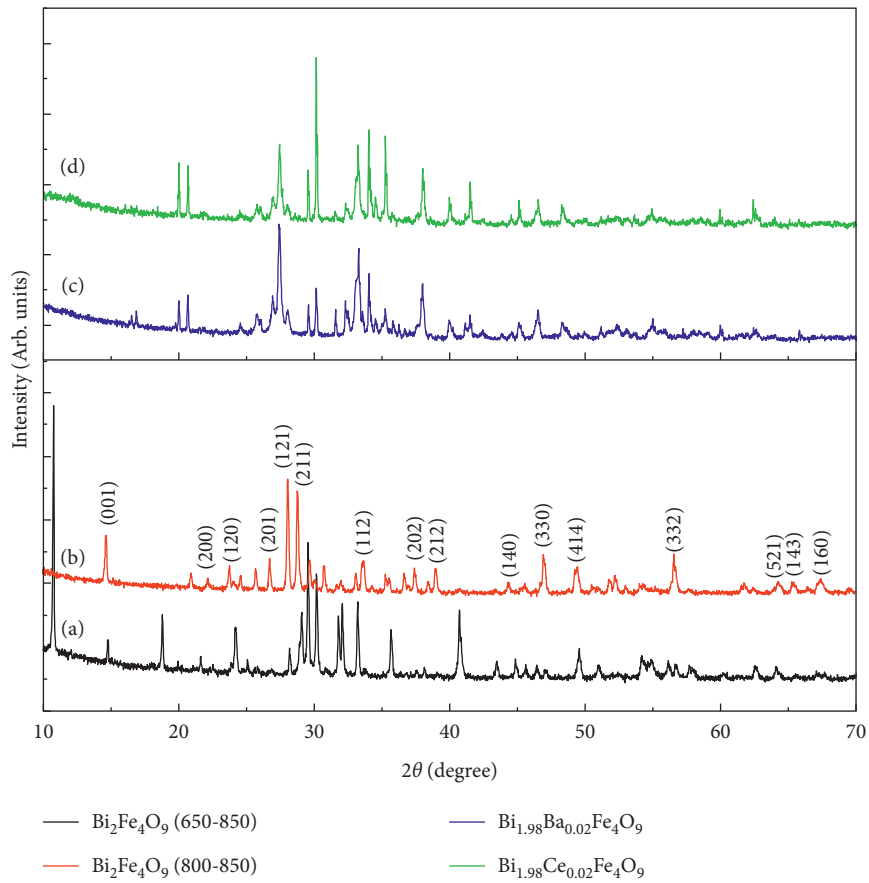


FIGURE 1: Room temperature XRD pattern for (a) $\text{Bi}_2\text{Fe}_4\text{O}_9$ (650–850), (b) $\text{Bi}_2\text{Fe}_4\text{O}_9$ (800–850), (c) $\text{Bi}_{1.98}\text{Ba}_{0.02}\text{Fe}_4\text{O}_9$, and (d) $\text{Bi}_{1.98}\text{Ce}_{0.02}\text{Fe}_4\text{O}_9$ samples.

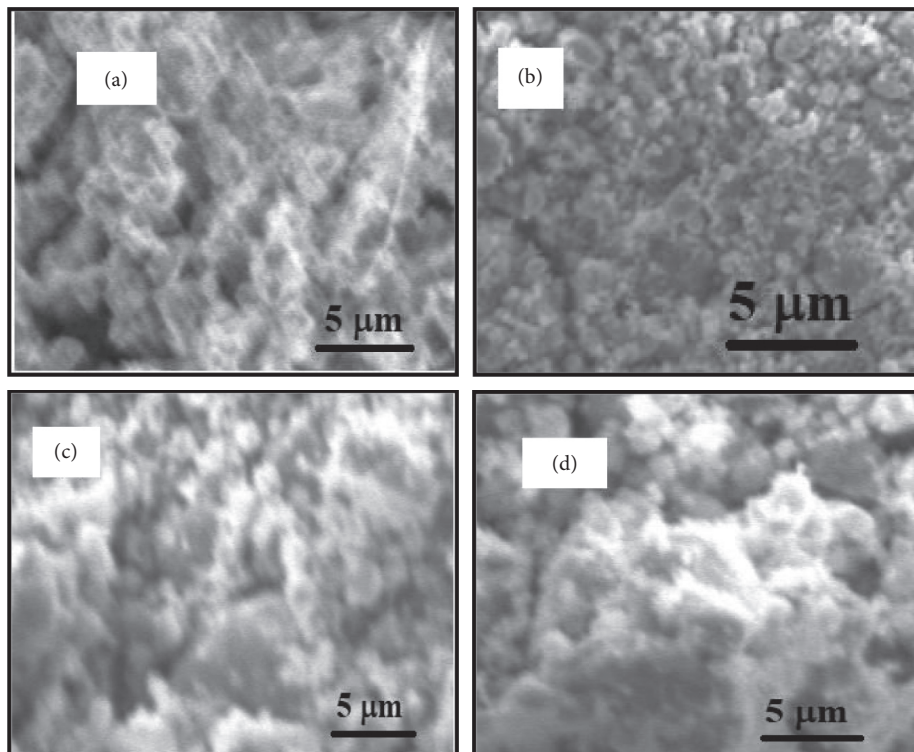


FIGURE 2: Scanning electron microscope (SEM) images of the as-prepared $\text{Bi}_2\text{Fe}_4\text{O}_9$ -based samples: (a) $\text{Bi}_2\text{Fe}_4\text{O}_9$ (650–850), (b) $\text{Bi}_2\text{Fe}_4\text{O}_9$ (800–850), (c) $\text{Bi}_{1.98}\text{Ba}_{0.02}\text{Fe}_4\text{O}_9$, and (d) $\text{Bi}_{1.98}\text{Ce}_{0.02}\text{Fe}_4\text{O}_9$ samples.

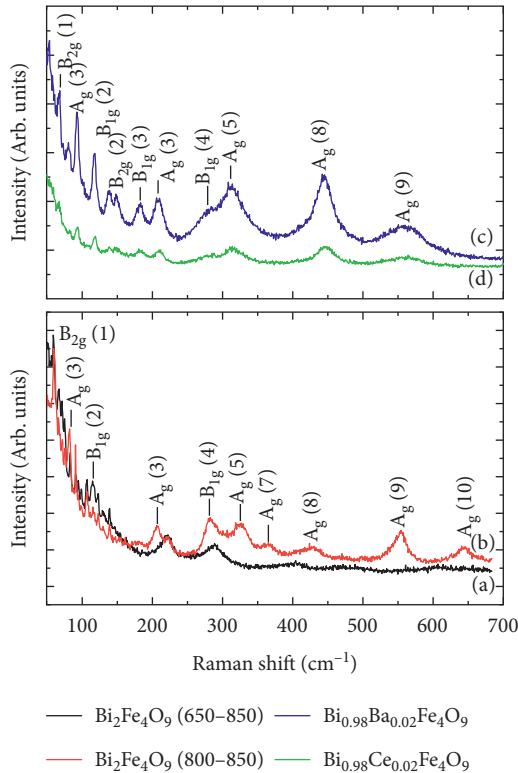


FIGURE 3: Raman spectra for (a) $\text{Bi}_2\text{Fe}_4\text{O}_9(650-850)$, (b) $\text{Bi}_2\text{Fe}_4\text{O}_9(800-850)$, (c) $\text{Bi}_{1.98}\text{Ba}_{0.02}\text{Fe}_4\text{O}_9$, and (d) $\text{Bi}_{1.98}\text{Ce}_{0.02}\text{Fe}_4\text{O}_9$ samples.

(*Pbam* space group) [25]. In the measured Raman spectra of $\text{Bi}_2\text{Fe}_4\text{O}_9(650-850)$, the A_g modes existed at 83, 95, 115, 122, 139, 222, 289, and 607 cm^{-1} . The agreement between experimental and predicted values is relatively good for the all frequency modes, dominated by Bi vibrations. The Raman peak centered at 472 cm^{-1} might be attributed to magnetic ordering effect on phonon line width consistent with earlier observation of bands at ~ 260 and 472 cm^{-1} due to magnon scattering. Similarly, for $\text{Bi}_2\text{Fe}_4\text{O}_9(800-850)$, the obtained Raman A_g modes are at 91, 206, 282, 326, 365, 430, 554, and 640 cm^{-1} . We can analyze that there are number of modes decreasing due to increase in calcination temperature. The A_g modes for $\text{Bi}_{1.98}\text{Ba}_{0.02}\text{Fe}_4\text{O}_9$ are as follows (53, 93, 119, 183, 209, 313, 446, and 558 cm^{-1}). Similarly, for $\text{Bi}_{1.98}\text{Ce}_{0.02}\text{Fe}_4\text{O}_9$, the A_g modes are at 53, 68, 118, 183, 206, 308, 442, and 560 cm^{-1} . It would be more practical to study the magnetic excitations in $\text{Bi}_2\text{Fe}_4\text{O}_9$ under the assumption that they involve two-magnon processes, like in the well-known cases of ferrites [28] or cuprates [11, 29]. At higher frequency ($>250\text{ cm}^{-1}$), it is unlikely that the magnetic-order-induced bands correspond to one-magnon excitations but rare-earth orthoferrites (RFeO_3 ; $R = \text{Dy, Ho, Er, Sm, and so on}$) have frequencies below 25 cm^{-1} for comparison of the zone-center magnons [30].

3.4. Dielectric Response. Figure 4 illustrates the frequency dependence of dielectric constant (ϵ') for $\text{Bi}_2\text{Fe}_4\text{O}_9$ ceramics in the frequency range of 1 Hz to 10 MHz with room temperature. As observed from Figure 4, the dielectric

constant (ϵ') decreases with increase in frequency and almost constant at high frequency due to dielectric relaxations in all prepared samples. The observed high value of dielectric constant and dielectric loss at low frequencies indicates the presence of significant *dc* conductivity, which may be due to space charge polarization that originated from oxygen vacancies, bismuth vacancies, and so on [31]. In general, the dipolar, electronic, ionic, and interfacial polarizations have effect on the dielectric constant of any material. At low frequencies, dipolar polarization and interfacial polarization are effective for the dielectric constant. However, at higher frequencies, the electronic polarization is effective and the dipolar contribution becomes insignificant. The decrease in dielectric constant with increased frequency could be explained based on the phenomenon of dipole relaxation. When the sample is placed under the field, charge carriers move freely within the crystal grains but contain at the boundary and temporarily stop until they pass the boundary. This will result in the formation of potential barrier across the sample and gets polarized. Therefore, it was found that the dielectric constant decreases with increasing frequency [32]. At higher frequencies, the decrease in the dielectric constant is obvious due to lagging behind of applied field. Beyond the certain frequencies, dipoles do not respond to the applied field and thus remain nearly constant.

The value of dielectric constant (ϵ') for all $\text{Bi}_2\text{Fe}_4\text{O}_9$ -based sintered samples at frequency of 10 Hz has been found to be 37, 75, 90, and 393 for $\text{Bi}_2\text{Fe}_4\text{O}_9(650-850)$, $\text{Bi}_2\text{Fe}_4\text{O}_9(800-850)$, $\text{Bi}_{1.98}\text{Ba}_{0.02}\text{Fe}_4\text{O}_9$, and $\text{Bi}_{1.98}\text{Ce}_{0.02}\text{Fe}_4\text{O}_9$, respectively, whereas the value of dielectric constant (ϵ') at higher frequency of 1 MHz has been found to be 11.68, 12.90, 5.06, and 5.36 for $\text{Bi}_2\text{Fe}_4\text{O}_9(650-850)$, $\text{Bi}_2\text{Fe}_4\text{O}_9(800-850)$, $\text{Bi}_{1.98}\text{Ba}_{0.02}\text{Fe}_4\text{O}_9$, and $\text{Bi}_{1.98}\text{Ce}_{0.02}\text{Fe}_4\text{O}_9$ samples, respectively. As shown in Figure 4, dielectric constant ϵ' relatively increases with increasing sintering temperature confirming that it exhibits space charge polarization, and it can be explained with the help of the Maxwell-Wagner effect. These results appear to be consistent with previous empirical analysis using the Maxwell-Wagner model with thermal activation across multiple band gaps in isolated impurities [33, 34]. Apart from this, it is observed that the dielectric constant shows enhancement after Ba and Ce substitution in $\text{Bi}_2\text{Fe}_4\text{O}_9$ at lower frequencies as compared with pristine $\text{Bi}_2\text{Fe}_4\text{O}_9$. This increase may be ascribed to large number of defects due to Ba and Ce doping in $\text{Bi}_2\text{Fe}_4\text{O}_9$ lattice. However, at higher frequencies, the dielectric constant shows reduction in the value and is obvious due to lagging behind the applied field. It can be noticed that Ba and Ce additions to $\text{Bi}_2\text{Fe}_4\text{O}_9$ lattice help to improve the dielectric constant. Figure 5 represents the dielectric loss ($\tan\delta$) as a function of frequency of $\text{Bi}_2\text{Fe}_4\text{O}_9$ -based ceramics at room temperature. Furthermore, Ba and Ce-doped $\text{Bi}_2\text{Fe}_4\text{O}_9$ exhibited higher value of dielectric constant and dielectric loss as compared with pristine $\text{Bi}_2\text{Fe}_4\text{O}_9$ due to large off-center displacement of Fe^{3+} ions in octahedral and reduced particle size [35]. As the hopping process of conducting electrons and holes increases, the band gap decreases and the conductivity increases [36]. We have observed that the value of dielectric loss is low for $\text{Bi}_2\text{Fe}_4\text{O}_9(650-850)$ among the entire prepared sample, and dielectric relaxation is possible in all prepared samples.

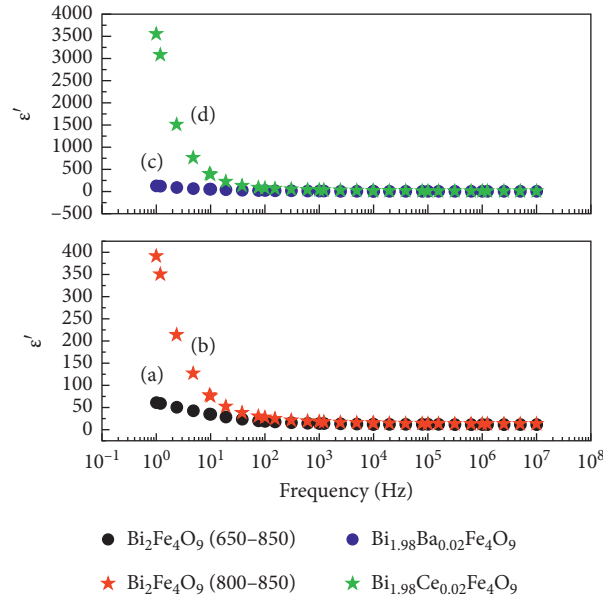


FIGURE 4: Dielectric constant behavior for $\text{Bi}_2\text{Fe}_4\text{O}_9(650-850)$, $\text{Bi}_2\text{Fe}_4\text{O}_9(800-850)$, $\text{Bi}_{1.98}\text{Ba}_{0.02}\text{Fe}_4\text{O}_9$, and $\text{Bi}_{1.98}\text{Ce}_{0.02}\text{Fe}_4\text{O}_9$ samples.

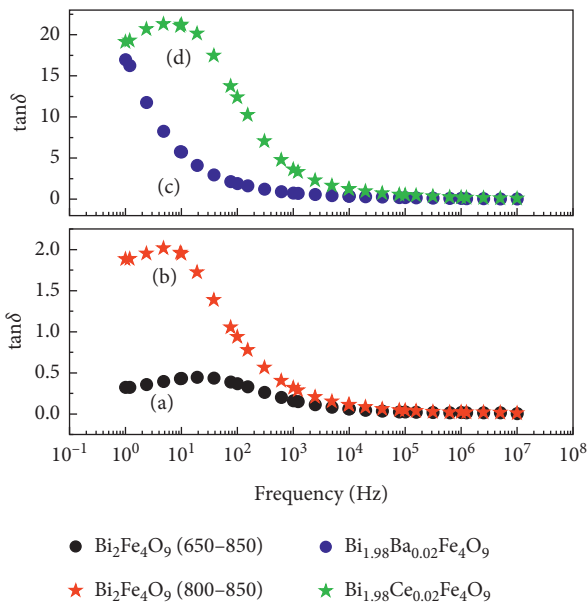


FIGURE 5: Dielectric loss behavior for $\text{Bi}_2\text{Fe}_4\text{O}_9(650-850)$, $\text{Bi}_2\text{Fe}_4\text{O}_9(800-850)$, $\text{Bi}_{1.98}\text{Ba}_{0.02}\text{Fe}_4\text{O}_9$, and $\text{Bi}_{1.98}\text{Ce}_{0.02}\text{Fe}_4\text{O}_9$ samples.

4. Conclusions

In conclusion, the polycrystalline samples of $\text{Bi}_2\text{Fe}_4\text{O}_9(650-850)$, $\text{Bi}_2\text{Fe}_4\text{O}_9(800-850)$, $\text{Bi}_{1.98}\text{Ba}_{0.02}\text{Fe}_4\text{O}_9$, and $\text{Bi}_{1.98}\text{Ce}_{0.02}\text{Fe}_4\text{O}_9$ samples were successfully prepared by sol-gel route. By the indexing of X-ray diffraction data, the formation of $\text{Bi}_2\text{Fe}_4\text{O}_9$ phase having orthorhombic structure with *Pbam* space group is confirmed. There is no evidence for structural change in the prepared samples. Raman spectra reveal that the presence of magnon peak is only in $\text{Bi}_2\text{Fe}_4\text{O}_9(650-850)$ sample. The value of ϵ' for all $\text{Bi}_2\text{Fe}_4\text{O}_9$ -based $\text{Bi}_2\text{Fe}_4\text{O}_9(650-850)$, $\text{Bi}_2\text{Fe}_4\text{O}_9(800-850)$, $\text{Bi}_{1.98}\text{Ba}_{0.02}\text{Fe}_4\text{O}_9$, and $\text{Bi}_{1.98}\text{Ce}_{0.02}\text{Fe}_4\text{O}_9$

samples is about 37, 75, 90, and 393, respectively, at frequency of 10 Hz. At higher frequency of 1 MHz, the values of ϵ' are 11.68, 12.90, 5.06, and 5.36 for $\text{Bi}_2\text{Fe}_4\text{O}_9(650-850)$, $\text{Bi}_2\text{Fe}_4\text{O}_9(800-850)$, $\text{Bi}_{1.98}\text{Ba}_{0.02}\text{Fe}_4\text{O}_9$, and $\text{Bi}_{1.98}\text{Ce}_{0.02}\text{Fe}_4\text{O}_9$ samples, respectively. Dielectric constant (ϵ') decreases with increasing frequency and becomes almost constant at high frequency region. The value of dielectric loss is low for $\text{Bi}_2\text{Fe}_4\text{O}_9(650-850)$ among the entire prepared sample, and dielectric relaxation is possible in all as-prepared samples. The decrease in dielectric constant with increased frequency could be explained on the basis of the ionic conduction phenomenon in the low frequency region. These properties make this material very useful in technological and practical applications.

Data Availability

The data used to support the findings of this study are available from the corresponding author upon request.

Conflicts of Interest

The authors declare that they have no conflicts of interest regarding the publication of this study.

Acknowledgments

The authors acknowledge the financial support from National Natural Science Foundation of China under grant no. 11774276. Kumar and Sharma acknowledge the Luzhou Vocational and Technical College for providing them start-up research grants and support and also acknowledge the Luzhou Talent Work Leading Group Office for job-incentive and resettlement subsidies for high-level talents. The authors are grateful to Dr. S. Satapathy for their long-term collaboration and numerous fruitful discussions.

References

- [1] G. Wang, S. Yan, J. Sun, S. Wang, and Q. Deng, "Visible light photocatalytic and magnetic properties of Nd doped $\text{Bi}_2\text{Fe}_4\text{O}_9$ powders," *Journal of Materials Science: Materials in Electronics*, vol. 28, no. 5, pp. 4371–4377, 2016.
- [2] N. I. Zakharchenko, "Catalytic properties of the Fe_2O_3 – Bi_2O_3 system in ammonia oxidation to nitrogen oxides," *Kinetics and Catalysis*, vol. 43, no. 1, pp. 95–98, 2002.
- [3] Y. Xiong, M. Wu, Z. Peng, N. Jiang, and Q. Chen, "Hydrothermal synthesis and characterization of $\text{Bi}_2\text{Fe}_4\text{O}_9$ nanoparticles," *Chemistry Letters*, vol. 33, no. 5, pp. 502–503, 2004.
- [4] Y. Takahashi, K. Nakamura, M. Osada, and T. Fujiwara, "Structural relaxation and quasi-elastic light scattering in glass: A," *Scientific Reports*, vol. 2, no. 1, p. 714, 2012.
- [5] A. K. Singh, S. D. Kaushik, B. Kumar et al., "Substantial magnetoelectric coupling near room temperature in $\text{Bi}_2\text{Fe}_4\text{O}_9$," *Applied Physics Letters*, vol. 92, no. 13, Article ID 132910, 2008.
- [6] M. M. Kumar, A. Srinivas, and S. V. Suryanarayana, "Structure property relations in $\text{BiFeO}_3/\text{BaTiO}_3$ solid solutions," *Journal of Applied Physics*, vol. 87, no. 2, pp. 855–862, 2000.
- [7] S. M. Selbach, M.-A. Einarsrud, and T. Grande, "On the TS," *Chemistry of Materials*, vol. 21, no. 1, pp. 169–173, 2009.
- [8] H. Koizumi, N. Niizeki, and T. Ikeda, N. I. Zakharchenko, "Russian journal of applied chemistry," *Jappense journal Applied Physics*, vol. 3, p. 495, 1964.
- [9] A. S. Poghossian, H. V. Abovian, P. B. Avakian, S. H. Mkrtchian, and V. M. Haroutunian, "Bismuth ferrites: n," *Sensors and Actuators B: Chemical*, vol. 4, no. 3–4, pp. 545–549, 1991.
- [10] T. Honma, N. Ito, T. Togashi, A. Sato, and T. Komatsu, "Triclinic $\text{Na}_{2-x}\text{Fe}_{1+x}/2\text{P}2\text{O}7/\text{C}$ glass-ceramics with high current density performance for sodium ion battery," *Journal of Power Sources*, vol. 227, pp. 31–34, 2013.
- [11] A. P. Litvinchuk, L. BO, C. Thomsen, and C. W. Chu, "Magnetic excitations in $\text{PrBa}_2\text{Cu}_4\text{O}_8$ explored by Raman scattering," *Physica Status Solidi (B)*, vol. 215, no. 1, pp. 507–512, 1999.
- [12] Z. M. Tian, S. L. Yuan, X. L. Wang et al., "Size effect on magnetic and ferroelectric properties in $\text{Bi}_2\text{Fe}_4\text{O}_9$ multiferroic ceramics," *Journal of Applied Physics*, vol. 106, no. 10, Article ID 103912, 2009.
- [13] K. J. D. MacKenzie, T. Dougherty, and J. Barrel, "The electronic properties of complex oxides of bismuth with the mullite structure," *Journal of the European Ceramic Society*, vol. 28, no. 2, pp. 499–504, 2008.
- [14] S. R. Mohapatra, B. Sahu, T. Badapanda, M. S. Pattanaik, S. D. Kaushik, and A. K. Singh, "Optical, dielectric relaxation and conduction study of $\text{Bi}_2\text{Fe}_4\text{O}_9$ ceramic," *Journal of Materials Science: Materials in Electronics*, vol. 27, no. 4, pp. 3645–3652, 2016.
- [15] Q. Zhang, W. Gong, J. Wang et al., "Size-dependent magnetic, photoabsorbing, and photocatalytic properties of single-crystalline $\text{Bi}_2\text{Fe}_4\text{O}_9$ semiconductor nanocrystals," *Journal of Physical Chemistry C*, vol. 115, no. 51, pp. 25241–25246, 2011.
- [16] A. Sakamoto and S. Yamamoto, "Glass-ceramics: engineering principles and applications," *International Journal of Applied Glass Science*, vol. 1, no. 3, pp. 237–247, 2010.
- [17] T. Furukawa and W. B. White, "Raman spectroscopic investigation of the structure and crystallization of binary alkali germanate glasses," *Journal of Materials Science*, vol. 15, no. 7, pp. 1648–1662, 1980.
- [18] K. Shioya, T. Komatsu, H. G. Kim, R. Sato, and K. Matusita, Y. Wang, G. Xu, L. Yang, Z. Ren, X. Wei, W. Weng et al., "Optical properties of transparent glass-ceramics in $\text{K}_2\text{O-Nb}_2\text{O}_5\text{-TeO}_2$ glasses," *Journal of Non-crystalline Solids*, vol. 189, no. 1–2, pp. 16–24, 1995.
- [19] S. R. Mohapatra, P. N. Vishwakarma, S. D. Kaushik, and A. K. Singh, "Effect of Holmium substitution on the magnetic and magnetodielectric properties of multiferroic $\text{Bi}_2\text{Fe}_4\text{O}_9$," *Journal of Applied Physics*, vol. 122, no. 13, Article ID 134103, 2017.
- [20] M. Verseils, A. P. Litvinchuk, J.-B. Brubach et al., "Infrared phonon spectroscopy on the Cairo pentagonal antiferromagnet $\text{Bi}_2\text{Fe}_4\text{O}_9$: a study through the pressure-induced structural transition," *Physical Review B*, vol. 103, no. 17, Article ID 174403, 2021.
- [21] Y. Y. Liang, J. X. Lei, X. X. Wang, L. G. Wang, and C. M. Zhu, "Structure, magnetic and electrical properties of Ba-modified $\text{Bi}_2\text{Fe}_4\text{O}_9$," *Journal of Materials Science: Materials in Electronics*, vol. 30, no. 2, pp. 1691–1698, 2019.
- [22] K. Subha Rao, S. Manjunath Kamath, R. Rajesh Kumar et al., "Delineating the photocatalytic properties of doped mullite $\text{Bi}_2\text{Fe}_4\text{O}_9$ by virtue of Gd^{3+} ions," *Materials Letters*, vol. 297, Article ID 129960, 2021.
- [23] S. Ameer, K. Jindal, M. Tomar, P. K. Jha, and V. Gupta, "Tunable electronic and magnetic properties of 3d transition metal doped $\text{Bi}_2\text{Fe}_4\text{O}_9$," *Journal of Magnetism and Magnetic Materials*, vol. 509, Article ID 166893, 2020.
- [24] M. Pooladi, I. Sharifi, and M. Behzadipour, "A review of the structure, magnetic and electrical properties of bismuth ferrite ($\text{Bi}_2\text{Fe}_4\text{O}_9$)," *Ceramics International*, vol. 46, no. 11, pp. 18453–18463, 2020.
- [25] Y. A. Park, K. M. Song, and N. Hur, "Frequency-dependent dielectric anomalies in magnetic oxides," *Journal of the Korean Physical Society*, vol. 53, no. 6, pp. 3356–3360, 2008.
- [26] L. Tröbs, M. Wilke, W. Szczerba, U. Reinholz, and F. Emmerling, "Mechanochemical synthesis and characterisation of two new bismuth metal organic frameworks," *CrystEngComm*, vol. 16, p. 5560, 2014.
- [27] N. Bajpai, M. Saleem, and A. Mishra, "Effect of bismuth (Bi^{3+}) substitution on structural, optical, dielectric and magnetic nature of $\text{La}_2\text{CoMnO}_6$ double perovskite," *Journal of Materials Science: Materials in Electronics*, vol. 32, no. 10, pp. 12890–12902, 2021.
- [28] M. J. Massey, U. Baier, R. Merlin, and W. H. Weber, "Effects of pressure and isotopic substitution on the Raman spectrum of $\alpha\text{-Fe}_2\text{O}_3$," *Physical Review B*, vol. 41, no. 11, pp. 7822–7827, 1990.
- [29] J. Holmlund, C. S. Knee, J. Andreasson, M. Granath, A. P. Litvinchuk, and L. Börjesson, "Two-magnon Raman scattering from the Cu_3O_4 layers in $(\text{Sr}_2\text{Ba}_2)\text{Cu}_3\text{O}_4\text{Cl}_2$," *Physical Review B: Condensed Matter*, vol. 79, Article ID 085109, 2009.
- [30] R. M. White, R. J. Nemanich, and C. Herring, "Light scattering from magnetic excitations in orthoferrites," *Physical Review B*, vol. 25, no. 3, pp. 1822–1836, 1982.
- [31] M. R. Islam, M. S. Islam, M. A. Zubair, H. M. Usama, M. S. Azam, and A. Sharif, "Evidence of superparamagnetism and improved electrical properties in Ba and Ta co-doped BiFeO_3 ceramics," *Journal of Alloys and Compounds*, vol. 735, pp. 2584–2596, 2018.
- [32] M. Soosen Samuel, J. Koshy, A. Chandran, and K. C. George, R. Kant, R. Singh, A. Bansal, and A. Kumar, "Dielectric behavior and transport properties of ZnO nanorods," *Physica B*:

- Condensed Matter*, vol. 406, no. 15-16, pp. 3023–3029, Article ID 114726, 2011.
- [33] A. Shukla and R. N. P. Choudhary, “Study of electrical properties of $\text{La}^{3+}/\text{Mn}^{4+}$ -modified PbTiO_3 nanoceramics,” *Journal of Materials Science*, vol. 47, no. 13, pp. 5074–5085, 2012.
- [34] R. R. Awasthi and B. Das, “Effect of temperature on physical properties of $\text{Bi}_2\text{Fe}_4\text{O}_9$ polycrystalline materials,” *Journal of the Australian Ceramic Society*, vol. 56, no. 1, pp. 243–250, 2020.
- [35] B. K. Vashisth, J. S. Bangruwa, S. P. Gairola, and V. Verma, “Structural, dielectric, ferroelectric and magnetic properties of Gd doped BiFeO_3 ,” *Integrated Ferroelectrics*, vol. 194, no. 1, pp. 21–27, 2018.
- [36] M. Umar, N. Mahmood, S. U. Awan, and S. Fatima, “Rationally designed La and Se co-doped bismuth ferrites with controlled bandgap for visible light photocatalysis,” *RSC Advances*, vol. 9, pp. 17148–21715, 2019.

Research Article

Design of Hydraulic Bulging Die for Automobile Torsion Beam and Optimization of Forming Process Parameters

Kefan Yang , Youmin Wang, and Kexun Fu

College of Mechanical Engineering, Anhui Polytechnic University, Wuhu, Anhui 241000, China

Correspondence should be addressed to Kefan Yang; 2200120138@stu.ahpu.edu.cn

Received 29 March 2021; Accepted 3 June 2021; Published 11 June 2021

Academic Editor: Ashwini Kumar

Copyright © 2021 Kefan Yang et al. This is an open access article distributed under the Creative Commons Attribution License, which permits unrestricted use, distribution, and reproduction in any medium, provided the original work is properly cited.

The hydraulic bulging technology of tubes can provide hollow parts with special-shaped cross sections. Its manufacturing process can effectively improve material utilization and product accuracy and reduce the number and cost of molds. However, the hydraulic bulging process of parts is very complicated. The size of the tube blank, the design of the loading route, and the forming process parameters will have an effect on the molding quality. Closed tubular torsion automobile beam is considered as the research object to study hydraulic bulging die design and optimize forming process parameters. CATIA software is used to design torsion beam product structure and hydraulic bulging die. AMESim software is employed to design hydraulic synchronous control system for cylinders on both sides of the hydraulic bulging die. Mathematical control model is established and verified in Simulink software. DYNIFORM software is applied to conduct numerical simulation of hydraulic expansion. The supporting pressure, molding pressure, friction coefficient, and feeding quantity are taken as orthogonal experiment level factors. Maximum thinning and maximum thickening rates are taken as hydraulic pressure expansion evaluation indexes to complete the orthogonal experiments. Main molding process parameters are analyzed via orthogonal experiment results and optimized by employing the Taguchi method. Optimal hydraulic bulging parameters are obtained as follows: supporting pressure of 20 MPa, molding pressure of 150 MPa, feeding quantity of 25 mm, and friction coefficient of 0.075. Simulation analysis results indicate that the maximum thinning rate is equal to 9.013%, while the maximum thickening rate is equal to 16.523%. Finally, the design of hydraulic bulging die for torsion beam was completed, and its forming process parameters were optimized.

1. Introduction

Molding plays an important role in modern machinery manufacturing industry [1]. Traditional mold design and manufacturing often rely on daily practical production experience to achieve the best effect in repeated debugging. With the development of lightweight automobiles, weight reduction of vehicle body is continuously pursued while maintaining vehicle performance. Thus, energy saving and emission reduction are achieved. This also means that traditional auto parts are transformed, while solid components with large quality and complex assembly are gradually transformed into hollow components with lightweight and integrated assembly. As a consequence, corresponding parts of product development and mold manufacturing methods are also altered. As one of new lightweight manufacturing

processes, tube hydraulic bulging technology can open tube internal high-pressure liquid integral bulging to produce hollow parts with complex cross sections. This simplifies the production process and improves the product quality. Furthermore, it is a widely applied prospect in achieving lightweight construction of an automobile.

Torsion beam suspension is a type of rear suspension which is mainly used to balance the vibration of two wheels during driving. Traditional open torsion beam is made of sheet metal stamping. Its parts are high quality products while the production process itself is cumbersome. However, closed torsion beam with hydraulic expansion can be formed on the premise of ensuring the performance of parts, which reduces the number of molds and manufacturing costs.

Yin et al. [2] used finite element method to study wall thickness variation law of typical sections during tubular

torsion forming. The results show that transition area wall thickness significantly changes during torsion beam hydraulic bulging. In addition, wall thickness variation in the middle area is not significant. Lu et al. [3] performed forward design of variable cross section hydraulic expansion type torsion beam. The authors obtained tubular torsion beam with special-shaped cross section which meets the requirements of design objectives.

Naeini et al. [4] studied and optimized pressure and force loading paths in the process of tube hydroforming via simulated annealing optimization method. Rao [5] employed Taguchi algorithm to optimize process parameters. Furthermore, the author determined optimal combination of process parameters according to the influence of tube expansion height and thinning distribution. Dhinakaran et al. [6] used CATIA to model the automotive steering knuckle and carried out stiffness analysis in OptiStruct; based on the analysis results, proposed design modifications and topology optimization were performed on the steering knuckle for lowering of the weight.

In the present study, torsion beam index parameters are designed and studied. In addition, all parameters regarding size and cross section of torsion beam studied in this paper are designed, and effects of feed quantity and friction coefficient on process parameters were further studied. Moreover, to analyze the influence degree of various factors, four-level experimental table was established by using the orthogonal experiment. In this paper, computer software CATIA is employed to design tubular torsion beam. Corresponding materials and initial tube blanks are selected for the processed products. Forming process of parts is determined, and calculation of relevant process parameters in hydraulic bulging is achieved. Hydraulic synchronous control system for automatic deviation correction is designed for synchronous cylinders on both mold sides. Synchronous displacement curves of two cylinder piston rods under two different operating conditions are obtained in AMESim. In addition, automatic hydraulic control system deviation correction function is successfully verified. Mathematical model of synchronous control system is established, and transfer function of a closed-loop control system is derived. Step response curve of the system is obtained via Simulink. Taking maximum thinning and maximum thickening rates of part's wall thickness as forming evaluation indexes, hydraulic bulging process simulation analysis of torsion beam is completed in DYNIFORM. Taguchi algorithm is employed to optimize process parameters of hydraulic bulging torsion beam. Finally, the accuracy of optimization results is verified via DYNIFORM.

2. Automobile Tubular Torsion Beam Structure Design

CATIA is used to carry out three-dimensional modeling design for the closed tubular torsion beam. Basic dimensions are as follows: the length is 1260 mm, the maximum height difference between two part ends is 85.2 mm, the surface area is 0.356 m^2 , and the basic wall thickness is 3 mm. This part is symmetrical from left to right, as shown in Figure 1.

The left half of the torsion beam is selected for analysis. Left side of section B-B is the port area, whose shape remains unchanged. Cross section B-B to cross section E-E is defined as the transition zone with complex and variable cross sections. Sections E-E and F-F are V-shaped with unaltered cross section areas, as shown in Figure 2.

Perimeter of each torsion beam characteristic section is shown in Table 1. Minimum transversal fillet radius of 5 mm on the outer surface of the torsion beam appears in the F-F section. Outer edge transversal perimeter value is equal to a minimum of 330.48 mm at section D-D and a maximum of 365.13 mm at section B-B.

According to Figure 2, minimum torsion beam section circumference is 330.48 mm. Selected pipe diameter must be lower than the minimum section circumference of the torsion beam. Therefore, according to the requirements of forming and convenient pipe fitting procurement, the initial diameter of the transverse pipe is proposed as $\varnothing 104 \text{ mm}$ with the corresponding wall thickness of 3 mm.

Length of pipe fittings is related to automobile torsion beam part size and ductility of pipe fittings. The length of the torsion beam is 1260 mm. To ensure material filling at both ends and fully formed part without causing excessive material waste, preliminary length of beam pipe fittings is 1290 mm. Therefore, the tube blank size is defined as $\varnothing 104 \text{ mm} \times 1290 \text{ mm} \times 3 \text{ mm}$.

3. Automobile Torsion Beam Hydraulic Bulging Die Design

3.1. Design of Hydraulic Bulging Die for Torsion Beam. Hydraulic bulging mold is mainly composed of an upper die and lower die bases, punch, matrix, left and right axial sealing plugs, positioning plates, guide columns, and guide sleeves. In Figure 3, assembly effect drawing is shown. Since there is currently no relevant standard for pipe fitting hydraulic forming die design, only standard design of traditional liquid bulging forming process die is employed in this paper. Thus, hydraulic pressure and tightness are considered when designing the hydraulic bulging die.

Parting surface selection should respect certain requirements. The parting surface should be selected at the largest part contour. Otherwise, the torsion beam cannot be removed from the cavity [7]. Precision requirements are higher for the transition zone of hydraulic expansion type torsion beam. Dimensional accuracy of parts is affected by the internal pressure, while selection of parting surface is also convenient for mold processing and manufacturing. According to these requirements, the parting line is opened on both sides of the widest side of the torsion beam surface, as shown in Figure 4, with a horizontal height of 62 mm from the bottom of the matrix.

Both punch and matrix of this design adopt the inlay manufacturing process, as shown in Figure 5. According to the role of different mold design and manufacture inserts, while taking into account wear resistance and strength of each part, manufacturing quality and efficiency of parts are improved. When processing other hydraulic bulging products, the insert can be replaced accordingly.



FIGURE 1: Original mathematical model diagram of the torsion beam.

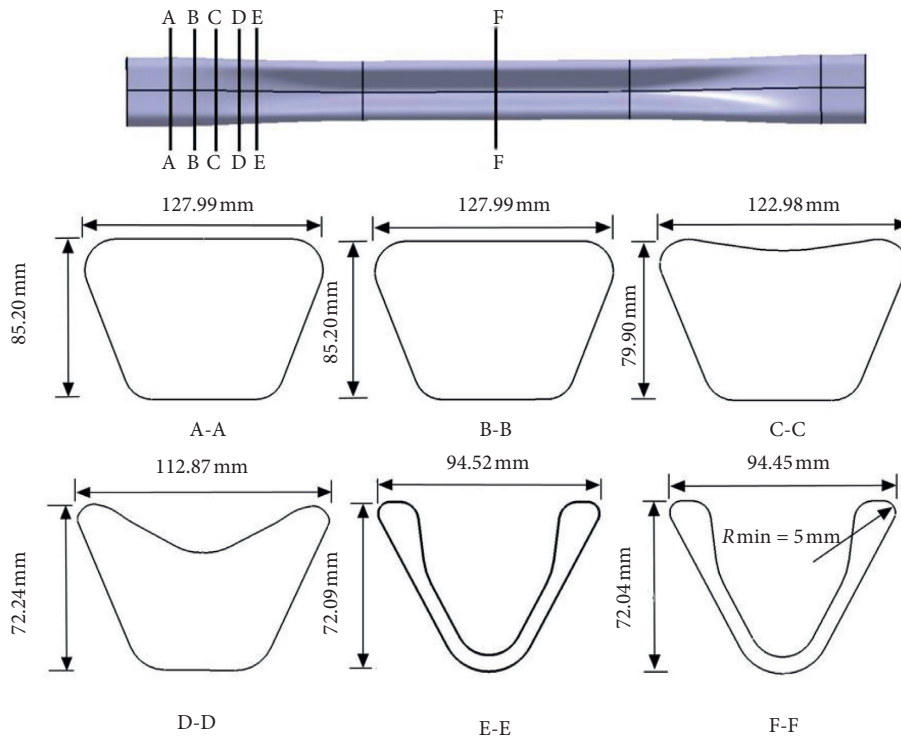


FIGURE 2: Section shape diagram of torsion beam.

TABLE 1: Typical section perimeter table.

Cross section	A-A	B-B	C-C	D-D	E-E	F-F
Perimeter (mm)	364.14	365.13	340.97	330.48	354.36	354.88

When designing the inlay structure, attention should be paid to avoid the splicing line of the punch and the matrix, which should be staggered for a minimum of 3~5 mm. Due to a complex cross section shape of the transition area on both part sides, an arc inlay block needs to be separately designed. The remaining inlay block parts are planar.

Front end of the plug is connected with the pipe billet, and the rear end is connected with the hydraulic cylinder piston rod. According to the shape of both part ends, the plug is designed as a cone type. Front end length of the plug is 15 mm, and the middle part, which is in direct contact with the die, is 40 mm long. Junction of two parts is the sealing part, which is in contact with the end of the plug and the tube billet.

During hydraulic bulging, water injection holes on both piston rod sides are filled with water. The water flows into the mold from four plug outlet holes through an internal pressurization channel. In this paper, front end of the plug is directly in contact with the pipe fitting end. Based on axial feed force extrusion of hydraulic cylinders on both sides, small deformation is generated at the connection to achieve sealing [8]. Compared with the soft seal, this type of hard seal with direct contact between metals is suitable for high-pressure environments. Furthermore, it demonstrates beneficial wear resistance and mechanical properties.

Liquid internal pressure of hydraulic bulging can generally reach approximately 300~400 MPa. In order to ensure that the axial force and cavity axis overlap during axial pressure after mold closing and that the hydraulic cylinder does not vibrate or bend, the upper die base is fixed in the top worktable surface chute via eight T-bolts on both sides [9, 10]. Four corners of the upper die base are fixed with guide columns, and left and right sides are arranged with

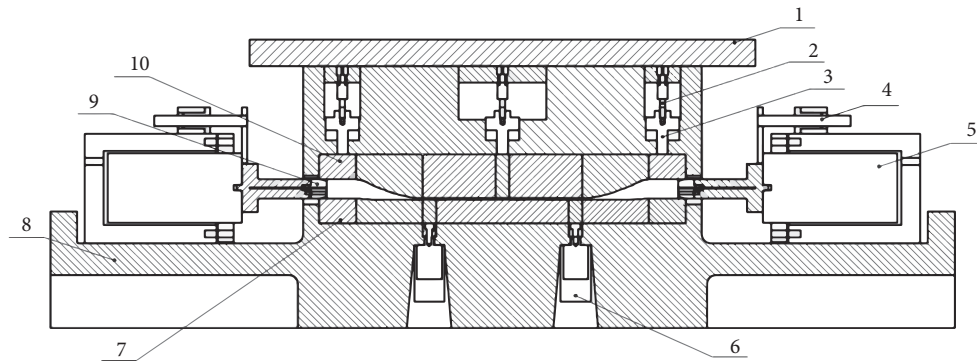


FIGURE 3: General assembly diagram of hydraulic expansion die for torsion beam: (1) upper die base; (2) cylinder; (3) pull-out rod of upper die; (4) displacement sensor; (5) hydraulic cylinder; (6) ejection cylinder; (7) matrix; (8) lower die base; (9) sealing plug; (10) punch.



FIGURE 4: Location diagram of die parting line.

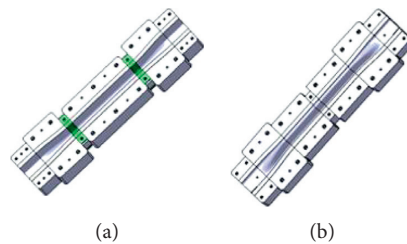


FIGURE 5: Structure drawing of punch and matrix insert: (a) structure of an inlaying matrix; (b) structure of an inlaying punch.

three-side guide blocks. When the die is closed, guide columns and guide blocks are matched with the corresponding guide sleeves and grooves of the lower die base to complete the guide. Therefore, hydraulic expansion type upper die base of automobile torsion beam is designed.

Since lower die base bears the weight of the entire die, its strength is very important [11]. The lower die base is fixed on the worktable by T-bolts. Guide sleeve corresponding to the upper die guide column is arranged at four corners of the lower die base. In addition, symmetrical guide block is also arranged in the middle, which is convenient for positioning during mold closing. Four limit plates are symmetrically arranged on both sides with respect to the middle. Their length \times width \times height is 50 mm \times 30 mm \times 5 mm. The guide block plays a limit buffer role when the mold is closed. Hydraulic cylinders, which ensure axial feeding, are fixed on both sides on corresponding platforms via bolts.

3.2. Design of Hydraulic Control System for Synchronous Cylinders on Both Sides of Hydraulic Bulging Die. Automotive torsion beam is a type of symmetrical hollow pipe fitting. During hydraulic bulging die design, synchronization of hydraulic cylinders on both sides is particularly important. If poor synchronization is achieved, uneven material flow in the forming process may occur. Wrinkling, cracking, buckling, and other defects may be caused, thus affecting the forming quality of the final part. In order to solve these problems, synchronization of hydraulic control system for automobile torsion beam hydraulic bulging die is investigated in this paper. Combined with the actual operating conditions, a new axial feed control hydraulic system is designed. This system provides the feed required in the forming process, while simultaneously ensuring the synchronization accuracy of two cylinders via automatic deviation correction.

In this paper, control volume for bidirectional shunt servo valve core displacement, which is represented by X_v , is designed. Controlled quantity is the transmission deviation, which is represented by ΔX_p . When hydraulic cylinders no. 1 and no. 2 are not simultaneously active, the gear in the middle rotates to produce deviation displacement. Valve core displacement is used to change the oil outlets denoted as no. 1 and no. 2, so as to change the flow into the two hydraulic cylinders and finally make the displacement of the two hydraulic cylinders the same. The designed hydraulic control system is shown in Figure 6.

The oil supply branch supplies the hydraulic oil in the oil source to the hand-directional valve through the motor driving the hydraulic pump, presses the handle of the hand-directional valve, and connects the left end of the hand-directional valve to the loop; the hydraulic oil enters into the bidirectional shunt follow-up valve through the hand-directional valve. At this time, the valve core of the bidirectional shunt follow-up valve is in the middle of the chamber; that is, the section areas of oil outlet no. 1 and oil outlet no. 2 valve are equal, and the flows through outlets no. 1 and no. 2 into hydraulic cylinders no. 1 and no. 2 are equal. Because the two cylinders are of the same size, the two cylinders move at the same speed and in the opposite direction, and the speed of rack no. 1 and that of rack no. 2 connected with the two hydraulic cylinders are equal and opposite, which drives the gear to move. Since the speed values of the two racks are equal and opposite, the axis of the gear does not shift.

When the speed of hydraulic cylinder no. 1 is faster than that of hydraulic cylinder no. 2, rack no. 1 drives the axle center of the gear to shift to the left, and through the action of the connecting rod, the follow-up valve core moves to the right, thus reducing the cross section area of the valve port of oil outlet no. 1. The section area of the valve port of oil outlet no. 2 is increased, so that the flow into hydraulic cylinder no. 1 decreases, the speed of hydraulic cylinder no. 1 decreases, the flow into hydraulic cylinder no. 2 increases, and the speed of hydraulic cylinder no. 2 increases, until the two cylinders are of equal speed.

Similarly, when the speed of hydraulic cylinder no. 1 is less than that of hydraulic cylinder no. 2, rack no. 2 drives the shaft center of the gear to shift to the right, and through the action of the connecting rod, the follow-up valve core moves to the left, increasing the cross section area of the valve port of oil outlet no. 1, the section area of the valve port of oil outlet no. 2 is reduced, so that the flow into hydraulic cylinder no. 1 increases, the speed of hydraulic cylinder no. 1 increases, the flow into hydraulic cylinder no. 2 decreases, and the speed of hydraulic cylinder no. 2 decreases, until the two cylinders are of equal speed.

After the selection of hydraulic system components and calculation of system pressure loss, AMESim simulation software is used to simulate designed hydraulic system and explore whether the designed synchronous hydraulic system with automatic deviation correction can be established. The model is set to two different operating conditions, simulation time is set to 10 s, and

piston rod displacement is set to 80 mm. The results show that piston rod displacement of two cylinders can be obtained. Displacement curve of two-way shunt servo valve middle spool is acquired. The system designed in this paper can achieve synchronous displacement of two cylinder piston rods. These rods have high synchronization, which meets the requirement of hydraulic expansion axial feed hydraulic system. When the same load pressure is applied to both cylinders, displacement curves of corresponding piston rods completely coincide, and the displacement error is equal to 0 mm. When different load pressures are applied to two cylinders, the servo valve can adjust the flow via diversion port according to valve core displacement. Therefore, the displacement of two piston rods is consistent, and the automatic deviation correction function is realized. Hence, the system is successfully verified. The system model is shown in Figure 7.

In order to properly analyze automatic deviation correction hydraulic system designed in this paper, mathematical modeling for hydraulic control system is carried out in this section. The block diagram of the hydraulic control system is shown in Figure 8.

According to the above-established mathematical model, the flow equation of the following slide valve is obtained:

$$q_L = (q_1 + q_2), \quad (1)$$

where q_L is the load flow, L/min; q_1 is the flow rate into hydraulic cylinder no. 1, L/min; and q_2 is the flow rate into hydraulic cylinder no. 2, L/min.

According to fluid mechanics, valve orifice flow should satisfy Bernoulli equation:

$$q_1 = C_d A_1 \sqrt{\frac{2(p_s - p_1)}{\rho}}, \quad (2)$$

where C_d is the throttle flow coefficient; p_s is the oil supply pressure, MPa; ρ is the oil density, kg/m³; A_1 is the flow area of the throttle port of hydraulic cylinder no. 1, m²; and p_1 is the right chamber pressure of hydraulic cylinder no. 1, MPa.

$$q_2 = C_d A_2 \sqrt{\frac{2(p_s - p_2)}{\rho}}, \quad (3)$$

where A_2 is the flow area of hydraulic cylinder throttle port no. 2, m², and p_2 is the left chamber pressure of hydraulic cylinder no. 2, MPa.

$$q_L = C_d A_1 \sqrt{\frac{2(p_s - p_1)}{\rho}} + C_d A_2 \sqrt{\frac{2(p_s - p_2)}{\rho}}. \quad (4)$$

Equation (4) is linearized to obtain pressure-flow characteristics near zero:

$$q_L = (k_q x_v - k_c p_L), \quad (5)$$

where k_q is the flow gain factor and k_c is the flow pressure coefficient.

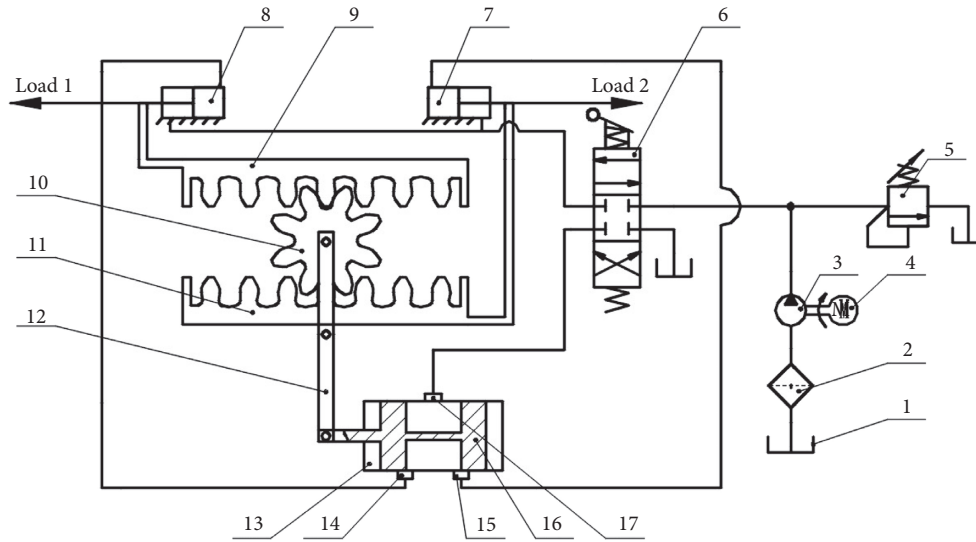


FIGURE 6: Schematic diagram of hydraulic control system: (1) oil source; (2) filter; (3) hydraulic pump; (4) motor; (5) overflow valve; (6) hand-directional valve; (7) hydraulic cylinder no. 2; (8) hydraulic cylinder no. 1; (9) rack no. 1; (10) displacement gear; (11) rack no. 2; (12) lever; (13) bidirectional shunt follow-up valve; (14) oil outlet no. 1; (15) oil outlet no. 2; (16) valve core; (17) oil inlet.

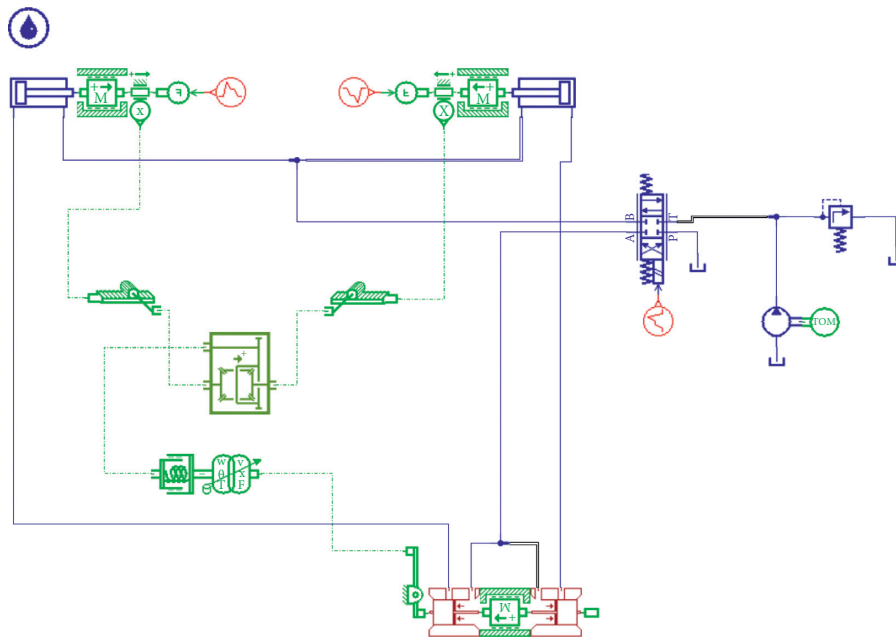


FIGURE 7: Modeling diagram of AMESim hydraulic system.

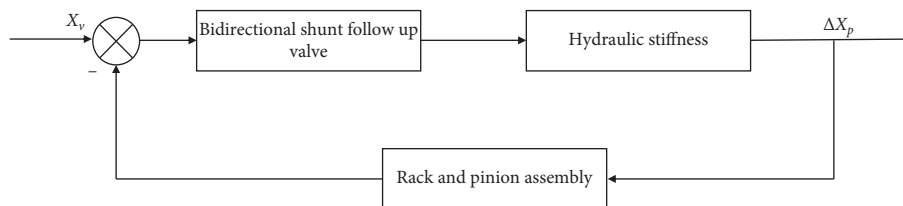


FIGURE 8: Block diagram of the hydraulic control system.

$$\begin{aligned}
k_q &= \frac{\partial q_L}{\partial x_v} \\
&= C_d W_1 \sqrt{(1/\rho)(p_s - p_1)} + C_d W_2 \sqrt{(1/\rho)(p_s - p_2)}, \\
k_c &= \frac{\partial q_L}{\partial p_L} \\
&= \frac{C_d W x_v \sqrt{(1/\rho)(p_s - p_1)} p_L}{2(p_L - p_1)} + \frac{C_d W x_v \sqrt{(1/\rho)(p_s - p_2)} p_L}{2(p_L - p_2)},
\end{aligned} \quad (6)$$

where p_L is the load pressure, kN, and x_v is the valve core displacement, m .

Flow continuity equation of hydraulic cylinder is established. It is assumed that the connecting pipe is relatively short and thick, while pipe friction and pressure losses in the pipe as well as its dynamic state are assumed to be negligible. The pressure values in all working cavities of the hydraulic cylinder are equal, and the oil temperature and volume elastic modulus are assumed to be constant. Both internal and external hydraulic cylinder leakages are laminar; i.e., the load flow is equal to

$$\begin{aligned}
q_1 &= A_p \frac{dx_{p1}}{dt} + C_{ip} p_L + \frac{V_1}{\beta_e} \frac{dp_L}{dt}, \\
q_2 &= -A_p \frac{dx_{p2}}{dt} + C_{ip} p_L + \frac{V_2}{\beta_e} \frac{dp_L}{dt}, \\
q_L &= (q_1 + q_2),
\end{aligned} \quad (7)$$

where A_p is the effective area of hydraulic cylinder piston rod-free cavity, m^2 ; x_{p1} is the displacement of hydraulic cylinder piston rod no. 1, m ; x_{p2} is the displacement of hydraulic cylinder piston rod no. 2, m ; C_{ip} is the leakage coefficient in hydraulic cylinder; V_1 is the volume of hydraulic cylinder inlet chamber no. 1, m^3 ; V_2 is the volume of hydraulic cylinder inlet chamber no. 2, m^3 ; and β_e is the effective volume modulus of elasticity (including the mechanical flexibility of oil, connecting pipes, and cylinders).

$$\Delta x_p = (x_{p1} - x_{p2}), \quad (8)$$

where Δx_p is the transmission deviation, m .

$$V_t = V_1 + V_2, \quad (9)$$

$$q_L = A_p \frac{dx_p}{dt} + 2C_{ip} p_L + \frac{V_t}{\beta_e} \frac{dp_L}{dt}, \quad (10)$$

where V_t is the total compression volume, m^3 .

Based on the aforementioned relations, force balance equation and load of hydraulic cylinder are established. According to Newton's second law, the balance equation of the output force and the load force of hydraulic cylinder can be obtained as follows:

$$A_p p_L = m_t \frac{d^2 x_p}{dt^2} + B_p \frac{dx_p}{dt} + K x_p + F_L, \quad (11)$$

where m_t is the total mass of the piston and the load converted to the piston, kg ; B_p is the viscous damping coefficient of piston and load; K is the load spring stiffness; and F_L is any accidental load acting on the piston, kN .

Equations 5, (10), and (11) represent three basic equations of valve controlled hydraulic cylinder, which fully describe dynamic characteristics of valve controlled hydraulic cylinder. Laplace transform of three equations can be written as

$$\begin{aligned}
Q_L &= K_q X_v - K_c P_L, \\
Q_L &= A_p s X_p + 2C_{ip} P_L + \frac{V_t}{\beta_e} s P_L,
\end{aligned} \quad (12)$$

$$A_p P_L = m_t s^2 \Delta X_p + B_p s \Delta X_p + K \Delta X_p + F_L.$$

If only instruction signal X_v is present, intermediate variables Q_L and P_L can be eliminated:

$$\Delta X_p = \frac{(K_q/A_p)X_v - (1/A_p^2)(2C_{ip} + (V_t/\beta_e)s + K_c)F_L}{(m_t V_t/\beta_e A_p^2) + ((2m_t C_{ip}/A_p^2) + (2m_t K_c/A_p^2) + (B_p V_t/\beta_e A_p^2))s^2 + ((2B_p C_{ip}/A_p^2) + (B_p K_c/A_p^2) + (KV_t/\beta_e)A_p^2)s + (2C_{ip} + K_c/A_p^2)K}. \quad (13)$$

Most servo system loads consider inertia load as the main objective, while elastic load can be assumed to be negligible due to its minor effect. Since velocities $((2m_t C_{ip}/A_p^2)S, (2B_p C_{ip}/A_p^2)S, (B_p K_c/A_p^2))$ generated by the leakage

coefficient (C_{ip}) and viscous damping coefficient (B_p) in the hydraulic cylinder are much smaller than the moving speed of the piston, the above equation can be disregarded. When $K=0$, the transfer function can be simplified as

$$\Delta X_p = \frac{(K_q/A_p)X_v - (1/A_p^2)(2C_{ip} + (V_t/\beta_e)s + K_c)F_L}{((S^2/\omega_0^2) + (2\xi/\omega_0)S + 1)S} \quad (14)$$

When feedback gain $K_f = 1/2$ is added, the transfer function for input instruction X_v can be written as

$$G(s) = \frac{\Delta X_p}{X_v} = \frac{K_q K_f / A_p}{((S^2/\omega_0^2) + (2\xi/\omega_0)S + 1)S} \quad (15)$$

Once known parameters are inserted into the equation, the following expression is obtained:

$$G(s) = \frac{\Delta X_p}{X_v} = \frac{39.48}{((S^2/221^2) + (0.4/221)S + 1)S} \quad (16)$$

Equation (16) is loaded into Simulink environment to obtain the simulation model shown in Figure 9. Step response curve of the system is finally obtained (Figure 10.)

When the step signal is acting as the input signal, the system reaches a stable state at approximately 0.2 s without overshoot. It can be concluded that the output signal is consistent with the input signal; i.e., the performance is satisfactory.

4. Automobile Torsion Beam Hydraulic Bulging Simulation Based on DYNIFORM

4.1. Simulation of Hydraulic Bulging Torsion Beam. Typical process of torsion beam manufacturing is stamping. In this paper, in order to improve the end forming condition of parts and quality of the final product, traditional stamping is improved. Furthermore, the end shaping is simultaneously carried out during the stamping process. Movement mode of the preform die is as follows: during the downward process of the upper die, the plug at both ends is fed 415 mm axially for shaping purposes until the die is fully closed. The preform model is designed according to the requirements and shown in Figure 11.

First, CATIA software is employed to establish the selected pipe blank model, whose size is $\varnothing 104 \text{ mm} \times 1290 \text{ mm} \times 3 \text{ mm}$. Then, the model is imported into DYNIFORM for meshing with prebuilt IGS files of punch, matrix, and plug surface. DP780 high-strength steel is selected as the material. Since die and plug can be regarded as rigid bodies, linear loading path is adopted. The overall simulation time is 0.02 s, and software default trapezoidal loading path is adopted for the mold closing speed. The mold closing is completed at 0~0.02 s descending from the upper die, and the axial displacement of the plug is equal to 415 mm during 0~0.01 s timespan.

As shown in Figures 12 and 13, no wrinkling and cracking occurred during the preforming process.

Maximum thinning rate of parts is equal to 7.889%, while maximum thickening rate is equal to 16.188%, both of which are within a reasonable range. Maximum thinning rate is located at the junction of the middle V-shaped zone and the transition zone, which occurs because this is the place where the tube body first gets in contact with the punch, thus altering the shape most significantly. This is in accordance with the actual situation. The maximum thickening position is at the junction of the transition area and the port area. This is due to the cross section shape of this area being relatively complex, which makes it easy for material to accumulate. Torsion beam can be flattened by later applying internal pressure via liquid, which is in accordance with the actual processing situation. Therefore, it can be concluded that torsion beam performance is adequate.

4.2. Simulation of Torsion Beam Hydraulic Bulging.

According to the mold design, mold cavity of hydraulic bulging is consistent with the final part. First, IGS files of each die surface modeled by CATIA are imported into DYNIFORM and meshed. Simultaneously, the dynain file (the forming results with stress and strain) of preformed tube blank is imported. After establishing the finite element model, simulation parameters are added. According to the results of the torsion beam structure design, high-strength steel material denoted as DP780 is employed. Initial yield pressure and integral pressure are calculated as reference values. Since the integral pressure is approximately equal to 1/10~1/4 of the material yield strength [12], the support pressure is obtained as 31 MPa for the comprehensive preforming of the torsion beam. Integral pressure is equal to 180 MPa. Friction coefficient is 0.125, and the loading time is defined as 0.02 s.

The entire molding process is also divided into two stages. The first stage, feeding pressure stage, lasts for 0.01 s. Then, the bulging stage occurs and lasts for 0.01~0.02 s. The results indicate that the feeding amount behaves as linear loading, with the ideal feeding amount being a minimum of 30 mm. The internal pressure is equal to 0~0.01 s, while a certain amount of bulging is carried out along the linear loading path. The internal pressure is 180 MPa in 0.01~0.015 s range, followed by the pressure maintaining molding which is carried out in 0.015~0.02 s range. This, in turn, improves the molding effect. The molding effect is shown in Figure 14.

In Figure 15, distribution of torsion beam wall thickness reduction rate after forming according to the above loading path is shown. For the convenience of discussion, four characteristic areas, A, B, C, and D, are marked in the figure [13]. Overall, the simulation results of torsion beam hydraulic bulging are good and meet the actual processing needs.

Areas A and D at the side edge of the end represent main thickness reduction areas. Area A is located in the contact area between both ends of the plug and the tube billet, where the material has relatively large fluidity. Moreover, high-pressure liquid at the end accelerates wall thickness thinning. Maximum thickness reduction appears in D region. This is

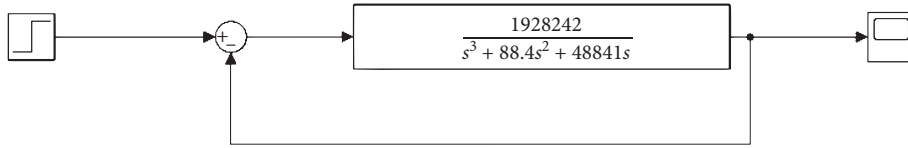


FIGURE 9: Simulation diagram of hydraulic synchronous system transfer function.

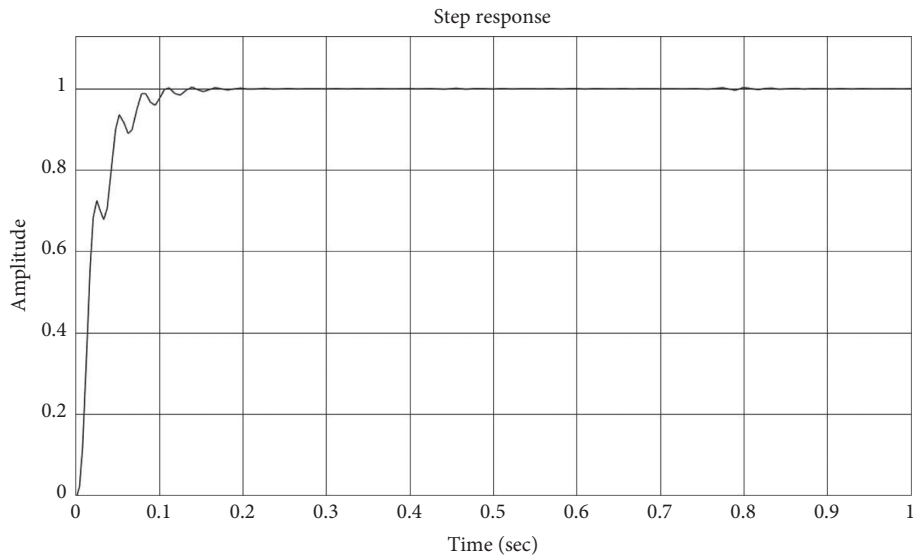


FIGURE 10: Step response curve of hydraulic synchronous system.

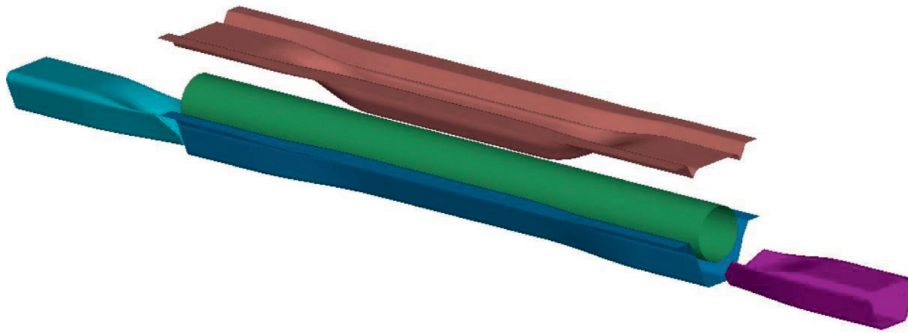


FIGURE 11: Preforming process scheme diagram.

because the area is the contact area between the first punch and preforming parts. At the border of V-shaped area and transition area, mold clamping shape changes significantly. Axial and circular tensile stresses cause wall thickness reduction. More specifically, the minimum value of wall thickness is equal to 2.713 mm with the corresponding maximum thinning rate of 9.577%.

Transition section *B* represents main thickening area, which is caused by excessive hoop expansion during mold closing, thus resulting in hoop compression. Maximum *B* area wall thickness is 3.527 mm, which corresponds to a maximum thickening rate of 17.574% and a maximum wall thickness difference of 0.814 mm. Compared with preforming results, it is found that the change is very small. This

can be attributed to irregularity of area shape. When compared with other areas, cross-sectional shape change is relatively small. This area has been adequately formed in the early stage, and the later hydraulic bulging only improves the film precision of the fillet part.

5. Optimization of Process Parameters Based on Orthogonal Experimental Design and Taguchi Algorithm

5.1. Orthogonal Experiment and Evaluation Index of Torsion Beam Hydraulic Bulging. In the process of automobile torsion beam hydraulic bulging, many factors affect the

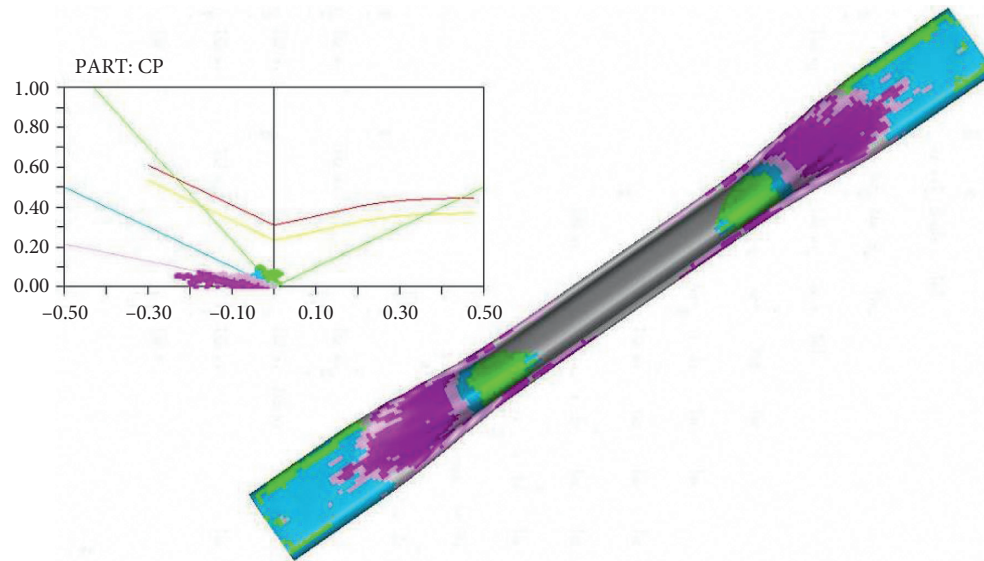


FIGURE 12: FLD of torsion beam preform.

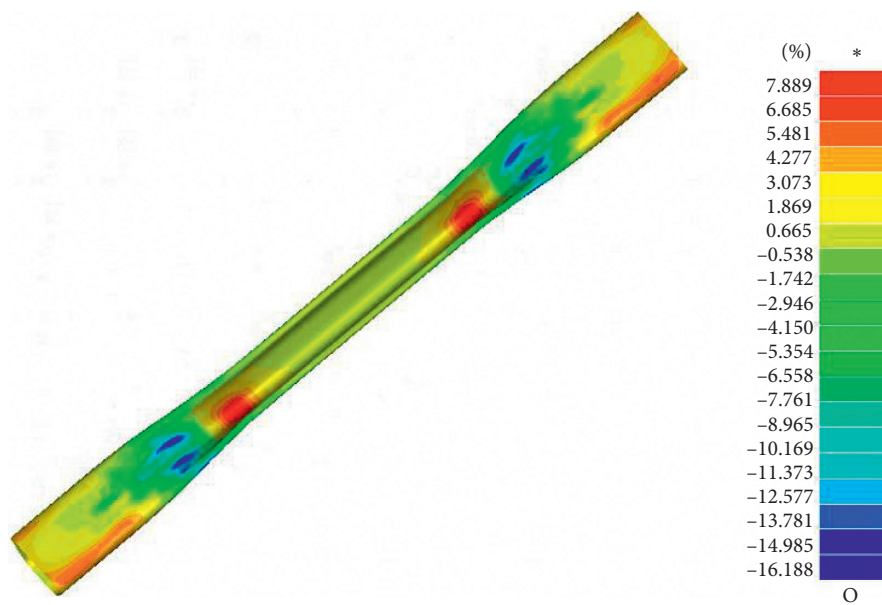


FIGURE 13: Nephogram of torsion beam wall thinning rate.

forming quality of the final product, such as the selection of the initial pipe diameter, the loading path of internal pressure, and the feeding quantity. Based on the cost effectiveness, experimental research on these factors and levels cannot be carried out individually. In this paper, the orthogonal experiment method is applied to hydraulic bulging of torsion beam. According to the orthogonal table, representative simulated verification process parameter combination is selected.

Based on previous discussion and results, wall thickness change is considered as one of the main factors affecting the product surface quality and assembly accuracy. If the thickness of each product part changes beyond the allowable range, wrinkling, warping, and rupture defects can occur.

This, in turn, affects the forming quality of the parts. Therefore, maximum thinning and maximum thickening rates are selected as evaluation indexes in this paper.

5.2. Orthogonal Experimental Table and Analysis of Results.

In this paper, four process parameters are selected as experimental level factors: supporting pressure, molding pressure, friction coefficient, and feeding quality. In order to ensure the experimental effect, the range of process parameters should be as large as possible [14]. By assuming negligible interaction between process parameters, four levels are evenly selected, and design level factors are shown in Table 2.

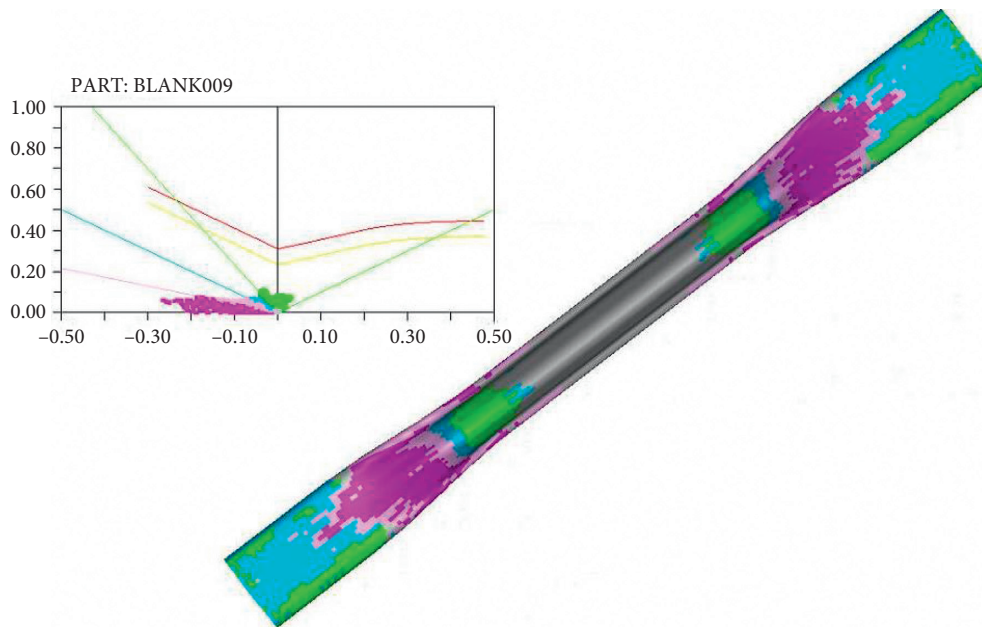


FIGURE 14: FLD of torsion beam hydraulic expansion.

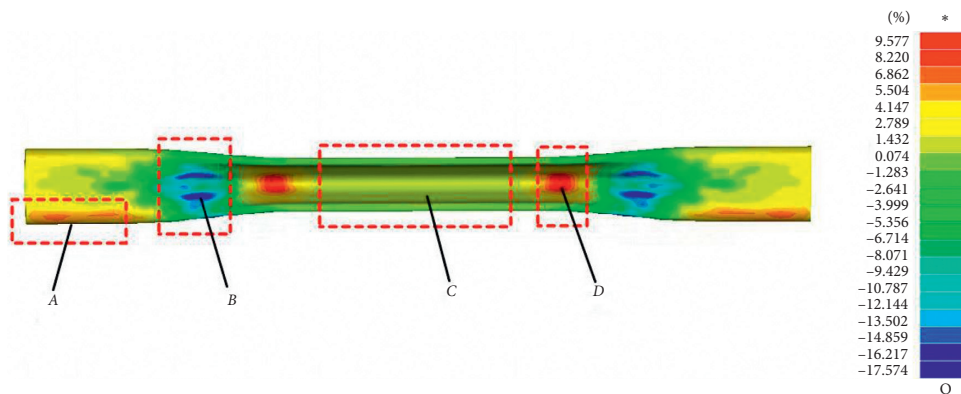


FIGURE 15: Nephogram of torsion beam hydraulic bulging wall thinning rate.

TABLE 2: Level factor setting table.

Level	Factor			
	A Supporting pressure (MPa)	B Molding pressure (MPa)	C Feeding quality (mm)	D Friction coefficient
1	20	150	25	0.075
2	40	180	30	0.1
3	60	210	35	0.125
4	80	240	40	0.15

Level factors are input into the orthogonal table to generate 16 groups of process parameter combinations. These data groups are, respectively, simulated and analyzed, and corresponding maximum thinning rate and maximum thickening rate are obtained, as shown in Table 3.

In the orthogonal table, if one wishes to obtain the index value at the j -th level of column i , average number R_{ij} of the sum of the experimental indexes in this column can be

used, where $i = 1, 2, 3, 4, \dots, p$ and $j = 1, 2, 3, 4, \dots, m$. The index range R_i is as follows:

$$R_i = (R_{ij_{\max}} - R_{ij_{\min}}), \quad (17)$$

where $R_{ij_{\max}}$ is the maximum mean value of indicators at different levels and $R_{ij_{\min}}$ is the minimum mean value of indicators at different levels.

TABLE 3: Experimental design and results.

Test number	Factor				Indicator	
	A	B	C	D	Maximum thinning rate	Maximum thickening rate
1	20	150	25	0.075	9.01	16.52
2	20	180	30	0.1	9.53	17.52
3	20	210	35	0.125	8.79	19
4	20	240	40	0.15	9.01	20.89
5	40	210	40	0.075	9.53	18.79
6	40	240	35	0.1	10.7	20.42
7	40	150	30	0.125	8.77	16.58
8	40	180	25	0.15	8.62	17.56
9	60	240	30	0.075	9.45	20.18
10	60	210	25	0.1	10.07	18.91
11	60	180	40	0.125	9.61	17.66
12	60	150	35	0.15	8.76	16.64
13	80	180	35	0.075	9.58	17.6
14	80	150	40	0.1	9.59	16.54
15	80	240	25	0.125	9.91	20.8
16	80	210	30	0.15	8.72	19.26

TABLE 4: Range analysis table of maximum thinning rate.

Level	A	B	C	D
Mean 1	9.085	9.033	9.403	9.393
Mean 2	9.405	9.335	9.118	9.973
Mean 3	9.473	9.278	9.458	9.270
Mean 4	9.450	9.768	9.435	8.778
Range	0.365	0.735	0.340	1.195

By employing 17, range of maximum thinning rate under different factor levels can be obtained, as shown in Table 4.

Range presented in Table 4 reflects the influence relationship of maximum thinning rate at the factor level. According to Table 4, friction coefficient has the greatest influence on maximum thinning rate of automotive torsion beam hydraulic bulging. The influence degree of each factor on the index is as follows: friction coefficient > molding pressure > supporting pressure > feeding quality. Material thickness reduction is a process of mutual restriction by many factors. According to the above obtained range analysis, the combination should be selected as $A_1B_1C_2D_4$. The molding effect is shown in Figure 16. In other words, the supporting pressure is 20 MPa, the molding pressure is 150 MPa, the feeding rate is 30 mm, and the friction coefficient is 0.15. DYNAFORM simulation analysis results are shown in Figure 17. Maximum thinning rate of parts is 8.591%, maximum thickening rate is 16.579%, and maximum thinning rate reaches the minimum. The results are in accordance with the range analysis.

Next, maximum thickening rate is analyzed. It is observed that maximum thickening rate has a greater impact on parts. If the maximum product thickening amount is large enough, it may lead to wrinkling defects of the torsion beam and consequently inability to assemble the product. The range of maximum thickening rate under different factor levels can be obtained as shown in Table 5.

The analysis shows that the molding pressure has a significant influence on maximum thickening rate of the product. Influence degree of four factors can be classified as follows: molding pressure > friction coefficient > supporting pressure > feeding quality. The optimal parameter combination obtained by range analysis is $A_2B_1C_2D_1$, molding effect is shown in Figure 18, supporting pressure is 40 MPa, molding pressure is 150 MPa, feeding quality is 30 mm, and friction coefficient simulated by DYNAFORM is 0.075. As shown in Figure 19, maximum thinning rate is 9.848%, maximum thickening rate is 16.504%, and maximum thickening rate reaches the minimum. The results are in line with the conducted range analysis.

5.3. Torsion Beam Hydraulic Bulging Parameter Optimization Based on Taguchi Algorithm.

Many evaluation indexes are employed for hydraulic bulging quality of an automobile torsion beam. In this paper, maximum thinning rate and maximum thickening rate are selected as forming evaluation indexes. However, by assuming negligible simultaneous influence of two evaluation indexes on parts range analysis, orthogonal experiment is employed to investigate two evaluation indexes. Therefore, Taguchi algorithm is utilized to combine them by weight coefficient into an evaluation index Y for comprehensive analysis [15]. Proportions of maximum thinning rate and maximum thickening rate of wall thickness before and after molding are set to 50% [16]. As shown in Table 6, supporting pressure, molding pressure,

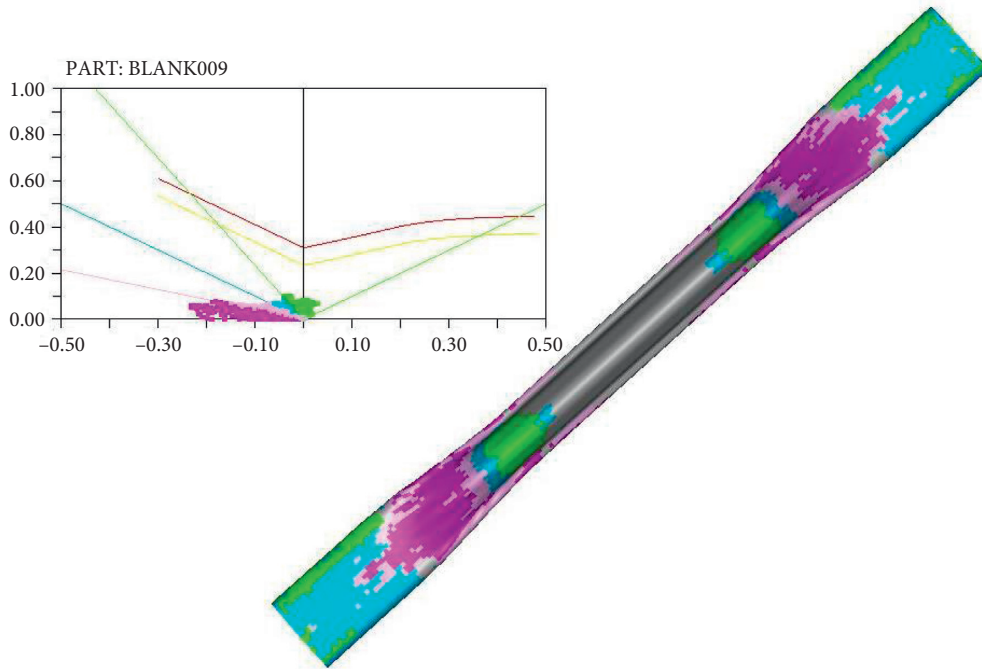


FIGURE 16: FLD of $A_1B_1C_2D_4$ combination.

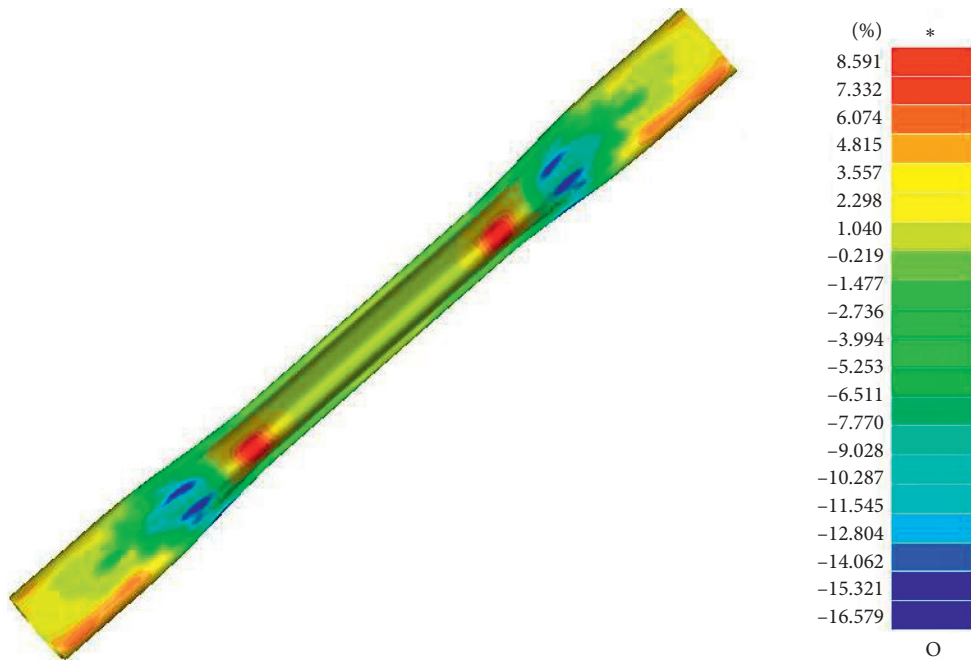


FIGURE 17: Nephogram of thinning rate of $A_1B_1C_2D_4$ combination.

TABLE 5: Range analysis table of maximum thickening rate.

Level	A	B	C	D
Mean 1	18.483	16.570	18.448	18.273
Mean 2	18.338	17.585	18.385	18.348
Mean 3	18.348	18.990	18.415	18.510
Mean 4	18.550	20.573	18.470	18.588
Range	0.213	4.003	0.085	0.315

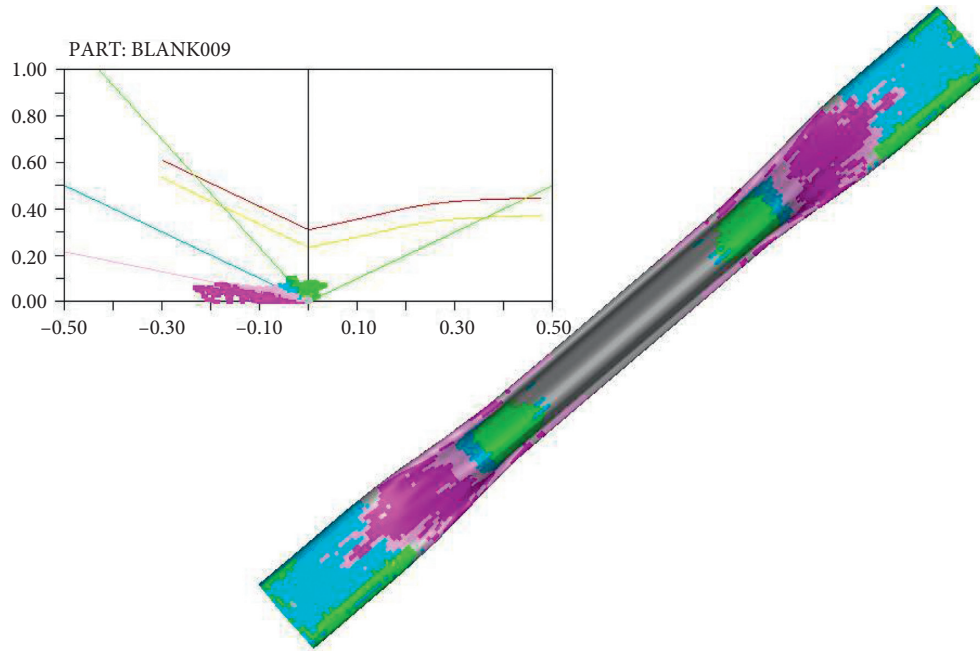


FIGURE 18: FLD of $A_2B_1C_2D_1$ combination.

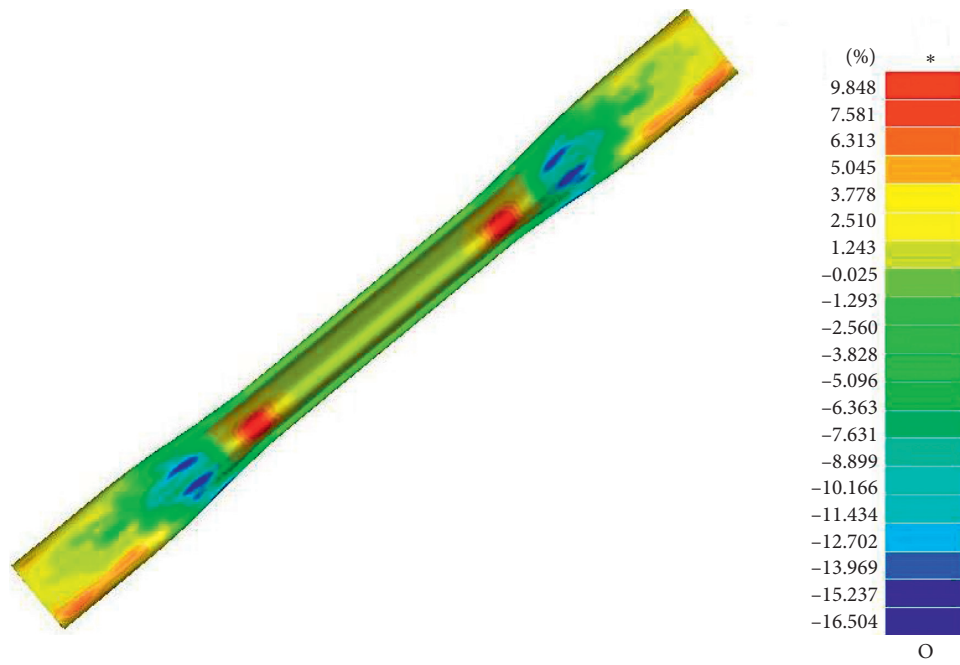


FIGURE 19: Nephogram of thinning rate of $A_2B_1C_2D_1$ combination.

TABLE 6: Level factor setting table.

Level	Factor			
	A supporting pressure (MPa)	B molding pressure (MPa)	C feeding quality (mm)	D friction coefficient
1	20	150	25	0.075
2	40	180	30	0.1
3	60	210	35	0.125
4	80	240	40	0.15

TABLE 7: Orthogonal inner table.

Test number	Factor				Indicator	
	A	B	C	D	Maximum thinning rate	Maximum thickening rate
1	20	150	25	0.075	9.01	16.52
2	20	180	30	0.1	9.53	17.52
3	20	210	35	0.125	8.79	19
4	20	240	40	0.15	9.01	20.89
5	40	210	40	0.075	9.53	18.79
6	40	240	35	0.1	10.7	20.42
7	40	150	30	0.125	8.77	16.58
8	40	180	25	0.15	8.62	17.56
9	60	240	30	0.075	9.45	20.18
10	60	210	25	0.1	10.07	18.91
11	60	180	40	0.125	9.61	17.66
12	60	150	35	0.15	8.76	16.64
13	80	180	35	0.075	9.58	17.6
14	80	150	40	0.1	9.59	16.54
15	80	240	25	0.125	9.91	20.8
16	80	210	30	0.15	8.72	19.26

feeding quality, and friction coefficient are selected as controllable factors of the level table, and four levels are selected for each factor.

Level factors are input into the orthogonal Table 7, and 16 groups of process parameter combinations are generated.

Signal-to-noise ratio is the ratio between signal and noise. Types of signal-to-noise ratios are different according to various experimental optimization objectives. For hydraulic bulging process considered in this paper, numerical evaluation index is expected to be as small as possible within a reasonable range. Thus, signal-to-noise ratio η is chosen as

$$\eta = -10 \log_{10} \left(\frac{1}{n} \sum_{j=1}^n S_j^2 \right). \quad (18)$$

The expected minimum value of maximum thinning ratio is set as Y_1 , and SNR is set as η_1 . The expected minimum value of maximum thickening ratio is set as Y_2 , and SNR is set as η_2 . Hence, the comprehensive SNR is

$$\eta = (0.5\eta_1 + 0.5\eta_2). \quad (19)$$

Equation (19) is used to calculate signal-to-noise ratio, and the results are shown in Table 8.

According to direct observation, the first group has the largest comprehensive signal-to-noise ratio and the best molding condition. Combination of process parameters can be obtained as $A_1B_1C_1D_1$.

Finally, SNR calculation results are analyzed: In the first step, sum of SNR is found, which is expressed as T [17]. In the second step, sum and average value of SNR of each factor and each level is found. In the third step, range of each column is obtained, which is expressed as R . In the fourth step, sum of total fluctuation squares of SNR is acquired, which is expressed as S_T . Finally, in step five, sum of SNR square fluctuations of each factor is found, which is, respectively, expressed as S_1, S_2, S_3, S_4 . The results are presented in Table 9.

TABLE 8: SNR calculation results table.

Test number	η_1	η_2	η
1	-19.0945	-24.3602	-21.7273
2	-19.3450	-24.6229	-21.9840
3	-19.1954	-24.9640	-22.0797
4	-19.1704	-25.3695	-22.2700
5	-19.2559	-25.3916	-22.3237
6	-19.5082	-25.5374	-22.5228
7	-19.4213	-25.3911	-22.4062
8	-19.3385	-25.3316	-22.3350
9	-19.3577	-25.4238	-22.3908
10	-19.4334	-25.4349	-22.4341
11	-19.4539	-25.3922	-22.4231
12	-19.4067	-25.3192	-22.3629
13	-19.4241	-25.2891	-22.3566
14	-19.4396	-25.2295	-22.3346
15	-19.4734	-25.3149	-22.3942
16	-19.4348	-25.3395	-22.3872

TABLE 9: Variance data table.

	A	B	C	D	
T_1	-88.0610	-88.8310	-88.8907	-88.7984	$T = -365.7321$
T_2	-89.5877	-89.0986	-89.1681	-89.2755	$S_T = 0.6058$
T_3	-89.6109	-89.2247	-89.3220	-89.3031	
T_4	-89.4724	-89.5777	-89.3513	-89.3551	
t_1	-22.0153	-22.2078	-22.2227	-22.1996	
t_2	-22.3969	-22.2747	-22.2920	-22.3189	
t_3	-22.4027	-22.3062	-22.3305	-22.3258	
t_4	-22.3681	-22.3944	-22.3378	-22.3388	
Range (R)	0.3875	0.1867	0.1151	0.1392	
Wave (S)	0.4224	0.0721	0.0333	0.0501	

In the sixth step, variance is analyzed. The results are presented in Table 10.

TABLE 10: Variance analysis table.

Source	<i>S</i>	<i>f</i>	<i>V</i>	<i>F</i> value	<i>R</i> square
<i>A</i>	0.4224	3	0.1408	12.6737	0.1502
<i>B</i>	0.0721	3	0.0240	2.1641	0.0349
<i>C</i>	0.0333	3			0.0132
<i>D</i>	0.0501	3	0.0167	1.5042	0.0194
(<i>e</i>)	(0.0333)	(3)	0.0111		
<i>T</i>	0.583	3			

TABLE 11: SNR response table.

Level	Factor		
	Molding pressure (MPa)	Feeding quantity (mm)	Friction coefficient
1	-100.3000	-100.4416	-100.4646
2	-100.6358	-100.7773	-100.8248
3	-101.1300	-101.1097	-101.0622
4	-102.6957	-101.3828	-101.3598

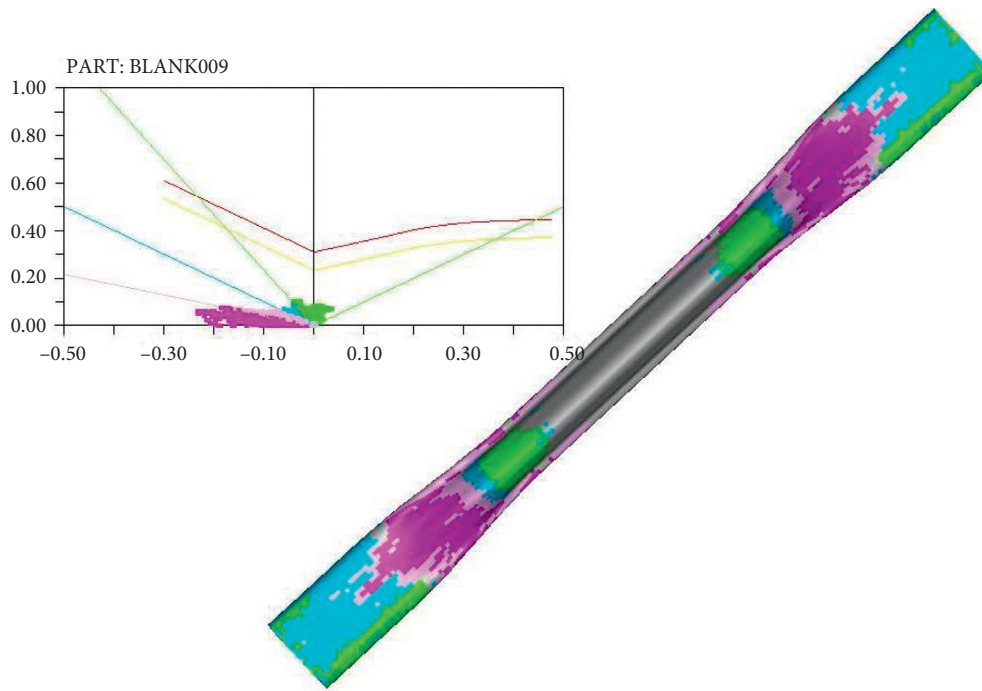


FIGURE 20: FLD of $A_1B_1C_1D_1$ combination.

Based on SNR variance analysis ratio, factor *A* has a significant impact on quality fluctuation characteristics. Factor *A* is considered a stable factor, while factors *B*, *C*, and *D* are adjustable factors. For stable factors, the level is A_1 . SNR values of maximum thickening ratio fraction of factors *B*, *C*, and *D* are listed in Table 11.

As factors *B*, *C*, and *D* have minor influence on quality fluctuation characteristics, maximum thinning rate can be neglected, and parameters *B*, *C*, and *D* can be simply

adjusted to minimize the maximum thickening rate. According to Table 11, optimal process parameter is $B_1C_1D_1$ when only maximum thickening rate is considered.

As shown in Figures 20 and 21, final optimized combination is $A_1B_1C_1D_1$, maximum thinning rate is 9.013%, and maximum thickening rate is 16.523%. These results are basically consistent with the optimized combination $A_1B_1C_1D_1$ obtained via intuitive method.

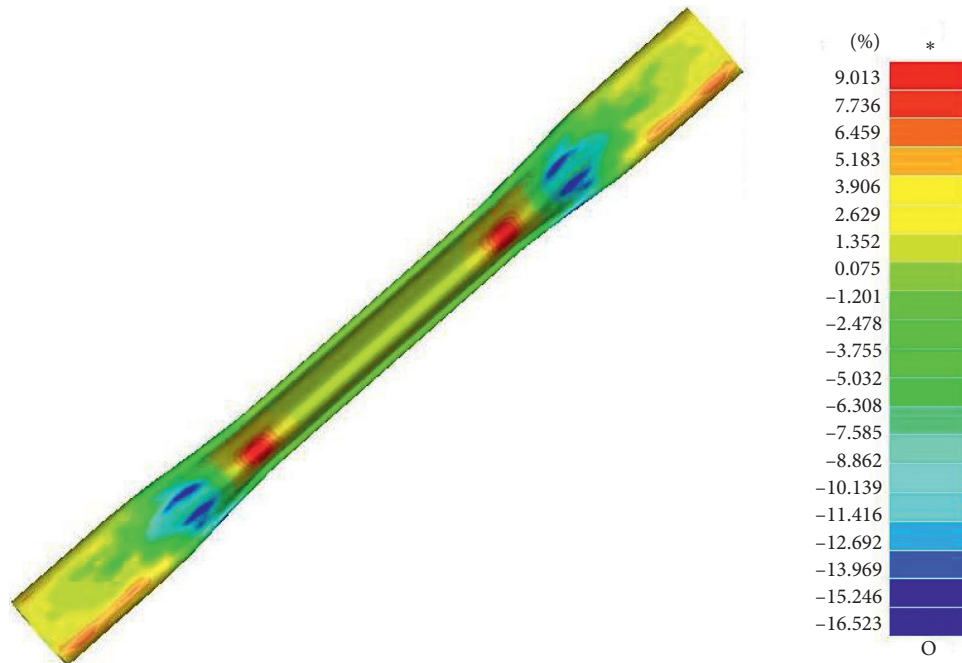


FIGURE 21: Nephogram of thinning rate of $A_1B_1C_1D_1$ combination.

6. Conclusions

- (1) CATIA is used to design three-dimensional modeling of tubular torsion beam, and corresponding materials and initial tube blank are selected for the processed products. The forming process of parts is determined, and calculation of relevant process parameters in hydraulic bulging is completed.
- (2) CATIA is used to design hydraulic bulging torsion beam die. In addition, hydraulic synchronous control system, which can automatically correct deviation, is designed for synchronous cylinders on both sides of the die. Synchronous displacement curves of two cylinder piston rods under two different working conditions are obtained in AMESim. When the same load pressure is applied to both hydraulic cylinders, displacement curves of cylinder piston rods are completely coincident, and the corresponding displacement error is 0 mm. The moving valve core is in the middle position. When different load pressures are applied to cylinders, the servo valve can adjust the flow at the diversion port based on valve core displacement. Therefore, displacement of two piston rods is kept consistent. Hence, automatic deviation correction function of hydraulic control system is successfully verified. Mathematical model of hydraulic control system is established, and system synchronization is verified via Simulink.
- (3) Maximum thinning rate and maximum thickening rate are taken as forming evaluation indexes. Simulation analysis of torque beam hydraulic bulging process was completed via DYNAFORM. Maximum thinning rate and maximum thickening

rate of preformed parts were 7.889% and 16.188%, respectively. No wrinkle or flash defects were observed. After hydraulic bulging, maximum thinning rate and maximum thickening rate of parts were 9.577% and 17.574%, respectively, which were in the qualified range. The forming parts were divided into four regions, A, B, C, and D. Wall thickness variation of each region was analyzed.

- (4) Process parameters of hydraulic bulging torsion beam were optimized by employing Taguchi algorithm, and accuracy of optimization results was verified via DYNAFORM. Optimal molding parameters are as follows: supporting pressure is 20 MPa, molding pressure is 150 MPa, feeding quantity is 25 mm, friction coefficient is 0.075, maximum thinning rate is 9.013%, and maximum thickening rate is 16.523% [18–26].

Data Availability

The data used to support the findings of this study are included within the article.

Conflicts of Interest

The authors declare that they have no conflicts of interest.

Acknowledgments

This article belongs to the major projects of the University Synergy Innovation Program of Anhui Province (GXXT-2019-004) and the project of the Teaching Research Project of Anhui Education Department (2019jyxm0229).

References

- [1] E. Liu, *Fea of Stress and Deflection in Dies of Tube Hydroforming*, Harbin Institute of Technology, Harbin, China, 2006.
- [2] X. Yin and R. Lu, "Finite element simulation and experiment on hydroforming tubular twist beam," *Forging and Stamping Technology*, vol. 42, no. 9, pp. 82–86, 2017.
- [3] R. Lu, X. Chen, and X. Hu, "Study on tube hydroforming torsion beam design based on topological analysis," *Automobile Applied Technology*, vol. 45, no. 3, 59 pages, 2020.
- [4] M. Mirzaali, S. M. H. Seyedkashi, G. H. Liaghat, H. Moslemi Naeini, G. K. Shojaee, and Y. H. Moon, "Application of simulated annealing method to pressure and force loading optimization in tube hydroforming process," *International Journal of Mechanical Sciences*, vol. 55, no. 1, pp. 78–84, 2012.
- [5] P. Venkateshwar Reddy, B. Veerabhadra Reddy, and P. Srinivasa Rao, "A numerical study on tube hydroforming process to optimize the process parameters by Taguchi method," *Materials Today: Proceedings*, vol. 5, no. 11, pp. 25376–25381, 2018.
- [6] V. Dhinakaran, A. R. Kumar, R. Ramgopal, S. Kannan, B. Stalin, and T. Jagadeesha, "Topology optimization of steering knuckle," in *Advances in Industrial Automation and Smart Manufacturing. Lecture Notes in Mechanical Engineering*, A. Arockiarajan, M. Duraiselvam, and R. Raju, Eds., Springer, Singapore, pp. 197–206, 2021.
- [7] P. Xie, *Injection Mold Design of Automobile Dash Panel Decorative Panel and Optimization of its Process Parameters*, Anhui Polytechnic University, Wuhu, China, 2019.
- [8] L. Yang, *Research and Development of Internal High Pressure Hot Forming Equipment and Forming Technology*, Nanjing University of Science and Technology, Nanjing, China, 2017.
- [9] Yu. Meng, *Study on Influence of Pulsating Loading on Tube Formability in Hydroforming and its Mechanism*, Northeastern University, Boston, MA, USA, 2010.
- [10] X. Lin, *Research and Design of Advanced High-Pressure Tube Hydroforming System with the Function of Pulsating Loading*, Northeastern University, Boston, MA, USA, 2011.
- [11] P. Wan, *Simulation of Forming Process and Optimization of Forming Process Parameters of Automobile Fender Based on Taguchi Algorithm*, Anhui Polytechnic University, Wuhu, China, 2017.
- [12] S. Yuan, *Modern Hydroforming Technology (fine)*, National Defense Industry Press, Arlington, VA, USA, 2009.
- [13] Y. Jin, *Study on Simulation of Bulging-Pressing Torsion Beam*, Yanshan University, Qinhuangdao, China, 2016.
- [14] J. Sun, *Parameter Optimization and Performance Prediction Research on Desulfurization Dust Removal Pump*, Anhui Polytechnic University, Wuhu, China, 2014.
- [15] J. Zheng, A. Cheng, L. Dong, and P. Lei, "The application of taguchi robust design to vehicle crashworthiness optimization," *Automotive Engineering*, vol. 33, no. 9, pp. 772–776, 2011.
- [16] Y. Tan, *Optimization Research of Plastic Centrifugal Pump Cavitation Performace Based on Cfd Flow Field*, Anhui Polytechnic University, Wuhu, China, 2015.
- [17] B. Hu, Q. Zhang, X. Zhao, and J. Dong, "Research on optimization design of CRT thermal explosion cutting equipment based on taguchi method," *Machinery Design and Manufacture*, no. 5, pp. 15–17, 2010.
- [18] C. Nikhare, M. Weiss, and P. D. Hodgson, "Buckling in low pressure tube hydroforming," *Journal of Manufacturing Processes*, vol. 28, pp. 1–10, 2017.
- [19] A. Fethi, A. Furqan, G. Sana, B. Touhami, K. Ali, and S. C. Heung, "Design of T-shaped tube hydroforming using finite element and artificial neural network modeling," *Journal of Mechanical Science and Technology*, vol. 34, no. 1, 2020.
- [20] M. Mehran, S. K. Javad, and J. H. Seyed, "Forming limit diagram of aluminum/copper bi-layered tubes by bulge test," *The International Journal of Advanced Manufacturing Technology*, vol. 92, no. 5-8, pp. 1539–1549, 2017.
- [21] S. Haidi, L. Jian, R. Jili, and X. Gao, "Analysis of tubes with rectangular section forming process by fluid–solid coupling method," *The International Journal of Advanced Manufacturing Technology*, vol. 102, no. 5-8, pp. 2491–2509, 2019.
- [22] H. Minsu, Y. Jaemin, L. Jaejun, and H. Seung-Jin, "Development of coupled torsion beam axle dynamic model based on beam elements," *International Journal of Precision Engineering and Manufacturing*, vol. 22, no. 1, pp. 1–15, 2020.
- [23] Y. Kai, X. Fei, L. Kai, and H. Cheng, "Research on torsion beam with high strength steel materials forming," *Key Engineering Materials*, vol. 4332, pp. 136–141, 2017.
- [24] A. Ramaswamy, A. V. Perumal, J. Jagadeesan, and P. Kaladharan, "Optimization of WEDM process parameters for D3 die steel using RSM," vol. 37, no. 1, <https://www.researchgate.net/journal/Materials-Today-Proceedings-2214-7853>, 2020.
- [25] Z. Chen, F. Yu, W. Han, and H. Hai, "Multi-objective optimization of process parameters during low-pressure die casting of AZ91D magnesium alloy wheel castings," *China Foundry*, vol. 15, no. 5, pp. 327–332, 2018.
- [26] S. Samaneh, H. Mohammad, H. Ghassem, and P. Hadi, "Multi-objective optimization of underfloor air distribution (UFAD) systems performance in a densely occupied environment: a combination of numerical simulation and Taguchi algorithm," vol. 32, 2020 <https://www.researchgate.net/journal/Journal-of-Building-Engineering-2352-7102>, Article ID 101495.

Research Article

Study on Injection Molding Process Simulation and Process Parameter Optimization of Automobile Instrument Light Guiding Support

Hu Wu , Youmin Wang , and Mingyue Fang

School of Mechanical Engineering, Anhui Polytechnic University, Wuhu, Anhui 241000, China

Correspondence should be addressed to Youmin Wang; wymtlf@ahpu.edu.cn

Received 29 March 2021; Revised 28 April 2021; Accepted 12 May 2021; Published 24 May 2021

Academic Editor: Ashwini Kumar

Copyright © 2021 Hu Wu et al. This is an open access article distributed under the Creative Commons Attribution License, which permits unrestricted use, distribution, and reproduction in any medium, provided the original work is properly cited.

In the present study, Moldflow® software is applied to simulate the injection molding of automobile instrument light guide bracket and optimize the injection gate position. In this regard, Taguchi orthogonal experimental design is adopted, and five processing parameters, the mold temperature, melt temperature, cooling time, packing pressure, and packing time, are considered as the test factors. Moreover, volume shrinkage and warping amount are considered as quality evaluation indices. Then range analysis and variance analysis are carried out to obtain the optimal combination of molding parameters with the volume shrinkage rate and the warpage amount. The grey correlation analysis was used to analyze the test results and obtain the optimal combination of volume shrinkage rate and amount of warping. Based on the performed simulations, it is found that the maximum volume shrinkage rate and the maximum amount of warping in the optimal design are 6.753% and 1.999 mm, respectively. According to the optimal process parameters, the injection molding of the automobile instrument light guide bracket meets the quality requirements.

1. Introduction

With the rapid development of the plastic industry, plastic products are widely used in different automobile parts due to their unique properties such as lightweight, low price, high insulation, and reasonable corrosion resistance. Currently, plastic parts have a large share in reducing car weight and reducing manufacturing costs. However, inappropriate parameters in the injection molding process may result in numerous defects in the final plastic products. Therefore, it is of significant importance to simulate and analyze each link of the injection molding process before the production of plastic parts to obtain the optimized injection molding process parameters, control defects, ensure the product quality, and improve the production efficiency.

Moldflow® is the most widely applied commercial software in simulating plastic injection molding. Currently, Moldflow Insight can be applied to simulate the whole injection molding process, including the flow, packing

pressure, warpage, shrinkage, cavitation, and fiber orientation [1]. Moreover, Moldflow can be applied to simulate the injection molding process of plastic parts and predict probable defects in plastic parts. Accordingly, the injection molding process parameters can be optimized, which can reduce the production cost and improve the production efficiency, and effectively avoid the defects such as bubbles, weld marks, shrinkage holes, and excessive warping deformation in plastic parts [2].

Studies show that many parameters affect the forming process, and each parameter is interrelated and mutually restricted. Moreover, the influence degree of each parameter on the product quality is different [3]. In this regard, scholars studied the influence of numerous molding parameters on the quality of plastic parts through orthogonal experimental design methods or the combination of an intelligent algorithm and CAE (Computer Aided Engineering) technology [4]. Wang [5] used an orthogonal experimental design method to analyze the influence of molding parameters on

the warpage of the wall switch bracket. Within the allowable range, the process parameters were taken as 4 levels and 5 factors, and the optimal process parameters were found through the range analysis. Tang et al. [6] took volume shrinkage rate and amount of warping as quality evaluation indices and established a response surface model between molding parameters and quality evaluation indices to optimize affecting parameters. Jing et al. [7] optimized the process parameters by Moldflow and Taguchi orthogonal test methods and obtained the influence of process parameters on the warpage and shrinkage mark. Kumar et al. [8] studied the influence of process parameters on the injection molding of PMC cam bushing and optimized the process parameters to improve the cam bushing quality. The design was carried out according to the Taguchi orthogonal test, while the optimization was carried out through the grey correlation analysis and response data. Hentati et al. [9] used Taguchi orthogonal test to conduct injection molding experiments with 4 factors and 3 levels through the statistical design method. To this end, they employed the Moldflow software in the simulation and analysis and obtained the optimal process parameters accordingly. It was found that the optimal combination parameters provide better shear stress for injection molding of PC/ABS parts. Mukras et al. [10] determined the optimal molding process parameters to minimize the molding defects through experimental multiobjective optimization and then studied the warpage and volume shrinkage of the product quality.

In the present study, the automobile instrument light guide bracket is considered as the research object. In this regard, the mold gate and cooling systems are simulated by Moldflow software to obtain the optimal gate position. Then the range analysis and variance analysis are carried out to optimize the molding process parameters, volume shrinkage rate and amount of warping. Finally, the grey correlation analysis is applied to process the test results and obtain the optimal combination of the volume shrinkage rate and warping.

2. Numerical Simulation of Injection Molding Process of the Automobile Instrument Light Guide Bracket

Prior to the numerical simulation of injection molding, it is necessary to establish a 3D model of parts, determine optimal gate position, and simulate the gating system and the cooling system.

2.1. Establishment of the 3D Model for Light Guide Bracket of the Automobile Instrument. In this section, Creo is used to draw the 3D model of the light guide bracket of the automobile. Figure 1 shows that the part shape is complex, and there are many cavities and strong ribs at the bottom. The overall dimension of the part is 367 mm × 169 mm × 25 mm, and a 2.5 mm thick wall is evenly distributed around the part. It should be indicated that the bracket should fit with the lower PCB board and the top plate, so it is necessary to provide a good flatness in the bracket. Consequently, the

volume shrinkage rate and the warping of the part during the molding process should be minimized.

2.2. Finding the Optimal Gate Location. The optimal gate location area recommended by the optimal gate matching should be combined with the structural characteristics of the plastic part. Figure 2 reveals that the recommended optimal gate position is on the part surface. However, the shape of automobile instrument light guide bracket is complex, and there are many cavities and ribs at the bottom, so the gate position cannot be on the part surface. After synthesizing these points, four gate schemes are preliminarily considered. Figure 3 shows the gate positions of each scheme, where Figures 3(a)–3(d) correspond to gate schemes I, II, III, and IV, respectively.

Then Moldflow software is applied to simulate and analyze the four configurations and compare the corresponding filling times, flow front temperatures, clamping forces, and weld line filling results. Finally, the optimal gate position can be determined, which can reduce the mold revising expenses and improve the quality of the parts.

2.2.1. Filling Time. In the injection molding process, the filling time is defined as the required time for the molten plastic to fill the whole cavity. In this regard, Moldflow is used to analyze the four configurations. Figure 4 shows the filling time of different schemes.

2.2.2. Flow Front Temperature. The flow front temperature is defined as the temperature of the intermediate material flow when the molten plastic is filled to a certain node. This temperature can be considered as the intermediate temperature of the section [11]. Figure 5 presents contours of the flow front temperature for different gate configurations.

2.2.3. Clamping Force. The maximum clamping force exerted on the mold by the injection molding machine is called the clamping force [12]. Figure 6 shows the clamping force of different gate configurations.

2.2.4. The Welding Line. In order to ensure the appropriate appearance and good strength of the molded plastic part, the number and length of the welding lines should be minimized. Moreover, the welding wires are not allowed in places with stress concentration or visible areas [13]. Figure 7 shows the welding wiring of different gate configurations.

The simulation results of filling time, flow front temperature, clamping force, and weld line of the four configurations are summarized in Table 1.

It is found that configuration 4 with four gates has the lowest clamping force, so this gate position is selected as the optimal configuration.

2.3. Simulation and Analysis of Injection Molding Process of the Automobile Instrument Light Guide Bracket. After determining the material, gate position, main channel, shunt channel, and cooling system of the automobile instrument

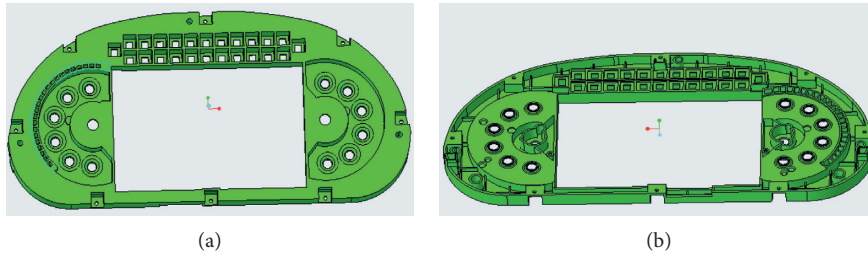


FIGURE 1: 3D model of automobile instrument light guide bracket: (a) front view and (b) the reverse view.

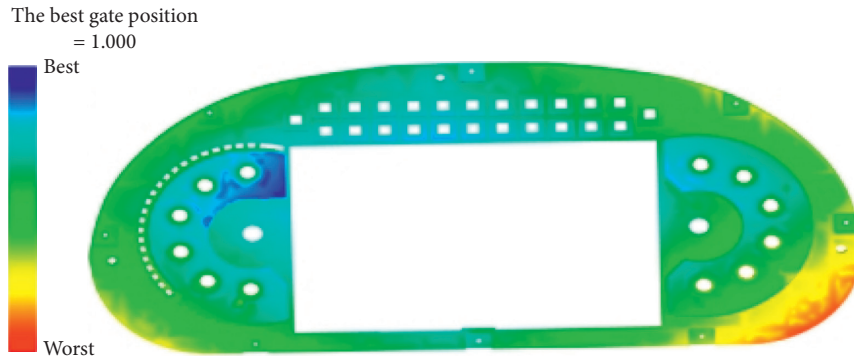


FIGURE 2: Cloud chart of optimal gate matching.

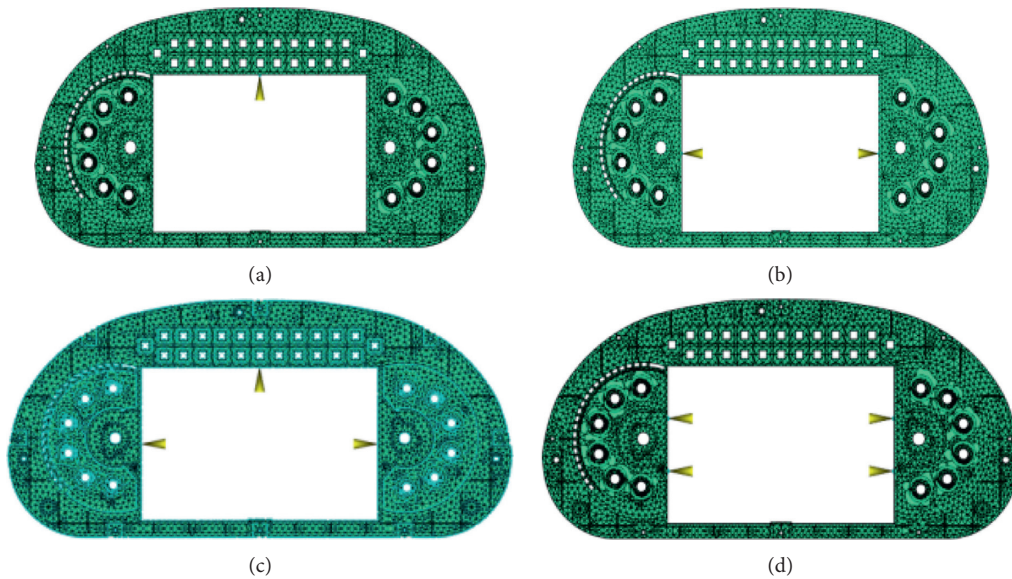


FIGURE 3: Configurations of four gate locations.

light guide, the molding process parameters are set to analyze the molded product. Figures 8 and 9 show contours of the volume shrinkage rate and the warping, respectively.

It is observed that the volume shrinkage rate of the edge part is large, and the volume shrinkage rate is small near the sprue. This is because the edge is far from the sprue position, leading to a weak packing pressure. The performed analysis shows that the maximum volume shrinkage rate and warping are 11.82% and 2.081 mm, respectively.

3. Design of the Taguchi Orthogonal Experiment of the Molding Process Parameter

During the injection molding process, many factors affect the part warpage. Studies show that, among all affecting parameters, the molding parameter is one of the important factors. Generally, the process parameters can be optimized by performing a continuous trial and repair process on the

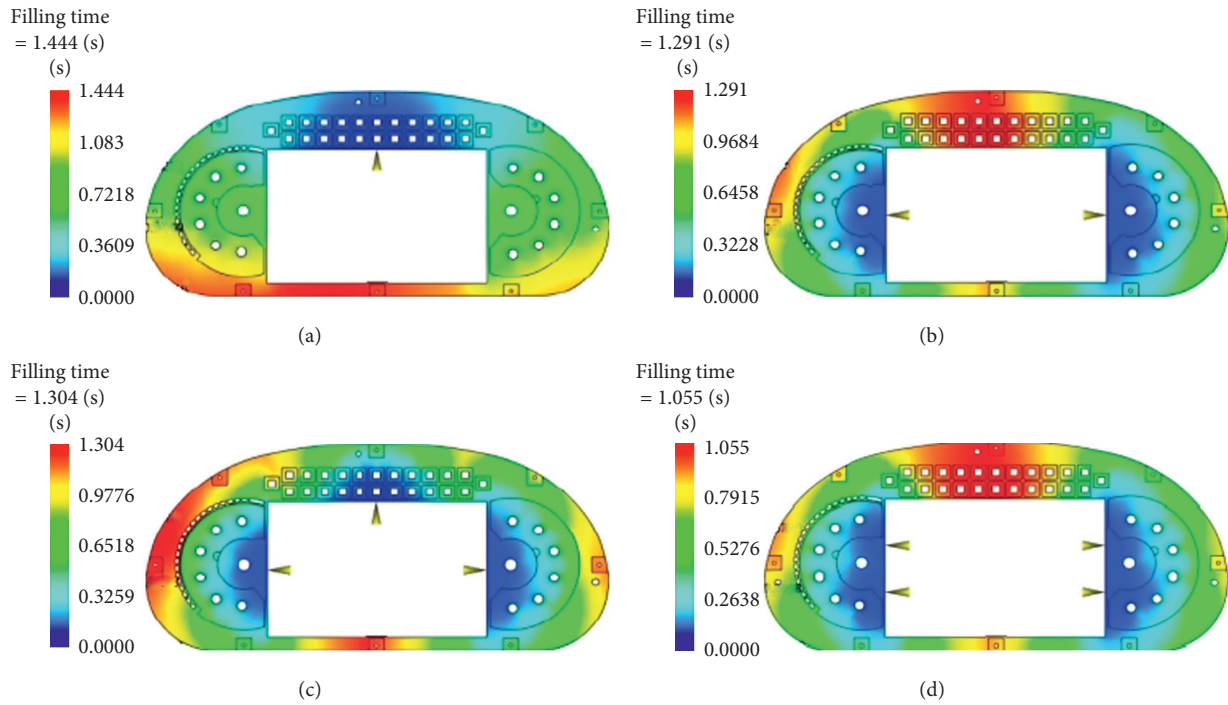


FIGURE 4: Filling times of the part with different gate locations.

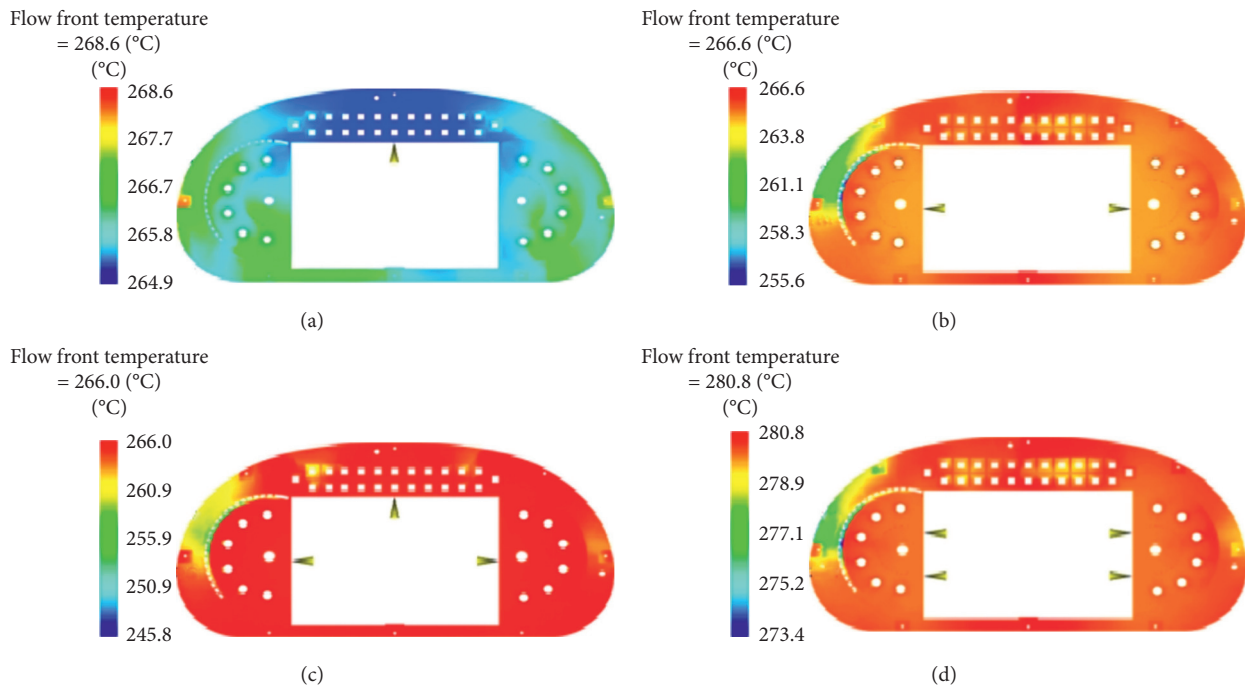


FIGURE 5: Flow front temperature of four gate configurations.

die, which cannot meet the requirements of modern designs [14]. In this section, it is intended to use the Taguchi orthogonal experimental design method to study the influence of molding parameters on volume shrinkage rate and warping, thereby optimizing the parameters.

3.1. Design of Taguchi Orthogonal Test for Automobile Instrument Conduit Bracket. Taguchi orthogonal test index refers to the effects that should be considered during the test. The volume shrinkage rate and the bracket warping are the main influencing factors on the product surface quality and

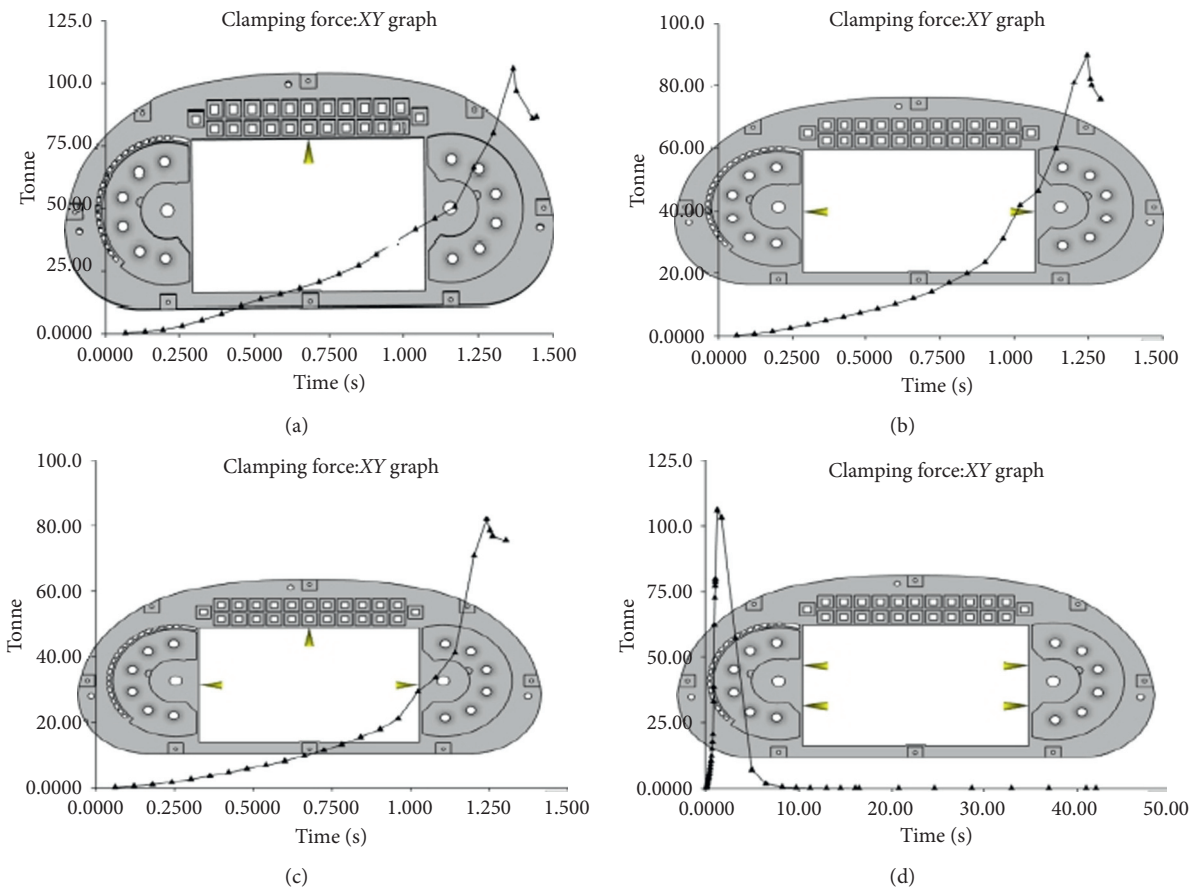


FIGURE 6: Clamping force of different gate configurations.

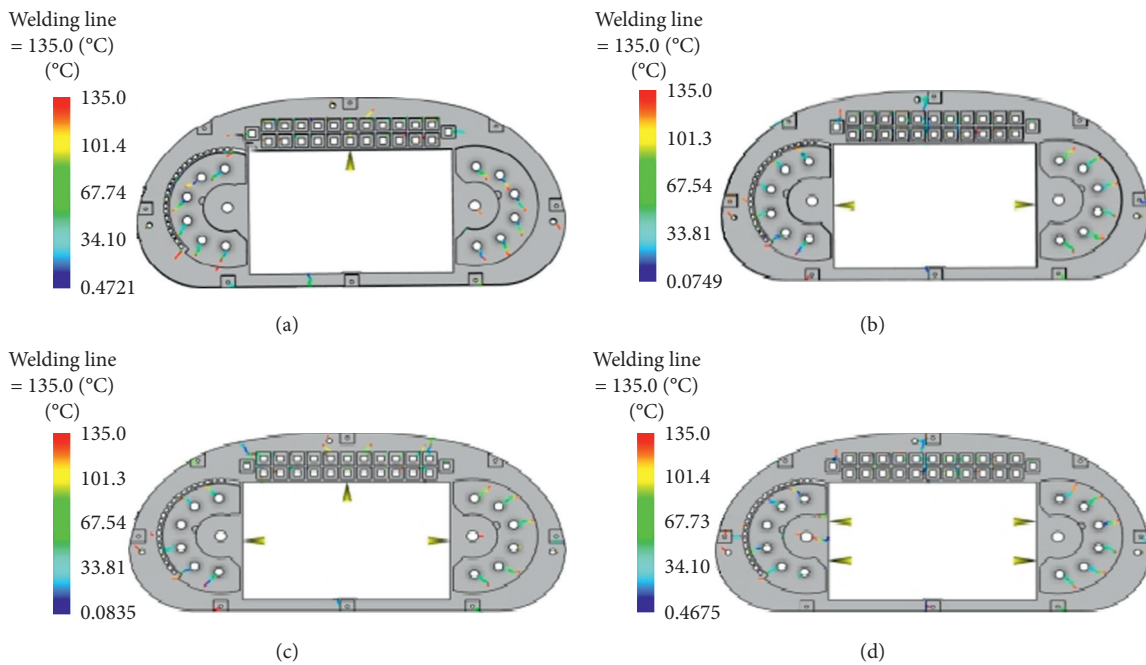


FIGURE 7: Welding line of different gate configurations.

TABLE 1: Simulation results of the four configurations.

Gate number/a	Filling time/s	Temperature difference at the flow front/°C	Clamping force/kN	Characteristics of welding line
I	1.444	3.7	1059	The number of pieces is more and the length is larger
II	1.291	11	907	
III	1.304	20.2	821.2	The number is less and the distribution is reasonable
IV	1.055	7.4	1060	

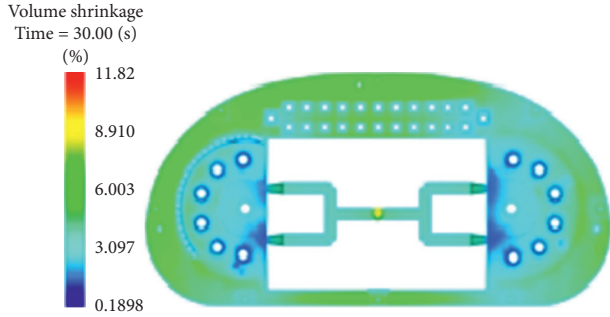


FIGURE 8: Volume shrinkage contour.

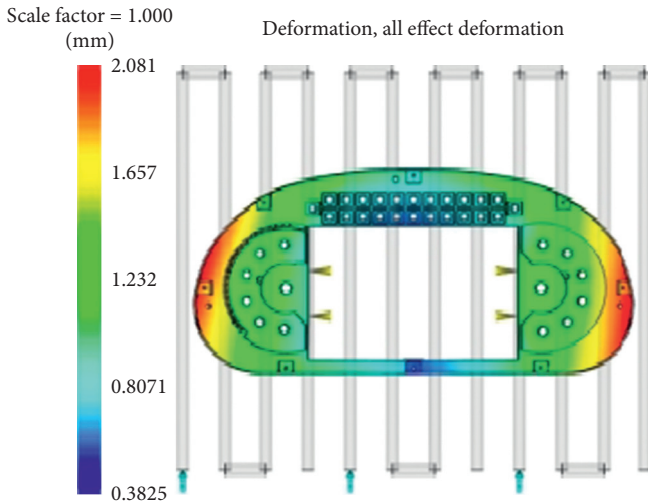


FIGURE 9: Warp quantity contour.

assembly precision. Therefore, these two quality evaluation indices are selected as the testing indicators.

Test factors are parameters that have a certain influence on the test indices [15]. It is worth noting that the setting of molding parameters is the main factor that affects the volume shrinkage rate and the bracket warpage. Among all molding parameters, the mold temperature, melt temperature, cooling time, packing pressure, and packing time have the highest influence on the test indices. Accordingly, these factors are taken as the test factors. The Moldflow analysis results show that the maximum injection pressure required in the filling process is 101.5 MPa.

In the present study, these parameters are selected as the experimental factors of the orthogonal table, where each experimental factor takes four levels. Through the Taguchi orthogonal test, it is intended to investigate the influence of

molding parameters on the volume shrinkage rate and the amount of warping and obtain the optimal combination of molding parameters corresponding to two groups of experimental indices. Table 2 presents the process parameters in the simulations. Based on the principle of Taguchi's orthogonal test, an orthogonal test table $L_{32}(5^4)$ was established, and combinations of 32 process parameters in the table were analyzed through the Moldflow software. Accordingly, 32 groups of volume shrinkage rate and part warping were obtained, as shown in Table 3.

3.2. Data Analysis of the Taguchi Orthogonal Test for Light Guide Bracket of the Automobile Instrument. In this section, the range and variance analysis were carried out on the orthogonal test data of Taguchi. It should be indicated that the influence trend of the test factors on the test indices can be obtained from the range analysis, while the variance analysis yields the influence degree of the former on the latter parameters [16].

The obtained parameters by the Taguchi orthogonal test are the optimal parameter factors, and the ratio between the main effect and error effect is the signal-to-noise ratio, which can be calculated through the following expression:

$$\eta = \frac{S}{N}, \quad (1)$$

where η , S , and N are the signal-to-noise ratio, main effect of the factor, and the error effect, respectively.

Since the combination of signal-to-noise ratio and different response characteristics will produce different results, different signal-to-noise ratio expressions can be defined [17]. Then the signal-to-noise ratio of the small feature is calculated through the following expression:

$$\eta = -10 \log \left(\frac{1}{n} \sum_{i=1}^n y_i^2 \right). \quad (2)$$

The two test indices of the bracket are analyzed by the signal-to-noise ratio. The smaller the test index, the better. Combined with the signal-to-noise ratio expression, it is a subtraction function. Therefore, the data in Table 4 can be obtained by substituting the index values into equation (2) by adopting its signal-to-noise ratio with small expected characteristics.

For range analysis, in order to investigate the influence trend of various molding process parameters on the test indices, presented data in Table 4 are processed to obtain the mean value of the signal-to-noise ratio of each index. Table 5 presents the obtained results in this regard.

TABLE 2: Level factor setting.

Levels	Factors				
	A Mold temperature/°C	B Melt temperature/°C	C Cooling time/s	D Packing pressure/MPa	E Packing time/s
1	55	250	10	40	5
2	65	260	15	50	10
3	75	270	20	60	15
4	85	280	25	70	20

TABLE 3: Orthogonal design and results.

Test number	Factors					Indexes	
	A	B	C	D	E	Shrinkage rate (%)	Amount of warping (mm)
1	55	250	10	40	5	10.81	2.081
2	55	260	15	50	10	8.19	1.991
3	55	270	20	60	15	7.68	1.936
4	55	280	25	70	20	7.493	1.905
5	65	250	10	50	10	7.740	2.029
6	65	260	15	40	5	11.35	2.002
7	65	270	20	70	20	7.105	1.930
8	65	280	25	60	15	8.261	1.991
9	75	250	15	60	20	6.758	1.991
10	75	260	10	70	15	7.710	1.952
11	75	270	25	40	10	12.01	1.951
12	75	280	20	50	5	12.56	1.850
13	85	250	15	70	15	6.950	1.978
14	85	260	10	60	20	7.662	1.954
15	85	270	25	50	5	12.01	1.883
16	85	280	20	40	10	12.55	1.931
17	55	250	25	40	20	6.756	2.025
18	55	260	20	50	15	7.368	1.992
19	55	270	15	60	10	9.315	1.921
20	55	280	10	70	5	12.56	1.712
21	65	250	25	50	15	6.984	2.018
22	65	260	20	40	20	7.000	1.985
23	65	270	15	70	5	12.00	1.784
24	65	280	10	60	10	12.56	1.893
25	75	250	20	60	5	10.81	1.958
26	75	260	25	70	10	8.730	1.928
27	75	270	10	40	15	8.565	1.962
28	75	280	15	50	20	7.963	1.938
29	85	250	20	70	10	8.242	1.968
30	85	260	25	60	5	11.37	1.885
31	85	270	10	50	20	8.293	1.948
32	85	280	15	40	15	8.354	1.937

A is the mold temperature, B is the melt temperature, C denotes the cooling time, D is the packing pressure, and E is the packing time. Based on the discussed procedure, the signal-to-noise ratio of the minimum feature is adopted. It is worth noting that the larger the signal-to-noise ratio, the smaller the corresponding test index. In other words, the larger the SNR, the smaller the volume shrinkage rate and warpage amount. Table 6 reveals that when the mold temperature, melt temperature, cooling time, packing pressure, and packing time are set to 55°C, 250°C, 15 s, 70 MPa, and 20 s (hereafter called A1B1C2D4E4 parameters), the average shrinkage of the signal-to-noise ratio is the

highest, while the volume shrinkage is the minimum. On the other hand, when these parameters are set to 85°C, 280°C, 10 s, 70 MPa, and 5 s (hereafter called A4B4C1D4E1 parameters), the average warpage of the signal-to-noise ratio is the largest, while the warpage amount is the minimum. Then the combination of these two groups of parameters is simulated and analyzed through the Moldflow software. Obtained results are shown in Figures 10 and 11.

Figures 10 and 11 show that the minimum volume shrinkage rate for A1B1C2D4E4 parameters is 6.721% and the minimum amount of warping for A4B4C1D4E1 parameters is 1.763.

TABLE 4: Signal-to-noise ratio of volume shrinkage rate and amount of warping.

Test number	Signal-to-noise ratio of volume shrinkage rate and amount of warping.	
	S/N shrinkage rate/%	S/N amount of warping/mm
1	-20.677	-6.365
2	-18.266	-5.981
3	-17.707	-5.738
4	-17.493	-5.598
5	-17.775	-6.146
6	-21.100	-6.029
7	-17.031	-5.711
8	-18.341	-5.981
9	-16.584	-5.981
10	-17.741	-5.810
11	-21.591	-5.805
12	-21.980	-5.343
13	-16.840	-5.925
14	-17.687	-5.818
15	-21.591	-5.497
16	-21.973	-5.716
17	-16.594	-6.129
18	-17.347	-5.986
19	-19.384	-5.671
20	-21.980	-4.670
21	-16.882	-6.098
22	-16.902	-5.955
23	-21.584	-5.028
24	-21.980	-5.543
25	-20.676	-5.836
26	-18.820	-5.702
27	-18.655	-5.854
28	-18.022	-5.747
29	-18.321	-5.881
30	-21.115	-5.506
31	-18.374	-5.792
32	-18.438	-5.743

For analysis of variance, the influence trend of test factors on indices was processed by analysis of variance [18]. This analysis is conducted in five steps as follows:

- (1) Calculate the sum of partial squares of each test factor through the following expression:

$$S_a = \sum_{i=1}^n (\bar{I}_j - \bar{Y})^2, \quad (3)$$

where \bar{I}_j and \bar{Y} are the mean signal-to-noise ratio of the volume shrinkage rate at a certain level of a test factor \bar{Y} and the signal-to-noise ratio of volume shrinkage rate at all levels of all test factors which was taken as the mean value, respectively.

- (2) Calculate the sum of squares of the total deviation:

$$S_e = \sum_{i=1}^n S_{ai}, \quad (4)$$

where S_{ai} is the partial sum of squares of a test factor.

- (3) Calculate the degree of freedom of test factors:

$$f_a = g - 1. \quad (5)$$

- (4) Calculate the sum of squares of the average deviation:

$$\hat{S}_a = \frac{S_a}{f_a}. \quad (6)$$

- (5) Finally, the influence degree P can be calculated in the following form:

$$P = \frac{S_a}{S_e} \times 100\%. \quad (7)$$

For each factor, the ratio of the sum of squares of deviations to the sum of squares of total deviations in the analysis of variance reflects the influence of the processing parameters on the test indices [19]. \bar{I}_j is the mean signal-to-noise ratio of the volume shrinkage rate at a certain level of a test factor; \bar{Y} is the signal-to-noise ratio of volume shrinkage rate at all levels of all test factors which was taken as the mean value. Similarly, the mean value of the signal-to-noise ratio of warpage amount can be obtained. Table 6 presents the obtained results from the variance analysis.

Table 6 shows that, among the studied parameters, packing time has the greatest influence on the volume shrinkage rate and accounts for about 75.2% of the total shrinkage rate. It is found that as the packing time increases, the volume shrinkage rate gradually decreases. On the other hand, the melt temperature has a greater influence on the volume shrinkage rate, and as the melt temperature decreases, the volume shrinkage rate gradually decreases too. Moreover, the effects of the mold temperature, cooling time, and packing pressure on the volume shrinkage rate are almost the same. The higher the mold temperature, the greater the volume shrinkage rate. The volume shrinkage rate decreases first and then increases with the increase of the cooling time. As the packing pressure increases, the volume shrinkage rate fluctuates.

It is also found that the cooling time is the most important factor to the warpage amount. With the increase of the cooling time, the warpage amount increases first and then decreases. The second effective factor is the melt temperature, accounting for 24.29% of the warpage amount. When the melt temperature increases, the warpage amount decreases gradually. The influences of the packing pressure and packing time on the warpage amount are similar, accounting for 14.33% and 12.66% of the warpage amount, respectively. When the packing pressure increases, the warpage amount gradually decreases. Meanwhile, when the packing time increases, the warpage amount first increases and then decreases. Table 6 indicates that the die temperature has the lowest influence on the warpage amount. When the mold temperature increases gradually, the warpage amount first increases and then decreases.

Based on the Taguchi orthogonal test design, the influence degree of various molding parameters on volume shrinkage rate and warpage amount can be obtained. Accordingly, the optimal combination of molding parameters

TABLE 5: Mean signal-to-noise ratio of shrinkage and warpage.

Optimization objective	Mean	A	B	C	D	E
Shrinkage rate	\bar{I}_1	-18.681	-18.044	-19.359	-19.491	-21.338
	\bar{I}_2	-18.949	-18.622	-18.717	-18.780	-19.764
	\bar{I}_3	-19.259	-19.490	-18.992	-19.184	-17.744
	\bar{I}_4	-19.292	-20.026	-19.053	-18.726	-17.336
	\bar{Y}			-19.004		
Amount of warping	\bar{J}_1	-5.767	-6.045	-5.750	-5.949	-5.534
	\bar{J}_2	-5.811	-5.848	-5.763	-5.824	-5.806
	\bar{J}_3	-5.76	-5.637	-5.771	-5.759	-5.892
	\bar{J}_4	-5.735	-5.543	-5.189	-5.541	-5.841
	\bar{X}			-5.738		

TABLE 6: Results of the variance analysis.

Optimization objective	Sources of variance	Sum of squares of deviations/Sa	Degrees of freedom/fa	The mean square value/ \hat{S}_a	Influence degree P (%)
Shrinkage rate	A	0.255	3	0.085	1.84
	B	2.584	3	0.861	18.69
	C	0.211	3	0.070	1.53
	D	0.378	3	0.126	2.73
	E	10.395	3	3.465	75.2
	Se	13.823	15		
Amount of warping	A	0.0067	3	0.0022	1.05
	B	0.1546	3	0.0515	24.29
	C	0.3033	3	0.1011	47.66
	D	0.0912	3	0.0304	14.33
	E	0.0806	3	0.0269	12.66
	Se	0.6364	15		

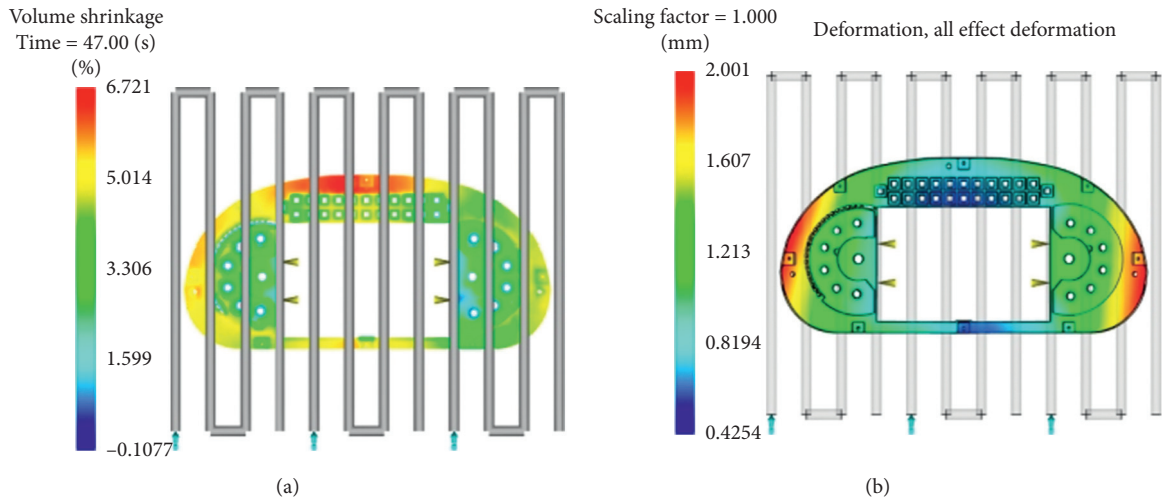


FIGURE 10: Analysis results for A1B1C2D4E4 parameters.

can be obtained to minimize the volume shrinkage rate and the warpage amount.

3.3. Multiobjective Optimization of Grey Correlation Analysis. The foregoing discussions demonstrate that range and variance processing are effective methods to analyze and optimize a single factor. However, these methods cannot be applied to optimize multiple objectives at the same time. In

this regard, grey correlation analysis is often used in the data processing of the Taguchi orthogonal test, which can transform a multiobjective problem into a single-objective problem so that it is beneficial to analyze the test data.

The basic principle of the grey correlation analysis is to determine the degree of correlation according to the similarity degree of the curve geometry for each factor. The more similar the curve geometries, the higher the correlation degree between factors.

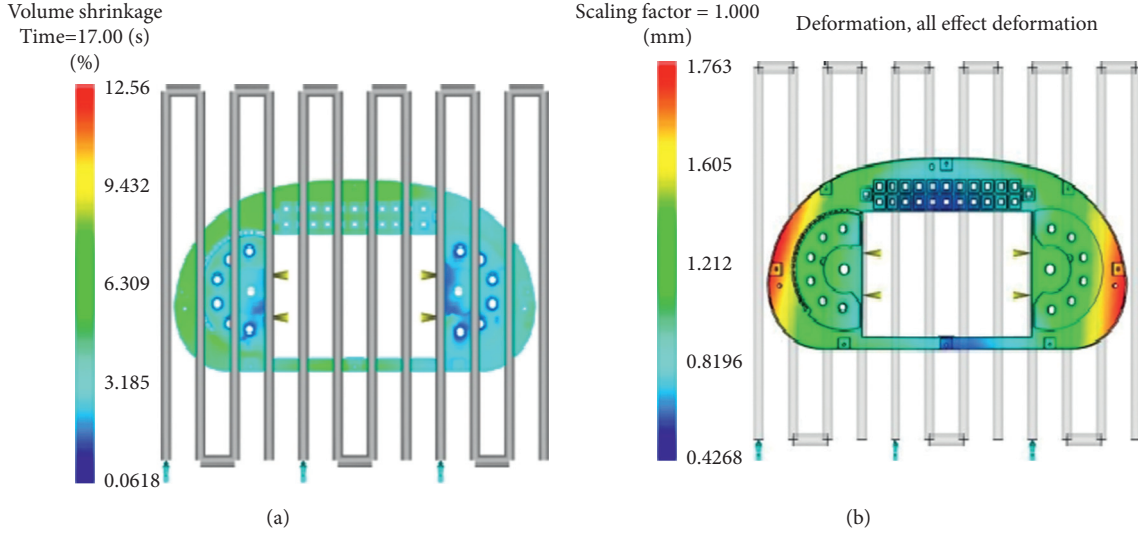


FIGURE 11: Analysis results for A4B4C1D4E1 parameters.

3.3.1. Evaluation Index Data Matrix. Based on the objective analysis, the evaluation index matrix can be established with evaluation indices. This matrix can be expressed in the following form:

$$A = \begin{bmatrix} X_1(1) & X_1(2) & \dots & X_1(j) & \dots & X_1(m) \\ X_2(1) & X_2(2) & \dots & X_2(j) & \dots & X_2(m) \\ \dots & \dots & \dots & \dots & \dots & \dots \\ X_i(1) & X_i(2) & \dots & X_i(j) & \dots & X_i(m) \\ \dots & \dots & \dots & \dots & \dots & \dots \\ X_n(1) & X_n(2) & \dots & X_n(j) & \dots & X_n(m) \end{bmatrix}, \quad (8)$$

where n is the number of tests, m is the number of evaluation indices, and $x_i(j)$ is the raw data.

3.3.2. Normalizing the Evaluation Target Data. In order to ensure the equivalence of each index, it is necessary to normalize the original sequence to eliminate its dimension. In the present study, the normalization is carried out through the following expression:

$$X_i^*(k) = \frac{\max X_{iVj}(j) - X_i(j)}{\max X_{iVj}(j) - \min X_{iVj}(j)}, \quad (9)$$

where $x_i^*(k)$ denotes the index value after normalization, $\max X_{iVj}(j)$ is the maximum value of columns in the data matrix of evaluation index, $\min X_{iVj}(j)$ is the minimum value of columns in the data matrix of evaluation index, $x_i(j)$ is a vector in the data matrix of evaluation index, and $X_{ob}(j)$ is the target value of $X_i(j)$.

3.3.3. Determination of the Grey Correlation Coefficient Matrix. The maximum value of each index can be considered as the reference sequence.

$$K = (k_1, k_2, k_3, \dots, k_j, \dots, k_m),$$

$$k_j = \max(X_i(j), X_2(j), \dots, X_j(j), \dots, X_n(j)), \quad (10)$$

$$\xi_i = \frac{\min(\Delta \min) + \rho \bullet \max(\Delta \max)}{\Delta_{0,i}(j) + \rho \bullet \max(\Delta \max)},$$

where $\Delta_{0,i}(j) = |k_j - X_i(j)|$ is the absolute value of the reference sequence and comparison sequence, $\min(\Delta \min) = \min(\min|k_j - X_i(j)|)$ is the minimum absolute value of each reference sequence and the comparison sequence, $\max(\Delta \max) = \max(\max|k_j - X_i(j)|)$ denotes the maximum absolute value of each reference sequence and comparison sequence, ξ_i is the correlation coefficient of each evaluation index, and ρ is the resolution coefficient, which is usually set to 0.5 [20].

Accordingly, the grey correlation coefficient matrix can be established in the following form:

$$\xi = \begin{bmatrix} \xi_{11} & \xi_{12} & \dots & \xi_{1m} \\ \xi_{21} & \xi_{22} & \dots & \xi_{2m} \\ \dots & \dots & \dots & \dots \\ \xi_{n1} & \xi_{n2} & \dots & \xi_{nm} \end{bmatrix}. \quad (11)$$

3.3.4. Determination of the Grey Correlation Degree.

$$\gamma_i = \frac{1}{m} \sum_{j=1}^m \xi_{ij}, \quad (i = 1, 2, \dots, n). \quad (12)$$

For evaluation of the grey correlation degree of automobile instrument light guide bracket, the grey correlation degree of volume shrinkage rate and warpage amount can be obtained from equations (8) to (12), respectively. Then the multiobjective problem can be transformed into a single-

TABLE 7: Evaluation index matrix, correlation coefficient matrix, and grey correlation degree.

Serial number	Evaluation index matrix		Normalized matrix		Correlation coefficient matrix		Grey correlation degree
	$X_i(1)$	$X_i(2)$	$X_i^*(1)$	$X_i^*(2)$	ξ_{i1}	ξ_{i2}	ξ
1	10.81	2.081	0.302	0	0.417	0.333	0.375
2	8.19	1.991	0.753	0.244	0.669	0.398	0.5335
3	7.68	1.936	0.841	0.393	0.759	0.452	0.6055
4	7.493	1.905	0.873	0.477	0.797	0.489	0.643
5	7.740	2.029	0.830	0.141	0.746	0.368	0.557
6	11.35	2.002	0.208	0.214	0.387	0.389	0.388
7	7.105	1.930	0.940	0.409	0.893	0.458	0.6755
8	8.261	1.991	0.741	0.244	0.659	0.398	0.5285
9	6.758	1.991	1	0.244	1	0.398	0.699
10	7.710	1.952	0.836	0.350	0.753	0.435	0.594
11	12.01	1.951	0.095	0.352	0.356	0.436	0.396
12	12.56	1.850	0	0.626	0.333	0.572	0.4525
13	6.950	1.978	0.967	0.279	0.938	0.410	0.674
14	7.662	1.954	0.844	0.344	0.762	0.433	0.5975
15	12.01	1.883	0.095	0.537	0.356	0.519	0.4375
16	12.55	1.931	0.001	0.407	0.334	0.457	0.3955
17	6.756	2.025	1	0.152	1	0.371	0.6855
18	7.368	1.992	0.895	0.241	0.826	0.397	0.6115
19	9.315	1.921	0.559	0.434	0.531	0.469	0.5
20	12.56	1.712	0	1	0.333	1	0.6665
21	6.984	2.018	0.961	0.171	0.928	0.376	0.625
22	7.000	1.985	0.958	0.260	0.923	0.403	0.663
23	12.00	1.784	0.096	0.805	0.356	0.719	0.5375
24	12.56	1.893	0	0.509	0.333	0.505	0.419
25	10.81	1.958	0.302	0.333	0.417	0.428	0.4225
26	8.730	1.928	0.660	0.415	0.595	0.461	0.528
27	8.565	1.962	0.688	0.322	0.616	0.424	0.52
28	7.963	1.938	0.792	0.388	0.706	0.450	0.578
29	8.242	1.968	0.744	0.306	0.661	0.419	0.54
30	11.37	1.885	0.205	0.531	0.386	0.516	0.451
31	8.293	1.948	0.735	0.360	0.654	0.439	0.5465
32	8.354	1.937	0.725	0.390	0.645	0.450	0.5475

objective problem. Table 7 presents the warpage amount and volume shrinkage rate data based on grey correlation analysis.

For range analysis of the grey correlation degree, the mean value and the corresponding range values can be calculated from the range analysis of the grey correlation degree. Table 8 indicates that the larger the value of the evaluation factor, the stronger the grey correlation and the higher the influence on the evaluation index.

Table 8 indicates that the highest value of the grey correlation degree is obtained when the mold temperature, melt temperature, cooling time, packing pressure, and the packing time are set to 55°C, 250°C, 25 s, 70 MPa, and 20 MPa, respectively. These settings (hereafter called A1B1C4D4E4) have the greatest influence on the volume shrinkage rate and the warpage amount, which is the optimal combination of process parameters. Then these molding parameters are introduced to the Moldflow software and the simulation results are shown in Figure 12.

Figure 12 shows that the grey correlation analysis is an effective scheme to optimize the molding parameters. It is

TABLE 8: Range analysis of the grey correlation degree.

Level	A	B	C	D	E
1	0.578	0.576	0.534	0.496	0.466
2	0.553	0.546	0.540	0.546	0.484
3	0.524	0.527	0.546	0.528	0.592
4	0.524	0.529	0.557	0.607	0.636
Range	0.054	0.049	0.023	0.111	0.170

Note: A is the mold temperature, B is the melt temperature, C is the cooling time, D is the packing pressure, and E is the packing time.

found that the optimal volume shrinkage rate and warpage amount are 6.753% and 1.999 mm, respectively.

Based on the performed Taguchi orthogonal test and grey correlation analysis, the optimal molding parameters can be obtained. In this regard, Table 9 presents the optimal results.

Table 9 demonstrates that the Taguchi orthogonal test and the grey correlation analysis are effective ways to optimize the molding process parameters and obtain different quality index values. It is found that the optimal volume shrinkage rate and warpage amount are 6.753% and 1.999%, respectively.

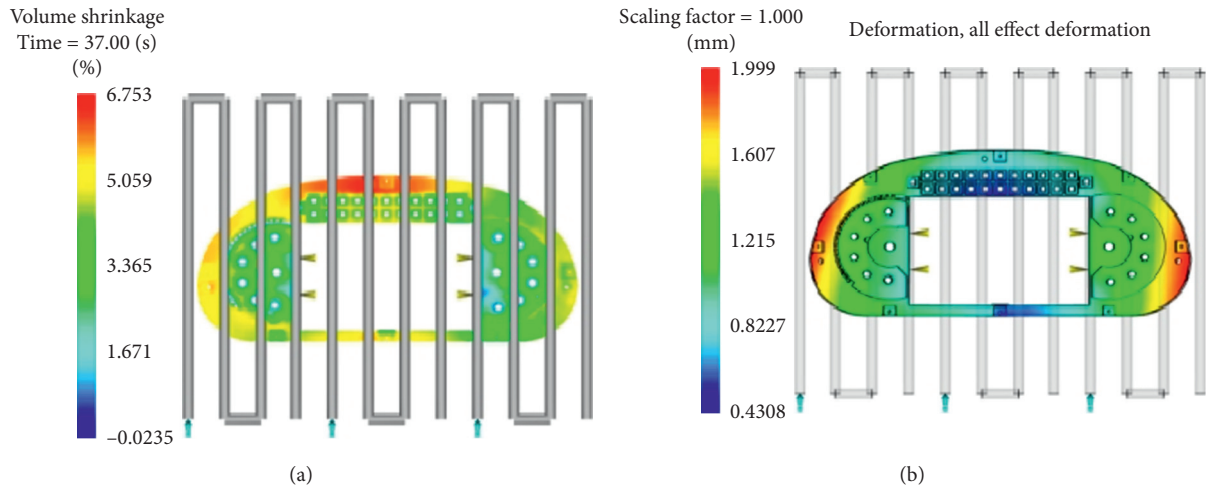


FIGURE 12: Analysis results of A1B1C4D4E4 parameter.

TABLE 9: Comparison of quality evaluation indices of the Taguchi orthogonal test and the grey correlation degree.

Index	Influence factors	Process parameter combination	Volume shrinkage (%)	Amount of warping (mm)
Warpage amount analysis based on Taguchi orthogonal test	$C > B > D > E > A$	A1B1C2D4E4	6.721	2.001
Volume shrinkage rate analysis based on Taguchi orthogonal test	$E > B > D > A > C$	A4B4C1D4E1	12.56	1.763
Grey correlation analysis	$E > D > A > B > C$	A1B1C4D4E4	6.753	1.999

Note: A is mold temperature, B is melt temperature, C is cooling time, D is packing pressure, and E is packing time.

4. Conclusion

In the present study, four gate configurations are preliminarily proposed for the injection molding of the automobile light guide bracket. Then numerical simulations are performed through the Moldflow software. Accordingly, filling time, flow front temperature, clamping force, and weld line are analyzed and compared. It is found that, in the best configuration, the filling time is 1.055 s, the temperature difference of flow front is 7.4°C, the clamping force is 1060 kN, the number of welding lines is low, and the weld distribution is reasonable. Finally, volume shrinkage and warpage are calculated as quality evaluation indices through the simulation in the Moldflow software. The obtained results show that the maximum volume shrinkage rate and the maximum warpage amount are 11.82% and 2.081 mm, respectively.

The volume shrinkage rate and warpage amount of the bracket are selected as experimental evaluation indices, and different molding process parameters such as the mold temperature, melt temperature, cooling time, packing pressure, and packing time are taken as experimental level factors. Then the range analysis of the Taguchi orthogonal test is conducted, where the obtained results show that when the process parameters are set to A1B1C2D4E4 (55°C, 250°C, 15 s, 70 MPa, and 20 s), the mean shrinkage signal-to-noise ratio is the maximum and the volume shrinkage is the minimum. Meanwhile, when the process parameters

are set to A4B4C1D4E1 (85°C, 280°C, 10 s, 70 MPa, and 5 s), the mean warpage signal-to-noise ratio is the maximum and the warpage is the minimum. Moreover, the minimum volume shrinkage rate for A1B1C2D4E4 parameters is 6.721% and the minimum warpage amount for A4B4C1D4E1 parameters is 1.763 mm. Through variance analysis, it is found that the packing time is the molding parameter with the greatest influence on the volume shrinkage rate accounting for about 75.2% of the total shrinkage rate, and the cooling time has the greatest influence on the warpage amount. The performed simulations reveal that as the cooling time increases, the warpage amount increases first and then decreases. Through the Taguchi orthogonal test design, the influence degree of various molding parameters can be obtained on the volume shrinkage rate and warpage amount.

Finally, the range analysis of the grey correlation is carried out to optimize the volume shrinkage rate and warpage amount simultaneously. Accordingly, it is found that the largest grey correlation can be obtained when the processing parameters are set to A1B1C4D4E4 (55°C, 250°C, 25 s, 70 MPa, and 20 MPa). The combination has the greatest influence on the volume shrinkage rate and warpage amount, which is the optimal combination of process parameters. Then the combination of processing parameters is analyzed, and the optimal volume shrinkage rate and warpage amount were obtained as 6.753% and 1.999 mm, respectively.

Data Availability

The data used to support the findings of this study are included within the article.

Conflicts of Interest

The authors declare that they have no conflicts of interest.

Acknowledgments

This article belongs to the major projects of the University Synergy Innovation Program of Anhui Province (GXXT-2019-004) and the Teaching Research Project of Anhui Education Department (2019jyxm0229).

References

- [1] M. Yan, L. Liu, C. Huang, H. Geng, and X. Han, "CAE analysis of plastic handle based on moldflow," *China Shipping (Second Half)*, vol. 2, no. 1, pp. 131-132, 2009.
- [2] X. Li and L. Xiao, "Mould design and NC machining of beverage bottle based on Pro/E and master cam," *Packaging Engineering*, vol. 35, no. 6, pp. 76-78, 2014.
- [3] H. Yu, *Research on Numerical Simulation of Injection Molding of Thin-Walled Plastic Parts and Optimization of Molding Process Parameters*, Zhejiang University of Technology, Hangzhou, China, 2008.
- [4] F. Beibei, *Numerical Simulation and Process Optimization in Injection Mold Design*, Hefei University of Technology, Hefei, China, 2016.
- [5] H. Wang, "Optimization of injection molding parameters based on orthogonal test method," *Shanghai Plastics*, vol. 47, no. 2, pp. 58-62, 2019.
- [6] C. Tang, Q. Xia, and B. Zhang, "Hybrid optimization of injection molding process for instrument shell based on response surface model," *Plastics Industry*, vol. 46, no. 6, pp. 37-40, 2018.
- [7] L. Jing, X. Guo, X. Yang et al., "Optimization of injection molding process parameters of automobile air conditioning shell mounting plate based on moldflow and taguchi orthogonal test," *Journal of Lanzhou Institute of Technology*, vol. 23, no. 3, pp. 76-78, 2016.
- [8] B. P. Kumar, P. Venkataramaiah, and J. S. Ganesh, "Optimization of process parameters in injection moulding of a polymer composite product by using gra," *Materials Today: Proceedings*, vol. 18, no. Pt 7, pp. 4637-4647, 2019.
- [9] F. Hentati, H. Ismail, N. Masmoudi, and C. Bradai, "Optimization of the injection molding process for the PC/ABS parts by integrating taguchi approach and CAE simulation," *The International Journal of Advanced Manufacturing Technology*, vol. 104, no. 9-12, pp. 4353-4363, 2019.
- [10] S. M. S. Mukras, H. M. Omar, and F. A. al-Mufadi, "Experimental-based multi-objective optimization of injection molding process parameters," *Arabian Journal for Science and Engineering*, vol. 44, no. 9, pp. 7653-7665, 2019.
- [11] L. Wang, *Research on Mold Design and CAE Application of Automobile Thin Wall Injection Parts*, Jilin University, Changchun, China, 2010.
- [12] X. Guo and G. Ma, "Design of injection mold for charger shell based on UG," *Mold Industry*, vol. 39, no. 4, pp. 50-52, 2013.
- [13] Yi Liu, *Research on Improving Weld Line of Products by Hot Runner Sequential Injection Molding*, South China University of Technology, Guangzhou, China, 2009.
- [14] J. Wang, P. Wang, and F. Zhu, "Application status and research progress of injection mold CAE technology," *Inner Mongolia Petrochemical Industry*, vol. 15, no. 8, pp. 5-6, 2005.
- [15] Y. Zhang and Y. Li, "Analysis of variance of orthogonal design for void grouting material at slab bottom," *Low Temperature Building Technology*, vol. 35, no. 11, pp. 16-18, 2013.
- [16] I. Lizhen, Q. Liang, J. pan et al., "Optimization of molding process parameters of automobile gear lever based on orthogonal test," *China Plastics*, vol. 33, no. 7, pp. 50-56, 2019.
- [17] Y. Shi, W. fan, M. sang et al., "Study on optimization of power spinning parameters of connecting rod bushing based on signal to noise ratio and grey correlation analysis," *Foundry Technology*, vol. 38, no. 9, pp. 2261-2264, 2017.
- [18] W. Meng, *Application Research on Process Parameter Optimization of Automobile Top Cover Based on Taguchi Method and Finite Element Analysis*, Shenyang University, Shenyang, China, 2017.
- [19] H. Wu, X. Qin, L. Yang et al., "Optimization of process parameters of plastic parts based on taguchi method," *Intelligent Manufacturing*, vol. 23, no. 7, pp. 35-37, 2016.
- [20] L. Chen and H. Wang, "Optimization of process parameters of thin-walled asymmetric injection molded parts with one mold and two cavity by taguchi method," *Plastics Industry*, vol. 40, no. 11, pp. 50-53, 2012.

Research Article

Study on Automotive Back Door Panel Injection Molding Process Simulation and Process Parameter Optimization

Guoqing Wang , Youmin Wang, and Deyu Yang

School of Mechanical Engineering, Anhui Polytechnic University, Wuhu 241000, Anhui, China

Correspondence should be addressed to Guoqing Wang; 2190130102@stu.ahpu.edu.cn

Received 26 March 2021; Revised 13 April 2021; Accepted 27 April 2021; Published 4 May 2021

Academic Editor: Ashwini Kumar

Copyright © 2021 Guoqing Wang et al. This is an open access article distributed under the Creative Commons Attribution License, which permits unrestricted use, distribution, and reproduction in any medium, provided the original work is properly cited.

A plastic back door car panel was considered as the research object. In order to obtain optimal injection molding simulation parameters, Moldflow2018 is used to simulate injection molding process of plastic back door car panel. Orthogonal experiment is conducted to analyze the influence of injection process parameters on the evaluation index. Melt temperature, mold temperature, cooling time, packing pressure, and packing time are selected as process parameters. Warpage and volumetric shrinkage are taken as evaluation indicators. Test groups are designed to obtain data, and range analysis method is employed to analyze warpage and volumetric shrinkage. Warpage range analysis shows that optimal warpage is 9.3 mm for volumetric shrinkage rate of 14.3%. Range analysis of volumetric shrinkage rate indicates that the best warpage is 8.3 mm for the corresponding volumetric shrinkage rate of 15.05%. A comprehensive evaluation index is established using the gray relational analysis. This analysis shows that warpage is 8.3 mm and volumetric shrinkage rate is 14.2%. Taguchi method is employed to obtain signal-to-noise ratio, while range and variance methods are used for the analysis. Optimal warpage is obtained as 8.2 mm, while the volume shrinkage rate is 10.3%. For a single evaluation index warpage, least squares method and artificial fish swarm algorithm are used to find the optimal parameter combination. Moldflow2018 is employed for simulation verification, and minimum warpage is obtained as 6.405 mm.

1. Introduction

Due to an increase in demand of plastic products, injection molds have been rapidly developing. A relatively large number of plastic products are used in automobile industry. As the requirements for lightweight and low energy consumption of automobile are getting higher, steel parts are more frequently being replaced with plastic ones. In recent years, many scientific researchers have employed CAE technology for simulation of injection molding processes in automotive industry. BP neural network was used by Kejian et al. [1] to establish the relationship between process parameters and warpage. The authors reduced warpage via genetic algorithm optimization. In order to reduce warpage, Yan et al. [2] predicted deformation trends of plastic parts through Moldflow and corrected the molding parameters related to plastic parts. Li et al. [3] observed that the amount of stable warpage deformation was proportional to the volume shrinkage. Furthermore, the authors concluded that

unstable warpage was caused by the bending of the product itself. The aforementioned researchers used algorithms to optimize the relationship between parameters and warpage. In addition, the authors modified relevant parameters of injection molding to reduce warpage, where they demonstrated the relationship between warpage and volume shrinkage. In addition, the authors pointed out main causes of warpage. However, there is no detailed study on correlation optimization between volume shrinkage and warpage. Doerffel et al. [4] studied deformation of injection molded parts and validated the quality of plastic parts based on laminated sheet parts. Through experimental investigations, the authors found that crystalline conformable materials were prone to large warpage and shrinkage during the injection molding process. Huszar et al. [5] minimized the warpage by selecting the optimal injection material and gate positions. The authors found that PP and PS materials produced the largest and smallest warpings, respectively, while the warpage of polypropylene was mainly determined

by the gate position and injection pressure. Shiroud et al. [6] employed simulation and variance analyses of important components of artificial skeletal joints to control optimal values of warpage and volume shrinkage at 0.287222 mm and 13.6613%, respectively. Sateesh et al. [7] considered the top cover of water meter as the research object. The authors used gray correlation analysis method to optimize injection molding parameters. The above-mentioned researchers analyzed various types of injection molding materials, pointed out the influence of different injection molding materials on warpage, and optimized the injection parameters using the gray correlation degree. However, for the selection of optimization methods, a combination of multiple optimization methods had not yet been employed. In this paper, vehicle plastic back door is taken as the research object. Injection molding simulation is performed, for which five injection molding process parameters are selected: melting temperature, mold temperature, pressure holding time, pressure holding pressure, and injection time. By taking warpage and volume shrinkage as evaluation indicators, process parameters that affect injection molding are studied based on the orthogonal test method. Furthermore, degree of influence of each parameter on evaluation indicators is obtained by employing different analysis methods. Least two multiplication and artificial fish school algorithms are employed to optimize process parameters during injection molding process.

2. Process Simulation of Back Door Outer Panel Injection Molding

In this section, injection molding process is simulated. Next, influence of gate positioning and number on process parameters during the injection molding process is investigated based on Moldflow. Finally, the best gate position is determined.

2.1. Introduction to Injection Molding Process Theory

2.1.1. Filling Stage. This stage plays an important role in plastic parts molding. The following mathematical model is used to describe the process:

$$\eta = \frac{\eta_0}{1 + A(\eta_0\gamma)^{1-n}}, \quad (1)$$

$$\eta_0 = B \exp\left(\frac{T_0}{T} + \beta p\right),$$

where η_0 stands for zero shear viscosity, p stands for injection pressure, n stands for flow index, γ represents shear rate, and T denotes melting temperature.

2.1.2. Packaging Stage. Continuity equation is as follows:

$$\frac{\partial p}{\partial t} + \frac{\partial(\rho\mu)}{\partial x} + \frac{\partial(\rho v)}{\partial y} + \frac{\partial(\rho\omega)}{\partial z} = 0. \quad (2)$$

Equation of motion is as follows:

$$\frac{\partial P}{\partial x} - \frac{\partial}{\partial z} \left(\eta \frac{\partial x}{\partial z} \right) = 0. \quad (3)$$

Energy equation is as follows:

$$\rho C_p (T) \left(\frac{\partial T}{\partial t} + \mu \frac{\partial T}{\partial x} + v \frac{\partial T}{\partial y} \right) = \frac{\partial}{\partial z} \left[K(T) \frac{\partial T}{\partial z} \right] + \eta \dot{\gamma}^2. \quad (4)$$

2.1.3. Cooling Phase. Simplified conduction equation of temperature field is as follows:

$$\rho c_p \left(\frac{\partial T_p}{\partial t} \right) = \frac{\partial}{\partial z} \left(K_p \frac{\partial T_p}{\partial z} \right), \quad (5)$$

where T_p stands for plastic parts temperature, T stands for time, K_p denotes thermal conductivity, ρ represents plastic parts density, and C_p denotes equivalent specific heat capacity.

2.2. Mesh Division of the Outer Panel of the Back Door. CATIA is employed to design the outer panel structure of the plastic back door, as shown in Figure 1. The part is imported into Moldflow for mesh division. Mesh side length is set to 5 mm [8], mesh type is set to double-layer, mesh division is shown in Figure 2, and mesh division results are shown in Table 1.

According to Table 1, the matching percentage of grid analysis is equal to 97.1%, which is suitable for a double-layer analysis. However, maximum aspect ratio of the grid is 11.57. Thus, maximum aspect ratio has to be reduced to approximately 6 through grid repair [9]. Analysis results following the reparation are shown in Table 2.

According to the results from Table 2, maximum aspect ratio is now equal to 6.59, while the grid matching percentage is 97.2%. Thus, the repaired grid meets the requirements and analysis can be continued.

2.3. Selection of Injection Materials. PP-LGF-30 is selected as the material of the inner panel and PP-EPDM-T30 is selected as the material of the outer panel. Some basic material parameters are shown in Table 3 [10].

2.4. Selection of Gate Location. The outer panel of the plastic rear door is a large car cover. Based on actual production experience, number of gates is set to four, six, and eight. Moldflow is used to simulate and analyze three gate positions, and the results are shown in Figure 3.

Main process parameters during injection molding are the clamping force, filling time, flow front temperature, air pockets, and welding line. The effect of these parameters is investigated in the following sections.

2.4.1. Clamping Force. Clamping force must be greater than the thrust generated by the melt flow. Moldflow is used to analyze the clamping force, and the results are shown in Figure 4. It can be observed that maximum clamping forces

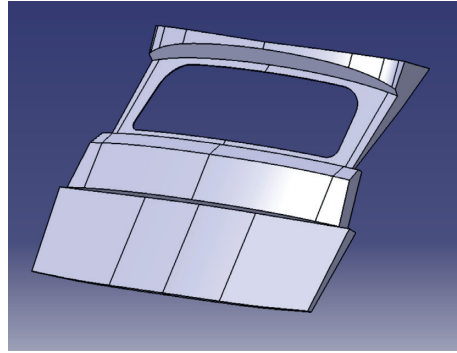


FIGURE 1: 3D parts design.

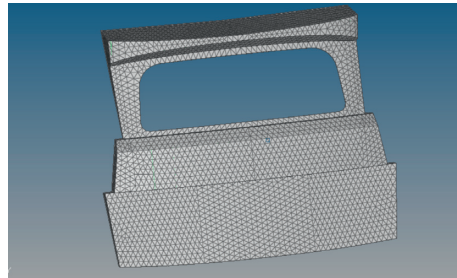


FIGURE 2: Meshing diagram.

TABLE 1: Meshing results.

Number of free edges	Number of multiple sides	Incorrectly aligned unit	Intersecting and fully overlapping cells	Grid matching percentage (%)	Average aspect ratio	Maximum aspect ratio
0	0	0	0	97.1	1.64	11.57

TABLE 2: Result of mesh repair.

Number of free edges	Number of multiple sides	Incorrectly aligned unit	Intersecting and fully overlapping cells	Grid matching percentage (%)	Average aspect ratio	Maximum aspect ratio
0	0	0	0	97.2	1.62	6.59

TABLE 3: Basic properties of two modified PP.

Material	Elastic modulus (MPa)	Poisson's ratio	Shear modulus (MPa)	Maximum shear stress (MPa)	Density (g/cm ³)
PP-LGF-30	6502.3	0.387	1482.5	0.25	1.1443
PP-EPDM-T30	2005.3	0.365	660	0.25	1.0314

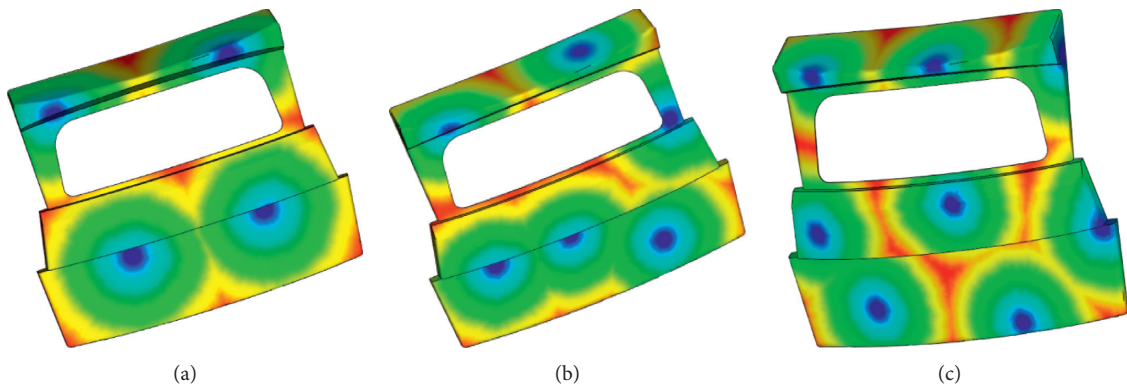


FIGURE 3: Gate location with (a) four gates, (b) six gates, and (c) eight gates.

of three gate positions are 969.7 t, 1167.9 t, and 1159.8 t, respectively. It is found that clamping forces between three gates demonstrate negligible differences.

2.4.2. Filling Time. Filling time is an important key result. Filling times of three different gate solutions are shown in Figure 5. It can be observed that the filling times of four-gate and six-gate schemes are approximately the same, while the filling time of the eight-gate scheme is longer.

2.4.3. Flow Front Temperature. Flow front temperature differences should not be significant, with generally allowable difference being less than 20°C. Analysis result is shown in Figure 6. Temperature differences of three gate scheme models are 9.3°C, 10.7°C, and 12.2°C, respectively. Moreover, all temperatures meet the difference requirement. Lastly, it should be noted that the leading edge temperature should be as high as possible within a reasonable range.

2.4.4. Welding Line. Weld marks directly affect the surface quality of plastic parts. Therefore, they should be reduced when possible. Analysis results are shown in Figure 7. It can be seen that the number of weld lines is increased with the number of gates.

In Table 4, results of the above conducted analysis are shown.

It can be seen from Table 4 that six gates are selected.

3. Optimization of Process Parameters Based on the Orthogonal Experiment

The influence of each process parameter on evaluation index is analyzed via orthogonal experiment.

3.1. Introduction to Orthogonal Experiment. Orthogonal test is an experimental method that studies the influence of multiple factors and multiple levels on experimental results [11]. When designing an orthogonal experiment, it is necessary to first determine objectives of the experimental research. Then, experimental measurement indicators are formulated according to objectives of the experimental research. Lastly, influencing factors of the experiment are selected. The general design is as follows:

(1) Selection of evaluation indicators

First step of the orthogonal test is to reasonably select evaluation indicators according to the actual situation

(2) Selection of test influence factors and determination of influence factors test levels

In the orthogonal experiment, letters A, B, C, D, and E are used to represent influencing factors of the experiment. Generally, the number of influencing factors is 3-6, and

numerical difference between each level should be determined according to the calculation and difference of field conditions. Moreover, numerical difference should conform to a certain interval range.

3.2. Orthogonal Design. Basic steps of orthogonal test are as follows:

- (1) Determining the value range of each process parameter
- (2) Obtaining a reasonable evaluation index for adequate orthogonal test table design
- (3) Simulation of combined process parameters via CAE software

3.2.1. Influencing Factors and Evaluation Options. Based on actual production experience, five factors are selected: melting temperature, mold temperature, cooling time, packing pressure, and packing time. Two evaluation indicators of product warpage and volume shrinkage are selected. Based on actual process parameter values, the level of each factor should be selected according to Table 5.

Selected level value of each influencing factor is placed into the orthogonal table. The system automatically generates 16 sets of process parameter combinations. Moldflow is used to simulate 16 sets of process parameter combinations and evaluate each set of tests. Index results are shown in Table 6.

3.2.2. Orthogonal Test Table Data Analysis. (1) Analysis of warpage results: Range analysis method is used to analyze test data of a single warpage. The analysis results are shown in Table 7 and Figure 8.

Based on the presented results in Table 7 and Figure 8, degree of influence of various factors on warpage can be ordered as follows: packing pressure > packing time > melting temperature > mold temperature > cooling time. Through warpage range analysis, a better combination of process parameters A4B1C3D4E1 can be obtained. After analyzing and verifying combination of process parameters, the final result is shown in Figure 9. The warpage is 9.3 mm, while the volume shrinkage rate is 14.3%.

(2) Volume shrinkage result analysis: Range analysis method is also used to perform range analysis on a single volume shrinkage rate, as shown in Table 8.

According to data presented in Table 8 and Figure 10, degree of influence of various factors on volume shrinkage rate can be ordered as follows: melting temperature > mold temperature > cooling time > packing pressure > packing time. Favorable process parameter combination A1B1C4D4E4 can also be obtained via volume shrinkage range analysis. The group is verified, and final results are shown in Figure 11. The warpage is 8.38 mm, and the volume shrinkage rate is 15.05%.

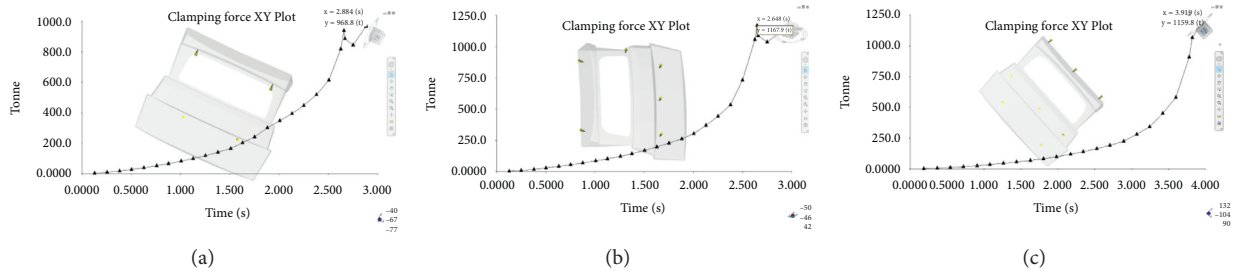


FIGURE 4: Clamping force with (a) four gates, (b) six gates, and (c) eight gates.

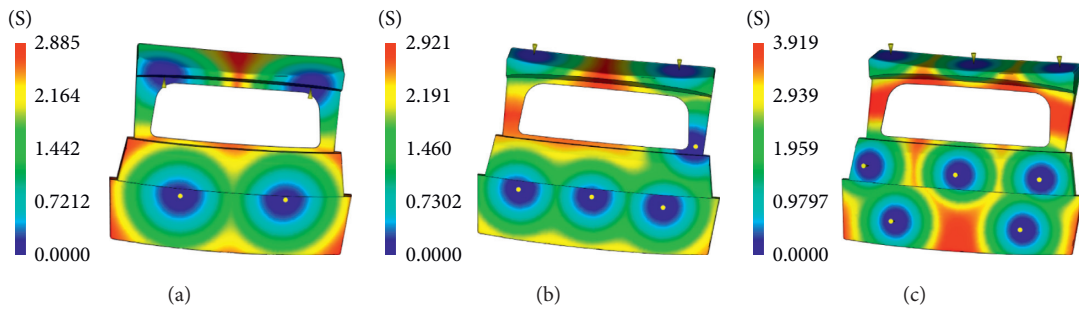


FIGURE 5: Filling time with (a) four gates, (b) six gates, and (c) eight gates.

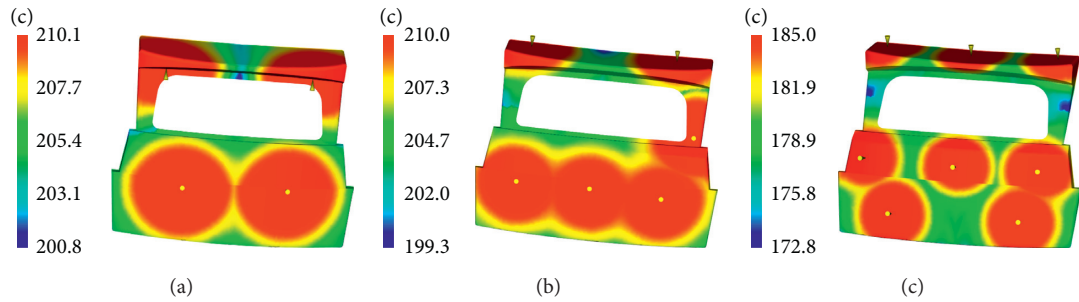


FIGURE 6: Flow front temperature with (a) four gates, (b) six gates, and (c) eight gates.

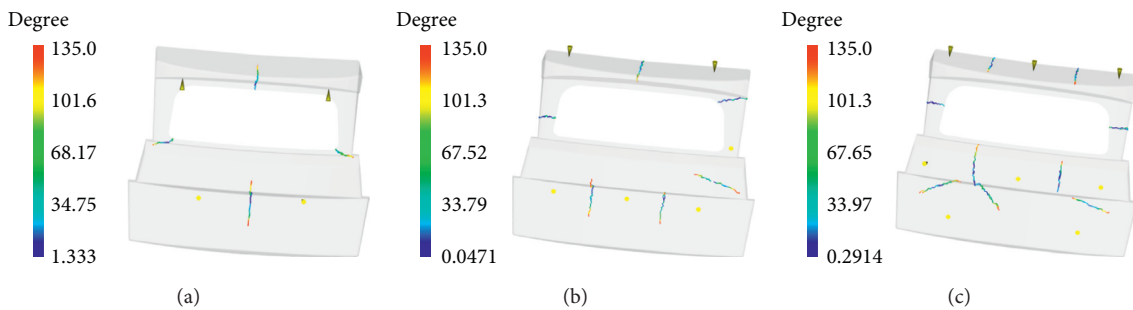


FIGURE 7: Welding line with (a) four gates, (b) six gates, and (c) eight gates.

TABLE 4: Analysis results of three different gate schemes.

The number of gates	Clamping force (t)	Filling time (s)	The difference of temperature (°C)	The number of welding lines
4	969.7	2.885	9.3	4
6	1167.9	2.921	10.7	6
8	1159.8	3.919	12.2	8

TABLE 5: Level factor settings.

Level	Factor				
	A Mold temperature (°C)	B Melt temperature (°C)	C Cooling time (s)	D Packing pressure (MPa)	E Packing time (s)
1	40	185	20	65	15
2	50	200	25	75	20
3	60	215	30	85	25
4	70	230	35	95	30

TABLE 6: Tests and results.

Numbering	Factors					Index	
	A	B	C	D	E	Warpage (mm)	Volumetric shrinkage (%)
1	40	185	20	65	15	10.35	14.26
2	40	200	25	75	20	10.35	15.05
3	40	215	30	85	25	11.35	14.86
4	40	230	35	95	30	10.59	12.35
5	50	185	25	85	30	10.33	14.29
6	50	200	30	95	25	9.10	15.05
7	50	215	35	65	20	11.44	15.85
8	50	220	20	75	15	10.27	16.64
9	60	185	30	95	20	7.84	14.24
10	60	200	35	85	15	8.27	15.05
11	60	215	20	75	30	12.01	15.85
12	60	230	25	65	25	13.52	16.63
13	70	185	35	75	25	8.84	14.24
14	70	200	20	65	30	11.41	15.05
15	70	215	25	95	15	8.61	15.86
16	70	230	30	85	20	1.91	16.63

TABLE 7: Warpage range analysis (mm).

Level	A	B	C	D	E
Mean value 1	10.66	9.34	11.01	11.68	8.826
Mean value 2	10.29	9.79	10.15	10.37	11.04
Mean value 3	10.41	10.30	9.67	10.09	10.71
Mean value 4	9.26	11.19	9.79	8.487	11.09
Range analysis	1.4	1.85	1.344	3.2	2.264

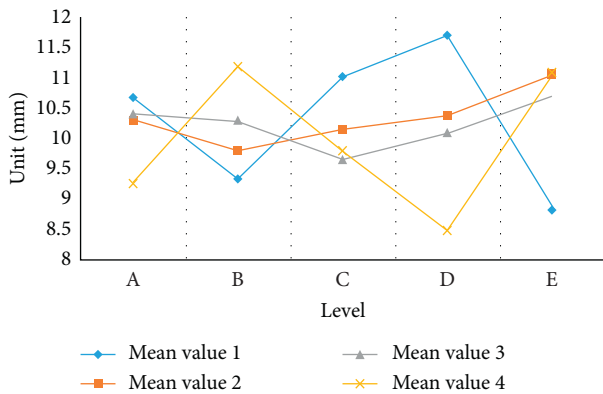


FIGURE 8: Warpage mean analysis.

4. Parameter Optimization Based on Gray Correlation Degree and Taguchi Algorithm

The further optimization of influence of process parameters on evaluation index via dual-index analysis of gray correlation degree and Taguchi algorithm based on SNR (signal-to-noise ratio) is conducted.

4.1. Dual-Index Analysis Based on Gray Correlation. Orthogonal experiment is employed to analyze single warpage or volume shrinkage rate. It is impossible to determine whether there is an inherent connection between two evaluation indicators due to changes in process parameters. Therefore, the concept of gray correlation is introduced. Moreover, gray correlation integration and in-depth analysis are conducted [12].

4.1.1. Gray Correlation Theory. Calculation of gray relation theory is as follows:

- (1) Initial value sequence is determined through nondimensionalization:

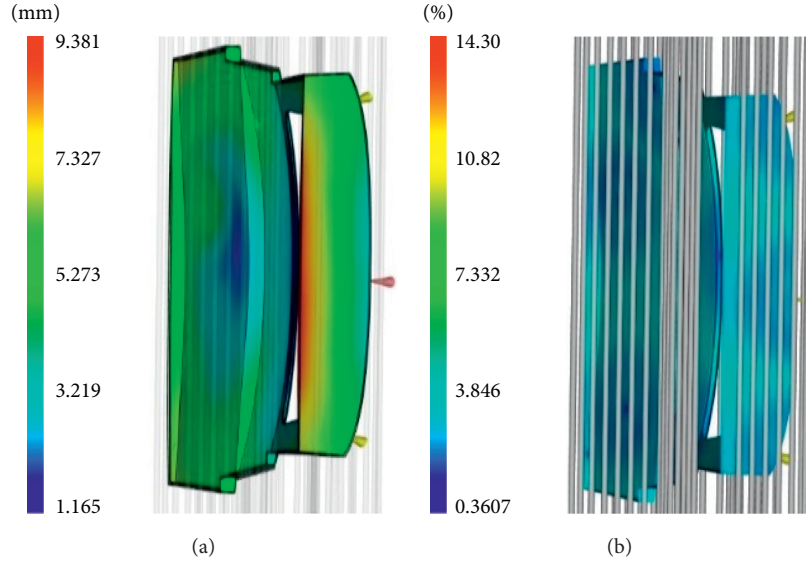


FIGURE 9: A4B1C3D4E1 combined simulation results with (a) warpage and (b) volume shrinkage.

TABLE 8: Range analysis of volume shrinkage (%).

Level	A	B	C	D	E
Mean value 1	14.13	14.26	15.45	15.45	15.45
Mean value 2	15.45	15.05	15.46	15.44	15.44
Mean value 3	15.44	15.61	15.20	15.21	15.20
Mean value 4	15.45	15.56	14.37	14.37	14.39
Range analysis	1.32	1.35	1.09	1.08	1.06

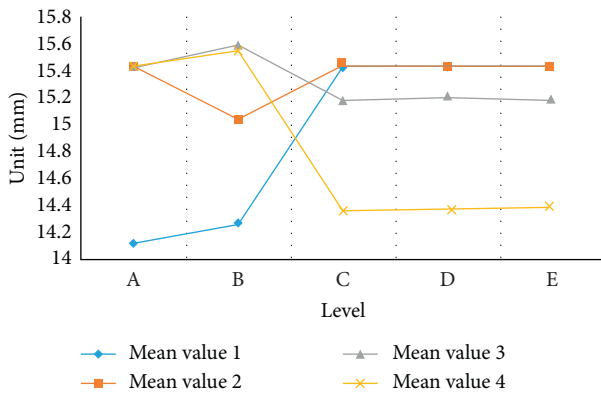


FIGURE 10: Mean analysis of volume shrinkage.

$$y_i = x_i D = (y_i(1), y_i(2), y_i(3) \dots y_i(n)), \quad (6)$$

$$i = 0, 1, 2, 3 \dots m.$$

(2) Sequence difference is obtained:

$$\Delta_{0,i}(k) = |y_0(k) - y_i(k)|, \quad (7)$$

$$i = 1, 2, 3 \dots m; \quad k = 1, 2 \dots n.$$

(3) Range value between indicators is found:

$$M = \max_i \max_k \Delta_{0i}(k), m = \min_i \min_k \Delta_{0i}(k). \quad (8)$$

(4) Correlation coefficient is obtained:

$$r_{0i}(k) = \frac{m + \rho M}{\Delta_i(k) + \rho M}, \quad (9)$$

where ρ represents resolution coefficient, $i = 1, 2, \dots, m$, $k = 1, 2, \dots, n$, and $\rho \in [0, 1]$, $\rho = 0.5$.

(5) Gray correlation degree between indicators is calculated:

$$r(x_0, x_i) = \frac{1}{n} \sum_{k=1}^n r_{0i}(k); \quad (i = 1, 2, 3 \dots m). \quad (10)$$

Actual experimental data and equations (6)–(10) are combined, and correlation coefficient between two indicators is calculated.

4.1.2. Gray Correlation Calculation. A series of numerical values, such as the range of gray correlation degree and correlation coefficient, are calculated. Gray correlation degree for two different evaluation indicators is calculated according to equation (10). Results are shown in Table 9. Range analysis method is used to postprocess gray correlation data, and the results are shown in Table 10. Two evaluation indicators are integrated via gray correlation degree. Therefore, a set of improved combination parameters can be obtained by employing gray correlation degree range analysis results. Improved combination parameters are denoted as A1B1C4D4E1. Simulation analysis results of parameter combination are

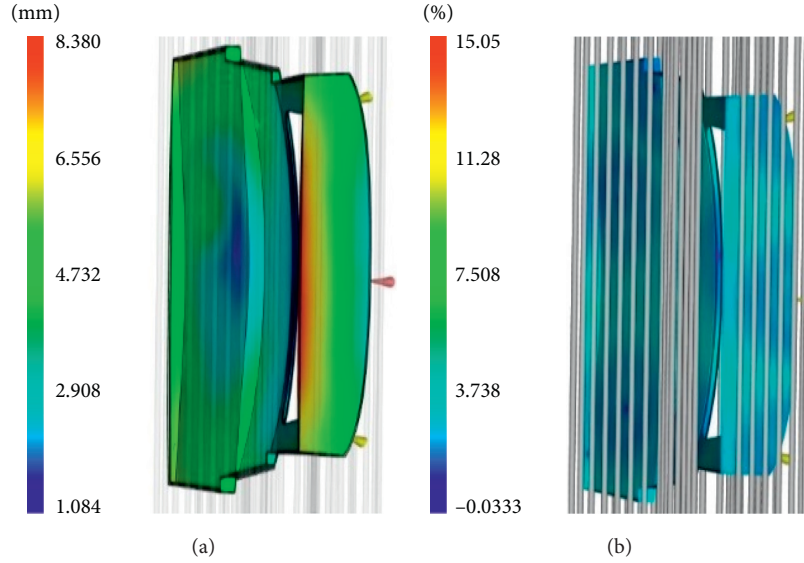


FIGURE 11: A1B1C4D4E4 combined simulation results with (a) warpage and (b) volume shrinkage.

TABLE 9: Gray correlation results.

Numbering	Correlation	Numbering	Correlation
1	0.51	9	0.62
2	0.46	10	0.55
3	0.44	11	0.39
4	0.73	12	0.34
5	0.51	13	0.57
6	0.51	14	0.43
7	0.40	15	0.69
8	0.41	16	0.41

TABLE 10: Gray correlation range analysis.

Level	A	B	C	D	E
Mean value 1	0.54	0.55	0.44	0.42	0.54
Mean value 2	0.46	0.49	0.5	0.46	0.47
Mean value 3	0.48	0.48	0.5	0.48	0.47
Mean value 4	0.53	0.47	0.57	0.64	0.52
Range analysis	0.08	0.08	0.13	0.22	0.07

shown in Figure 12. Warpage is equal to 8.37 mm, while the volume shrinkage rate is 14.26%.

4.2. Taguchi Algorithm Data Processing Based on SNR. Contrary to the orthogonal experiment method, Taguchi algorithm introduces the concept of SNR on the basis of orthogonal experiment. In Taguchi algorithm, the index for measuring test results is no longer warpage or volume shrinkage rate. Instead, SNR is employed [13].

4.2.1. SNR Calculation. For the injection molding process considered in this paper, numerical evaluation index should be as small as possible but within a reasonable range. In other words, the smaller the chosen index, the better the SNR

calculation. SNR is calculated according to the following equation:

$$\eta = -10 \log_{10} \left(\frac{1}{n} \sum_{j=1}^n S_j^2 \right). \quad (11)$$

Minimum characteristic warpage value is set to Y_1 and SNR to η_1 . Minimum volume shrinkage characteristic value is set to Y_2 with the corresponding SNR value of η_2 . The overall SNR is obtained as

$$\eta = 0.5\eta_1 + 0.5\eta_2. \quad (12)$$

Equations (11) and (12) are used to calculate SNR, and the results are shown in Table 11.

4.2.2. Analysis of SNR Calculation Results

(1) SNR sum and its average are found:

$$N = \sum_{j=1}^{16} \eta_j. \quad (13)$$

Data in Table 11 is substituted into equation (13):

$$\begin{aligned} N = \sum_{j=1}^{16} \eta_j &= -(21.6906 + 21.8109 + \dots + 21.9005 + 21.9329) \\ &= -349.6783. \end{aligned} \quad (14)$$

SNR sum is equal to -349.6783 , and the mean value is equal to -21.8549 .

(2) Mean value and range of each SNR factor are calculated.

According to Table 11, SNR mean value and range corresponding to each process parameter are calculated, and the results are shown in Table 12.

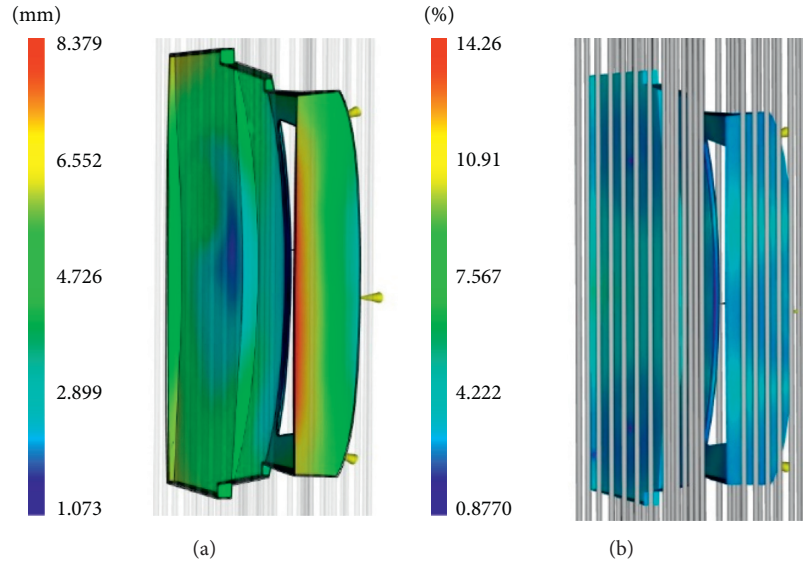


FIGURE 12: A1B1C4D4E1 combined simulation results with (a) warpage and (b) volume shrinkage.

TABLE 11: SNR calculation results.

Numbering	SNR η_1	SNR η_2	SNR η
1	-20.2988	-23.0824	-21.6906
2	-20.2988	-23.3229	-21.8109
3	-20.5826	-23.3624	-21.9725
4	-20.5616	-23.0276	-21.7946
5	-20.5071	-23.0423	-21.7747
6	-20.3133	-23.1313	-21.7223
7	-20.4463	-23.2666	-21.8565
8	-20.4200	-23.4292	-21.9246
9	-20.2016	-23.3907	-21.7962
10	-20.0489	-23.4070	-21.7280
11	-20.2140	-23.4644	-21.8392
12	-20.4739	-23.5524	-21.0132
13	-20.3732	-23.5171	-21.9425
14	-20.4332	-23.5196	-21.9764
15	-20.2472	-23.5537	-21.9005
16	-20.2526	-23.6131	-21.9329

Sum of SNR squared total fluctuations can be obtained as

$$S_N = \sum_{j=1}^{16} (N_j - \bar{N})^2 = 0.15. \quad (15)$$

SNR sum of squared fluctuations of each influencing factor is calculated as

$$S_i = \frac{1}{4} (N_1^2 + N_2^2 + N_3^2 + N_4^2) - \frac{1}{16} N^2. \quad (16)$$

According to Table 12 and the above data, equation (16) is employed for calculation:

$$S_1 = 0.0393; S_2 = 0.0403; S_3 = 0.0039; S_4 = 0.0166; S_5 = 0.0218.$$

(3) Variance analysis

In variance calculation, degree of freedom f has to be first determined. Degree of freedom f is the number of influencing factors lowered by one. Variance V is equal to the square sum of S_i /degree of freedom f of each influencing factor SNR fluctuation. Parameter F is equal to variance error of the influencing factor. When the error variance does not exist, value with the smallest SNR fluctuation square and influencing factor S_i can be selected as the error variance for calculation (e.g., factor C), and the variance can be calculated based on the above data. Volatility sum of squares, degrees of freedom, variance, and F value are all calculated, and the results are shown in Table 13.

According to Table 13, influence of A and B on quality fluctuation characteristics can be observed. Therefore, the two can be regarded as stable factors. Factors C, D, and E,

TABLE 12: SNR range analysis.

Level	A	B	C	D	E
Mean value 1	-21.8172	-21.8017	-21.8577	-21.8842	-21.8109
Mean value 1	-21.8195	-21.8094	-21.8748	-21.8800	-21.8491
Mean value 1	-21.8442	-21.8922	-21.8560	-21.8520	-21.9133
Mean value 1	-21.9388	-21.9163	-21.8311	-21.8034	-21.8426
Range analysis	0.1216	0.0304	0.0438	0.0808	0.1024

TABLE 13: Variance data analysis.

Level	Fluctuation square sum S	Degree of freedom f	Variance V	Value F
Factor A	0.0393	3	0.0131	10.1
Factor B	0.0403	3	0.0134	10.1
Factor C	0.0039	3		
Factor D	0.0166	3	0.0055	4.2
Factor E	0.0218	3	0.0073	5.6

TABLE 14: Warpage SNR analysis of factors C, D, and E.

Numbering	Cooling time	Packing pressure	Packing time
1	-81.366	-81.6522	-81.0149
2	-81.527	-81.306	-81.1993
3	-81.3501	-81.3912	-81.743
4	-81.43	-81.3237	-81.7159

are set as adjustable factors. For stable factors A and B, corresponding levels are A1 and B1, respectively. Factors A and B are kept constant, while the warpage SNR of factors C, D, and E is analyzed. Analysis results are shown in Table 14.

In Table 14, only influence of factors C, D, and E on warpage is analyzed. Furthermore, the best combination of process parameters is selected as C3D4E1. Combination of this set of process parameters is simulated, and the results are shown in Figure 13. The warpage is equal to 8.21 mm, and the volume shrinkage rate is equal to 10.3%.

4.3. Comprehensive Analysis. Warpage and volume shrinkage of the orthogonal experiment are analyzed via extreme difference. In addition, influence trend and degree of the injection molding process parameters on the evaluation index are obtained for two cases. Simultaneously, gray correlation analysis method and SNR Taguchi method are used to perform a simple optimization analysis on data obtained from the orthogonal experiment. Moreover, the influence trend and degree of the injection molding process parameters on the evaluation index are obtained for each case. Comprehensive analysis is shown in Table 15.

According to Table 15, the warpage is 8.2 mm and the volume shrinkage rate is 10.3% when Taguchi method is employed. Compared with previous analysis methods, improved process parameter combination is obtained by Taguchi method.

5. Parameter Optimization Based on Least Squares and Fish School Algorithm

In this section, least square method is employed to fit the obtained orthogonal test data for a single evaluation index warpage. Then, the fitted curve is optimized via fish school algorithm.

5.1. Least Squares Method. When each group of X and Y data is known, the fitting curve can be obtained using mathematical formulas or computer-aided methods [14].

5.2. Least Square Curve Fitting

5.2.1. Set Weight. When excessive amount of influencing factors is present in the process of injection molding parameter optimization, setting weights method is used to integrate five factors into one. Considering the actual situation during injection molding process, weight of each factor is set as follows:

$$\omega = (\omega_1, \omega_2, \omega_3, \omega_4, \omega_5) = (0.4, 0.3, 0.1, 0.1, 0.1). \quad (17)$$

5.2.2. Numerical Calculation. The weight value is used to weigh 16 sets of process parameter combinations. Parameter X in the least square method is obtained as the result, with its values being 81.5, 88, 90, 94, 94.5, 95, 96.5, 97, 97.5, 99.5, 100, 101, 101.5, 104.5, 106.5, and 110.5. Evaluation index in this chapter is the warpage. Thus, the Y value during least square

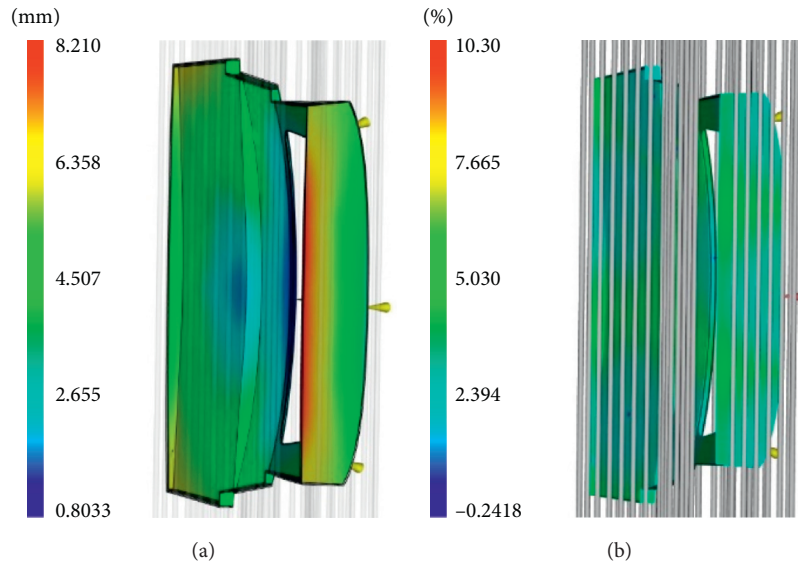


FIGURE 13: A1B1C3D4E1 combined simulation results with (a) warpage and (b) volume shrinkage.

TABLE 15: Comprehensive analysis and comparison.

Influencing factors		Parameter combination	Warpage (mm)	Volume shrinkage (%)
Warpage analysis	Packing pressure > packing time > melt temperature > mold temperature > cooling time	A1B1C3D4E1	9.3	14.3
Volume shrinkage analysis	Melt temperature > mold temperature > packing pressure > cooling time > packing time	A1B1C4D4E4	8.38	15.05
Gray relational analysis	Melt temperature > packing pressure > packing time > mold temperature > cooling time	A1B1C4D4E1	8.37	14.26
Taguchi method analysis	Melt temperature > mold temperature > packing time > packing pressure > cooling time	A1B1C3D4E1	8.21	10.3

fitting is the value of 16 warpage groups in the orthogonal test table. These values can be obtained by referring to Table 6.

5.2.3. *Curve Fitting.* In order to increase the accuracy of curve fitting, weighted data is imported into MATLAB and discrete points are connected. In Figure 14, data distribution obtained after using automatic import via

MATLAB software is shown. Then, the software is used to simulate the curve of this discrete data set. After multiple attempts and optimizations, the final fitted curve is shown in Figure 15.

According to Figures 15 and 16, sets of imported data sets are distributed on the fitted curve. Analytical equation with various corresponding parameter values fitted by the software is as follows:

General model *sin 4*:

$$F(x) = a1 * \sin(b1 * x + c1) + a2 * \sin(b2 * x + c2) + a1 * \sin(b2 * x + c2) + a3 * \sin(b3 * x + c) + a4 * \sin(b4 * x + c4)$$

其中:

$$\begin{aligned} a1 &= 11.41; b1 = 0.0006434; c1 = 7.279 \\ a2 &= 1.414; b2 = 0.3507; c2 = -11.73 \\ a3 &= 2.096; b3 = 0.8195; c3 = -18.83 \\ a4 &= 3.388; b4 = 1.646; c4 = -12.89. \end{aligned}$$

(18)

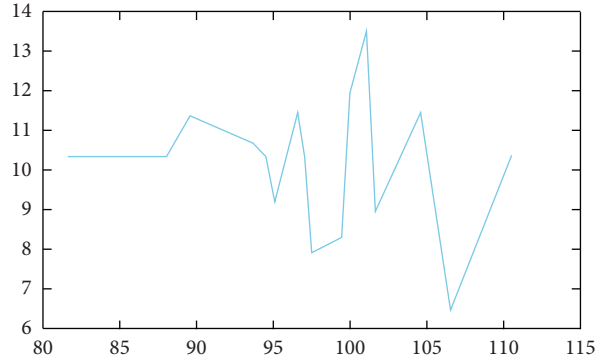


FIGURE 14: Data import.

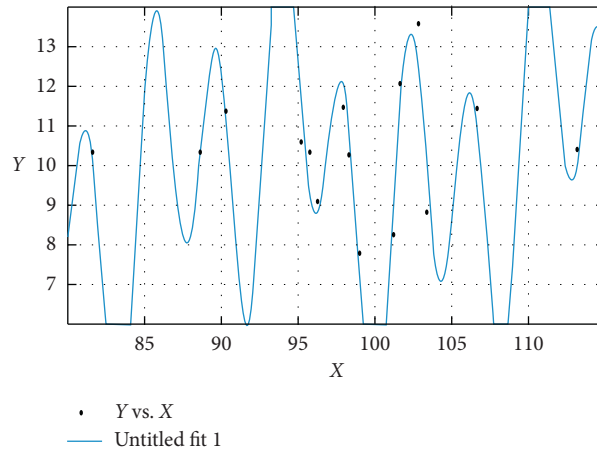


FIGURE 15: Curve fitting.

Least square method is employed for the above-presented data fitting. Next, the algorithm is used to optimize the analytical equation.

5.3. Optimization of Injection Process Parameters Based on Fish School Algorithm. In water, the place with the highest fish density is considered the most food abundant place. Artificial fish are constructed based on fish characteristics to imitate the behavior of fish schools. Each fish corresponds to an optimized solution. Virtual water area corresponds to optimization problem solution space. Food concentration corresponds to the value of the objective function. Therefore, the best optimization is obtained by swimming in virtual waters with schools of fish [15, 16].

5.3.1. Introduction to Fish School Algorithm

- (1) Foraging behavior: the current state of the artificial fish is assumed as X_a , while X_b represents a randomly selected state within its field of view:

$$X_b = X_a + \text{Visual} \cdot \text{Rand}(). \quad (19)$$

If the food concentration is $Y_a > Y_b$, one step forward in that direction is equal to

$$X_a^{t+1} = X_a^t + \frac{X_b - X_a^t}{\|X_b - X_a^t\|} \text{Step} \cdot \text{Rand}(). \quad (20)$$

- (2) Grouping behavior: current artificial fish state is set to X_a , while the number of partners in its neighborhood is nf . If $nf/N < \delta$, the partner center has more food, and it is not overly crowded. Therefore, $Y_a > Y_c$ and the fish moves forward to the center position X_c :

$$X_a^{t+1} = X_a^t + \frac{X_c - X_a^t}{\|X_c - X_a^t\|} \text{Step} \text{Rand}(). \quad (21)$$

- (3) Tail-catch behavior: current state of the artificial fish is X_i , while the best neighbor is X_{MAX} . If $Y_a > Y_{\text{MAX}}$, number of partners in the neighborhood of X_{MAX} is nf , and $nf/N < \delta$ criteria are met. If it is indicated that more food exists in X_{MAX} and it is not too crowded, one step towards X_{MAX} is taken:

$$X_a^{t+1} = X_a^t + \frac{X_{\text{max}} - X_a^t}{\|X_{\text{max}} - X_a^t\|} \text{Step} \text{Rand}(). \quad (22)$$

If the aforementioned is not true, foraging behavior is performed.

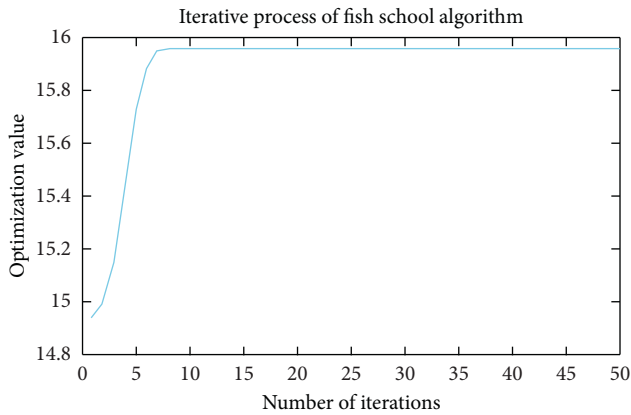


FIGURE 16: Number of iterations.

- (4) Random behavior: the essence of random behavior is a default behavior of foraging behavior:

$$X_a^{t+1} = X_a^t + \text{Visual Rand}(). \quad (23)$$

- (5) Bulletin board: optimal artificial fish state is recorded during the optimization process.

5.3.2. Fish School Algorithm Optimization Process

- (1) Mathematical model input

Mathematical model obtained after using curve fitting method is written into the artificial fish school algorithm.

- (2) Initialization setting

Before performing algorithm optimization, necessary parameter values in addition to analytical ones are determined.

In this paper, the number of artificial fish is set to 50 to ensure an adequate number of samples without increasing the complexity of the analysis. Maximum number of iterations is set to 50, while the maximum number of trials is set to 100. Perception distance is chosen as one, congestion factor is 0.618, and optimal step length is set to 0.1.

- (3) Analysis and calculation

Following the completion of initial settings, the algorithm is activated. The computer performs internal calculations according to predetermined parameters to solve the fitness value of the individual fish school. The best artificial fish state is selected by mutual comparison and assigned to the bulletin board.

- (4) Behavior selection

Each individual is evaluated separately, and various above-described fish school behaviors are selected.

- (5) Iterative optimization

Iterative optimization is carried out. Algorithm evaluates all individuals. When the result of an individual is better than the result shown on the

bulletin board, this individual is used to replace the individual of the original bulletin board. This process is repeated in the form of iterative analysis. The iteration stops when the specified error range is reached.

5.3.3. *Fish School Algorithm Optimization Results of the Injection Process Parameters of the Automobile Back Door Outer Panel.* According to initial settings described in Section 5.3.2, parameters required for the algorithm execution process are input into the algorithm program. Then, the fish school algorithm program is imported into MATLAB for optimization analysis.

After debugging and inspections, the results are shown in Figures 16 and 17. Figure 17 shows that the optimization result has stabilized after 10 times.

The results are presented in Figure 17. It can be concluded that the optimal solution X obtained by the artificial fish school algorithm optimization is 92.88298, which is approximately equal to 93.

5.3.4. Analysis and Verification of Optimization Results.

In Section 5.3.3, fish school algorithm is used to optimize weighted parameters for process parameters that affect the warpage. Final optimal solution is 92.88298. A total of 16 data sets are analyzed and optimal process parameter combination weighted value is obtained as 93.

Five process parameters corresponding to the value of 89.5 are as follows: mold temperature of 50°C, melting temperature of 185°C, cooling time of 25 s, packing pressure of 85 MPa, and packing time of 30 s. Five process parameters corresponding to the value 94 are as follows: mold temperature of 60°C, melting temperature of 185°C, cooling time of 30 s, packing pressure of 95 MPa, and packing time of 20 s. Orthogonal experiment is used to simulate the process combination with the weighted value between 90 and 94. Thus, six other verification test sets are conducted via Moldflow simulation analysis. The obtained results are shown in Table 16.

The group with the smallest warpage is the fifth group, with the corresponding deformation amount of 6.405. Weighted combination of process parameters of this group is 93, which is basically in line with the prediction. Warpage amount is compared with previous orthogonal test results, gray correlation results, and Taguchi SNR results (comparison in Table 6). The fifth group demonstrates the least amount of deformation. It can be concluded that the best combination of process parameters is obtained for the verification test group in the fifth group. Simulation results are shown in Figure 18.

It can be concluded that the results obtained via artificial fish swarm algorithm for injection molding process parameters optimization are better than the results obtained by previous methods such as range analysis, gray correlation analysis, and Taguchi SNR analysis using orthogonal experiments. Process parameters were successfully optimized.

The final optimal combination of process parameters is as follows: mold temperature of 60°C, melting temperature

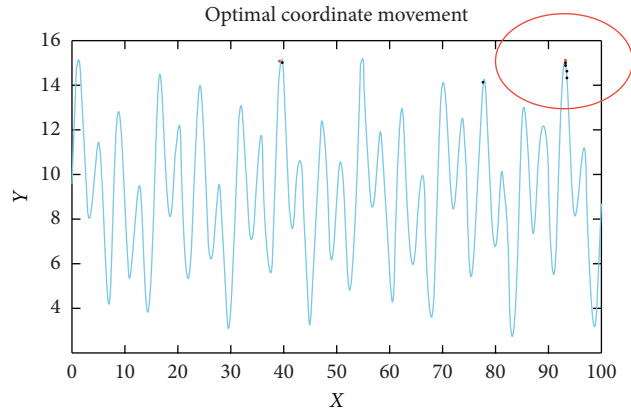


FIGURE 17: Optimal solution location.

TABLE 16: Verification test group.

Numbering	Factors					Index Warpage/mm
	A	B	C	D	E	
1	50	185	20	95	15	10.041
2	50	185	25	95	20	11.345
3	50	185	30	95	25	10.312
4	60	185	20	85	20	8.275
5	60	185	25	85	25	6.405
6	60	185	30	85	30	7.845

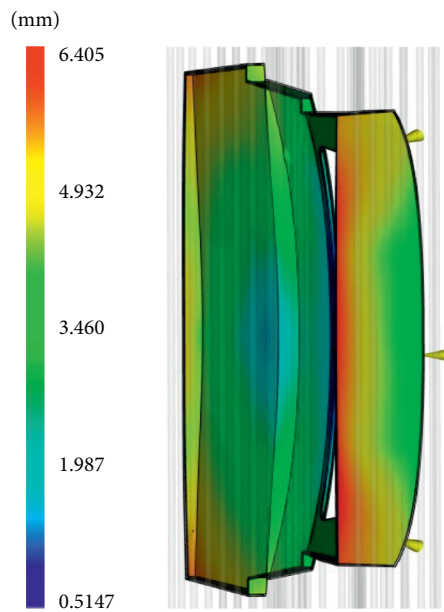


FIGURE 18: Warpage after optimization.

of 185°C, cooling time of 25 s, holding pressure of 85 MPa, and holding pressure time of 25 s. Corresponding deformation is obtained as 6.405 mm.

6. Conclusions

In this paper, outer panel of the plastic back door was considered as the research object. Moldflow2018 was used to

simulate the injection process of plastic back door outer panel. The orthogonal test method was used to study injection molding process parameters. Taguchi algorithm and manual are used. Fish school algorithm was used to optimize injection molding process parameters. The main research work and contributions of this paper can be summarized as follows:

- (1) Filling, packing, and cooling stages of back door outer panel injection molding process were

introduced. PP-EPDM-T30 was selected for the back door outer panel, and plastic parts were meshed using Moldflow and repair option. The best spur location was determined through injection molding process parameters analysis.

- (2) An orthogonal experiment was designed. Moldflow was used for simulation, while the effect of five test factors was considered: melting temperature, mold temperature, packing time, packing pressure, and injection time. Warpage and volume shrinkage rate were selected as evaluation indicators. Different analysis methods were used to obtain degree of influence of each test factor on the evaluation index. The results show that Taguchi method obtained better values, and the best combination of process parameters was A1B1C3D4E1: mold temperature of 40°C, melting temperature of 185°C, cooling time of 30 s, packing pressure of 95 MPa, and packing time of 15 s. The warpage was 8.2 mm, and the volume shrinkage rate was 10.3%.
- (3) Based on the orthogonal test data and warping as the evaluation index, the mathematical model was found by the least square method. Furthermore, based on the established mathematical model, fish school algorithm was used to optimize process parameters that affect the warpage. The best combination of process parameters was as follows: mold temperature of 60°C, melting temperature of 185°C, cooling time of 25 s, packing pressure of 85 MPa, and packing time of 25 s. Minimum corresponding deformation was 6.405 mm. It is concluded that the best results are obtained after algorithm optimization.

Data Availability

The data used to support the findings of this study are included within the article.

Conflicts of Interest

The authors declare that they have no conflicts of interest.

Acknowledgments

This article belongs to the major projects of “The University Synergy Innovation Program of Anhui Province (GXXT-2019-004)” and the project of the “Teaching Research Project of Anhui Education Department (2019jyxm0229).”

References

- [1] K. Fan, *Research on Numerical Simulation and Parameter Optimization Methods for the Warpage of Injection Molded Products*, Shandong University of Science and Technology, Qingdao, China, 2017.
- [2] Li Yan, Y. Li, and Z. Liang, “The application of CAE in improving the warpage of plastic parts,” *Die & Mould Industry*, vol. 40, no. 9, pp. 15–17, 2014.
- [3] G. Lu, “Injection molding warpage analysis and process optimization based on BP neural network,” *Plastics Industry*, vol. 2, pp. 58–60, 2017.
- [4] C. Doerffel, R. Decker, J. Heinrich et al., “Polypropylene based piezo ceramic compounds for micro injection molded sensors,” *Key Engineering Materials*, vol. 45, p. 49, 2017.
- [5] M. Huszar, F. Belblidia, H. M. Davies, C. Arnold, D. Bould, and J. Siens, “Sustainable injection moulding: the impact of materials selection and gate location on part warpage and injection pressure,” *Sustainable Materials and Technologies*, vol. 5, no. 5, pp. 1–8, 2015.
- [6] H. B. Shiroud, D. Seyed, M. Moghaddam, H. Amin et al., “Optimization simulated injection molding process for ultrahigh molecular weight polyethylene nanocomposite hip liner using response surface methodology and simulation of mechanical behavior,” *Journal of the Mechanical Behavior of Biomedical Materials*, vol. 81, no. 25, pp. 95–105, 2018.
- [7] N. Sateesh, S. Devakar Reddy, G. Praveen Kumar, and R. Subbiah, “Optimization of injection moulding process in manufacturing the top cap of water meter,” *Materials Today: Proceedings*, vol. 18, pp. 4556–4565, 2019.
- [8] T. Wang, “Analysis of lightweight design of automobile B-pillar based on manufacturability,” *Mechanical and Electrical Engineering*, vol. 37, no. 3, pp. 277–282, 2020.
- [9] Y. Wang, Y. Liu, and Y. Sun, “A hybrid intelligence technique based on the Taguchi method for multi-objective process parameter optimization of the 3D additive screen printing of athletic shoes,” *Textile Research Journal*, vol. 90, no. 9, pp. 100–101, 2020.
- [10] F. Wittemann, R. Maertens, L. Kärger et al., *Injection Molding Simulation of Short Fiber Reinforced Thermosets with Anisotropic and Non-newtonian Flow Behavior*, pp. 124–130, Elsevier Ltd, Amsterdam, Netherlands, 2019.
- [11] B. Yang and Y. Wang, “Research on the coupling development of agriculture and producer service industry in henan province—based on grey correlation analysis,” *Journal of Pingdingshan University*, vol. 34, no. 5, pp. 105–109, 2019.
- [12] G. Tosello and F. S. Costa, *High Precision Validation of Micro Injection Molding Process Simulations*, Elsevier Ltd, no. 3, pp. 48–50, Amsterdam, Netherlands, 2019.
- [13] G. Wang and Z. Han, “The relationship between the quality loss and the signal-to-noise ratio of the Wangda feature and the Wangxiao feature,” *Mechanical Science and Technology*, vol. 18, no. 2, pp. 236–238, 2015.
- [14] D. Tian, C. Bai, and Y. Xiao, “Scanner characterization based on least square support vector machine,” *Packaging Engineering*, vol. 41, no. 9, pp. 222–225, 2020.
- [15] X. Li and F. Long, “Infrared image segmentation based on two-dimensional Renyi entropy and adaptive artificial fish school algorithm,” *Ship Electronic Engineering*, vol. 36, no. 7, pp. 109–113, 2016.
- [16] L. Cheng-Jian, C. YunShiou, and M. Kuei, “Using 2D CNN with Taguchi parametric optimization for lung cancer recognition from CT images,” *Applied Sciences*, vol. 10, no. 7, pp. 222–240, 2020.

Research Article

Numerical Investigation and Mold Optimization of the Automobile Coat Rack Compression Molding

Youmin Wang, Xiangli Li , and He Sui

School of Mechanical Engineering, Anhui Polytechnic University, Wuhu, Anhui 241000, China

Correspondence should be addressed to Xiangli Li; 2190130114@stu.ahpu.edu.cn

Received 29 December 2020; Revised 7 April 2021; Accepted 20 April 2021; Published 30 April 2021

Academic Editor: Ashwini Kumar

Copyright © 2021 Youmin Wang et al. This is an open access article distributed under the Creative Commons Attribution License, which permits unrestricted use, distribution, and reproduction in any medium, provided the original work is properly cited.

In order to have more accurate control over the compression molding of automobile coat rack, improve the quality of molding products, and achieve the goal of lightweight design, a novel mechanical model for the main two-layer composite structure of the coat rack is proposed. In this regard, the main factors affecting the mechanical properties of the composite structure are obtained. The hot air convection is selected for the sheet preheating. During the experiment, the hot air temperature, preheating time, molding pressure, and pressing holding time are set to 250°C, 110 s, 13 MPa, and 80 s, respectively. Moreover, the error compensation method is applied to compensate for the shrinkage of the product during solidification and cooling. The LS-DYNA finite element software is used to simulate the molding process of the main body of the coat rack, and the node force information with large deformation is obtained accordingly. The load mapping is used as the boundary condition of mold topology optimization, and the compression molding of the main body of the coat rack is optimized. A lightweight design process and method for the compression molding of automotive interior parts and a mathematical model for the optimization of the solid isotropic material penalty (SIMP) (power law) material interpolation of the concave and convex molds are established. Based on the variable density method, OptiStruct is used for the lightweight design of the convex and concave molds of the main body of the coat rack, which reduces the mold weight by 15.6% and meets the requirements of production quality and lightweight.

1. Introduction

Car coat rack is defined as a vehicle accessory to provide beautiful coverage and protection for the covered area or system. In addition, it is an important acoustic component for blocking noise from the luggage compartment. Accordingly, the car coat rack has been widely used in almost all vehicles. With the increasing integration of automobile functions, the coat rack has become a carrier for many other parts. Recently, improving the molding quality of automotive interior parts has focused on controlling the mechanical properties of products, the optimal combination of process parameters, and mold optimization. More specifically, Zheng et al. [1] performed CAE analysis and physical tests on coat racks to find control parameters that affect the product strength and the load capacity. Moreover, they considered the requirements of product appearance and obtained optimal control parameter values to achieve the

design goals, including low-cost and high-performance products. However, the mechanical properties of the material and the mechanical model of the coat rack were not considered. Guo et al. [2] proposed a method for the recycling felt waste of PP glass fiber composite and studied the impact of the size of crushed particles and the proportion of crushed material on the formability and mechanical properties of the coat rack. However, the thickness impact of the glass fiber sheet on the mechanical properties of the material was not considered so that the formulation of process parameters was not reliable. Miao et al. [3] discussed the effect of the multicomponent fiber composition process on the performance of the car coat rack. Through investigating the ratio, pressure, temperature, and speed of multicomponent fibers, the orthogonal test was carried out to find the best component. Studies showed that the combination scheme is an effective way to produce car coat racks and investigate all aspects of their performance. However,

the experimental method was not used to calculate the material shrinkage so that the solidification shrinkage and the product cooling were not compensated. Yu [4] simulated, analyzed, and performed experiments on the non-woven fabric hot-molding mold and the molding process and showed that the molding temperature is the most influential factor in the hot-molding process. Moreover, the temperature distribution was studied, which solved the problem of repeatedly adjusting the molding temperature based on experience, but the number of research objects and simulation experiments was small. Shao [5] optimized the process parameters of glass mat reinforced thermoplastics (GMT) composite material compression molding and obtained the optimal combination from the theoretical point of view. In this optimization, no analysis software was applied to optimize the mold. Demirci and Yildiz [6] studied the effect of conventional steel, new generation DP-TRIP steels, AA7108-AA7003 aluminum alloys, AM60-AZ31 magnesium alloys, and crash-box cross-sections on crash performance of thin-walled energy absorbers which are investigated numerically for the lightweight design of vehicle structures. However, it does not involve numerical research on nonmetallic materials such as car coat racks. It is worth noting that none of the foregoing studies has simulated the compression molding, while the molding simulation can accurately evaluate the correlation between level factors and the mold quality. In order to resolve this shortcoming, it was intended to investigate the mechanical properties of thermoplastic composite materials and design the car coat structure. In this regard, the LS-DYNA finite element software was applied to simulate the molding process, and the load mapping was used as the boundary condition for mold topology optimization. Finally, mold structure optimization was established and the mold structure was optimized to improve the molding quality of the coat rack.

2. Investigating the Mechanical Properties and Structural Design of Thermoplastic Composites for Automobile Coat Racks

In this section, it is intended to establish a mechanical model for the thermoplastic composite of the car coat rack (the mechanical model is solved), analyze some test cases, determine the thickness of the main body, complete the formulation of the main body molding process parameters, determine the shrinkage compensation value, and calculate the heat transfer in the cooling system. These items are discussed in detail in the following.

2.1. Establishment of Structural Mechanical Model for GMT/PET Composite. In the present paper, the composite two-layer structure is taken as the research object. The upper layer is a decorative layer, the main specimen is made of needle-punched PET fabric, and the lower layer is a GMT sheet. It should be indicated that the mechanical properties of GMT sheet depend on the spatial distribution of the fiber and PP and the combination between them [7]. In the composite structure, the materials, thickness, and other physical parameters of the

upper and lower layers are different. Accordingly, the composite plate is regarded as a thin plate, and then its mechanical model is established by considering variations of different physical parameters along the Z -axis. Figure 1 shows the mechanical model of the composite structure.

In order to simplify the mechanical model and the corresponding solving method, it is assumed that the glass fiber and PP materials are evenly dispersed into the space occupied by the sheet, and the overall material performance is linearly combined by the volume fraction of each component. Under a specific glass fiber mass fraction, the GMT sheet has a specific material constant, which can be simplified to an isotropic material in the analysis.

The volume fraction of PP and glass fiber in the GMT sheet can be expressed as follows:

$$\begin{aligned} V_p &= \frac{\rho_1 \cdot M_p}{\rho_p}, \\ V_b &= \frac{\rho_1 \cdot M_b}{\rho_b}, \end{aligned} \quad (1)$$

where ρ_1 , ρ_p , and ρ_b are the total density of GMT sheets, the bulk density of polypropylene, and glass fiber at room temperature, respectively. Moreover, M_p and M_b denote the mass ratio of polypropylene and glass fiber, respectively. Then the material constant of the GMT sheet can be calculated. It is worth noting that the sum of quality scores satisfies the following expression:

$$M_b + M_p = 1. \quad (2)$$

Since the GMT sheet may contain air and cavities during the molding process, the sum of the practical volume fraction of glass fiber and PP is

$$V_b + V_p \leq 1. \quad (3)$$

Moreover, the void volume rate is defined as

$$V_c = 1 - (V_p + V_b) = 1 - \frac{\rho_1 \cdot M_b}{\rho_p} - \frac{\rho_1 \cdot M_p}{\rho_b}. \quad (4)$$

Let the physical property parameter of the GMT sheet be P , where P can represent the elastic modulus of the material E , Poisson's ratio μ , linear expansion coefficient α , and so on. Then this parameter in the composite is defined as follows [8]:

$$P = P_p \cdot V_p + P_b \cdot V_b, \quad (5)$$

where P_p and P_b are the physical properties of polypropylene and glass fiber, respectively. Similarly, the elastic modulus and Poisson's ratio of the GMT sheet can be calculated from equations (6) and (7), respectively.

$$E_1 = E_p \cdot V_p + E_b \cdot V_b, \quad (6)$$

$$\mu_1 = \mu_p \cdot V_p + \mu_b \cdot V_b, \quad (7)$$

where E_p and E_b are the elastic modulus of polypropylene and glass fiber, respectively. Moreover, μ_p and μ_b are

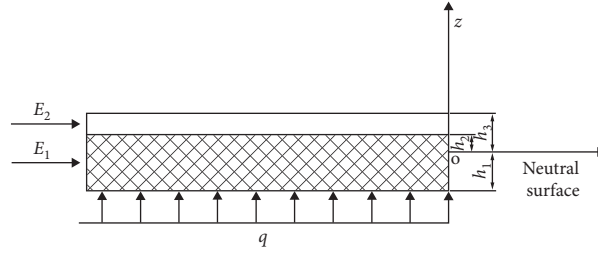


FIGURE 1: Mechanical model of the composite structure.

Poisson's ratio of polypropylene and glass fiber, respectively. The upper layer is a single material of needle-punched PET fabric, so the elastic modulus and Poisson's ratio are E_2 and μ_2 . Then the elastic modulus of the two-layer composite structure is divided into two layers:

$$E(z) = \begin{cases} E_1, & (-h_1, h_2), \\ E_2, & (h_2, h_3). \end{cases} \quad (8)$$

The same operation can be conducted for Poisson's ratio in the following form:

$$\mu(z) = \begin{cases} \mu_1, & (-h_1, h_2), \\ \mu_2, & (h_2, h_3). \end{cases} \quad (9)$$

The differential equation of the elastic surface of the thin plate can be expressed in the following form:

$$D\nabla^4 w = q, \quad (10)$$

where D is the bending stiffness of the sheet, $D = Eh^3/12(1 - \mu^2)$, and h is the total thickness of the sheet. The left side of equation (10) $D\nabla^4 w$ denotes the elastic resistance per unit area, and w is the deflection. Moreover, the left side q is the lateral load per unit area. The stress differential equation can be simplified as follows:

$$\frac{\partial \sigma_z}{\sigma_z} = \frac{E(z)}{2 \cdot (1 - \mu(z)^2)} \cdot \left(\frac{h^2}{4} - z^2 \right) \cdot \nabla^4 w. \quad (11)$$

Integrating both sides with respect to z from $-h_1$ to h_3 yields the following expressions:

$$\int_{-h_1}^{h_3} \frac{\partial \sigma_z}{\sigma_z} dz = \sigma_z \Big|_{-h_1}^{h_3} = 0 - q = -q, \quad (12)$$

$$\int_{-h_1}^{h_3} \frac{E(z)}{2(1 - \mu(z)^2)} \left(\frac{h^2}{4} - z^2 \right) \nabla^4 w dz = \int_{-h_1}^{h_3} \frac{E(z)}{2(1 - \mu(z)^2)} \left(\frac{h^2}{4} - z^2 \right) dz \nabla^4 w.$$

In order to simplify expressions, parameter D is defined as follows:

$$D = - \int_{-h_1}^{h_3} \frac{E(z)}{2(1 - \mu(z)^2)} \left(\frac{h^2}{4} - z^2 \right) dz. \quad (13)$$

Then the integral can be decomposed into the sum of integrals of each layer:

$$-D = \int_{-h_1}^{h_2} \frac{E(z)}{2(1 - \mu(z)^2)} \left(\frac{h^2}{4} - z^2 \right) dz + \int_{h_2}^{h_3} \frac{E(z)}{2(1 - \mu(z)^2)} \left(\frac{h^2}{4} - z^2 \right) dz = -D_1 - D_2. \quad (14)$$

2.2. The Mechanical Model of the Composite Structure Is Solved. When solving the thin plate deflection-bending problem by the Navier method, the deflection w should be initially obtained from the elastic surface differential

equation under the boundary conditions of the plate edge [9].

During the unsupported subsidence, the length and width for a rectangular thin plate, which is simply supported on four sides, are a and b , respectively. In this case, the boundary conditions are

$$\left. \begin{aligned} (w)_{x=0} &= 0, \left(\frac{\partial^2 w}{\partial x^2} \right)_{x=0} = 0 \\ (w)_{x=a} &= 0, \left(\frac{\partial^2 w}{\partial x^2} \right)_{x=a} = 0 \\ (w)_{y=0} &= 0, \left(\frac{\partial^2 w}{\partial x^2} \right)_{y=0} = 0 \\ (w)_{y=b} &= 0, \left(\frac{\partial^2 w}{\partial x^2} \right)_{y=b} = 0 \end{aligned} \right\}. \quad (15)$$

The deflection w can be calculated from the following trigonometric series:

$$w = \sum_{m=1}^{\infty} \sum_{n=1}^{\infty} w_m = \sum_{m=1}^{\infty} \sum_{n=1}^{\infty} A_{mn} \sin \frac{m\pi x}{a} \sin \frac{n\pi y}{b}, \quad (16)$$

where m and n are positive integers. Substitute this expression into equation (15) which indicates that all boundary conditions are satisfied. In order to find the coefficient A_{mn} , equation (16) is introduced into equation (10):

$$\pi^4 D \sum_{m=1}^{\infty} \sum_{n=1}^{\infty} \left(\frac{m^2}{a^2} + \frac{n^2}{b^2} \right) A_{mn} \sin \frac{m\pi x}{a} \sin \frac{n\pi y}{b} = q, \quad (17)$$

and expanding the load q on the right side of equation (17) into a multiple triangle series results in the following expression:

$$q = \sum_{m=1}^{\infty} \sum_{n=1}^{\infty} A_{mn} \sin \frac{m\pi x}{a} \sin \frac{n\pi y}{b}, \quad (18)$$

where A can be solved through the method of determining the triangle series, and the solution is

$$A_{mn} = \frac{16q_0}{\pi^6 mnD \left(\left(\frac{m^2}{a^2} \right) + \left(\frac{n^2}{b^2} \right) \right)^2}, \quad (m = 1, 3, 5, \dots; n = 1, 3, 5, \dots). \quad (22)$$

Then equation (16) can be applied to calculate the deflection:

$$w = \frac{16q_0}{\pi^2 D} \sum_{m=1,3,5,\dots}^{\infty} \sum_{n=1,3,5,\dots}^{\infty} \frac{\sin(m\pi x/a) \sin(n\pi y/b)}{mn \left(\left(\frac{m^2}{a^2} \right) + \left(\frac{n^2}{b^2} \right) \right)^2}. \quad (23)$$

Internal forces can be expressed in the following form:

$$\begin{cases} M_x = -D \left(\frac{\partial^2 w}{\partial x^2} + \mu \frac{\partial^2 w}{\partial y^2} \right), \\ M_y = -D \left(\frac{\partial^2 w}{\partial y^2} + \mu \frac{\partial^2 w}{\partial x^2} \right), \\ M_{xy} = M_{yx} = -D(1 - \mu) \frac{\partial^2 w}{\partial x \partial y}, \\ F_{S,x} = -D(1 - \mu) \frac{\partial^2}{\partial x} \nabla^2 w, \\ F_{S,y} = -D(1 - \mu) \frac{\partial^2}{\partial y} \nabla^2 w. \end{cases} \quad (24)$$

Based on the performed calculations and analyses, the two-layer composite structure is simply supported on four sides, where the length a , width b , and GMT sheet thickness are 0.1 m, 0.1 m, and 3.5 mm, respectively. Moreover, the

$$A_{mn} = \frac{4}{ab} \int_0^a \int_0^b q(x, y) \sin \frac{n\pi y}{b} \sin \frac{m\pi x}{a} dx dy. \quad (19)$$

Then equation (18) can be rewritten in the following form:

$$q = \frac{4}{ab} \sum_{m=1}^{\infty} \sum_{n=1}^{\infty} \frac{4}{ab} \int_0^a \int_0^b q(x, y) \sin \frac{n\pi y}{b} \sin \frac{m\pi x}{a} dx dy \cdot \sin \frac{n\pi y}{b} \sin \frac{m\pi x}{a}, \quad (20)$$

$$A_{mn} = \frac{4 \int_0^a \int_0^b q(x, y) \sin(n\pi y/b) \sin(m\pi x/a) dx dy}{\pi^4 abD \left(\left(\frac{m^2}{a^2} \right) + \left(\frac{n^2}{b^2} \right) \right)}. \quad (21)$$

When the thin plate is subjected to a uniform load, q becomes a constant q_0 . Under this circumstance, equation (21) can be rewritten in the following form:

composite density is 1.3 g/cm³ and the void ratio is assumed to be 0. The mass fraction and density of the glass fiber are 30% and 2.6 g/cm³, respectively. In the present study, alkali-free fibers (E) with an elastic modulus of 72 GPa and Poisson's ratio of 0.2 are applied. Furthermore, the density, elastic modulus, and Poisson's ratio of PP are 0.93 g/cm³, 1.4 GPa, and 0.4, respectively. The lateral uniform load is 10 MPa, the thickness of the transition layer is 1.5 mm, and the specimen is made of needle-punched PET with an elastic modulus of 4000 MPa.

Based on the established mathematical model, the thickness impact on the mechanical properties of the thin plate can be investigated by changing the thickness of the GMT sheet under the condition that the glass fiber content is maintained 30%, while the applied load and constraints remain constant. The iterative calculations are performed in the MATLAB environment. The maximum deflection and stress value of the two-layer structure are shown in Table 1. The stress value can be obtained from the internal force value through the generalized Hook definition of the thin plate.

Table 1 indicates that, for a constant load and constraint, as the thickness of the GMT sheet increases, the deflection of the two-layer composite structure gradually decreases, thereby reducing the normal stress and the shear force. It is inferred that, as the sheet thickness increases, flexural, tensile, and shear resistance of the whole plate improve.

When the thickness is fixed and different glass fiber ratios are used, the deflection and internal force of the plate are shown in Table 2.

TABLE 1: Maximum deflection and stress values for different thicknesses.

GMT plate thickness (mm)	Deflection (m)	σ_x, σ_y (Pa)	τ_{xy}, τ_{yx} (Pa)
3.3	0.0022899	34.914	24.598
3.4	0.0019380	30.428	21.478
3.5	0.0016547	26.357	18.759
3.6	0.0014242	23.458	16.102
3.7	0.0011984	19.857	13.478

Table 2 indicates that, under the condition of unchanged load and restraint, as the content of glass fiber increases, the deflection value and bending moment value decrease, while the corresponding torque increases. Therefore, the optimal content of GMT sheet glass fiber is selected according to the required mechanical performance index.

2.3. Thickness of the Car Coat Rack. Based on the foregoing discussions, it is concluded that the rigidity design requirements can be achieved by increasing the thickness of the GMT sheet without changing the main structure of the car coat rack. However, the material consumption for too thick products cannot be justified. More specifically, the production cost increases, the product becomes prone to stress concentration, and the molding quality reduces.

The stiffness test principle is as follows: as a support frame, the sample deflects continuously at the midpoint of the span until the fracture or deformation reaches a certain predefined value. In this process, the applied stress to the sample is measured. Figure 2 illustrates the schematic configuration of composite layers, indicating that the composite consists of a PET fabric and the GMT sheet.

Since the fabric and the substrate are subjected to stress in parallel, the mixed law of elastic modulus of the parallel composite structure can be used [9]:

$$E_0 = E_1V_1 + E_2V_2, \quad (25)$$

where E_0 , E_1 , and E_2 denote the elastic modulus of the composite material, PP glass fiberboard, and PET fabric, respectively. Substituting equations (6) into (25) gives

$$E_0 = (E_pV_p + E_bV_b)V_1 + E_2V_2. \quad (26)$$

Then the predicted value of the elastic modulus in the composite shown in Figure 2 can be expressed in the following form:

$$E_0 = (E_pV_p + E_bV_b) \frac{d_1}{d_1 + d_2} + E_2 \frac{d_2}{d_1 + d_2}, \quad (27)$$

where d_1 and d_2 denote the thickness of PP glass fiber and PET fabric, respectively. In order to meet the rigidity design requirements, the following conditions should be satisfied:

$$E_0I \geq \sigma, \quad (28)$$

$$I = \frac{b \cdot (d_1 + d_2)^3}{12},$$

where σ is the required stiffness; I is the moment of inertia; and b is the width of the coat rack. In order to solve the equations easily, a thick needle-punched PET fabric with a thickness of 1.5 mm, elastic modulus of 4000 MPa is considered in the calculations, and GMT sheet porosity is assumed to be 0. The glass fiber is made of alkali-free fiber (E) with an elastic modulus of 72 GPa, while the elastic modulus of PP is 1.4 GPa. Moreover, the coat rack width b is 600 mm and the required bending stiffness is $\sigma \geq 60 \text{ N/mm}^2$.

The combination of glass fiber content and thickness of the GMT sheet that satisfy the stiffness requirements can be calculated from equations (27) and (28). The proposed combination is shown in Table 3.

Based on the obtained results, a glass fiber content of 30% and a thickness of 4.5 mm is proposed as the selected composition. To maximize the safety factor, the thickness of the GMT sheet is rounded to 4.5 mm. Since the thicknesses of the GMT sheet and PET fabric are 4.5 mm and 1.5 mm, the overall thickness of the composite is 6 mm.

2.4. Formulation of the Process Parameters to Mold the Main Body of the Automobile Coat Rack. By analyzing the common quality defects and causes of the main body of the coat rack, the main processing parameters that affect the molding process of the car coat rack are determined. These parameters are the molding pressure, holding time, and the molding temperature.

2.4.1. Sheet Warm-Up Time. In order to heat the GMT sheet, hot air convection preheating is used. In this case, the sheet can be expanded to 2-3 times the thickness of the cold sheet. It should be indicated that the sheet temperature should be less than 230°C; otherwise, the PP polypropylene will degrade, thereby affecting the surface of the molded product and reducing the heat resistance and strength of the product [10, 11]. The preheating time of the GMT sheet can be calculated through the following expression [12] (29):

$$t = 70.9521 + 0.2318d - 0.2810T, \quad (29)$$

where t is the appropriate preheating time, min; d is the sheet thickness, mm; and T is the hot air temperature, °C.

During the experiment, hot air flow from an oven is used to preheat the sheet. The thickness of the GMT sheet is 4.5 mm and the preheating temperature of the hot air is 250°C. Based on equation (29), the preheating time is adjusted to 99 s. In the experiment, the sheet is taken out of the oven and transferred to the mold. Since the temperatures of the material and the oven reduce during the material transfer, the preheating time of the sheet is set to 110 s.

TABLE 2: Deflection and internal force values for different glass fiber contents.

GMT plate glass fiber content (%)	Deflection (mm)	Bending moment (N · m)	Torque (N · m)
25	0.0016732	25.434	29.562
30	0.0016547	25.293	29.646
35	0.0016238	25.177	29.739
40	0.0015966	25.054	29.822
45	0.0015624	24.964	29.018

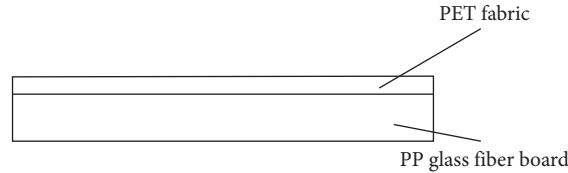


FIGURE 2: Schematic configurations of the composite layers.

TABLE 3: Proposed GMT sheet glass fiber ratio and thickness combination.

GMT sheet glass fiber content (%)	GMT sheet thickness (mm)	Round thickness (mm)
20	4.886	5
25	4.636	4.8
30	4.386	4.5
35	4.136	4.3
40	3.886	4

2.4.2. *Molding Pressure and Mold Clamping Speed.* Appropriate molding pressure not only improved the product quality but also made up for the shortage if other industrial parameters were not adequate [13].

- (1) The method of maximum gauge pressure:

$$f_{\text{table}} = \frac{f_1 f_2 S}{T}, \quad (30)$$

where f_{table} , f_1 , and f_2 denote the gauge pressure, unit pressure required by the product, and the rated gauge pressure of the press, respectively. Meanwhile, S and T denote the projected area of the product in the compression direction and the pressing force, respectively.

$$x = \frac{f_1 S}{T}, \quad (31)$$

where x is the ratio of the force acting on the pressure direction of the product to the pressing force. When $x > 1$, the pressing force is too small to meet the production requirements. On the other hand, when $x < 1$, the pressing force is sufficient to meet the production demand.

- (2) The method of Piston area method:

$$f_{\text{table}} = \frac{f_1 S}{F}, \quad (32)$$

where F is the cross-sectional area of the piston of the press.

In the present study, for a four-post-servo-hydraulic machine (model; company) with $F = 0.5 \text{ m}^2$ and $S = 0.84 \text{ m}^2$, the molding pressure is 13 MPa and $f_{\text{table}} = 22 \text{ MPa}$. For these parameters, equation (31) indicates that $x > 1$, so that the selected hydraulic pressure meets the molding requirements.

In the molding process to produce the main body of the automobile coat rack, the mold clamping speed is not a fixed value. It should be indicated that the molding process can be divided into 5 main stages:

- ① When the sheet is placed in the mold, the concave mold decreases at a speed of 60 mm/s.
- ② The interval between the convex and concave mold gradually decreases. Consequently, when the guide column enters the guide sleeve, the speed becomes 8 mm/s. Moreover, when the convex and concave molds are closed, the sheet is molded under pressure.
- ③ Cooling and solidification.
- ④ After holding the pressure for 80 s, the concave mold is split at a speed of 8 mm/s.
- ⑤ After the split mold is completed, the concave mold is 60 mm/s. Then the speed rises and when the die is reset, the product is removed.

These five stages are also shown in Figure 3.

2.4.3. *Holding Time.* The cooling time calculation results are utilized as a reference to select the holding time. For large products such as car coat racks, the length and width are far

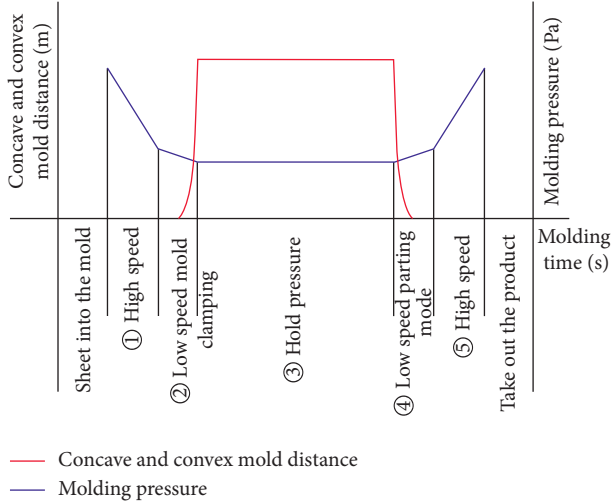


FIGURE 3: Speed variation graph during the mold clamping.

beyond their thickness, and they have two-dimensional characteristics. However, the heat is only transferred in the one-dimensional direction, that is, the thickness direction of the part. Therefore, the cooling of such products can be conducted as follows.

Heat transfer can be calculated from the following expression:

$$\frac{\partial T}{\partial \theta'} = k \frac{\partial^2 T}{\partial x^2}, \quad (33)$$

where T and k denote the average temperature when the sheet is demolded and the thermal diffusion coefficient of the sheet, respectively.

In order to separate the variables, the following equation is used:

$$\theta' = -\left(\frac{2}{\pi}\right)^2 \frac{x_1^2}{k} \ln \left[\frac{\pi(T - T_w)}{T_0 - T_w} \right], \quad (34)$$

$$k = \frac{\lambda}{\rho \cdot c_p},$$

where x_1 is half the thickness of the part, m ; T_w is the mold cavity temperature, $^{\circ}\text{C}$; T_0 is the sheet molding temperature, $^{\circ}\text{C}$; ρ is the density of the sheet, kg/m^3 ; λ is the thermal conductivity of the sheet, $\text{kW}/\text{m} \cdot ^{\circ}\text{C}$; and c_p is the specific heat capacity of the sheet, $\text{kJ}/\text{kg} \cdot ^{\circ}\text{C}$.

The process parameter values are shown in Table 4.

Substituting the abovementioned parameters into equation (34), the cooling time of the molding of the main body of the automobile coat rack is mathematically expressed as follows:

$$k = \frac{0.33 \times 10^{-3}}{1130 \times 1550 \times 10^{-3}} = 1.88 \times 10^{-7}, \quad (35)$$

$$t = -\left(\frac{2}{\pi}\right)^2 \frac{0.00225^2}{k} \ln \left[\frac{\pi(80 - 40)}{4(220 - 40)} \right] \approx 74 \text{ s}.$$

Combining with the previous pressure holding time, the pressure holding time is determined to be 80 s.

TABLE 4: The value of process parameters.

Parameter name	Value
The thickness of the main body of the car coat rack (mm)	4.5
The average temperature of the mold cavity wall T_w ($^{\circ}\text{C}$)	40
The molding temperature T_0 ($^{\circ}\text{C}$)	220
The average temperature when the sheet is demolded T ($^{\circ}\text{C}$)	80
The density of the sheet ρ (kg/m^3)	1130
The specific heat capacity of the sheet c_p ($\text{kJ}/\text{kg} \cdot ^{\circ}\text{C}$)	1.55
The thermal conductivity of the sheet λ ($\text{kW}/\text{m} \cdot ^{\circ}\text{C}$)	0.33×10^{-3}

2.5. Shrinkage Compensation Value. The molding shrinkage rate of the product is measured experimentally. The experimental process is as follows: the main model of the coat rack of the reference model is selected. Moreover, 20 pieces of GMT plates with a thickness of 4.5 mm glass fiber content of 30% and a needle-punched PET fabric of 1.5 mm thickness are selected. It should be indicated that, in the experiment, the sheet preheating time, the pressure holding time, molding pressure, and mold closing speed utilize the abovementioned parameters. When the mold is opened, the distance between the selected positioning points is measured, and each piece is averaged at one measurement in the length and width directions. After the product is left at room temperature for 24 hours, the selected positioning point is measured again, using equation (29). Finally, the average shrinkage rate of the composite two-layer structure of GMT sheet + needle-punched PET fabric is 0.354%.

2.6. Heat Transfer Calculation for the Cooling System of the Automobile Coat Rack Compression Molding Mold. The cooling system adopts the water cooling method, and a cooling water channel is laid on the mold surface to pass the cooling water. In this section, the design and calculation of the cooling system of the forming mold of the main body of the car coat rack are established.

2.6.1. The Total Heat of the Sheet into the Cavity. In a molding process, the total heat transferred from the sheet to the mold is mathematically expressed as follows:

$$Q_1 = C_p \cdot (T_0 - T) \cdot V \cdot \rho, \quad (36)$$

where T_0 and T denote the sheet molding temperature and the average temperature when the sheet is demolded, respectively. Moreover, ρ , c_p , and V are the density of the sheet, the specific heat capacity of the sheet, and the volume of the sheet, respectively. It is worth noting that the volume of the sheet is set to $1.4 \text{ m} \times 0.6 \text{ m} \times 0.0045 \text{ m}$.

2.6.2. Heat Taken away by the Cooling Water. The heat taken away by the mold cooling water in one press molding is expressed as follows:

$$Q_2 = Q_1 - Q_c - Q_R - Q_L, \quad (37)$$

where Q_c , Q_R , and Q_L denote the convection heat transfer from the mold to the air, the radiation heat transfer from the mold to the air, and the heat transfer from the mold to the hydraulic machine through the upper and lower mold bases, respectively.

Under normal circumstances, 90%–95% of the heat brought into the sheet can be taken away by the cooling water through the mold cooling channel. Therefore, during the design process, $Q_2 = Q_1$.

Since the main body of the car coat rack is a large thin-walled product, it can be designed according to 50% of the heat taken by the concave mold and the convex mold; then,

$$Q_{2a} = Q_{2t} = 0.5Q_2. \quad (38)$$

2.6.3. Cooling Water Hole Diameter. The volume flow of the cooling water can be calculated according to equation (39) during the molding process of the die and the die of the die in one molding process:

$$\begin{cases} V_{2a} = \frac{Q_{2a}}{\rho_1 c_1 (\theta_1 - \theta_2) \cdot t}, \\ V_{2t} = \frac{Q_{2t}}{\rho_1 c_1 (\theta_1 - \theta_2) \cdot t}, \end{cases} \quad (39)$$

where θ_1 and θ_2 are the inlet and outlet temperatures of the mold cooling water, respectively. It should be indicated that the temperature difference should not be too large and its maximum value should not exceed 5°C. Moreover, V ($\text{m}^3 \cdot \text{min}^{-1}$) and ρ_1 (kg/m^3) denote the volume flow of cooling water and the density of water, respectively. Furthermore, c_1 ($\text{kJ}/\text{kg} \cdot ^\circ\text{C}$) and t (min) are the specific heat capacity of water and the cooling time of one molding, respectively.

The density of water is $1000 \text{ kg}/\text{m}^3$, and the specific heat capacity of water is $4.2 \text{ kJ}/\text{kg} \cdot ^\circ\text{C}$, which is calculated according to equations (36) and (38):

$$\begin{aligned} V_{2a} = V_{2t} &= \frac{0.5Q_2}{\rho_1 c_1 (\theta_1 - \theta_2) \cdot t} = \frac{0.5 \cdot C_p \cdot (T_0 - T) \cdot V \cdot \rho}{\rho_1 c_1 (\theta_1 - \theta_2) \cdot t} \\ &= 16.275 \text{ m}^3/\text{min}. \end{aligned} \quad (40)$$

According to the correlation between the cooling water pipe volume flow and the pipe diameter, the cooling water pipe diameter is determined as $D = 27 \text{ mm}$.

The correlation between the distance P of the cooling water pipe, the distance H from the profile, and the diameter D of the channel is $P = (3 \sim 5) D$, $H = (1 \sim 2) D$; from $D = 27 \text{ mm}$, take the pipe distance $P = 80 \text{ mm}$, $H = 30 \text{ mm}$.

3. Simulation of the Molding Process

In the present study, the Ls-Dyna finite element program is used to simulate the molding process of the main body of the car coat rack to obtain the nodal force information of the

stress concentration area of the mold during the molding process [14]. Therefore, the boundary conditions for the topological optimization of the convex and concave mold are obtained. Moreover, the design of the mold is optimized.

3.1. The Main Influencing Factors of the Modeling Process.

The molding process is a complicated nonlinear challenging process. The influencing factors in this process include the compression molding of the sheet, the elastic deformation of the mold under high temperature and high pressure, and the frictional contact between the mold and the sheet during the mold clamping process; it is a complex finite element problem of thermal and mechanical coupling [15].

3.1.1. Grid Division. The density distribution of the grid is one of the important factors that affect the calculation accuracy [16]. In order to simplify the meshing and improve the quality and solution rate of meshing, the CATIA software is utilized to simplify the model in the early stage. The convex and concave molds use sweeping meshing, SOLID168 elements are used to mesh, and the length direction is divided into 60. It should be indicated that the width direction is divided into 3 equal parts with a total of 942,000 units. The sheet adopts shell163 thin shell unit and the sheet grid is a regular quadrilateral unit with 15000 units. Moreover, the unit has 11 different algorithms. In the present study, the Belytschko – Tsay algorithm is used because its calculation speed is high. Figure 4 illustrates the grid division diagram.

3.1.2. Heat Transfer Model Settings. According to the characteristics of the molding process, the following two heat transfer methods are described:

(1) Radiation and air-cooling heat exchange

Owing to the small proportion of the air-cooled heat transfer, air-cooling and radiation can be written as a unified heat transfer equation [17]:

$$q = (h_1 + h_2)(T - T_0), \quad (41)$$

where q is the heat flux, density, $\text{J}/\text{m}^2 \cdot \text{s}$. Moreover, h_1 and h_2 denote the convective heat transfer coefficient, $\text{W}/\text{m}^2 \cdot \text{K}$, and the radiant heat transfer coefficient, $\text{W}/\text{m}^2 \cdot \text{K}$, respectively.

$$h_2 = \varepsilon \delta (T + T_0)(T^2 - T_0^2), \quad (42)$$

where ε and δ are the blackness coefficient and the Boltzmann constant, J/K , respectively. Moreover, T and T_0 are the surface temperature of the sheet, $^\circ\text{C}$, and the ambient temperature, $^\circ\text{C}$, respectively.

Table 5 presents the specific values.

(2) Contact heat transfer

A contact heat transfer exists between the sheet and the mold, and calculation of the contact heat transfer

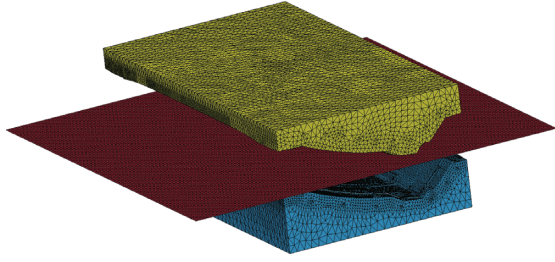


FIGURE 4: Grid division diagram.

TABLE 5: Heat transfer constant.

$h_1 + h_2$	ϵ	δ	T	T_0
200 W/(m ² ·K)	0.6	5.672×10^{-8} J/K	220°C	20°C

is challenging. Empirical equation [18] (43) is used in this regard:

$$q = h_{\text{cond}}(T - T_1). \quad (43)$$

In the abovementioned equation, $h_{\text{cond}} = K/l_{\text{gap}}$, where $K = 10$ and l_{gap} is the contact gap between the workpiece and the mold, which is automatically calculated in the LS-DYNA program, and its unit is mm. Moreover, T_1 denotes the mold cavity temperature, °C.

3.1.3. Contact and Friction Settings. The keyword *CONTACT_FORMING_ONE_WAY_SURFACE_TO_SURFACE_THERMAL defines the contact method of the compression molding, and FORMING_ONE_WAY is the type of contact specifically used for molding. It should be indicated that the penalty function algorithm is used to calculate the contact interface force. Since LS-DYNA is originally used for the collision analysis, if it is used for the forming analysis, the default parameter settings should be modified [19]. In the present study, the penalty function stiffness factor SLSFAC is modified to 0.1.

In the compression molding process, there is friction between the mold and the sheet. Therefore, the friction coefficient should be determined. In LS-DYNA, the friction force is calculated by the Coulomb model. In this study, the average friction coefficient is 0.1.

3.1.4. Hourglass Control. In order to verify the validity of the calculation result, the ratio of the hourglass energy to total energy should be less than 10%. On the other hand, the hourglass control coefficient cannot be too large. When the hourglass control coefficient is greater than 0.15, the calculation will be unstable. Therefore, the hourglass control sets IHQ=4, and the hourglass energy coefficient is set to QH=0.1.

3.1.5. Energy Dissipation Control. In the numerical simulation of the compression molding, the main reference index to determine the accuracy of the simulation result is the

change in energy. The control of energy is set by the keyword *CONTROL_ENERGY. In this study, set HGEN=2, RWEN=2, SLNTEN=2, and RYLEN=2. The purpose of the abovementioned setting is to consider various energy dissipations in the energy balance.

3.1.6. Control of the Time Step. In the LS-DYNA software, the convergence of the time integration algorithm is conditional, and it is stable only when the time step Δt is less than the critical time step, which is mathematically expressed as

$$\Delta t < \frac{\Delta l}{c + \dot{x}}, \quad (44)$$

$$c = \sqrt{\frac{E}{(1 - \nu^2) \cdot \rho}},$$

where Δl , c , and x denote the characteristic length of the element, m , the sound velocity of the material, m/s, and the velocity of the node, m/s, respectively.

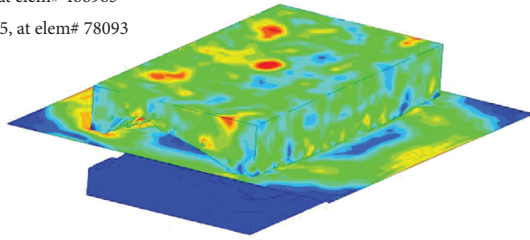
In the compression molding simulation, as time passes, the deformation increases. Then, Δt quickly decreases, indicating that the integration algorithm divergence interrupts the simulation. In order to avoid this phenomenon, the mass scaling technique is used to set a duration value Δt_{sz} through the keyword *CONTROL_TIMESTEP. In the simulation, if $\Delta t < \Delta t_{sz}$, the program automatically increases the density of the structural material and the time step size. In the present study, Δt_{sz} is set as 0.0000025, time step size scaling factor TSSFAC=0.9, and DTINIT=0. Moreover, the initial step size is set by the program.

3.2. Setting of Materials and Boundary Conditions

- (1) Material: the sheet material is selected from the constitutive equation of the thermoplastic material. The thickness of the sheet is defined by the actual thickness of the part. The material of the convex and concave mold is 45#. The sheet is made of PP-based GMT composite material with a glass fiber content of 30%.
- (2) Initial boundary conditions: the initial process parameters of the automobile coat rack compression molding are set as follows. Moreover, the punch is set to fix the lower table of the hydraulic press, and the concave mold should be closed under the pressure of the press. The molding pressure is set to 13 MPa, the mold closing speed after the upper mold contacts the sheet is 8 mm/s, and the initial temperature of the sheet is 220°C. The mold temperature is 40°C, the cooling channel water temperature is 20°C, and the pressure holding time is 80 s.

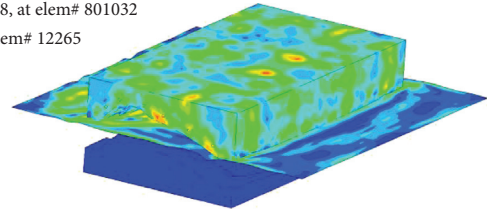
3.3. Finite Element Numerical Calculation Results. Figures 5–7 show the numerical simulation results in the molding process, which are obtained after the software calculation.

Time = 1.2199
 Contours of effective stress ($v-m$)
 Reference shell surface
 Min = 0, at elem# 466963
 Max = 345, at elem# 78093



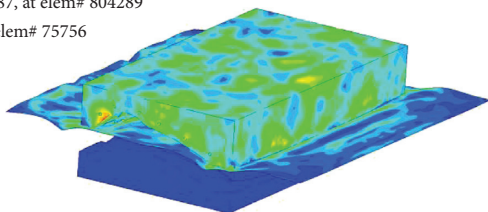
(a)

Time = 2.44
 Contours of effective stress ($v-m$)
 Reference shell surface
 Min = 0.0906078, at elem# 801032
 Max = 345, at elem# 12265



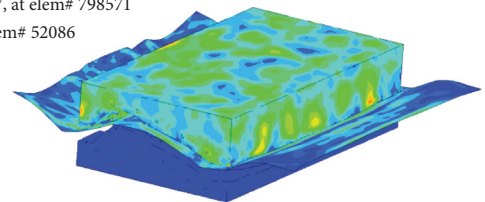
(b)

Time = 3.6599
 Contours of effective stress ($v-m$)
 Reference shell surface
 Min = 0.0779287, at elem# 804289
 Max = 345, at elem# 75756



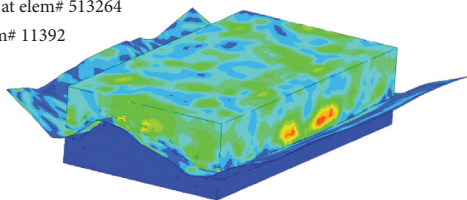
(c)

Time = 5.7947
 Contours of effective stress ($v-m$)
 Reference shell surface
 Min = 0.0725777, at elem# 798571
 Max = 345, at elem# 52086



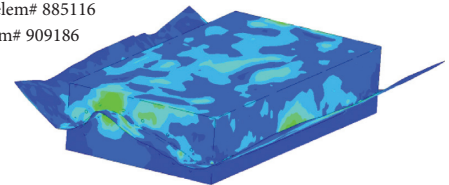
(d)

Time = 7.9299
 Contours of effective stress ($v-m$)
 Reference shell surface
 Min = 0.0533153, at elem# 513264
 Max = 345, at elem# 11392



(e)

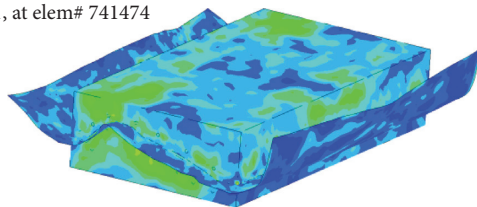
Time = 9.4549
 Contours of effective stress ($v-m$)
 Reference shell surface
 Min = 0.0829849, at elem# 885116
 Max = 711.588, at elem# 909186



(f)

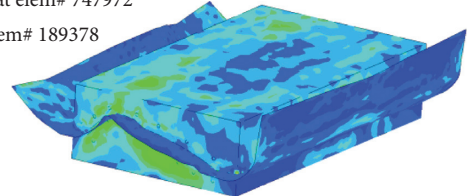
FIGURE 5: The equivalent stress diagram of the forming process.

Time = 14.335
 Contours of effective stress ($v-m$)
 Reference shell surface
 Min = 3.63642, at elem# 876981
 Max = 345.001, at elem# 741474



(a)

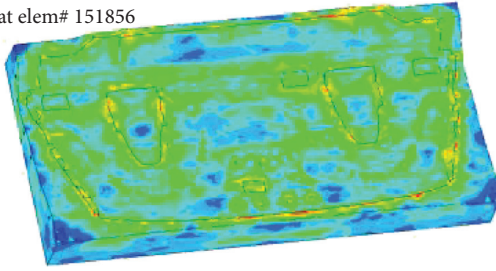
Time = 28.365
 Contours of effective stress ($v-m$)
 Reference shell surface
 Min = 1.06772, at elem# 747972
 Max = 345, at elem# 189378



(b)

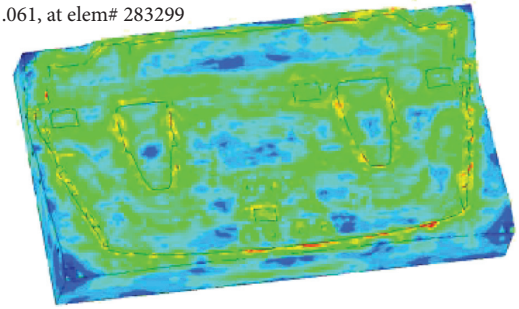
FIGURE 6: Continued.

Time = 19.215
Contours of effective stress ($v-m$)
Reference shell surface
Min = 2.89149, at elem# 13894
Max = 345, at elem# 151856



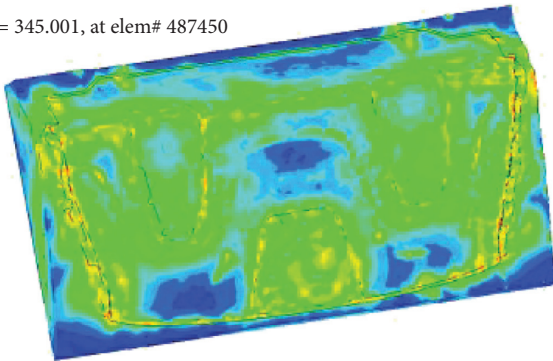
(c)

Time = 43.005
Contours of effective stress ($v-m$)
Reference shell surface
Min = 2.45393, at elem# 13429
Max = 341.061, at elem# 283299



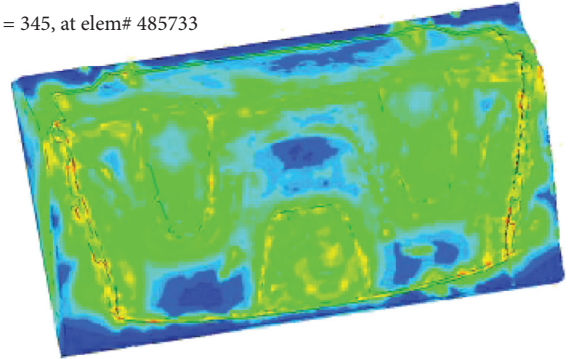
(d)

Time = 52.155
Contours of effective stress ($v-m$)
Reference shell surface
Min = 0.766231, at elem# 536714
Max = 345.001, at elem# 487450



(e)

Time = 57.34
Contours of effective stress ($v-m$)
Reference shell surface
Min = 0.527726, at elem# 536714
Max = 345, at elem# 485733



(f)

FIGURE 6: Cloud diagram of stress changes during the packing process.

Time = 9.76



(a)

Time = 9.76



(b)

FIGURE 7: The main body shape of the car coat rack.

3.3.1. *Equivalent Stress during Forming.* The simulation results of the equivalent stress during the molding process show that, during the molding process of the main body of the automobile coat rack, the stress concentration area is located at the outer contour of the mold and the slope is steeper.

3.3.2. *Equivalent Stress during the Holding Pressure.* The simulation results of the equivalent stress during the packing process show that the node displacement is the largest when the packing time is 11 s. As the packing time passes, the mold temperature decreases and the deformation gradually decreases too. After 64 s, it remains unchanged until the end of the packing process.

3.3.3. *Appearance of the Molding Process.* The above-mentioned simulation results show that the nodal force information of the mold during the compression molding process is obtained. Therefore, the load mapping is used as the boundary condition for the next topology optimization.

4. Optimized Mold Design

Currently, the lightweight design of molds is the development direction of mold optimization [20]. Based on the empirical design, CAE tools are used to perform mold structure analysis and optimization design before processing. Aiming at the problem of excessive quality of molds and due to the current empirical design of compression molding dies for automotive interior parts, in the present study, a lightweight design process and method is proposed for compression molding dies.

4.1. *Lightweight Design Process of the Mold Structure.* According to the numerical simulation method for the molding process of automotive interior parts and the topology optimization theory of the variable density method [21], a lightweight design method for the mold structure of interior parts molding is proposed.

- (1) According to the mold design requirements, the structure of the compression molding convex and concave mold is designed in accordance with the traditional mold design guidelines.
- (2) With the help of the LS-DYNA finite element program, the compression molding process of the main body of the coat rack is numerically simulated to obtain the force information of the convex and concave mold nodes in the actual working conditions.
- (3) Load mapping is used to construct convex and concave boundary conditions of die structure optimization.
- (4) The improvement space of the mold structure design is clarified, and the design area and nondesign area are determined.

- (5) Based on the OptiStruct, the topological optimization of the convex-concave structure is iteratively solved.
- (6) The final shape is optimized according to the topology of the convex and concave mold structure, and the three-dimensional software is utilized to redesign the mold structure.
- (7) According to the redesigned mold structure for mold processing and manufacturing.

4.2. *OptiStruct-Based Optimization Design of the Mold Topology.* OptiStruct uses LS-DYNA for preprocessing and definition of structural optimization problems. After completing the finite element modeling in LS-DYNA, the optimization definition panel is used to define optimization variables, constraints and goals, and optimization parameters. Then, OptiStruct is submitted for structural analysis and optimization. Figure 8 shows the OptiStruct structure optimization design flowchart [22].

4.2.1. *The Establishment of the Topological Optimization Model of the Mold Convex and Concave Mold Structure.* In the optimization process of the convex and concave dies, the problem of the mass minimization can be equated to the problem of the volume minimization. The real working conditions of the convex and concave molds are analyzed. Moreover, based on the solid isotropic material penalty (SIMP) method and according to the numerical simulation calculation results of the compression molding, the maximum displacement of the nodes in the stress concentration area is used as the constraint condition. Furthermore, the material element density is used as the design variable. The minimum volume of the convex-concave structure is the SIMP optimization model [23], and the density penalty factor P is set to 3. The model is formulas (45) and (46),

$$\begin{cases} E_e = \rho_e^P \cdot E_0, \\ 0 < \rho_{\min} \leq \rho_e \leq 1, \end{cases} \quad (45)$$

$$\begin{cases} \min : V \\ \text{subject to: } KU = F, \\ 0 < \rho_{\min} \leq \rho_e \leq 1, \\ U_j \leq U_j^*, \end{cases} \quad (46)$$

where ρ_i are V denote the design variable for the topology optimization with the variable density method and the overall structure volume, respectively. Moreover, U , K , and F are the overall displacement column vector, the overall structure stiffness matrix, and the external load vector, respectively.

4.2.2. *Topological Optimization of Convex and Concave Dies Structure.* According to the analysis of the real working conditions of the convex and concave molds, based on the SIMP material interpolation optimization model of the convex and concave molds, OptiStruct is used to solve.

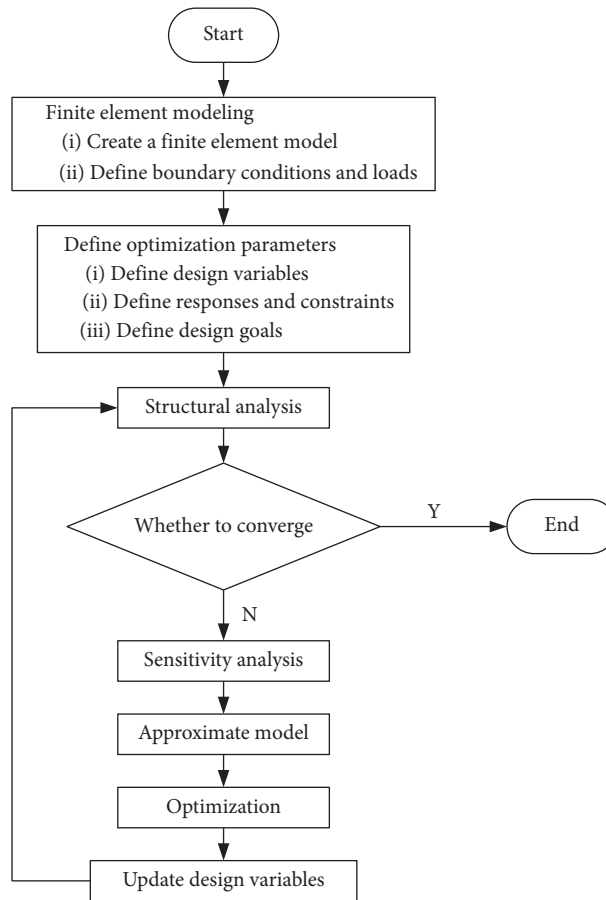


FIGURE 8: Topology optimization flowchart.

OptiStruct describes the three elements of the optimal design through different types of information cards.

(1) Set optimization variables

In the topology optimization of convex and concave molds, the tighter the optimized cell density is, the more important the material is. Moreover, this should be retained when redesigning the convex and concave mold structure [24]. As it tends to 0, it can be determined according to the analysis of the convex and concave structure. Therefore, the design area and nondesign area should be selected when designing optimization variables.

(2) Define optimization goals and constraints

Through the numerical simulation of the molding process of the main body of the car coat rack, the node number of the stress concentration and deformation of the mold during the molding process are obtained. Moreover, the number and displacement values with time change are obtained by applying LS-Prepositi postprocessing. Export as a .txt file, and define the corresponding node displacement load in Hyperworks according to these results, in order to optimize the mold design. Figure 9 shows the nodal displacement results derived from the concave and convex molds.

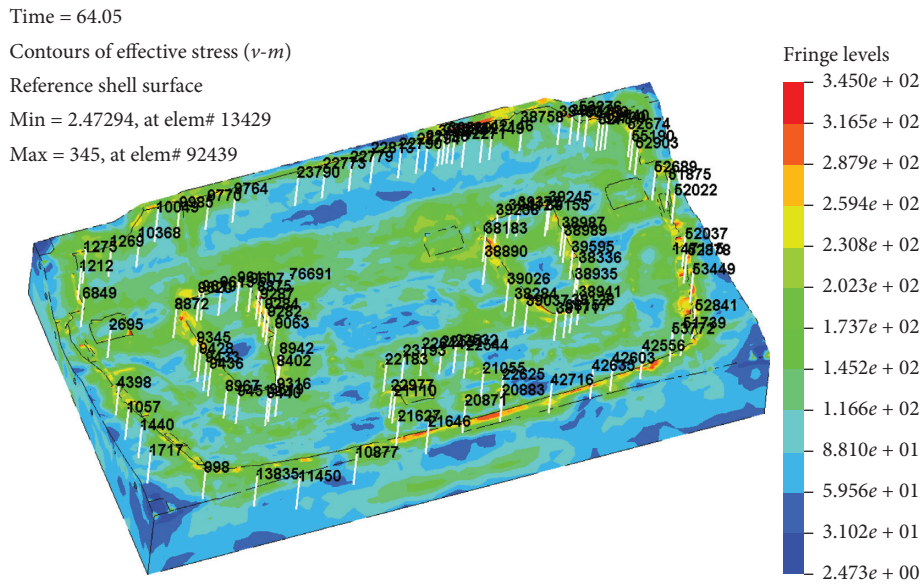
Figures 10 and 11 show that boundary conditions are applied and the optimization area is determined. The analysis of the mold structure shows that, in the optimized design, the concave and convex model surfaces and the location of the cooling water channel will remain unchanged. Moreover, the design area and the nondesign area are divided according to this, and the pink area of the concave mold is determined as the nondesign area. Furthermore, the blue part is the design area, the light color of the punch is the nondesign area, and the dark color is the design area. The boundary conditions are as described above.

(3) Trial calculation

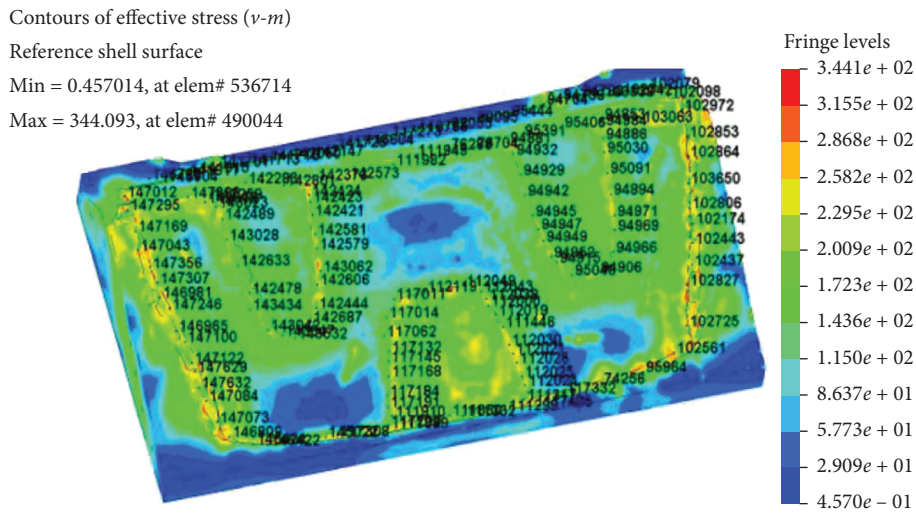
The preliminary trial calculation is passed, as shown in Figure 12, through the topology optimization algorithm and through the iterative calculation of this process to find the best path for load transfer, to obtain the optimal solution for topology optimization, and thus to obtain the best distribution of convex and concave mold materials.

(4) Topology optimization results

After the lamination calculation, the topological results of the die and punch of the die are obtained. Figure 13 illustrates a topographic cloud image with a density threshold of 0.2.



(a)



(b)

FIGURE 9: Derived node displacement result graph. (a) Nodal displacement results derived from the die. (b) Nozzle displacement results derived from punch.

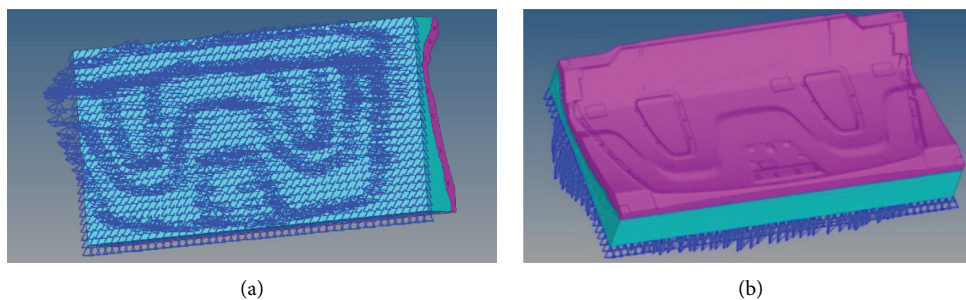


FIGURE 10: Boundary condition diagram of the upper die definition. (a) The upper die defines the boundary conditions. (b) The upper die defines the boundary conditions.

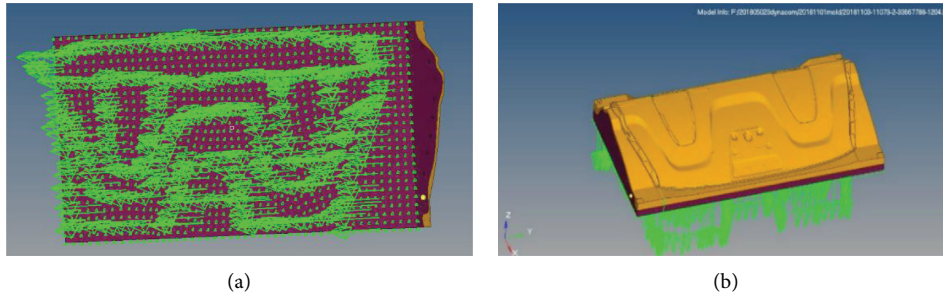
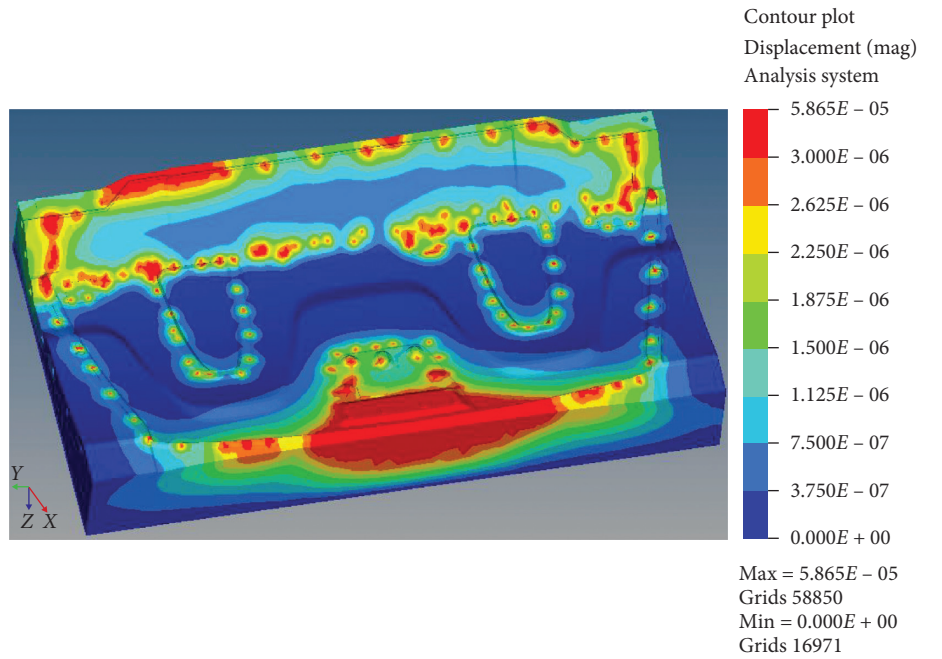
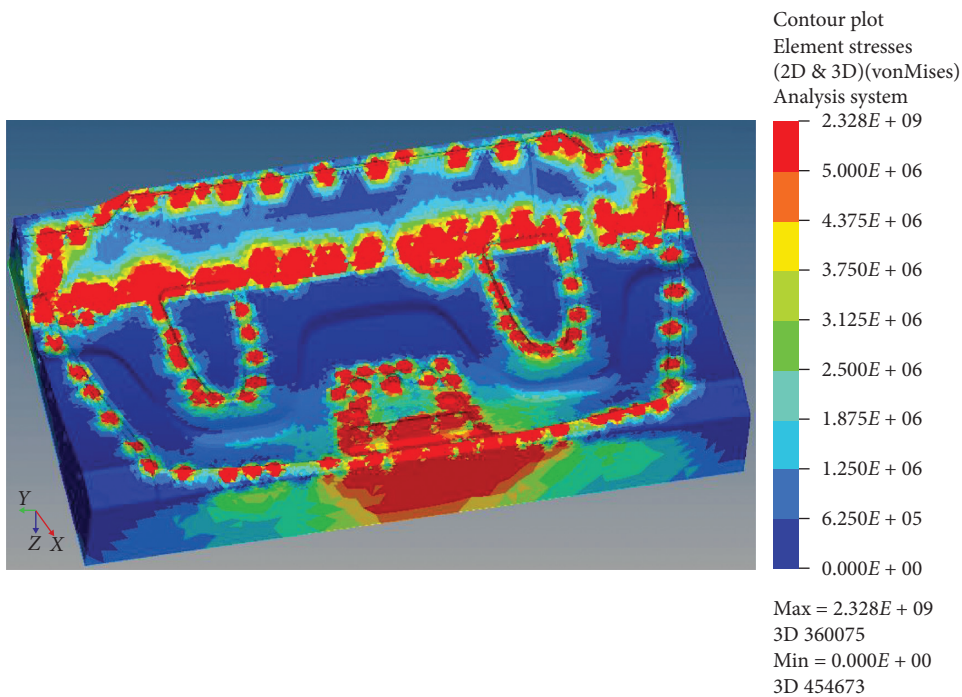


FIGURE 11: Boundary condition diagram of the lower die definition. (a) The lower die defines the boundary conditions. (b) The lower die defines the boundary conditions.



(a)



(b)

FIGURE 12: Continued.

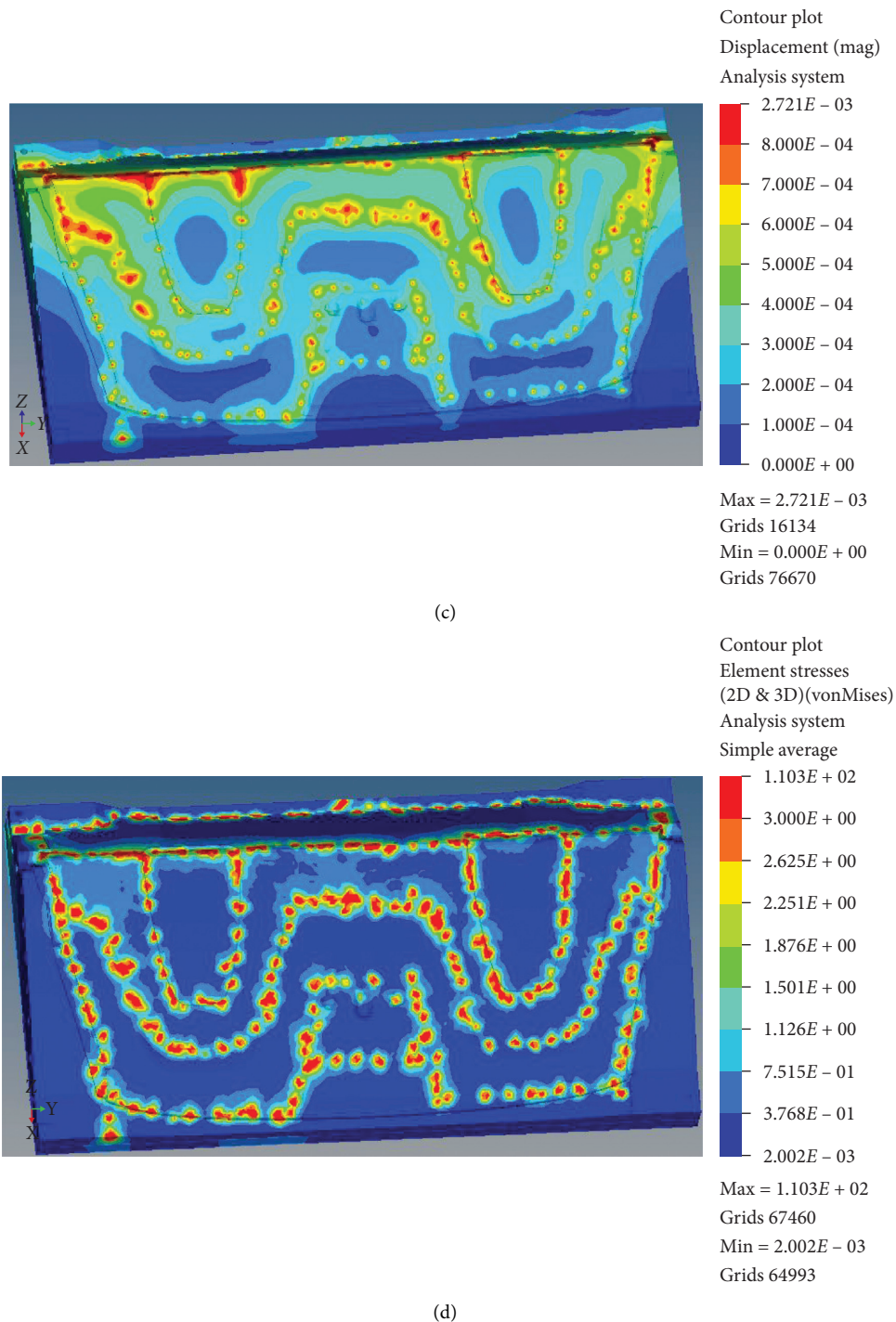
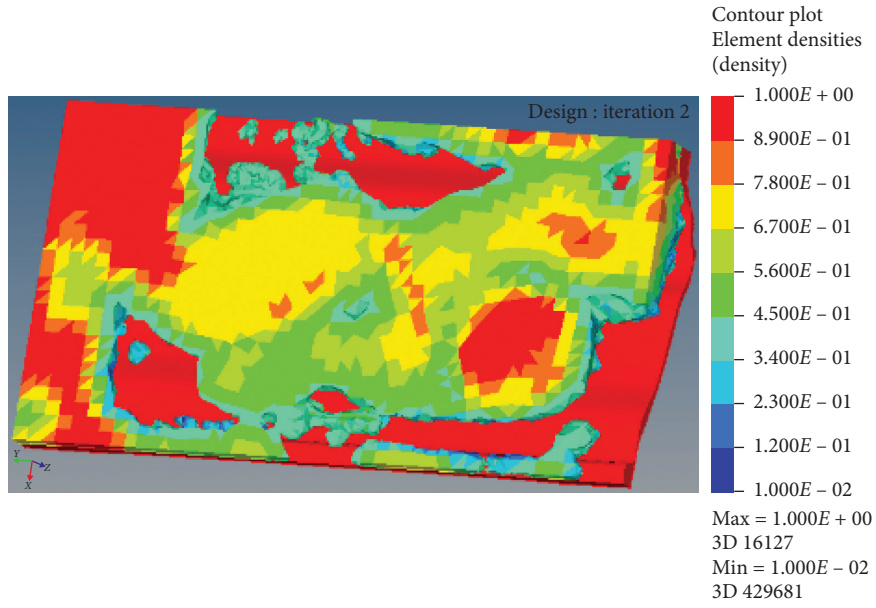


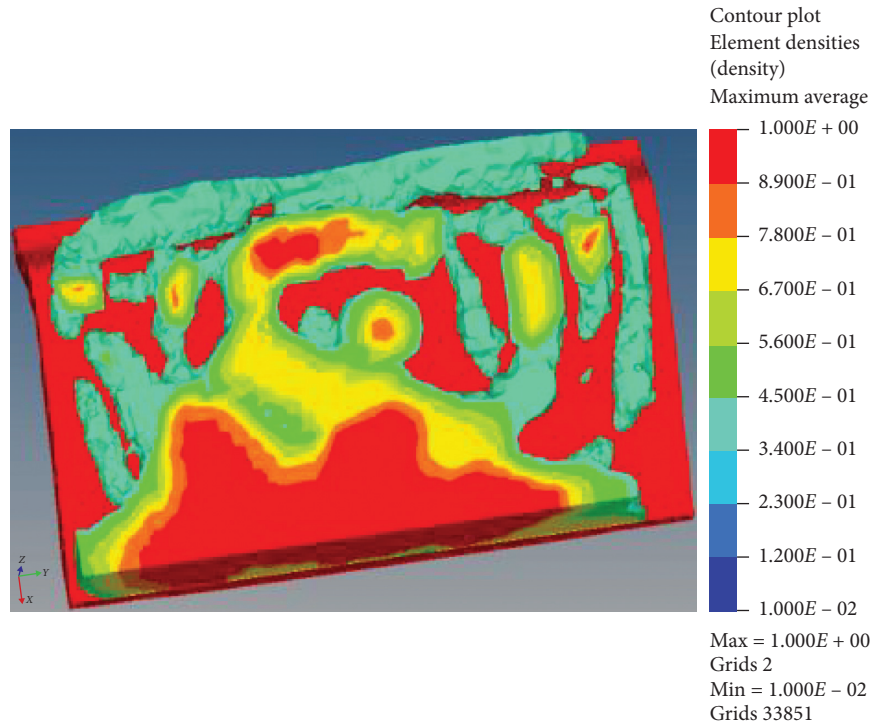
FIGURE 12: Preliminary calculation results. (a) Calculation result of upper die displacement. (b) Calculation result of upper mold equivalent stress. (c) Calculation result of lower die displacement. (d) Calculation result of equivalent stress of lower die.

4.2.3. Redesign of the Convex and Concave Mold Structure.
According to the topological optimization of the optimal path of the material distribution, the topological shape of the model can be obtained. Through the OptiStruc-OSSmooth program, the IGES general CAD file is exported and fed back to CATIA. The CATIA software is used to reverse the convex and concave mold structure to obtain the topology. Figure 14 presents the optimized convex-concave structure.

By optimizing the topology of the convex and concave mold structure of the automobile coat rack compression mold, the optimized design results of the convex and concave mold structures of the automobile coat rack mold are obtained. After the CATIA volume measurement, the optimized design of the convex and concave mold can meet the strength and on the premise of stiffness, weight loss was 15.6%.



(a)



(b)

FIGURE 13: Topology optimization morphology. (a) Top mold topography. (b) Topology of the lower die.

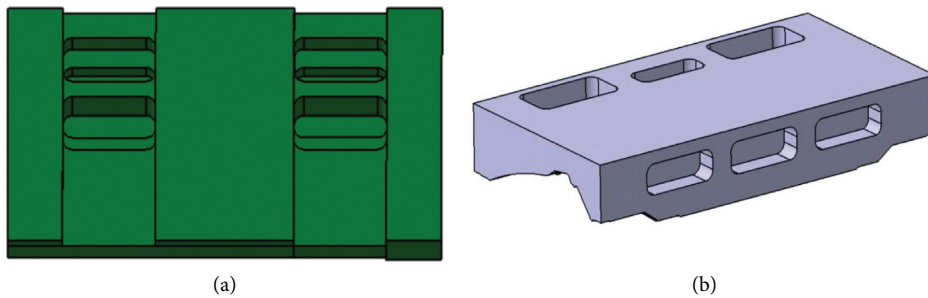


FIGURE 14: Optimal design of the convex and concave die. (a) Punch optimization design results. (b) Die optimization design results.

5. Conclusion

The following conclusions are drawn from the present study:

- (1) A mechanical model of the composite two-layer structure of the main body of the car coat rack is established. By solving the model, it is found that the main factors affecting the mechanical properties of the composite two-layer structure are the thickness of the PP glass fiber sheet and the content of glass fiber. The process parameters of the molding of the main body of the hat rack are prepared: the sheet preheating is performed by convection with hot air; the temperature of the hot air is 250°C; the preheating time is 110 s; the molding pressure is 13 MPa; and the holding time is 80 s. Using the experimental method, the average shrinkage rate of the material is calculated to be 0.354%, and the shrinkage rate of the solidification and cooling of the product is compensated by error compensation.
- (2) Aiming at the current empirical design of mold designers, a lightweight design process for molding molds for interior parts is proposed. The LS-DYNA finite element program is used to simulate the molding process to obtain the actual working conditions. Under the stress concentration area of the mold, the nodal force information with large deformation is obtained. Therefore, the load mapping is used as the boundary condition of the next mold topology optimization.
- (3) A mathematical model for SIMP material interpolation optimization of the male and female molds is established. Based on the variable density method, OptiStruct software is used to design the male and female molds of the main body of the automobile coat rack compression mold. The weight of the mold is reduced by 15.6%, while ensuring the structural rigidity and strength of the mold.

Data Availability

The data used to support the findings of this study are included within the article.

Disclosure

This paper is part of the major projects of the “The University Synergy Innovation Program of Anhui Province (GXXT-2019-004) and the project of the “Teaching Research Project of Anhui Education Department (2019jyxm0229).”

Conflicts of Interest

The authors declare that they have no conflicts of interest.

References

- [1] J. Zheng, Y. Wei, and Z. Wei, “Rear window trim stiffness research on hatchback vehicle,” *Industrial Technology Innovation*, vol. 3, no. 3, pp. 510–513, 2016.
- [2] X. Guo, B. Ke, X. Liu, and D. Gong, “Reuse of waste PP glass-fiber composite felt,” *Shanghai Textile Science & Technology*, vol. 42, no. 4, pp. 18–19, 2014.
- [3] T. Miao, Y. Feng, and R. Zhang, “Multicomponent fibre composition process effect the properties of automotive coatrack,” *Journal of Wuhan Textile University*, vol. 30, no. 3, pp. 30–34, 2017.
- [4] R. Yu, *Research on Key Technologies of Nonwoven Fabric Hot Molding*, Soochow University, Suzhou, China, 2016.
- [5] C. Shao, *Research on Compression Molding Technology of Hatchback Door Plate with Glass Mat Reinforced Thermoplastics*, Jilin University, Changchun, China, 2015.
- [6] E. Demirci and A. R. Yildiz, “An investigation of the crash performance of magnesium, aluminum and advanced high strength steels and different cross-sections for vehicle thin walled energy absorbers,” *Materials Testing*, vol. 60, no. 7–8, pp. 661–668, 2018.
- [7] M. Li, P. Xue, M. Jia, and K. Chen, “Research development of processing technology of fiber-reinforced thermoplastic resin composites,” *China Plastics Industry*, vol. 44, no. 11, pp. 5–11, 2016.
- [8] J. Wang, C.-y. Fu, Y. Yu, J. Yanagimoto, and W. Zhu, “Effect of temperature on formability of glass mat reinforced thermoplastic sheets with ductile dummy sheets,” *Journal of Central South University*, vol. 26, no. 4, pp. 779–786, 2019.
- [9] M. Fellah, K. Draiche, H. M. S. Ahmed et al., “A novel refined shear deformation theory for the buckling analysis of thick isotropic plates,” *Structural Engineering and Mechanics*, vol. 69, no. 3, pp. 335–345, 2019.
- [10] J. Hartikainen, M. Lindner, T. Harmia, and K. Friedrich, “Mechanical properties of polypropylene composites reinforced with long glass fibres and mineral fillers,” *Plastics, Rubber and Composites*, vol. 33, no. 2–3, pp. 77–84, 2004.
- [11] Y. Wang, Z. Zhu, L. Tang et al., “Research on the molding design and optimization of the molding process parameters of the automobile trunk trim panel,” *Advances in Materials Science and Engineering*, vol. 2020, Article ID 5629717, 19 pages, 2020.
- [12] Y. Zhu, H. Lu, and G. Dai, “Study on preheating technology for GMT thermoplastic sheet,” *China Plastics Industry*, vol. 3, pp. 35–37, 2000.
- [13] M. J. Song, K. Kwon-Hee, and H. Seok-Kwan, “Simulation-based optimization of cure cycle of large area compression molding for LED silicone lens,” *Advances in Materials Science and Engineering*, vol. 2015, Article ID 573076, 11 pages, 2015.
- [14] E. Demirci and A. R. Yildiz, “An experimental and numerical investigation of the effects of geometry and spot welds on the crashworthiness of vehicle thin-walled structures,” *Materials Testing*, vol. 60, no. 6, pp. 553–561, 2018.
- [15] V. Goodship, I. Brzeski, B. M. Wood et al., “Gas-assisted compression moulding of recycled GMT: effect of gas injection parameters,” *Journal of Materials Processing Technology*, vol. 214, no. 3, pp. 515–523, 2014.
- [16] H. Li, *Research on Topology Optimization Methods of Continuum Structure Based on Variable Density Method*, Huazhong University of Science and Technology, Wuhan, China, 2011.
- [17] S. V. Patankar, *Numerical Heat Transfer and Fluid Flow*, CRC Press, Boca Raton, FL, USA, 1980.
- [18] LS-DYNA, *Keyword User’s Manual, Material Models, II*, Livermore Software Technology Corporation (LSTC), Livermore, CA, USA, 2014.
- [19] M. Stolpe and K. Svanberg, “An alternative interpolation scheme for minimum compliance topology optimization,”

- Structural and Multidisciplinary Optimization*, vol. 22, no. 2, pp. 116–124, 2001.
- [20] D. Yan, W. Liu, G. Huang, and S. Xu, “Design study for composites autoclave forming mould,” *Aeronautical Manufacturing Technology*, vol. 7, pp. 49–52, 2012.
- [21] B. S. Lazarov, F. Wang, and O. Sigmund, “Length scale and manufacturability in density-based topology optimization,” *Archive of Applied Mechanics*, vol. 86, no. 1-2, pp. 189–218, 2016.
- [22] O. Sigmund and K. Maute, “Topology optimization approaches,” *Structural and Multidisciplinary Optimization*, vol. 48, no. 6, pp. 1031–1055, 2013.
- [23] A. Rietz, “Sufficiency of a finite exponent in SIMP (power law) methods,” *Structural and Multidisciplinary Optimization*, vol. 21, no. 2, pp. 159–163, 2001.
- [24] Q. Liu and X. Hou, “Structure topology optimization design of vehicle parts based on HyperMesh/OptiStruct,” *Equipment Manufacturing Technology*, vol. 10, pp. 42–44, 2008.

Research Article

Thermal Analysis and Structural Optimization of High-Efficiency Fuel Submersible Hot Water Machine

Zhaozhe Zhu , Youmin Wang , and Yingshuai Zhang 

School of Mechanical and Automotive Engineering, Anhui Polytechnic University, Wuhu, Anhui 241000, China

Correspondence should be addressed to Zhaozhe Zhu; 2190130110@stu.ahpu.edu.cn

Received 26 January 2021; Revised 5 March 2021; Accepted 9 March 2021; Published 25 March 2021

Academic Editor: Ashwini Kumar

Copyright © 2021 Zhaozhe Zhu et al. This is an open access article distributed under the Creative Commons Attribution License, which permits unrestricted use, distribution, and reproduction in any medium, provided the original work is properly cited.

Based on the oil quality of diesel oil, the thermal efficiency and fuel consumption of the fuel-burning submersible hot water machine were calculated. The structure of the fuel-burning submersible hot water machine was designed. The heat transfer calculation of the flame tube and convection surface of the high-efficiency fuel submersible hot water machine was carried out, and the overall heat balance of the system was checked. ANSYS was used to analyze and study the mechanical and thermodynamic properties of the fuel-based submersible hot water machine, and the simulation results were compared with the theoretical calculation results. The thermal field of the flame tube and the threaded tube was simulated, and the influence of the temperature field on the flame tube was analyzed. The changes in the total deformation and strength of the flame tube under the thermal structure coupling were studied. The thermal efficiency of oil-fired submersible hot water machine was studied, and the relevant factors affecting the thermal efficiency of oil-fired submersible hot water machine were put forward. The main factors affecting thermal efficiency were analyzed and mathematically modeled. The air supply model and the convective heat transfer model of the threaded tube were established. The main parameters that affected the thermal efficiency of the threaded tube were optimized. In the end, the design scheme of a high-efficiency fuel-type submersible hot water machine was obtained.

1. Introduction

Hot water machines have been widely used in various fields, especially in areas where the demand for hot water is relatively large. There are many types of hot water machines, and the application types of hot water machines are also different in different working locations and environments. For example, in residential areas, the residents use gas-fired hot water machines; in school bathrooms, electric heating hot water machines are often used; in some areas abroad, hot water machines using geothermal energy have appeared [1, 2]. In some engineering fields, such as the diving industry, electric-heated diving hot water machines have appeared. Researchers at home and abroad have done some research studies on different types of hot water machines to varying degrees. However, there has been a lot of research on related water boiler [3–5]. But there are very few research studies on oil-fired submersible hot water machines at home and abroad. Johnson and Beausoleil-Morrison [6] designed a

model for the performance prediction of gas tankless water heaters and calibrated and verified the model, but they did not study and optimize the mechanical properties of the water heater structure, nor did they conduct in-depth thermal research on the hot water machine. Lenhard and Malcho [7] established a mathematical model for heating hot water by an indirect heating water heater and made a CFD simulation of the established mathematical model. Based on the simulation results, the parameters of the indirect heating hot water machine were optimized. But they did not research and optimize the structure and mechanical properties of indirect heating hot water machines. Liu et al. [8] proposed a high-throughput screening method (HTS) based on machine learning to design and screen the best combination of external characteristics of water-in-glass evacuated tube solar water heaters (WGET-SWHs) with high heat collection rate, but there is no research on the relationship between the structure and heat of the hot water machines. This paper not only researches and optimizes the structure and mechanical

performance of the hot water machine, but also conducts in-depth thermal research on the hot water machine and optimizes the thermal efficiency of the submersible hot water machine by establishing a mathematical model.

2. Analysis and Calculation of Original Data and Fuel Characteristics of Oil-Fired Submersible Hot Water Machine

2.1. The Original Data of the Fuel-Type Diving Hot Water Machine. This article comes from a diving equipment factory. According to the actual needs of the project and the previous experience in the development of electric-heated submersible hot water machines, the author finally plans to develop an oil-fired submersible hot water machine with 0# diesel as fuel. The original data of the fuel oil type submersible water heater to be developed by a diving equipment factory are as follows: the fuel is 0# diesel, the input liquid is seawater and fresh water, the water input pressure is 3.4–10 bar, the input flow is at least 45 L/min, the output pressure is the highest 68 bar, and the output flow is about 38 L/min. The volume of the water heater is about 250 L, the maximum temperature rise is 60°C, and the temperature difference control range is $\pm 1.5^\circ\text{C}$.

2.2. Fuel Characteristic Analysis and Calculation. The high-efficiency fuel oil submersible hot water machine uses 0# diesel as fuel. According to the percentage of each component of 0# diesel, the theoretical air volume V^0 consumed when 1 kg of 0# diesel is completely burned under standard conditions can be calculated. And the volume of produced CO_2 , SO_2 , N_2 , H_2O , and triatomic gas RO_2 and the volume of flue gas V_y are shown in Table 1 [9].

2.3. Enthalpy of Fuel Flue Gas. When 0# diesel and air are sent to the water heater for combustion, the heat carried is composed of two parts: one is the enthalpy brought by 0# diesel and air and the other is the chemical heat of 0# diesel itself. Therefore, it is necessary to calculate the enthalpy of fuel gas and the enthalpy of air [10].

The enthalpy value of 0# diesel flue gas is calculated based on 1 kg of 0# diesel, and it is calculated from 0°C . When the temperature is $t^\circ\text{C}$, the enthalpy value I_y^0 of the theoretical flue gas volume is shown as follows:

$$I_y^0 = (V_{\text{RO}_2}C_{\text{RO}_2} + V_{\text{N}_2}C_{\text{N}_2} + V_{\text{H}_2\text{O}}C_{\text{H}_2\text{O}})t, \quad (1)$$

where V_{RO_2} is the theoretical triatomic gas RO_2 volume, m^3/kg ; C_{RO_2} is the average volume heat capacity of theoretical triatomic gas RO_2 at constant pressure, $\text{kJ}/\text{m}^3\cdot\text{k}$; V_{N_2} is the theoretical N_2 volume, m^3/kg ; C_{N_2} is the theoretical N_2 average volume heat capacity at constant pressure, $\text{kJ}/\text{m}^3\cdot\text{k}$; $V_{\text{H}_2\text{O}}$ is the theoretical water vapor H_2O volume, m^3/kg ; $C_{\text{H}_2\text{O}}$ is the average volume heat capacity of theoretical water vapor H_2O at constant pressure, $\text{kJ}/\text{m}^3\cdot\text{k}$; and t is the flue gas temperature, $^\circ\text{C}$.

It can be seen from the above calculation that the theoretical SO_2 volume ratio is very small, so $C_{\text{RO}_2} = C_{\text{CO}_2}$ can be

used in the calculation. The enthalpy value of the theoretical air volume I_y^0 is shown as follows:

$$I_k^0 = V^0 C_k t_k, \quad (2)$$

where V^0 is the theoretical air volume of the hot water machine, m^3/kg ; C_k is the average volume heat capacity of air at constant pressure, $\text{kJ}/\text{m}^3\cdot\text{k}$; and t_k is the air temperature, $^\circ\text{C}$.

The flue gas enthalpy value I_y is shown as follows:

$$I_y = I_y^0 + (\alpha - 1)I_k^0, \quad (3)$$

where I_y^0 is the enthalpy value of the theoretical flue gas volume of the hot water machine, kJ/m^3 ; α is excess air coefficient; and I_k^0 is the enthalpy of theoretical air volume, kJ/m^3 .

The specific heat of each temperature of air and flue gas is shown in Table 2. The excess air coefficient is 1.1, and the calculation results of equations (1) and (2) are substituted into equation (3) to obtain the flue gas enthalpy as shown in Table 3.

3. Analysis of the Heat Balance of the Oil-Fired Submersible Hot Water Machine System

In order to ensure that the heat enters the hot water machine, the effective utilization of the hot water machine and the heat loss of the hot water machine reach a certain balance, so the heat balance calculation of the hot water machine system is required. After completing the heat balance calculation, the thermal efficiency of the hot water machine system and the consumption of the hot water machine per hour should be obtained initially, so that the subsequent structural design of the fuel-based submersible hot water machine can be carried out. The heat balance calculation of the oil-fired submersible hot water machine is based on the operation of the hot water machine system under stable thermal conditions. In the standard state, the calculation is based on the complete combustion of 1 kg of 0# diesel.

3.1. The Input Heat of the Fuel Submersible Hot Water Machine. Since 0# diesel fuel produces very little ash and can be ignored, so $Q_6 = 0$. At the same time, when 0# diesel is atomized and then burned, incomplete solid combustion will not occur, so $Q_4 = 0$. Therefore, the heat balance equation can be written as follows:

$$Q_r = Q_1 + Q_2 + Q_3 + Q_5, \quad (4)$$

where Q_r is 1 kg of 0# diesel fuel sent to the heat of the submersible hot water machine system, $Q_r = 42900 \text{ kJ}/\text{kg}$; Q_1 is the efficient use of heat in the hot water machine system, kJ/kg ; Q_2 is the heat loss during exhaust of the hot water machine, kJ/kg ; Q_3 is the heat lost when the oil mist of the hot water machine is incompletely burned, kJ/kg ; and Q_5 is the heat transferred from the hot water machine system to the surrounding environment, kJ/kg .

TABLE 1: Summary table of smoke composition.

Data name	Code name	Unit	Value
Theoretical air volume	V^0	m^3/kg	11.153276
Theoretical flue gas	V_y	m^3/kg	12.086479
Theoretical CO_2 volume	V_{CO_2}	m^3/kg	1.596363
Theoretical SO_2 volume	V_{SO_2}	m^3/kg	0.001750
Theoretical N_2 volume	V_{N_2}	m^3/kg	8.811408
Theoretical triatomic gas RO_2 volume	V_{RO_2}	m^3/kg	1.598113
Theoretical water vapor H_2O volume	$V_{\text{H}_2\text{O}}$	m^3/kg	1.676958
Theoretical CO_2 volume ratio	r_{CO_2}	%	13.21
Theoretical SO_2 volume ratio	r_{SO_2}	%	0.01
Theoretical N_2 volume ratio	r_{N_2}	%	72.90
Theoretical RO_2 volume ratio	r_{RO_2}	%	13.22
Theoretical water vapor H_2O volume ratio	$r_{\text{H}_2\text{O}}$	%	13.87

TABLE 2: Specific heat table of air flue gas.

Temperature ($^{\circ}\text{C}$)	Specific heat of combustion products of various gases ($\text{Kcal}/\text{m}^3\cdot^{\circ}\text{C}$)	
	Natural gas, coke oven gas, mixed gas, liquid fuel bituminous coal, and anthracite	Specific heat of air ($\text{Kcal}/\text{m}^3\cdot^{\circ}\text{C}$)
0–200	0.33	0.31
200–400	0.34	0.31
400–700	0.35	0.32
700–1000	0.36	0.33
1000–1200	0.37	0.34
1200–1500	0.38	0.35
1500–1800	0.39	0.35
1800–2000	0.40	0.36

TABLE 3: Flue gas enthalpy temperature table.

Temperature ($^{\circ}\text{C}$)	Theoretical smoke enthalpy I_y (kJ/m^3)	Air enthalpy I_k (kJ/m^3)	Flame tube outlet $\alpha'' = 1.1 I_y$ (kJ/m^3)	Smoke pipe outlet $\alpha_{py} = 1.1 I_y$ (kJ/m^3)
15	250	222	272	272
50	833	738	907	907
100	1666	1477	1814	1814
120	2007	1776	2185	2185
200	3372	2971	3669	3669
300	5123	4491	5572	5572
400	6923	6043	7527	7527
450	7847	6836	8531	8531
500	8771	7630	9534	9534
600	10667	9254	11592	11592
700	12612	10911	13703	13703
800	14599	12593	15858	15858
850	15609	13448	16954	16954
900	16619	14302	18050	18050
1000	18673	16031	20277	20277
1100	20760	17788	22539	22539
1200	22872	19556	24828	24828
1300	25012	21350	27147	27147
1400	27167	23156	29483	29483
1500	29344	24971	31841	31841
1600	31539	26800	34219	34219
1700	33753	28634	36617	36617
1750	34864	29552	37819	37819
1800	35974	30470	39021	39021
1900	38206	32331	41440	41440
2000	40451	34181	43869	43869

If the heat balance equation of the oil-fired submersible hot water machine is expressed by the percentage of each heat in the total heat input of the system, it can be written as shown in the following equation:

$$q_1 + q_2 + q_3 + q_5 = 100\%, \quad (5)$$

where q_i is the percentage of each heat to the total heat input to the system, $q_i = Q_i/Q_r \times 100\%$, %; q_1 is the heat utilization rate that the hot water machine effectively utilizes, %; q_2 is the exhaust smoke loss rate generated when the hot water machine exhausts the smoke, %; q_3 is the loss rate of incomplete combustion of the hot water machine oil mist, %; and q_5 is the heat loss rate of the hot water machine, %.

3.2. Exhaust Heat Loss. Exhaust heat loss is the most important heat loss in the entire oil-fired submersible hot water machine system. Among them, the temperature and volume of the exhaust are important factors that affect the heat loss of the exhaust. For a certain quality of fuel, the value of the excess air coefficient determines the amount of smoke emitted, and the combustion state directly affects the size of the excess air coefficient.

The exhaust heat loss q_2 can be expressed by the difference between the enthalpy of the flue gas discharged from the hot water machine system and the enthalpy of the cold air, which can be written as follows:

$$q_2 = \frac{(I_{py} - \alpha_{py} I_{lk}^0)(100 - q_4)}{Q_r} \times 100\%, \quad (6)$$

where I_{py} is the enthalpy of the flue gas discharged after the combustion of 1 kg of 0# diesel under the excess air coefficient of the flue gas and the flue gas temperature, kJ/m^3 ; α_{py} is excess air coefficient of exhaust flue gas; and I_{lk}^0 is, at the temperature of the air entering the hot water machine, the enthalpy of the theoretical air required when 1 kg of 0# diesel is burned, kJ/m^3 .

According to the research [11], the exhaust gas temperature is 200°C , and the temperature of the cold air sent to the hot water machine is 20°C , taking the excess air coefficient $\alpha_{py} = 1.1$ and substituting the value calculated according to Table 3 into equation (6). It can be obtained that the heat loss of exhaust gas of the oil-fired submersible water heater is $q_2 = 7.10\%$.

3.3. Incomplete Combustion of Oil Mist Heat Loss. The heat loss of incomplete combustion of oil mist refers to the incomplete combustion of the 0# diesel after atomization. This part of the incompletely burned oil mist will directly reduce the total heat input to the oil-fired submersible hot water machine system. However, according to the actual situation, under the current technical control, as long as the combustion is good, the heat loss of this part can be controlled within a small range. In the design calculation, $q_3 = 1.25\%$.

3.4. The Effective Use of Heat of the Oil-Fired Submersible Hot Water Machine. The effective heat utilization of the oil-fired

submersible hot water machine refers to the difference between the total enthalpy of the flue gas produced by the combustion of 0# diesel and the enthalpy of the medium water input to the hot water machine. For the fuel submersible hot water machine, its effective use of heat Q_1 is shown as follows:

$$Q_1 = Gc_s(t_{rs} - t_{hs}), \quad (7)$$

where G is the flow rate of circulating water, kg/s ; t_{rs} is the temperature of the hot water, $^\circ\text{C}$; t_{hs} is backwater temperature, $^\circ\text{C}$; and c_s is the specific heat of water, $\text{MJ}/(\text{kg}\cdot^\circ\text{C})$, generally taken $c_s = 0.0041868\text{MJ}/(\text{kg}\cdot^\circ\text{C})$.

According to the original design data of the fuel-burning submersible hot water machine in Section 2.1, substituting equation (7), the effective heat Q_1 of the fuel-burning submersible hot water machine can be calculated as 0.23 MW.

3.5. The Heat Loss of Fuel Oil Submersible Hot Water Machine. The heat dissipation loss of the oil-fired submersible hot water machine refers to the heat that the hot water machine system loses to the outside of the environment under the action of the surrounding environment. The heat loss of the oil-fired submersible hot water machine is designed and calculated according to the relevant standards provided in TSG G0003-2010 "Industrial Boiler Energy Efficiency Testing and Evaluation Rules" [12], as shown in Table 4.

According to the calculation result of equation (7) and the data in Table 4, it can be seen that $q_5 = 2.1\%$.

3.6. Thermal Efficiency and Fuel Consumption of the Oil-Fired Submersible Hot Water Machine. The thermal efficiency of the oil-fired submersible hot water machine is shown as follows:

$$\eta = 100 - (q_2 + q_3 + q_5), \quad (8)$$

where q_2 is the smoke loss rate during smoke exhaust, %; q_3 is the loss rate when incomplete combustion of oil mist occurs, %; and q_5 is the heat loss rate of hot water machine, %.

Substituting the q_2 , q_3 , and q_5 obtained above into equation (8), $\eta = 89.55\%$ is obtained. The fuel consumption of the oil-fired submersible hot water machine is shown as follows:

$$B = \frac{Q_1}{\eta Q_r} \times 100, \quad (9)$$

where Q_1 is the effective use of heat by hot water machine, MW; η is the thermal efficiency of the hot water machine, %; and Q_r is the heat sent to the submersible hot water machine system, kJ/kg .

Substituting the calculated values into equation (9), $B = 21.55 \text{ kg/hcan}$ be obtained.

When calculating the heat of oil-fired boilers, the volume of flue gas is used to calculate the temperature enthalpy table, so the heat calculation should be calculated by calculating the fuel consumption. The fuel consumption is calculated as shown in the following equation:

$$B_j = B \frac{100 - q_4}{100}, \quad (10)$$

where B is the fuel consumption of the hot water machine, kg/h, and q_4 is the heat loss rate when solid fuel is incompletely burned, %.

Substituting $q_4 = 0$ and the value of equation (9) $B = 21.55$ kg/h into equation (10), $B_j = 21.55$ kg/h is obtained.

4. The Overall Structure Design of the Fuel-Type Submersible Hot Water Machine

The overall structure of the oil-fired submersible hot water machine includes the boiler tube, flame tube, smoke chamber, fire tube, bracket, flange, and flange cover, etc. The connecting parts of each part are selected by general standard parts to meet the interchangeability during maintenance reduces the maintenance cost of the hot water machine. For some nonuniversal standard parts, they are required to be designed.

The oil-fired submersible hot water machine adopts the central flame-return structure in the horizontal structure. After the flame is sprayed from the burner, the special structure of the flame tube will form an entrainment phenomenon, and the high-temperature smoke in the tube will continuous movement to the wall of the flame tube can form a very uniform temperature field, which is beneficial to heating the working fluid [13–15] as shown in Figure 1.

The burner of the oil-fired submersible water heater is the heating device of the hot water machine. As the core component of the hot water machine heating [16], when the burner is selected, there must be a corresponding value when meeting the basic power consumption [17]. According to the working characteristic curve of the burner, the working point of the burner must be in its corresponding full-load area, and the closer the working point is to the right side of the working curve, the better. The burner work curve is shown in Figure 2, and the final selected burner model is the UNIGAS LO280 AB burner.

The flame tube is designed according to the parameters of the selected burner. The flame tube consists of three parts, namely, the flange, the cylinder, and the head, which are connected by welding. The head adopts a standard elliptical head, and the flanging is to ensure the stability when connecting with the front smoke chamber, and the flame tube structure is shown in Figure 3.

The smoke chamber is a structure for storing high-temperature flue gas. The structure used in this article is the central flame-back type. The smoke chamber of the central flame-back hot water machine is arranged inside the drum. This structure can effectively reduce the heat loss. The smoke chamber has two parts, namely, the front smoke chamber and the rear smoke chamber. The front smoke chamber is connected with the flame tube, the threaded tube, and the inlet of the burner, and the rear smoke chamber is connected with the threaded tube and the chimney. The structures of the front smoke chamber and the rear smoke chamber are shown in Figures 4 and 5.

TABLE 4: Boiler heat loss table.

Boiler rated output	t (h)	≤4	6	10	15	20	35	≥65
	MW	≤2.8	4.2	7.0	10.5	14	29	≥46
Heat loss	%	2.1	2.4	1.7	1.5	1.3	1.1	0.8

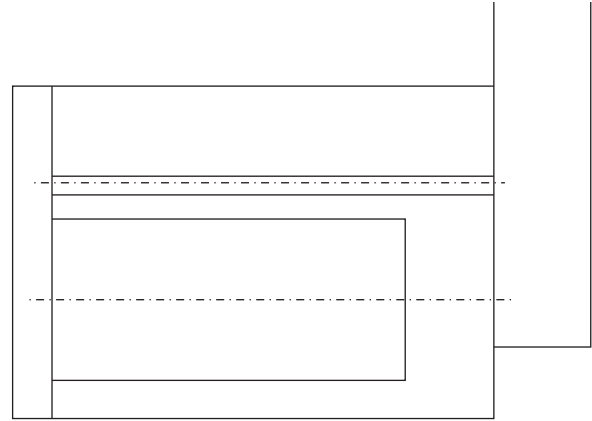


FIGURE 1: Schematic diagram of the central flame-return structure of a horizontal hot water machine.

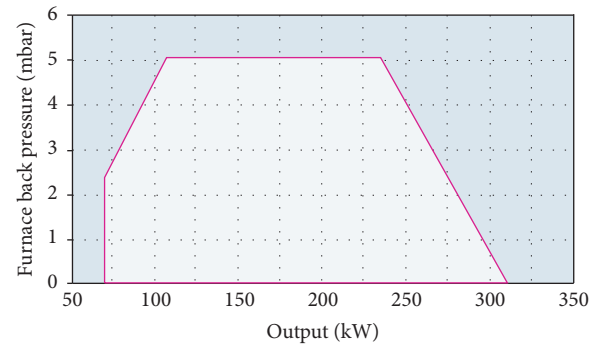


FIGURE 2: Burner working curve.

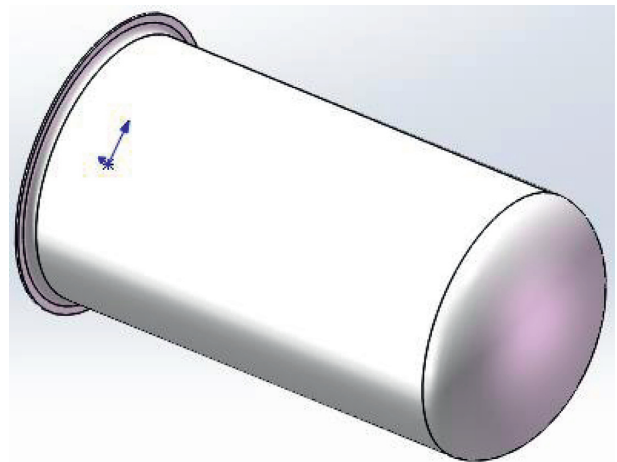


FIGURE 3: Structure diagram of the flame tube.

The central flame-back water heater is equipped with threaded pipes, and the number of threaded pipes and the pipe distance have strict requirements. The threaded tube is

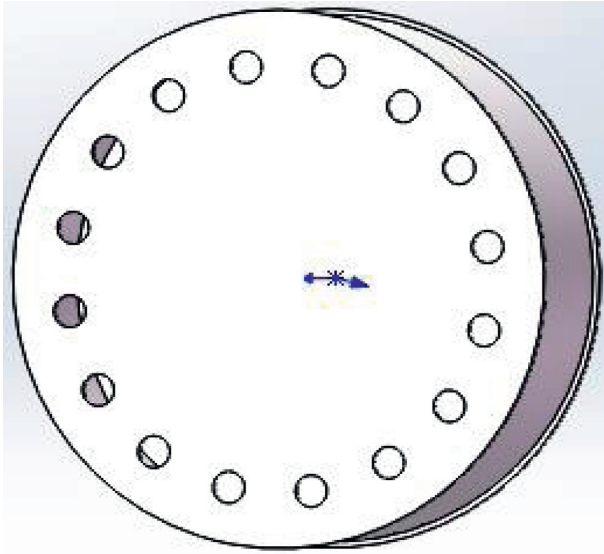


FIGURE 4: Structure of the front smoke chamber.

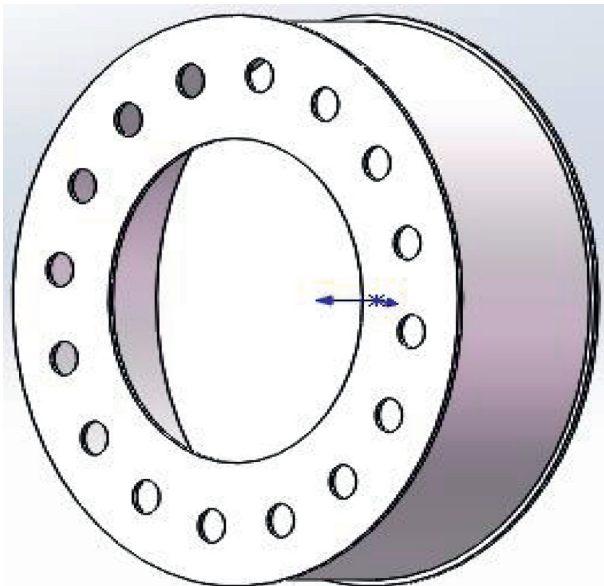


FIGURE 5: Structure diagram of the rear smoke chamber.

formed by rolling and forming an ordinary smooth tube. The purpose of increasing the thread is to enhance the intensity of turbulence in the tube and enhance the convective heat transfer capacity of flue gas. The size of the threaded pipe is $\phi 32 \times 710$, and the size of the flange is designed according to the outer diameter of the drum.

The drum is designed according to the volume of the water heater. The design capacity of the drum in this article is 250 L. When designing the drum, a partition was added to the back half of the drum. The purpose of adding the partition was two: one is to provide support for the rear smoke chamber, and the other is to separate the hot and cold water. The drum structure is shown in Figure 6.

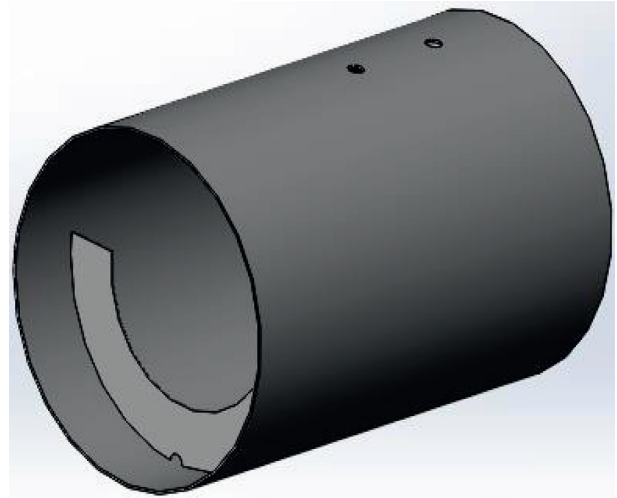


FIGURE 6: Drum structure diagram.

5. Heat Transfer Calculation of Flame Tube of the Oil-Fired Submersible Hot Water Machine

5.1. Basic Data Calculation of the Hot Water Machine. The total area of the furnace wall on each side of the flame tube $F_b = \pi \times (0.394)^2 + \pi \times 0.788 \times 1.2 = 3.946 \text{ m}^2$.

Since the flame tube is composed of a head and a cylinder, the covering area is not a conventional surface. Since the three-dimensional structure model of the flame tube has been established, the covering area $F_l = 0.595 \text{ m}^2$ of the flame tube can be obtained through software calculation.

Similarly, the volume of the flame tube is not a conventional volume. Using software calculations, the volume of the flame tube $V_l = 0.041 \text{ m}^3$ can be obtained.

5.2. The Effective Radiation Heating Area in the Boiler of the Oil-Fired Submersible Hot Water Machine. The effective radiation heating area in the boiler of the oil-fired submersible hot water machine can be obtained by the following equation:

$$H_f = xF_b, \quad (11)$$

where x is the effective angle factor and F_b is the area of the boiler wall where the water wall is arranged, m^2 .

Because the flame sprayed by the burner radiates all the heat to the wall of the flame tube, the effective angle factor is 1. Therefore, substituting the values of F_b and x into equation (11), it can be known that the effective radiation heating area in the boiler of the hot water machine is $H_f = 3.946 \text{ m}^2$.

5.3. The Effective Radiation Heating Area in the Boiler of the Oil-Fired Submersible Hot Water Machine. The effective heat release of the fuel-type submersible hot water machine can be obtained by the following equation:

$$Q_l = Q_r \times \frac{100 - q_3 - q_4 - q_6}{100 - q_4} + Q_k, \quad (12)$$

where Q_r is the heat sent to the hot water machine, kJ/kg; q_3 is loss rate when incomplete combustion of oil mist occurs, %; q_4 is the heat loss rate of incomplete combustion of solid fuel, %; q_6 is the heat loss rate taken away by the ash in the fuel, %; and Q_k is the amount of heat in the air required for combustion, kJ/kg.

When the fuel is burned, the heat required to send the air into the hot water machine is as shown in the following equation:

$$Q_k = a_1'' I_{rk}^0, \quad (13)$$

where a_1'' is excess air coefficient at the outlet of the flame tube of the hot water machine and I_{rk}^0 is the enthalpy of the air entering the flame tube of the hot water machine, kJ/kg.

According to the research, take $a_1'' = 1.1$, and select the enthalpy value of the outlet air $I_{rk}^0 = 295$ kJ/kg. Substituting the selected value into equation (13), we can obtain $Q_k = 324.5$ kJ/kg, and substituting the obtained Q_k and the previously calculated values into equation (12), the effective heat output of the water heater can be obtained as $Q_l = 42688$ kJ/kg.

Querying the smoke enthalpy table shows that the absolute combustion temperature corresponding to the effective heat release Q_l is $\theta_u = 1953^\circ\text{C}$, so the absolute combustion temperature $T_u = \theta_u + 273 = 2226$ K.

5.4. Calculation of the Flame Blackness of the Oil-Fired Submersible Hot Water Machine and the Flame Blackness of the Flame Tube. When the fuel is liquid, the flame blackness is formed by the superposition of the blackness of the luminous part of the flame and the blackness of the nonluminous part. The blackness of the luminous part of the flame and the blackness of the nonluminous part of the flame are, respectively, represented by the following equations:

$$a_{fg} = 1 - e^{-(k_q r_q + k_{th})PS}, \quad (14)$$

$$a_{bfg} = 1 - e^{-k_q r_q PS}, \quad (15)$$

where k_q is the triatomic gas radiation attenuation coefficient, $1/(\text{m} \cdot \text{MPa})$; r_q is the volume share of flame triatomic gas, %; k_{th} is the flame carbon black particle radiation attenuation coefficient, $1/(\text{m} \cdot \text{MPa})$; P is flame tube pressure, MPa; and S is the effective radiation layer thickness, m.

The effective radiation thickness is shown as follows:

$$S = 3.6 \frac{V_l}{F_l}, \quad (16)$$

where V_l is the effective volume of hot water machine flame tube, m^3 , and F_l is the covering area of the flame tube of the hot water machine, m^2 .

Substituting the values of the effective volume V_l of the flame tube and the coating area F_l of the flame tube into formula (16), the value of the effective radiation thickness can be obtained as $S = 0.248$ m.

The radiation attenuation coefficient of triatomic gas is shown as follows:

$$k_q = 10 \left(\frac{0.78 + 1.6r_{\text{H}_2\text{O}}}{\sqrt{10P_q S}} - 0.1 \right) \left(1 - 0.37 \frac{T_l''}{1000} \right), \quad (17)$$

where $r_{\text{H}_2\text{O}}$ is the volume ratio of water vapor to flue gas, %; P_q is the total partial pressure of the triatomic gas in the flame, MPa; S is the effective radiation thickness, m; and T_l'' is the smoke temperature at the exit of the flame tube, $^\circ\text{C}$.

Since the high-efficiency fuel oil submersible hot water machine works in a normal pressure environment, $P_q = 0.1$ MPa is taken. When the water heater is designed, the flue gas temperature at the outlet of the flame tube is set to 980°C , that is, $T_l'' = 980^\circ\text{C}$. Substituting the corresponding values into equation (17), we can get $k_q = 12.11$.

Substituting the corresponding values, the blackness of the luminous part of the flame $a_{fg} = 0.019$ and the blackness of the nonluminous part of the flame $a_{bfg} = 0.412$.

5.5. Calculation of Heat Release and Heat Transfer of Flame Tube Flue Gas of the Oil-Fired Submersible Hot Water Machine. The heat release of the flue gas from the flame tube is shown as follows:

$$Q_{rp} = \phi(Q_l - I_l''), \quad (18)$$

where ϕ is the heat preservation coefficient, %; Q_l is the heat of the flame tube, kJ/kg; and I_l'' is the enthalpy value corresponding to the flue gas temperature at the outlet of the flame tube, kJ/kg.

According to this research, setting the outlet temperature of the flame tube $k_l'' = 477^\circ\text{C}$, the corresponding smoke enthalpy $I_l'' = 8346$ kJ/kg. Substituting the corresponding values into equation (18), the heat release of the flame tube flue gas is $Q_{rp} = 33552.1$ kJ/kg.

The heat transfer of the flue gas in the flame tube is shown as follows:

$$Q_{cr} = C \frac{H_f}{B_j} \left[\left(\frac{T_{hy}}{100} \right)^4 - \left(\frac{T_b}{100} \right)^4 \right], \quad (19)$$

where C is the radiation and convection heat transfer coefficient, take $C = 11.72$ kW/($\text{m}^2 \cdot \text{K}$); B_j is the fuel consumption of the hot water machine, kg/h; T_{hy} is the average flame temperature, K; and T_b is the surface temperature of the water wall, K.

Substituting the corresponding values into equation (19), the heat transfer amount of the flame tube flue gas can be obtained as $Q_{cr} = 33573.7$ kJ/kg.

The calculation error of the flame tube of the hot water machine is shown as follows:

$$\Delta = \left| \frac{Q_{rp} - Q_{cr}}{Q_{rp}} \right| \times 100 = \left| \frac{33552.1 - 33573.7}{33552.1} \right| \times 100 = 0.064\%. \quad (20)$$

6. Calculation of Convective Heat Transfer in Hot Water Machine

Convection heat transfer is one of the important heat transfer methods of high-efficiency fuel-type submersible hot water machines. For high-efficiency fuel-type submersible hot water machines, the convective heating surface refers to the heating surface of the fire tube and smoke chamber of the hot water machine. In the heating surface of these hot water machine systems, heat is transferred to the medium water in a convective manner, and the calculation of convective heat transfer is also based on the heat released by the combustion of 1 kg of 0# diesel.

6.1. Basic Data Calculation of Convective Heat Transfer Surface. The fire tube takes the form of a threaded tube, which can improve the heat exchange efficiency to a certain extent, so that the medium absorbs more heat. The steel pipe is a standard steel pipe with a diameter of 32 mm and a thickness of 2.5 mm. The threaded pipe is pressed by a special threaded pipe with a guide rail bracket. The front and rear smoke chambers have smooth walls and cylindrical structures. The specific parameters are shown in Table 5.

According to the data in Table 5, the flue gas flow area Fr of the threaded tube, the heat transfer area Hr of the threaded tube, the heat transfer area Hs of the fume chamber, and the total flue gas flow area Fd can be further obtained. The total heat transfer area Hd is shown in Table 6.

6.2. Calculation of Heat Release of Flue Gas. The amount of heat emitted by the flue gas is shown as follows:

$$Q_{rp} = \varphi((I' - I''), \quad (21)$$

where φ is the heat preservation coefficient; I' is the enthalpy of inlet flue gas, kJ/kg; and I'' is the enthalpy of outlet flue gas, kJ/kg.

Now set the inlet flue gas temperature θ' to 477°C, check the flue gas enthalpy table, its corresponding enthalpy value $I' = 8328$ kJ/kg, the flue gas outlet temperature $\theta'' = 200$ °C, and its corresponding enthalpy value $I'' = 3372$ kJ/kg. The previously calculated heat preservation coefficient $\varphi = 0.977$. Therefore, the calorific value of the flue gas is $Q_{rp1} = 4842$ kJ/kg.

6.3. Average Flue Gas Temperature, Flow Velocity, and Temperature and Pressure Calculation. The average flue gas temperature is shown as follows:

$$\theta_p = \frac{\theta' + \theta''}{2}, \quad (22)$$

where θ' is the inlet flue gas temperature, °C, and θ'' is the outlet flue gas temperature, °C.

Substituting the corresponding values into equation (22), we can get $\theta_p = 338.5$ °C.

The average flue gas flow rate is shown as follows:

TABLE 5: Convection surface structure parameter table.

Project name	Code name	Unit	Value
Threaded pipe pitch	t	mm	45
Threaded pipe groove depth	ε	mm	2
Threaded pipe inner diameter	dr	mm	29.5
Number of threaded pipes	Nr	—	16
Longitudinal scour length of threaded pipe	L	M	0.7
Front and rear smoke chamber diameter	ds	mm	520
Longitudinal scour length of smoke chamber	L'	M	0.4

TABLE 6: Convection surface structure parameter table.

Project name	Code name	Unit	Value
Threaded pipe flue gas flow area	Fr	m ²	0.011
Heat transfer area of threaded tube	Hr	m ²	1.038
Heat transfer area of smoke chamber	Hs	m ²	0.372
Total flue gas circulation area	Fd	m ²	0.011
Total heat transfer area	Hd	m ²	1.410

$$\omega = \frac{B_j V_y}{3600 Fd} \cdot \frac{\theta_p + 273}{273}, \quad (23)$$

where B_j is the fuel consumption of the hot water machine, kg/h; V_y is the theoretical flue gas, m³/kg; Fd is the total flue gas circulation area, m²; and θ_p is the average flue gas temperature, °C.

Substituting the corresponding values obtained above into equation (23), the average flue gas flow velocity can be obtained as $\omega = 14.7$ m/s.

The logarithmic temperature and pressure are shown as follows:

$$\Delta t = \frac{\Delta t_d - \Delta t_x}{\ln \Delta t_d / \Delta t_x}, \quad (24)$$

where Δt_d is the large end temperature, °C, and Δt_x is the small end temperature, °C.

Among them, the large end temperature and pressure value is the difference between the inlet flue gas temperature and the working fluid outlet temperature, that is, $\Delta t_d = \theta' - t_2 = 477 - 60 = 417$ °C, and the small end temperature and pressure value is the difference between the outlet flue gas temperature and the working fluid inlet, that is, $\Delta t_x = \theta'' - t_1 = 200 - 4 = 196$ °C, and substituting the values obtained above into equation (24), the logarithmic temperature and pressure can be obtained as $\Delta t = 284.4$.

6.4. Calculation of Convective Heat Transfer Coefficient.

The convective heat transfer coefficient is used to express the heat transfer capacity between the medium water and the convection surface. For high-efficiency oil-fired submersible hot water machines, the convection heat transfer surface has a fire tube and a smoke chamber. Therefore, it is necessary to calculate the total convective heat transfer coefficient of the flue gas.

The Prandtl coefficient of the flue gas $Pr = 0.6211$, the kinematic viscosity coefficient of the flue gas $\nu = 0.00009 \text{ m}^2/\text{s}$, the thermal conductivity of the flue gas $\lambda = 0.0783 \text{ kW}/(\text{m}\cdot^\circ\text{C})$, and the average flue gas flow rate $\omega = 14.7 \text{ m/s}$, and it can be calculated that the Rayleigh number of the threaded tube $Rer = \omega dr/\nu = 14.7 \times 0.0295/0.00009 = 4818$, and the Rayleigh number of the smoke chamber $Res = \omega ds/\nu = 14.7 \times 0.52/0.00009 = 84933$.

The convective heat transfer coefficient of the threaded tube is shown as follows:

$$a_r = 0.0144 \left(\frac{t}{dr} \right)^{-0.08} \cdot \left(\frac{\varepsilon}{dr} \right)^{0.112} Rer^{0.926}, \quad (25)$$

where t is the pitch of the threaded pipe, mm; dr is the inner diameter of the threaded pipe, mm; ε is the groove depth of the threaded pipe, mm; and Rer is the Reynolds number of the threaded pipes.

Substituting the corresponding values into equation (23), the convective heat transfer coefficient of the threaded tube $a_r = 0.026 \text{ kW}/(\text{m}\cdot^\circ\text{C})$ can be obtained.

The convective heat transfer coefficient of the smoke chamber is shown as follows:

$$a_s = 0.023 \frac{\lambda}{ds} Res^{0.8} Pr^{0.4}, \quad (26)$$

where λ is the thermal conductivity of flue gas, $\text{kW}/(\text{m}\cdot^\circ\text{C})$; ds is the inner diameter of the smoke chamber, mm; Res is the Reynolds number of the smoke chamber; and Pr is the Prandtl coefficient of flue gas.

Substituting the corresponding values into equation (26), the convective heat transfer coefficient of the smoke chamber $a_s = 0.025 \text{ kW}/(\text{m}\cdot^\circ\text{C})$ can be obtained.

From the convective heat transfer coefficient of the threaded tube and the smoke chamber, the total convective heat transfer coefficient of the flue gas $a_d = (a_s Hs + a_r Hr)/Hs + Hr = 0.025 \times 0.372 + 0.026 \times 1.038/0.372 + 1.038 = 0.072 \text{ kW}/(\text{m}\cdot^\circ\text{C})$. can be further calculated.

6.5. Calculation of Radiation Heat Release Coefficient of Flue Gas. The radiation attenuation coefficient of triatomic gas is shown as follows:

$$k_q = \left(1 - 0.37 \frac{\theta_p + 273}{1000} \right) \left(\frac{2.47 + 5.06 r_{\text{H}_2\text{O}}}{\sqrt{r_q P S}} - 1 \right) r_q, \quad (27)$$

where θ_p is the average flue gas temperature, $^\circ\text{C}$; $r_{\text{H}_2\text{O}}$ is the volume ratio of water vapor to flue gas, %; r_q is the volume share of flame triatomic gas, %; P is the flame tube pressure, MPa; and S is the effective radiation layer thickness, m.

Substituting the corresponding values into equation (27), the radiation attenuation coefficient of triatomic gas $k_q = 2.050 (\text{MPa} \cdot \text{m})^{-1}$ can be obtained. From the radiation

attenuation coefficient of triatomic gas, the smoke blackness $a_y = 1 - e^{-k_q P S} = 1 - e^{-2.050 \times 1 \times 0.248} = 0.400$ can be further obtained.

The temperature ratio is shown as follows:

$$\tau = \frac{t_b + 273}{\theta_p + 273}, \quad (28)$$

where t_b is the surface temperature of the water wall, $^\circ\text{C}$, and θ_p is the average flue gas temperature, $^\circ\text{C}$.

The surface temperature t_b of the water wall is taken as 283°C , that is, $t_b = 283^\circ\text{C}$, and then the temperature ratio $\tau = 0.793$. According to the obtained temperature ratio, the radiation heat release coefficient of the flue gas $a_f = 0.026$ can be further obtained.

6.6. Calculation of Heat Transfer and Heat Transfer Error of the Main Heating Surface. The total heat transfer coefficient is shown as follows:

$$K = \psi (a_d + a_f), \quad (29)$$

where ψ is the thermal effective coefficient; a_d is the total convective heat transfer coefficient of flue gas; and a_f is the radiative heat release coefficient of flue gas.

Thermal effective coefficient $\psi = 0.73$; substituting the corresponding values into equation (29), the total heat transfer coefficient can be obtained as $K = 0.73 \times (0.072 + 0.026) = 0.072$.

The heat of the main heating surface is shown as follows:

$$Q_{cr} = \frac{KH d \Delta t}{B_j}, \quad (30)$$

where K is the total heat transfer coefficient; Hd is the total heat transfer area, m^2 ; Δt is the logarithmic temperature, $^\circ\text{C}$; and B_j is the fuel consumption of the hot water machine, kg/h .

Substituting the corresponding values into equation (30), the heat of the main heating surface can be obtained as $Q_{cr} = 4822 \text{ kJ}/\text{kg}$ and the heat transfer error of the main heating surface as $\Delta = |Q_{rp1} - Q_{cr}/Q_{rp1}| \times 100 = |4842 - 4822/4842| \times 100 = 0.41\%$.

6.7. Total Heat Balance Check of the Hot Water Machine. The overall calculation error of the water heater is shown as follows:

$$\Delta Q = \frac{Q_r \eta}{100 - q_4} - Q_{rp} - Q_{rp1}, \quad (31)$$

where Q_r is the total heat sent to the hot water machine system, kJ/kg ; η is the thermal efficiency of the hot water machine, %; q_4 is the heat loss rate of incomplete combustion of solid fuel, %; Q_{rp} is the heat release of flame tube smoke, kJ/kg ; and Q_{rp1} is the exothermic amount of flue gas, kJ/kg .

Substituting the corresponding values into equation (31), we can get the overall calculation error of the water heater $\Delta Q = 22.95\text{kJ/kg}$ and the overall relative calculation error of the hot water machine $\Delta = \Delta Q/Q_r \times 100 = 22.95/42900 \times 100 = 0.053\%$.

7. CAE Analysis of High-Efficiency Fuel Submersible Hot Water Machine

With the rise of computer-aided engineering, analyzing engineering problems in reality has become simple and quick [18]. For high-efficiency fuel-type submersible water heaters, the CAE analysis that needs to be done is mainly structural analysis and thermal analysis. In terms of structural analysis, the workbench is used to simulate the force of each main structure, so as to better predict the quality problems of the water heater before the manufacturing is completed.

7.1. CAE Analysis of Drum. The drum is made of 316L stainless steel with a thickness of 3.5 mm. There are three holes with a diameter of 40 mm on the surface of the drum. The through pieces are connected to these three holes by welding. The other ends of the three through pieces are connected to the overflow: flow valve, float, and plug match. A support plate is also welded inside the drum. On the one hand, the support plate is used to support the rear smoke chamber, and on the other hand, it is used to isolate cold and hot water, so that the temperature of the hot water output in the hot water machine is more stable. The structure is shown in Figure 6.

It can be seen from Figure 7 that the maximum deformation of the drum is 0.41344 mm and the minimum deformation is 0 mm. The area with the largest amount of deformation is mainly concentrated on the two sides of the line connecting the centers of the two openings. The deformation area around the opening is more evenly distributed. The deformation around the overflow valve hole is 0.091875 mm, and the half side around the float joint hole is even deformed. The amount is 0 mm. After the penetration piece is welded to the hole, such a small amount of deformation ensures the stability of the drum. The recession in the opening area is because the strength of the barrel wall is reduced after the opening of the hole, and the inside of the barrel is subjected to pressure, which ultimately leads to the deformation of the barrel. It can be seen from Figure 8 that the stress distribution of the drum is relatively uniform, and there is stress concentration around the opening of the drum, which is a normal phenomenon. It can be seen from Figure 9 that the strain near the opening of the drum shows a symmetrical state. Since the deformation near the opening is larger than that of other regions, the strain in this part of the region is also larger than that in other regions. Since the maximum stress of the drum is far less than the allowable stress, the strength and rigidity of the drum fully meet the working requirements, and there is no need to optimize the structure of the drum.

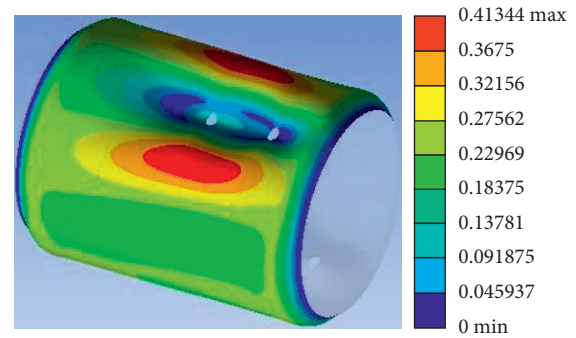


FIGURE 7: Cloud diagram of total deformation of the drum.

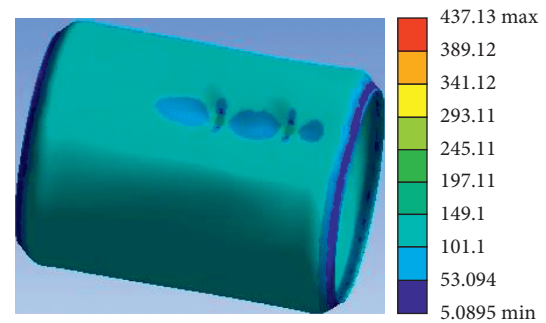


FIGURE 8: Equivalent stress cloud diagram of the drum.

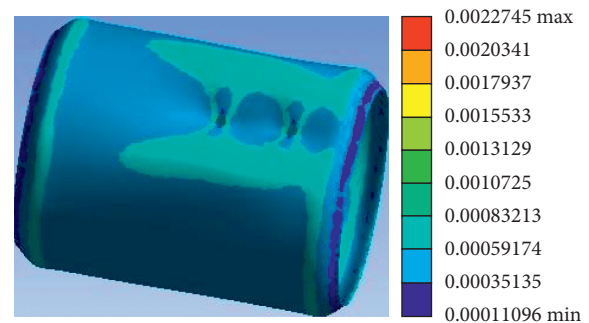


FIGURE 9: Equivalent strain cloud diagram of the drum.

7.2. Flange CAE Analysis. The flange is an important part to connect the drum and the end cover, and the flange and the drum are connected by welding. The material of the flange is 316L stainless steel. The three-dimensional view of the flange is shown in Figure 10.

The flange is meshed, and the mesh size is selected as 10 mm, and then the simulation is performed.

The flange inner ring and the drum are connected by welding, and the flange and the end cover are connected by bolts. The main bearing surface of the flange is the boss surface at the front end of the flange. This part of the area is in full contact with the gasket, and the force received comes from the internal pressure of the drum. The round hole on the flange end face matches the bolt, so the inner face of the round hole is subjected to shearing force. The total deformation cloud diagram of the flange is shown in Figure 11. The deformation area of the flange is mainly concentrated on

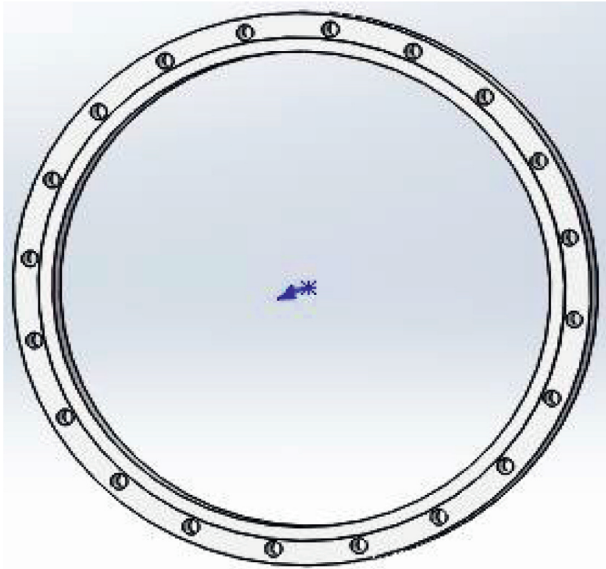


FIGURE 10: Three-dimensional view of the flange.

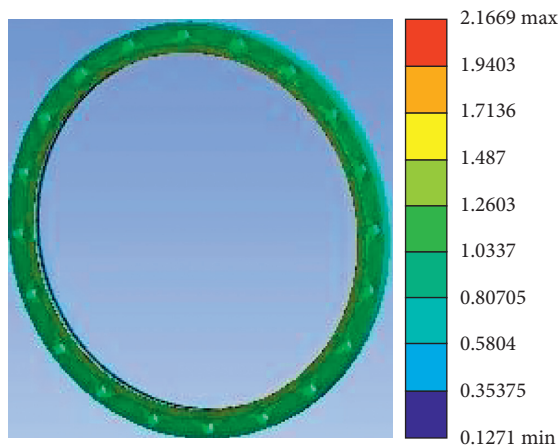


FIGURE 11: Cloud diagram of total flange deformation.

the edge of the flange, and the edge of the flange is relatively weak compared to other parts and is compressed by the bolt connection, so the deformation range of the region is larger than that of other regions. The stress and strain cloud diagrams of the flange are shown in Figures 12 and 13. From the cloud diagrams, the stress and strain distribution of the flange is very uniform and the values are very small. Therefore, the physical properties of the flange are very good.

7.3. Thermal Field Analysis of Flame Tube. The flame tube is the core thermal reaction element of the entire hot water machine. After the burner sprays the flame, the entire heating process of the hot water machine is carried out in the flame tube [19], so the thermal field of the flame tube is analyzed and studied. It is particularly important.

Using fluent software can simulate the state of the thermal field more accurately and quickly. It can be seen from Figure 14 that the pressure of the flame tube gradually increases along the tail of the flame tube until the pressure at

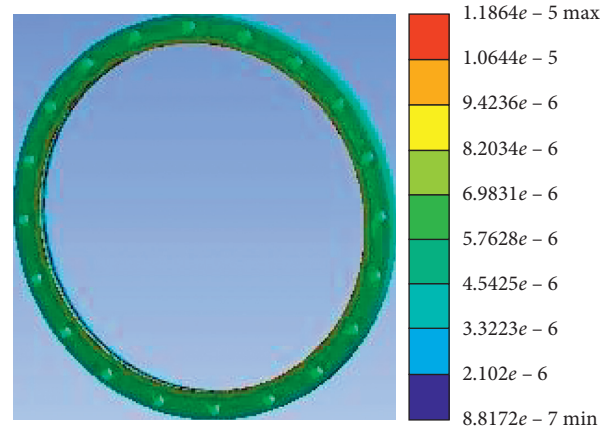


FIGURE 12: Equivalent stress cloud diagram of the flange.

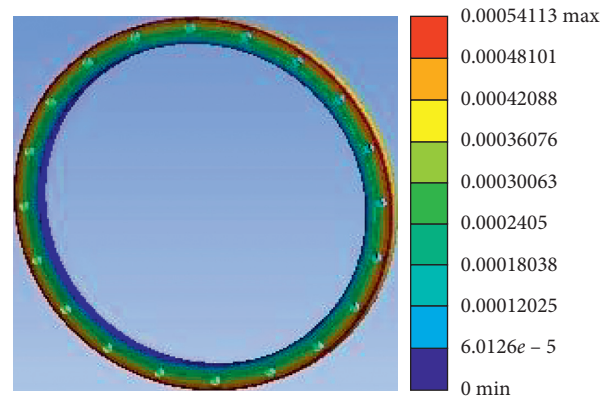


FIGURE 13: Equivalent strain cloud diagram of the flange.

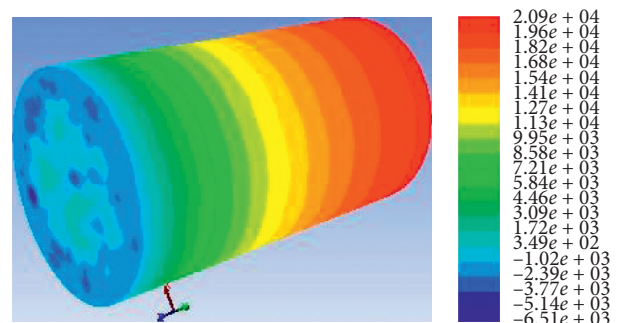


FIGURE 14: Pressure cloud diagram of the flame tube.

the head reaches the maximum. At the entrance of the flame tube, the center pressure of the flame tube is greater than the pressure around the flame tube, and the pressure around the flame tube is lower than the center pressure of the flame tube, forming an entrainment effect. It is precisely because of the entrainment effect that the heat of the flame tube is more uniform and the heat exchange efficiency is more efficient. It can be seen from Figure 15 that the temperature in the back half of the flame tube is in a stable state. Because the front wall of the flame tube has a shorter distance from the flame, the radiation intensity of the flame is also greater, so the temperature is higher. Figure 16 shows the change in the

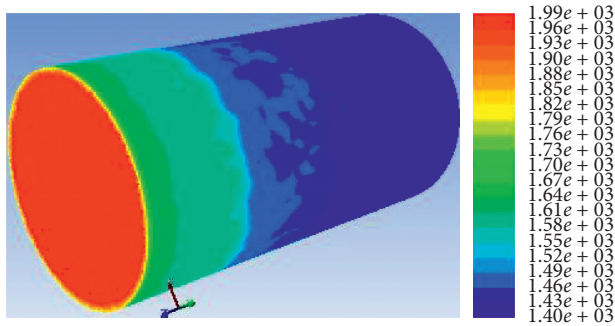


FIGURE 15: Temperature cloud diagram of the flame tube.

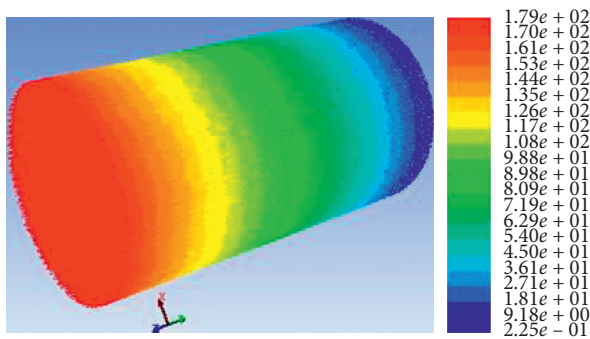


FIGURE 16: Flame cylinder velocity vector cloud diagram.

smoke velocity of the flame tube. The flame injected by the burner enters the flame tube from the entrance of the flame tube. The flue gas blocks the descending speed at the head of the flame tube and then turns back and enters from the inner cavity of the flame tube.

7.4. Thermal Field Analysis of Threaded Pipe. The threaded tube is one of the main components of the flue gas scouring. After the high-temperature flue gas is discharged from the flame tube, it enters the front smoke chamber, then enters the rear smoke chamber through the threaded tube, and is finally discharged into the atmosphere. As the main component of the flue gas scouring, the threaded tube is also very important to study its thermal field [20].

The fluent software is also used to simulate the thermal field. It can be seen from Figure 17 that the upper end of the threaded tube is the flue gas inlet, and the gas pressure gradually decreases from the inlet to the outlet. The inlet pressure is large and the outlet pressure is small, so that the flue gas can continuously flow from the inlet to the outlet. It can be seen from Figure 18 that the temperature distribution of the threaded pipe is relatively uniform, the temperature at the inlet end is higher, and the temperature at the outlet end decreases. The flue gas transfers heat to the threaded pipe wall in two forms of convection heat exchange and radiation heat exchange, and the threaded pipe wall transfers the heat to the working fluid water. It can be seen from Figure 19 that the threaded tube starts from the inlet, the first part of the flue gas velocity is relatively large, and as the length of the threaded tube increases, the resistance of the flue gas also increases, so the flue gas velocity decreases.

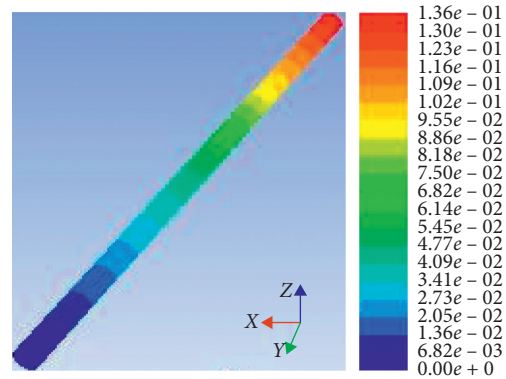


FIGURE 17: Pressure cloud diagram of the threaded pipe.

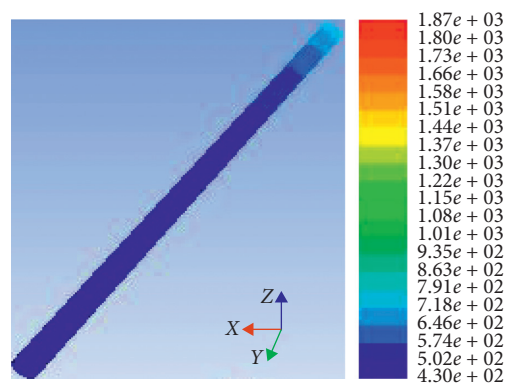


FIGURE 18: Temperature cloud diagram of the threaded pipe.

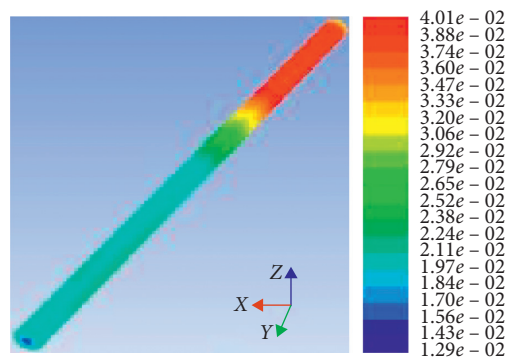


FIGURE 19: Speed vector cloud diagram of the threaded pipe.

8. CAE Analysis of High-Efficiency Fuel Submersible Hot Water Machine

The flame tube is the component with the largest temperature difference of the oil-fired hot water machine. In the analysis, not only the influence of the static field on the flame tube must be considered, but also the change in the intensity of the flame tube under the thermal field coupling. It is very important to conduct multifield coupling analysis on the flame tube [21]. The thermal structure coupling analysis is completed in the workbench software. In the above, the thermal field of the flame tube flue gas was studied, and this section focuses on the thermal field of the flame tube body.

The temperature cloud diagram of the flame tube body is shown in Figure 20. From Figure 20, it can be concluded that the temperature distribution of the flame tube body is extremely uniform. There are two reasons for this phenomenon: one is the entrainment of the smoke in the flame tube. The high-temperature flue gas moves uniformly on the wall of the flame tube, so that the temperature difference in the entire heat exchange process is small, and the flame tube body uniformly absorbs heat; second, the material of the flame tube is 316L stainless steel, and the heat transfer coefficient of 316L stainless steel is $16.3 \text{ W}/(\text{m}^2\cdot\text{K})$, the material itself has better heat transfer performance, so the temperature distribution of the flame tube is even.

After the temperature field analysis of the flame tube body, the flame tube is statically analyzed on the basis of the original temperature field. For 316 L stainless steel, on the basis of the temperature field, static analysis can describe the actual state of the flame tube more objectively. From the three aspects of total deformation, stress, and strain, the flame tube occurs due to the effect of the temperature field. The total deformation can intuitively reflect the appearance deformation of the flame tube due to external force. The stress objectively shows the internal reaction of the flame tube to the outside world after the external force is applied. The strain objectively shows the relative deformation of the internal structure of the flame tube.

Figures 21 and 22 are the total deformation cloud diagrams of the flame tube in the uncoupled and coupled conditions, respectively. By comparison, it can be seen that, in the case of multifield coupling, the temperature field has a certain influence on the flame tube. The main deformation changes are concentrated in the middle of the flame tube and the top of the head. Due to the coupling and superposition of the temperature field, the deformation of these parts has changed to different degrees. For the middle part of the flame tube, in the case of no coupling, there are two deformation areas in the middle part of the flame tube, and the middle part of the flame tube deforms unevenly. In the case of multifield coupling, the middle part of the flame tube has the same amount of deformation. For the top of the head, the change in total deformation is also more obvious. The effect of the temperature field increases the deformation of the head of the flame tube, and the edge transition of the deformation also tends to be gentle. But for the flame tube that is only subjected to the static force field, the difference in the amount of deformation is relatively obvious, and the transition of the deformation edge is not obvious. The reason for this phenomenon is that the temperature field affects the material properties of 316 L stainless steel. Under the action of the temperature field, the plasticity of the stainless steel material increases and the rigidity decreases. When subjected to the same static force field, it exhibits different properties.

Figures 23 and 24 are the equivalent stress cloud diagrams of the flame tube in the uncoupled and coupled conditions, respectively. From these two cloud diagrams, it can be clearly seen that the temperature field has a greater influence on the stress of the flame tube. In the case of no

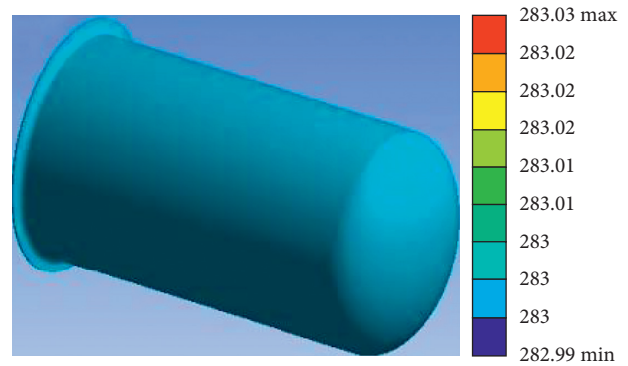


FIGURE 20: Temperature cloud diagram of the flame tube body.

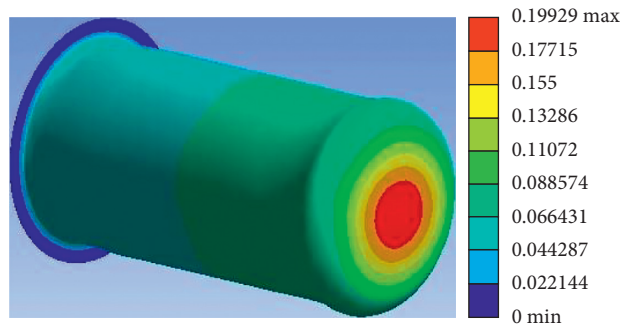


FIGURE 21: Total deformation cloud of the flame tube without coupling.

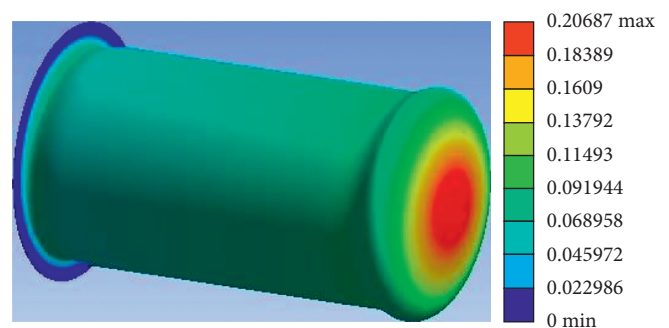


FIGURE 22: The total deformation cloud diagram of the flame tube in the coupled case.

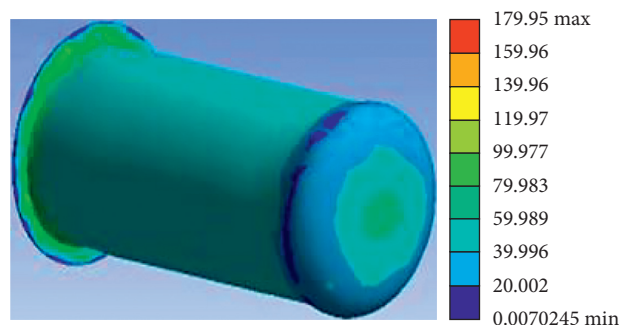


FIGURE 23: Equivalent stress cloud diagram of the uncoupled flame tube.

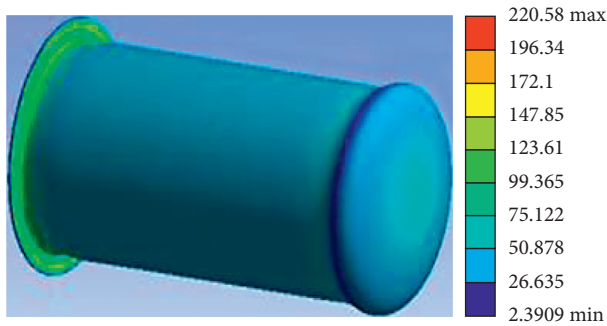


FIGURE 24: Equivalent stress cloud diagram of the coupled flame tube.

coupling, the stress distribution in the head part of the flame tube is very uneven, and the stress in the top area of the head is relatively high, and the stress gradually decreases to the surroundings with the center of the head as the origin. In the case of multifield coupling, the stress distribution of the flame tube body is very uniform, and the stress value is also significantly higher than the stress value of the static force field. The reason for this phenomenon is that the flame tube body is affected by the temperature field, which changes the physical properties of the material to a certain extent. The existence of the temperature field increases the thermal stress of the flame tube itself, so that the stress of the flame tube itself is clearly greater than the stress in the static field. Obviously, it can be seen that the temperature field affects the internal molecular motion state of 316 L stainless steel, and when the multifield coupling is superimposed, the material stress is more obvious.

Figures 25 and 26 are the equivalent strain cloud diagram of the flame tube in the uncoupled case and the equivalent strain cloud diagram of the flame tube in the coupled case. From these two cloud diagrams, the influence of the temperature field on the strain of the flame tube can be seen. In Figure 25, it can be seen that the strain distribution of the flame tube in the static field is uneven, and the strain on the tube section and the top of the head is larger, and this part of the region is similar to the region with greater stress. In Figure 26, the strain distribution of the flame tube is relatively uniform. Under the action of the temperature field, the strain of the flame tube has increased, and the strain values of each area are also relatively close. It can be seen that the temperature field has a great influence on the flame tube.

9. Structural Optimization and Thermal Efficiency Analysis of High-Efficiency Oil-Fired Submersible Hot Water Machine

The thermal efficiency of oil-fired hot water machines has always been one of the focuses of people's research. The level of thermal efficiency directly affects the performance of the hot water machine. People mainly use two ways to improve thermal efficiency. One is to make fuel burn more. Sufficient, the second is to reduce the exhaust heat temperature of the flue gas by designing a reasonable structure. The fuel can be

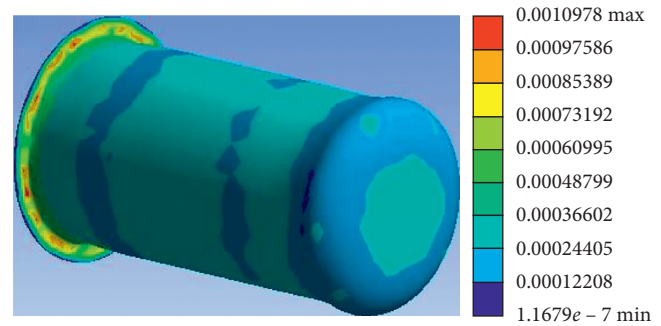


FIGURE 25: Equivalent strain cloud diagram of the uncoupled flame tube.

burned more fully by designing a reasonable combustion method.

9.1. Thermal Field Analysis of the Threaded Pipe. The factor of air supply is very important to whether the combustion reaction is sufficient. For this reason, it is necessary to establish the relationship between the change of the burner over time and the amount of air required. In Section 2.2, the theoretical air volume $V^0 = 11.153276 \text{ m}^3/\text{kg}$ has been calculated. The so-called theoretical air volume is the volume of air required when 1 kg of fuel is completely burned.

At time x , when y kg of 0# diesel is completely burned, the amount of air consumed is shown as follows:

$$dU = 11.153276 dx dy. \quad (32)$$

Integrating equation (32), we can get

$$U = \iint_D dU = \iint_D 11.153276 dx dy = 11.153276 xy, \quad (33)$$

where definition domain $D = \{(x, y) | x \geq 0, y \geq 0\}$, D is the consumption of 0# diesel oil, kg.

The actual amount of gas produced by the hot water machine can be obtained through experiments. The relationship between the air supply volume and the thermal efficiency can be established by curve fitting through multiple sets of data.

9.2. Structural Optimization Model and Solution of Hot Water Machine. The parameters of the threaded pipe are thread radius (radius is divided into outer diameter, middle diameter, and inner diameter), length, wall thickness, pitch, arc radius, and thread groove depth. In order to ensure that the overall structure of the hot water machine does not undergo major changes, in the structural parameters of the threaded tube, the outer diameter of the threaded tube is limited to ensure that the structural parameters of the smoke chamber do not change. The relationship between the other parameters of the threaded tube and the thermal efficiency is now studied. By establishing the mathematical model of the relationship between the threaded tube of the hot water machine and the thermal efficiency, the influence of the threaded tube on the thermal efficiency is obtained.

The Newtonian cooling formula is shown as follows:

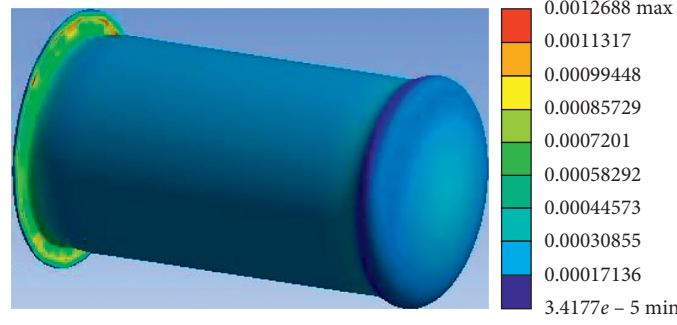


FIGURE 26: Equivalent strain cloud diagram of the coupled flame tube.

$$\Phi = hA(T_w - T_f), \quad (34)$$

where Φ is the convection heat transfer, W; h is the convection heat transfer coefficient, W/(m²·K); A is the heating surface area, m²; T_w is the temperature of the fire tube wall surface, °C; and T_f is the working fluid temperature, °C.

The general relationship of the convective heat transfer coefficient is shown as follows:

$$h = \frac{-\lambda \partial T / \partial y|_{y=0}}{T_w - T_f}, \quad (35)$$

where λ is the thermal conductivity of the working fluid water, $\lambda = 7.42 \times 10^{-2}$, W/(m²·K), and $\partial T / \partial y|_{y=0}$ is the temperature change rate of the working fluid water in the normal direction of the fire tube wall, °C.

The area of the heating surface is shown as follows:

$$A = N \left[L_1 \pi d + L_2 / s \cdot \sqrt{(\pi d_1)^2 + s^2} \cdot \left(\frac{\arccos \left(\sqrt{r'^2 - (r' - t')^2} / r' \right)}{\pi} 2\pi r' - 2\sqrt{r'^2 - (r' - t')^2} \right) \right]. \quad (36)$$

where N is the number of threaded pipes, $N = 16$; L_1 is the total length of the threaded pipe, $L_1 = 0.71$ m; L_2 is the thread length of the threaded pipe, m; d is the outer diameter of the threaded pipe, $d = 0.032$ m; d_1 is the inner diameter of the threaded pipe, m; s is the thread pitch of the threaded pipe, m; t' is the inner diameter of the thread groove, m; and r' is the arc radius of the threaded pipe, m.

When burning 1 kg of 0# diesel, the heat absorbed by the working fluid water through convection heat transfer is shown as follows:

$$Q_{dl} = \int_T \Phi dt. \quad (37)$$

9.2.1. *Objective Function.* After substituting the corresponding values, the objective function of the ratio of the heat absorbed by the working fluid through the convection of the fire tube wall to the total heat transfer can be obtained as follows:

$$f(X) = -\lambda \frac{\partial T}{\partial y} \Big|_{y=0} \frac{1.14x_3 + 32x_1 \cdot \sqrt{(\pi x_2)^2 + x_3^2} \cdot \left(x_4 \arccos \left(\sqrt{x_4^2 - (x_4 - x_5)^2} / x_4 \right) - \sqrt{x_4^2 - (x_4 - x_5)^2} \right)}{42900x_3}. \quad (38)$$

The design variables are shown as follows:

$$X = [x_1, x_2, x_3, x_4, x_5]^T, \quad (39)$$

where x_1 is the thread length of the threaded pipe, m; x_2 is the inner diameter of the threaded pipe, m; x_3 is the thread pitch of the threaded pipe, m; x_4 is the arc radius of the threaded pipe, m; and x_5 is the thread groove depth, m.

$$\begin{cases} 0 \leq x_1 \leq 0.700, \\ 0.028 \leq x_2 \leq 0.032, \\ x_3 > 0.010, \\ 0.005 \leq x_5 \leq 0.015, \\ 0 \leq x_5 \leq 0.004. \end{cases} \quad (40)$$

9.2.2. *Constraints.* The constraint condition is shown as follows:

9.2.3. *Optimization Methods and Results.* The thermal efficiency structure model of the hot water machine is optimized by genetic algorithm. Genetic algorithm is an

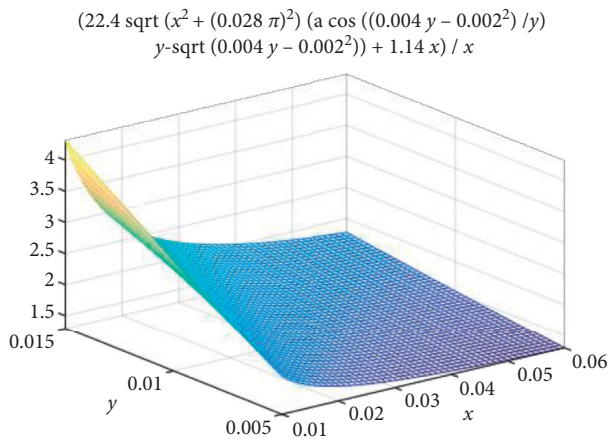


FIGURE 27: Change of heated area of the threaded pipe.

algorithm that simulates the evolutionary laws of the biological world. By searching from random initial solutions, after a series of selection, crossover, and mutation steps, new ones are gradually calculated solution. The genetic algorithm can solve the structural optimization model of the thermal efficiency of the water heater better and faster, making the structural optimization of the water heater more accurate.

The MATLAB genetic algorithm optimizes the heating area of the threaded tube and draws the coordinate image with the pitch of the threaded tube and the radius of the arc as the independent variables. It can be seen from Figure 27 that when the thread pitch is 15 mm and the arc radius is 10 mm, the heated area of the threaded tube reaches the maximum.

10. Conclusion

The simulation results were compared with the theoretical calculation results, and the reliability of the simulation and the rationality of the structure design were obtained. The fluent software was used to simulate the thermal field of the flame tube and the threaded tube, and the rationality and accuracy of the thermal field of the flame tube and the threaded tube were obtained.

- (1) The influence of the thermal structure coupling of the flame tube of the oil-fired submersible hot water machine was analyzed and studied. The total deformation cloud image, equivalent stress cloud image, and equivalent strain cloud image obtained by the thermal structure coupling results were compared with the corresponding cloud image under the action of the static force field. The influence of the temperature field on the flame tube of the oil-fired submersible hot water machine was explored.
- (2) The thermal efficiency of the oil-fired submersible hot water machine was studied, the air supply model of the burner and the thread convection heat transfer model were established, and the genetic algorithm was optimized for the established model.

This article was to study the process of material compression molding and took out the part that involved heat separately for more comprehensive and in-depth research, so as to gain more experience and ideas [22].

Data Availability

The data used to support the findings of this study are included within the article.

Conflicts of Interest

The authors declare that they have no conflicts of interest.

Acknowledgments

This article belongs to the project of the “The University Synergy Innovation Program of Anhui Province (GXXT-2019-004)” and to the project of the “Teaching Research Project of Anhui Education Department (2019jyxm0229).”

References

- [1] S. S. Rashwan, A. H. Ibrahim, T. W. Abou-Arab, M. A. Nemitallah, and M. A. Habib, “Experimental study of atmospheric partially premixed oxy-combustion flames anchored over a perforated plate burner,” *Energy*, vol. 122, pp. 159–167, 2017.
- [2] E. M. Wanjiru, S. M. Sichilalu, and X. Xia, “Optimal operation of integrated heat pump-instant water heaters with renewable energy,” *Energy Procedia*, vol. 105, pp. 2151–2156, 2017.
- [3] A. Yurtsev and G. P. Jenkins, “Cost-effectiveness analysis of alternative water heater systems operating with unreliable water supplies,” *Renewable and Sustainable Energy Reviews*, vol. 54, pp. 174–183, 2016.
- [4] H. Upadhye, R. Domitrovic, and A. Amarnath, “Using locational marginal pricing to implement peak load shifting with a grid connected water heater,” *Ashrae Transactions*, 2013.
- [5] K. Faloon, “Water heaters face 2015 mandate,” *Supply House Times*, vol. 56, no. 9, pp. 36–37, 2013.
- [6] G. Johnson and I. Beausoleil-Morrison, “The calibration and validation of a model for predicting the performance of gas-fired tankless water heaters in domestic hot water applications,” *Applied Energy*, vol. 177, pp. 740–750, 2016.
- [7] R. Lenhard and M. Malcho, “Numerical simulation device for the transport of geothermal heat with forced circulation of media,” *Mathematical & Computer Modelling*, vol. 57, no. 1–2, pp. 111–125, 2013.
- [8] Z. Liu, H. Li, K. Liu, H. Yu, and K. Cheng, “Design of high-performance water-in-glass evacuated tube solar water heaters by a high-throughput screening based on machine learning: a combined modeling and experimental study,” *Solar Energy*, vol. 142, pp. 61–67, 2017.
- [9] C. He, A. Giannis, and J.-Y. Wang, “Conversion of sewage sludge to clean solid fuel using hydrothermal carbonization: hydrochar fuel characteristics and combustion behavior,” *Applied Energy*, vol. 111, pp. 257–266, 2013.
- [10] J. Bujak and P. Sitarz, “Incineration of animal by-products—the impact of selected parameters on the flux of flue gas enthalpy,” *Waste Management*, vol. 50, pp. 309–323, 2016.
- [11] M. Qu, O. Abdelaziz, and H. Yin, “New configurations of a heat recovery absorption heat pump integrated with a natural

- gas boiler for boiler efficiency improvement,” *Energy Conversion and Management*, vol. 87, pp. 175–184, 2014.
- [12] GB/T10180-2003, “Industrial boiler energy efficiency test and evaluation rules,” *China Quality and Technical Supervision*, no. 12, pp. 20–23, 2010.
- [13] H. Wang and L. Meng, “Present situation and direction of development of model WNS oil/gas fired boiler technology,” *Journal of Engineering for Thermal Energy and Power*, no. 2, pp. 115–118 + 212, 2002.
- [14] H. Huang, Z. Wu, G. Li, and J. Tan, “Improved design of an oil-fired hot-water boiler and its analysis,” *Journal of Engineering for Thermal Energy and Power*, no. 5, pp. 461–464 + 543, 2006.
- [15] M. Souliotis, S. Papaefthimiou, Y. G. Caouris, A. Zacharopoulos, P. Quinlan, and M. Smyth, “Integrated collector storage solar water heater under partial vacuum,” *Energy*, vol. 139, pp. 991–1002, 2017.
- [16] A. Hossain and Y. Nakamura, “Thermal and chemical structures formed in the micro burner of miniaturized hydrogen-air jet flames,” *Proceedings of the Combustion Institute*, vol. 35, no. 3, pp. 3413–3420, 2015.
- [17] F. Song, Z. Wen, Z. Dong, E. Wang, and X. Liu, “Ultra-low calorific gas combustion in a gradually-varied porous burner with annular heat recirculation,” *Energy*, vol. 119, pp. 497–503, 2017.
- [18] L. Dong, Y. Suzuki, and N. Kobayashi, “Experimental study on the performance of a hybrid water heater,” *International Journal of Chemical Reactor Engineering*, vol. 7, no. 1, 2009.
- [19] K. Tanha, A. S. Fung, and R. Kumar, “Performance of two domestic solar water heaters with drain water heat recovery units: simulation and experimental investigation,” *Applied Thermal Engineering*, vol. 90, pp. 444–459, 2015.
- [20] R. Manimaran and R. Senthilkumar, “Performance analysis of solar water heater at possible flow rates with and without phase change material,” *Distributed Generation & Alternative Energy Journal*, vol. 31, no. 1, 2015.
- [21] S. Pudaruth, J. T. Devi, and U. Y. Koodruth, “Understanding the ecological adoption of solar water heaters among customers of island economies,” *Studies in Business & Economics*, vol. 12, no. 1, 2017.
- [22] Y. Wang, Z. Zhu, L. Tang, and Q. Jiang, “Research on the molding design and optimization of the molding process parameters of the automobile trunk trim panel,” *Advances in Materials Science and Engineering*, vol. 2020, Article ID 5629717, 19 pages, 2020.